

https://dspace.org/

Massive magnetitite layers of the bushveld complex, South Africa: geology, geochemistry, and genesis

Kruger, Willem Abram Jacobus

2021

https://hdl.handle.net/10539/32474

Downloaded from a DSpace repository. https://dspace.org/

MASSIVE MAGNETITITE LAYERS OF THE BUSHVELD COMPLEX, SOUTH AFRICA: GEOLOGY, GEOCHEMISTRY, AND GENESIS

Willem Abram Jacobus Kruger

A dissertation submitted to the Faculty of Science, University of the Witwatersrand, in fulfilment of the requirements for the degree of Doctor of Philosophy.

Johannesburg, 24 January 2021

DECLARATION

I declare that this thesis is my own, unaided work. It is being submitted for the Degree of Doctor of Philosophy at the University of the Witwatersrand, Johannesburg. It has not been submitted before for any degree or examination at any other University.



_____

(Signature of candidate)

24th of November 2021 at Brits

ABSTRACT

The petrogenesis of monomineralic rocks in layered intrusions is a petrological enigma containing important clues regarding the inner workings of magma chambers. Massive magnetitite layers of the Bushveld Complex, South Africa, are particularly useful to unravel magma chamber processes due to the exceptionally high crystal/liquid partition coefficients of Cr in magnetite. By studying the field relationships and distribution of Cr within and across the lowermost massive magnetitite layers of the Complex, new insights are derived regarding some of the most fundamental questions pertaining to our understanding of magmatic crystallization and differentiation. These include where and how do crystals accumulate, what is the thickness of crystal mushes in magma chambers, and how does crystal/liquid fractionation occur to drive magmatic evolution. Two-dimensional geochemical maps of magnetitite layers reveal fossilized solidification fronts that strongly argue for the *in situ* crystallization of this rock type as indicated by the presence of Cr-rich, dome-shaped growth nodes, the accumulation of magnetite on sub-vertical footwalls, and the outward growth of magnetitite on anorthositic inclusions. Extremely steep Cr gradients, coupled with a near-constant V concentration, show that the solidification front propagates as a near-solid surface, suggesting that crystal mushes may not be of significant thicknesses in layered intrusions. The latter requires effective exchange of liquid at the solidification front by the convective removal of thin compositional boundary layers surrounding magnetite crystals. Depressions in the anorthositic footwall underneath massive magnetitite layers together with the presence of an interconnected network of anorthosite inclusions suggest that thermochemical erosion (or magmatic karstification) of the basal cumulates occurred prior to massive magnetitite crystallization. This observation, along with large Cr reversals recorded in massive magnetitite layers, suggest magmatic recharge preceded the formation of this rock type. A pressure reduction associated with magmatic ascent from a deeper seated staging chamber, possibly coupled with contamination of the melt by crustal material, ensured the production of a relatively Cr-rich, superheated melt capable of crystallizing only magnetite upon entry and cooling in the Bushveld magma chamber. Mixing between the incoming and resident melt is responsible for the formation of anorthositic footwalls commonly associated with the massive magnetitite.

ACKNOWLEDGEMENTS

First and foremost I would like to thank my supervisor, Rais Latypov, for his dedication, commitment, and passion towards this project. His help and guidance significantly enhanced the quality of the work presented in this thesis. I would like to express my sincere gratitude for the funding provided by DST-NRF Centre of Excellence for Integrated Mineral and Energy Resource Analysis (CIMERA) without which this project would not have been possible. Special thanks goes out to all the kind staff members who assisted me with my fieldwork and data collection at the Rhovan and Vametco vanadium mines. Furthermore, I would like to thank Merrily Tau for his assistance in analysing outcrops with the portable XRF spectrometer in the Magnet Heights locality. Thanks to Sofya Chistyakova for her help improving the quality of figures presented in Chapter 2 of this thesis, as well as preparing supplementary figures for Chapter 3 and her occasional assistance with field work. Finally, I would like to thank Grant Bybee for assistance in performing modelling with the MELTS algorithm and his occasional advice provided during the course of this project.

TABLE OF CONTENTS

DECLARATION i

ABSTRACT ii

ACKNOWLEDGEMENTS iii

LIST OF FIGURES ix

CHAPTER 1: INTRODUCTION 1

1.1 Background information 1

1.2 Problem statement 2

1.2.1 Fundamentals regarding the inner workings of magma chambers 2

1.2.2 Origin of massive magnetitite layers in the Bushveld Complex 4

1.3 Aims and objectives 6

1.3.1 Data collection 6

1.3.2 Determining the thickness of the crystal mush during magnetitite crystallization 7

1.3.3 Determining the means of the accumulation of crystals in magnetitite layers 8

1.3.4 Constraining the mechanisms of differentiation during the crystallization of magnetitite 8

1.3.5 Unravelling the origin of massive magnetitite layers 9

1.4 Thesis outline 9

1.4.1 Chapter 2 9

1.4.2 Chapter 3 10

1.4.3 Chapter 4 10

1.4.4 Chapter 5 10

1.4.5 Chapter 6 11

CHAPTER 2: METHODOLOGY 12

2.1 Chemical analysis with the portable XRF and quantification of data. 12

2.2 Procedures for geochemical modelling for the Main Magnetite Layer in Chapter 3.... 14
2.2.1 Equations employed and two-dimensional modelling....14
2.2.2 Choice of partition coefficients....15
2.3 Properties of a compositional boundary layer....16
2.4 Sample collection, chemical analysis, and field observations for Chapter 5 17
CHAPTER 3 FOSSILIZED SOLIDIFICATION FRONTS IN THE BUSHVELD COMPLEX ARGUE FOR LIQUID-DOMINATED MAGMATIC SYSTEMS 19
3.1 Introduction 20
3.2 Results 22
3.2.1 Geochemical maps. 22
3.2.2 Geochemical modelling. 28
3.3 Discussion 33
3.4 Acknowledgements 37
3.5 Supplementary information....38
CHAPTER 4: MAGMATIC KARST REVEALS DYNAMICS OF CRYSTALLIZATION AND DIFFERENTIATION IN EARTH'S MAGMA CHAMBERS....39
4.1 Introduction 40
4.2 Chemical patterns in massive magnetitite....41
4.3 The phenomenon of the undercut-embayed floor 43
4.4 Magmatic karstification of the floor cumulates 44
4.5 Challenging the fundamentals of magma chamber dynamics....45
4.6 Most profound implications for magma chamber dynamics....49
4.7 Acknowledgements 51
4.8 Supplementary material....52
CHAPTER 5 FIELD AND GEOCHEMICAL CONSTRAINTS ON THE ORIGIN OF THE LOWERMOST MASSIVE MAGNETITITE LAYERS OF THE BUSHVELD COMPLEX, SOUTH AFRICA....55
5.1 Introduction 56

5.2 Regional geology....59
5.3 Methods....60
5.4 Results....60
5.4.1 Field relations....60
5.4.2 Petrography....65
5.4.3 Geochemistry....69
5.5 Review of previous models on magnetitite petrogenesis....73
5.5.1 Late gravitative liquid accumulation by Bateman (1951)....75
5.5.2 Contamination by granitic melt of Irvine (1975)....77
5.5.3 Pressure increase and latent heat build-up of Cawthorn and McCarthy (1980) 78
5.5.4 In situ fractionation of plagioclase to produce massive magnetitite of Reynolds (1985b) 80
5.5.5 Variation in oxygen fugacity of Klemm et al. (1985)....82
5.5.6 Magma addition and thermal erosion of Butcher and Merkle (1991) 84
5.5.7 Breakdown of density stratified liquid layers by Harney and Von Gruenewaldt (1995) 85
5.5.8 Crystallization of magnetitite in a double-diffusive-convective system by Tegner et al. 2006 87
5.5.9 Magmatic recharge and crystal settling of Scoon and Mitchell (2012)....88
5.5.10 Hydrodynamic sorting of cumulate slurries by Maier et al. (2013)....90
5.5.11 Magma mixing model of Yuan et al. (2017)....91
5.5.12 Pressure reduction during magmatic ascent by Latypov et al. (2018)....93
5.5.13 Magnetite accumulation by flotation on bubbles by Knipping et al. (2019) 94
5.5.14 Liquid immiscibility of Vukmanovic et al. 2019....95
5.6 Formation of massive magnetitite layers 96
5.6.1 In situ crystallization versus crystal settling/sorting....97
5.6.2 Possible origins for the Cr reversal associated with massive magnetitite 97
5.6.3 Origin of magnetitite footwall depressions and anorthositic inclusions....98

5.6.4 Upper Zone of the Bushveld Complex: open or closed system? 104
5.6.5 Origin of a magnetite-alone saturated melt 107
5.7 Magmatic differentiation during magnetitite crystallization 108
5.8 Controls on the magnetitite solidification front propagation pattern 110
5.9 Origin of gradational upper contact and non-massive portions of magnetitite layers 114
5.9.1 Previous work 114
5.9.2 Geochemical constraints on the formation of non-cotectic cumulates 116
5.9.3 Field constraints on the formation of the gradational upper contact 118
5.9.4 Model for the formation of the upper gradational contact 122
5.10 Origin of underlying anorthosite layers 125
5.10.1 Comments on previous work 125
5.10.2 Proposed model to produce underlying anorthosite layers 128
5.11 Conclusion 131
CHAPTER 6: CONCLUSIONS 134
6.1 Thickness of the crystal mush during magnetitite crystallization 134
6.2 Means of crystal accumulation in magnetitite layers 134
6.3 Mechanism of differentiation of during the crystallization of magnetitite 135
6.4 Origin of massive magnetitite layers in the Bushveld Complex 136
6.5 General implications for magma chamber dynamics and future research 137
REFERENCES 138
APPENDICES 156
Appendix A 156
Appendix B 158
Appendix C 184
Appendix D 202
Appendix E 214

Appendix F.....238

LIST OF FIGURES

Figure 3.1 Potential magma reservoirs geometries and mechanisms for their evolution 21

Figure 3.2 The Main Magnetite Layer at Magnet Heights from the Eastern Bushveld Complex.. 23

Figure 3.3 Two-dimensional geochemical maps of basal part of the Main Magnetite Layer with a planar basal contact. 24

Figure 3.4 Geochemical map of basal part of the Main Magnetite Layer that contains a sub-rounded anorthosite autolith.. 25

Figure 3.5 Geochemical map of basal part of the Main Magnetite Layer with a sub-vertical footwall contact. 26

Figure 3.6 Two-dimensional geochemical modelling of Cr in the Main Magnetite Layer. ...31

Figure 3.7 One dimensional geochemical modelling of Cr and V in the Main Magnetite Layer.. 32

Figure 3.8 The comparative behaviour of compatible trace elements in magmatic systems with perfect and imperfect liquid fractionation.....34

Figure 3.9 A physical model for chemical differentiation of the Main Magnetite Layer in the Bushveld Complex. 35

Figure 4.1 Massive magnetitite with two-dimensional Cr chemical patterns. 42

Figure 4.2 One-dimensional vertical profiles in Cr content across a massive magnetitite. 43

Figure 4.3 Physical model for the origin of the undercut-embayed chamber floor and propagation of a solidification front therein.. 46

Figure 4.4 Artistic impression of the undercut-embayed chamber floor in an evolving magma chamber along with interpretive sketches of relevant exposures.....47

Figure 5.1 Geological map of the Bushveld Complex. 58

Figure 5.2 Typical appearance of magnetitite from the Bushveld Complex.. 61

Figure 5.3 Appearance of the upper portion of the Bottom seam from the Western Bushveld Complex..62

Figure 5.4 Irregularities observed in the footwall contact between magnetitite and anorthosite..63

Figure 5.5 Anorthositic inclusions in magnetitite layers from the Bushveld Compex..64

Figure 5.6 Fragments of magnetitite layer 1 scattered in overlying magnetite anorthosite. ..65

Figure 5.7 Textural and mineralogical features of massive magnetitite layers and adjacent rock types of the Bushveld Complex.67

Figure 5.8 Variation in Cr in magnetite across a section of the base of the Upper Zone of the Bushveld Complex, Western Limb, Rhovan vanadium mine.71

Figure 5.9 Variation in Cr and V in magnetite across two thin magnetitite layers from the Rhovan drill core.72

Figure 5.10 Average, minimum, and maximum Cr contents measured at the very bases of the Main Magnetite Layer and the Bottom seam with a portable XRF spectrometer from the Western Bushveld Complex..73

Figure 5.11 Vertical profiles through the Bottom seam and the Main Magnetite Layer from the Western Limb of the Bushveld Complex.74

Figure 5.12 Lateral variation in the Cr contents along the base of the Main Magnetite Layer, Eastern Bushveld Complex, Magnet Heights.75

Figure 5.13 Late gravitative liquid accumulation model of Bateman (1951).76

Figure 5.14 Origin of massive magnetitite layers by the contamination of granitic roof rocks by Irvine (1975).77

Figure 5.15 Model for the origin of magnetitite based on a compilation of work from Cawthorn and McCarthy (1980; 1981; 1983), McCarthy et al. (1985), and Cawthorn (1994).79

Figure 5.16 A model involving the in situ fractionation of plagioclase by Reynolds (1985b) for the origin of massive magnetitite.81

Figure 5.17 Increase in the melt's oxygen fugacity to crystallize magnetitite of Klemm et al. (1985)..... 82

Figure 5.18 Average, minimum, and maximum V contents of titano-magnetite in disseminated and massive ore from the Rhovan vanadium mine, Western Bushveld Complex..... 83

Figure 5.19 Intermittent thermal erosion and crystallization model of Butcher and Merkle (1991)..... 85

Figure 5.20 Model for the origin of massive magnetitite layers of Harney and Von Gruenewaldt..... 86

Figure 5.21 Model for the origin of magnetitite layers of Scoon and Mitchell (2012).. 89

Figure 5.22 Model for the origin of massive magnetitite layers by Maier et al., (2013)..... 91

Figure 5.23 Model for the origin of massive magnetitite layers by Yuan et al. (2017)..... 92

Figure 5.24 Model for the origin of massive magnetitite layers by Latypov et al. (2018). 93

Figure 5.25 Model for the origin of magnetitite atop anorthosite by Knipping et al. (2019). 94

Figure 5.26 Model for the origin of massive magnetitite from Vuknamovic et al. (2019).... 96

Figure 5.27 Potential models to explain the origin of anorthosite inclusions in massive magnetitite..... 102

Figure 5.28 The origin of diverse one-dimensional Cr profiles across a magnetitite layer with inclusions.. 103

Figure 5.29 Compilation of strontium isotopic data across a section of the Lower Main Zone, Upper Main Zone, and the Upper Zone from the Western Bushveld Complex (modified from Tegner et al., 2006)..... 106

Figure 5.30 Magmatic differentiation during the crystallization of magnetite. 109

Figure 5.31 The formation of a magnetitite growth node and the transition from intially radial outwards growth to lateral growth. 112

Figure 5.32 Morphology of the solidification front above an inclusion in magnetitite. 113

Figure 5.33 Upper gradational contact of the Bottom seam from Rhovan.. 115

Figure 5.34 Variations in whole-rock Ce contents depending on the magnetite content of rocks containing only plagioclase and titano-magnetite primocrysts.....119

Figure 5.35 Variations in selected whole-rock incompatible element contents depending on the magnetite content of rocks containing only plagioclase and titano-magnetite primocrysts. 120

Figure 5.36 Detailed look at the variation in Cr in magnetite across a portion of the Bottom seam from Vametco containing non-cotectic proportions of primocrysts of plagioclase and magnetite......121

Figure 5.37 Transition from a solid solidification front in massive magnetitite to a partially liquid solidification front in the overlying magnetite anorthosite. 123

Figure 5.38 Evolution of melt within a liquid boundary layer atop a magnetitite solidification front......126

Figure 5.39 Variation of whole-rock of P_2O_5 in a section of the Rhovan drill core.. 128

Figure 5.40 Model for the origin of anorthosite layers underneath magnetitite layers.....129

Figure 5.41 Model for the origin of massive magnetitite layers of the Bushveld Complex 133

CHAPTER 1

INTRODUCTION

1.1 Background information

Through countless times in Earth's history, the mantle has undergone partial melting to produce basaltic melts that may rise to eventually intrude the planet's crust. As these melts slowly lose heat to their surroundings, they gradually crystallize, possibly producing layers that may in some cases consist of valuable ore deposits. When solidification is complete, a fossilized magma chamber is left behind, preserving important clues to the processes that occurred within the magmatic system. Through the processes of upheaval and erosion, the structure may eventually become exposed on the planet's surface, enabling us to study its various intricate features. Attempts to decipher the processes that occur within such layered intrusions have preoccupied the minds of igneous petrologists for more than a century. Curiously, even after all this time, very few petrologists can agree on some of the most fundamental questions on the topic. This thesis is an attempt to gain a better understanding of magma chamber dynamics by studying an extraordinary rock type capable of providing unique insights into this debate: the massive magnetitite layers of South Africa's Bushveld Complex.

In our simplest understanding of the evolution of basaltic magma chambers, melts are supposed to evolve primarily along cotectics and eutectics in temperature-compositional space as different phases are incrementally added to the liquidus. This crystallization trend results in rocks with well-defined proportions of minerals (Bowen, 1928; Roeder and Osborn, 1966; Kushiro, 1969). A great challenge that petrologists face is the occurrence of stratiform monomineralic rocks within layered intrusions that consist of a specific mineral that is only supposed to join the liquidus assemblage after other minerals have already started crystallizing. Examples of such rock types include chromitites, anorthosites, and magnetitite layers, all of which can be found within the Bushveld Complex. The existence of such monomineralic rocks indicates that some process occurs within magma chambers that we do not yet fully understand, although many diverse and conflicting hypotheses have been proposed (Wager and Brown, 1968; Cawthorn, 1996a; Charlier *et al*., 2015).

The problem most likely persists because we cannot understand the formation of monomineralic rocks in layered intrusions without understanding the fundamentals of how layered intrusions crystallize and differentiate. For example, one of the most important unresolved questions that stand in our way deals with the means by which crystals accumulate in magma chambers. Do they nucleate and crystallize within the interior of the magma chamber then settle out under the influence of gravity? Or do they rather crystallize *in situ*, i.e. crystals nucleate and grow directly on the outer margins of the chamber? A second important question is how crystal/liquid fractionation occurs to produce the wide variety of igneous rocks we observe in fossilized magma chambers. Common mechanisms proposed for this process include crystal settling, compaction of crystal mushes, diffusion, or compositional convection. A more recent paradigm also questions the degree to which magma chambers are dominated by crystal-free melt (Cashman *et al*., 2017). In contrast to the classic idea that magma chambers crystallize from large volumes of crystal-free melt, this new paradigm suggests that magma chambers are only composed of mixtures of crystal-rich mushes that form large trans-crustal magmatic systems. The aim of this study is to vigorously test the above hypotheses dealing with the inner workings of magma chambers by studying the field and geochemical characteristics of massive magnetitite layers in the Bushveld Complex. Only once this feat has been accomplished is an attempt made to solve the decades-old mystery regarding the origin of this rock type.

1.2 Problem statement

A brief discussion now follows of the different ideas regarding the issues outlined above by different investigators.

1.2.1 Fundamentals regarding the inner workings of magma chambers

1.2.1.1 The thickness of the crystal mush in magma chambers

In our classical view of basaltic magma chambers, they are envisioned as large bodies of liquid that crystallize from the margins inwards in structures called solidification fronts (Marsh, 1996; Marsh, 2013). Such structures have previously been observed by drilling into Hawaiian lava lakes (Heltz, 1987). A solidification front can be defined as the portion of the magma chamber that is thermally located between the liquidus of the chamber interior and the final solidus of the magma. Therefore, it consists of a mixture of both solids and melt, i.e. a crystal mush. The thickness of the crystal mush within magma chambers has been the topic of much debate. Some textural (Holness *et al*., 2017a) and field evidence (Hess, 1960; Thompson and Patrick, 1968)

seem to suggest that crystal mushes may be no more than 4 metres thick. On the other hand, Tait and Juapart (1989) argued that a 100 m thick crystal mush must form prior to the onset of compositional convection and magmatic differentiation in magma chambers. Maier *et al*. (2013) proposed that the hydrodynamic sorting of thick (possibly several dozens of metres) crystal mushes are responsible for the origin of layering in the Bushveld Complex, including the origin of massive magnetitite. On the extreme end of the argument, Cashman *et al*. (2017) argue that the classic view of liquid-dominated magma chambers is incorrect, and that magma chambers are entirely composed of crystal-rich mushes. The latter is based on a lack of geophysical data supporting the existence of a large magma chamber underneath Yellowstone supervolcano in the United States, as well as crystals from volcanic rocks recording complex zoning patterns suggesting complicated crystallization histories. Within the crystal mush, lenses of melt-rich areas may exist, but they are considered small and short-lived.

1.2.1.2 Means of accumulation of crystals in magma chambers

This issue deals with how new crystals are added to a solidification front during magmatic crystallization. One of the most influential papers on the subject was published by Bowen (1915) when he observed the settling of olivine crystals within small platinum crucibles. Since then, the concept of crystal settling became popular among igneous petrologists, with the process being heavily favoured to explain igneous layering in Wager and Brown's (1968) famous publication on layered igneous rocks. The idea of crystal settling generally involves the growth of crystals in areas where cooling is most significant (for example the flanks or roof of the chamber), and are then brought to the chamber floor under the influence of gravity. This may happen in the form of density currents (Irvine, 1980), or plumes of crystals and melt descending from the roof of the chamber, called two-phase convection (Morse, 1986a; 1988; Cawthorn, 2019). Alternatively, crystals that formed in the chamber interior may never settle out at all, as thermal convection keeps the crystal suspended until an immobile mush results (Bachman and Bergantz, 2004; Bea, 2010).

In contrast to the above models, Jackson (1961) reasoned that crystals crystallized and grew close to the bottom of the Stillwater Complex, a process referred to as bottom crystallization. This was deemed possible because, although most heat is lost through the chamber roof (e.g. Wager, 1963; Morse, 1986a), the density gradient may favour crystallization on the chamber floor. Campbell (1978) later presented several lines of evidence for the *in situ* crystallization for the Jimberlana intrusion in Australia, and also presented general arguments for why *in situ* crystallization may be more favourable in layered intrusions. Since then, several investigators

have accumulated additional geochemical and field data that may provide support for the *in situ* crystallization model (McBirney and Noyes, 1979; Cawthorn & McCarthy, 1980; Latypov and Egovora, 2012; Latypov *et al*, 2016; Latypov *et al*., 2020). Nevertheless, the relative degrees that crystal settling and *in situ* crystallization contributes to the formation of layered intrusions is an ongoing debate (e.g. Cawthorn, 2019; Latypov *et al*., 2020). Both models have been invoked to explain the origin of massive magnetitite as discussed later on.

1.2.1.3 Mechanisms of differentiation of magma chambers

Layered intrusions show a great diversity of the rock types and chemical composition of similar minerals found within. Understanding how such diversity originates is perhaps one of the most important questions to consider when studying these geological phenomena. As stated above, it is generally accepted that this diversity originates due to the separation of crystals and liquid, causing the liquid to continuously change in composition as the intrusion solidifies. There is, however, a lot of debate on the process that causes crystal/liquid fractionation. Once again, crystal settling is a popular hypothesis (Wager and Brown, 1968). Alternatives that are compatible with *in situ* crystallization models include compaction of crystal mushes (e.g. McKenzie, 2011; Namur and Charlier, 2012; Cashman *et al*., 2017), diffusion (possibly with the aid of thermal convection) (Cawthorn and McCarthy, 1980; Morse, 1986b), compositional convection within large crystal mushes (Tait & Juapart, 1989), or the convective removal of small compositional boundary layers surrounding individual crystals (Martin *et al*., 1987; Campbell, 1996; Seedhouse and Donaldson, 1996). As Morse (1986b) rightly put it, it is up to the petrologist to decipher which of these processes (if any) is responsible for the formation of a given suite of rock. Once the above fundamental issues regarding the inner working of magma chambers have received attention can be shifted to the origin of Bushveld magnetitite.

1.2.2 Origin of massive magnetitite layers in the Bushveld Complex

The intrusive and mafic part of the Paleoproterozoic Bushveld Complex, called the Rustenburg Layered Suite (RLS), has garnered fame among petrologists due to its immense size, well-developed layering in some sections, and the presence of world-class deposits of PGE, Cr and V. Despite the fact that the RLS formed via multiple magma recharge events (e.g. Kruger, 1994; Eales, 2002), on a large scale it displays a sequence of cumulates that is broadly consistent with a magmatic system that has undergone closed-system differentiation. On a stratigraphic bases the RLS is subdivided into different zones based on the cumulus mineral assemblage. Above a noritic Marginal Zone (the lowermost unit of the RLS) occurs the Lower

Zone that consists of ultramafic rocks containing cumulus olivine and orthopyroxene. The appearance of cumulus chromite marks the base of the so-called Lower Critical Zone, while the Upper Critical Zone is defined by the appearance of cumulus plagioclase. Above the Upper Critical Zone occurs the Main Zone, a sequence of mostly norite, gabbronorite, and gabbro that is generally poorly layered compared to the remainder of the intrusion. It is within the Upper Zone, marked by the appearance of cumulus magnetite, where massive magnetitite layers occur that are the focus of this study.

Several features are common to most magnetitite layers of the Bushveld Complex that any model dealing with their petrogenesis must be able to account for. These features include: (1) the pure adcumulate nature of these layers that essentially consist of pure titano-magnetite. Any interstitial material is virtually absent and, with some exceptions, other cumulus phases are rare; (2) these layers are commonly underlain by an anorthosite layer with which it shares a macroscopically sharp boundary. The common occurrence of this anorthosite is perhaps one of the most challenging features to explain when dealing with the origin of the magnetitite, to such an extent that most models simply ignore its presence. The occurrence of one monomineralic rock type already provides a significant challenge to petrologists so that the co-occurrence of magnetitite and anorthosite raises the bar of the challenge even higher; (3) the magnetitite layers have gradational contacts into overlying magnetite anorthosite. Pyroxene is notably absent from the cumulus assemblage surrounding many magnetitite layers; (4) magnetitite layers have extreme lateral extent, and some of them can be traced for hundreds of kilometres. No model has thus far been proposed that can adequately explain all these features.

The literature on magnetitite layers neatly illustrates the dilemmas we deal with in igneous petrology. Petrogenetic models are generally polarized in two respects, namely how magnetite crystals accumulate in magma chambers and if a magmatic recharge event is in some way responsible for their formation. In regards to the first issue, research conducted in the 1980s found evidence to support the *in situ* crystallization of these layers in the form of a rapid but very regular upwards depletion in Cr contents in magnetite layers (Cawthorn and McCarthy, 1980; 1981; 1983; McCarthy and Cawthorn, 1983; McCarthy *et al*., 1985). Most importantly, perhaps, is the discovery of Cawthorn (1994) a decade later. By collecting samples along the base of the MML, he noticed extreme lateral variability in the Cr content of the layer. He proposed that high Cr-spots were areas where magnetite first started nucleating and growing on the underlying anorthosite layer, by analogy similar to mould growing on cheese. Although the data appeared erratic with a sample spacing of 50 cm, on a figure he constructed he

demonstrated an anticipated growth of magnetite outwards from initial points where nuclei first appeared to form dome-like structures that he called growth nodes. However, in modern literature, these findings are mostly ignored, and researchers typically favour models that involve some form of crystal settling or sorting (Scoon & Mitchell, 2012; Maier *et al*., 2013; Bilenker *et al*., 2017; Yuan *et al*., 2017; Knipping *et al*., 2019; Vukmanovic *et al*., 2019). The second issue arises from apparently conflicting geochemical data on the Upper Zone of the Bushveld Complex where all massive magnetitite layers are located. For example, Sr-isotope data across the Upper Zone reveals a general consistency in the initial Sr^{87}/Sr^{86} ratios, suggesting the entire 1.5 km thick sequence of rocks crystallized from a single pulse of magma (Kruger *et al*., 1987). This is supported by some geochemical evidence, such as a general lack in significant An reversals in plagioclase in the hangingwall and footwall lithologies across magnetitite layers (Cawthorn and Ashwal, 2009). Some researchers have therefore proposed that magnetitite layers formed due to internal processes such as a pressure increase in the magma chamber (Cawthorn and McCarthy, 1980; Cawthorn and Ashwal, 2009). However, other researchers have recorded geochemical reversals in, for example, Cr in pyroxenes in the Bushveld's Upper Zone (Tanner *et al*., 2014), variations in Mg# of mafic silicates (Scoon & Mitchell, 2012), changes in chondrite normalized PGE patterns across one of the most prominent, 2 m thick magnetitite layers of the Complex, called the Main Magnetite Layer (Harney and Von Gruenewaldt, 1995), or An reversals recorded in the anorthositic footwalls of magnetitite layers (Yuan *et al*., 2017). Most of these authors thus opted for magmatic recharge to explain these features. Some have pointed out, however, that reversals can also be produced by the convective breakdown and mixing of melt layers in a density stratified magma chamber (Harney and Von Greundewaldt 1995; Tegner *et al*., 2006). These models are reviewed in more depth in Chapter 5.

1.3 Aims and objectives

1.3.1 Data collection

Uncertainties regarding the dynamics of magma chambers persist because most rock types in layered intrusions cannot record the processes that occur in the solidification front in sufficient chemical detail. Magnetitite layers are a remarkable exception in this respect because of the extraordinarily high crystal/liquid partition coefficients of Cr in magnetite. Cawthorn and McCarthy (1980) first realized the potential of Cr in magnetite as a very powerful indicator of magmatic processes when they recorded extremely steep chemical gradients in terms of this trace element in vertical profiles across the Main Magnetite Layer. However, since the 1980s

we have experienced a great technological advancement in analytical equipment with the advent of portable X-ray fluorescence spectrometers (pXRF). This instrument allows for rapid chemical analysis directly on field outcrops, enabling the acquisition of hundreds of chemical analyses in just a few hours. A major aim of this study is to analyse outcrops of two prominent magnetitite layers in two dimensions to construct geochemical contour maps focussing on the distribution of Cr. The first is the Main Magnetite Layer (MML) from the Bushveld's Eastern Limb, the same site where Cawthorn and McCarthy (1980) started studying the variation of Cr within these layers. The second is the lowermost magnetitite layer located in an open pit of the Rhovan vanadium mine in the Western Limb of the Bushveld Complex referred to here as the Bottom seam. Additional examples of the Bottom seam and Main Magnetite Layer will also be analysed in drill core provided by the Rhovan and Vametco vanadium mines, both located in the Western Limb of the Complex. Such mapping may provide an unparalleled visualization of the step-wise propagation of a solidification front. In addition, Cr contents in magnetite crystals across a 180 m-thick section near the base of the Upper Zone will also be analysed to observe large scale variations in this trace element across sections bearing several magnetitite layers.

Most previous studies that have focussed on the petrogenesis of massive magnetitite layers focus on their geochemistry (e.g. Cawthorn and McCarthy, 1980; McCarthy *et al*., 1985; Kruger and Smart, 1987; Cawthorn and Ashwal, 2009; Yuan *et al*., 2017) while a recent study has been conducted to look for textural clues regarding their origin (Vukmanovic *et al*., 2019). One aspect that has largely been ignored is the field characteristics of magnetitite layers. A major aim of this study is thus to record the appearance of magnetitite layers in the field and open pits, especially regarding the nature of their contacts with underlying anorthosite layers. In recent years a similar approach has proven fruitful to better understand the formation of chromititite layers and the Merensky Reef of the Bushveld Complex (Latypov *et al*., 2016; Latypov *et al*., 2017a; Pebane and Latypov, 2017; Chistyakova *et al*., 2019).

1.3.2 Determining the thickness of the crystal mush during magnetitite crystallization

As stated above, some researchers have employed field and textural evidence to try and ascertain the thickness of crystal mushes. Here, an approach will be used where the covariance of two trace element with markedly different compatibilities are studied as this can provide constraints on the degree of crystal/liquid fractionation that occurs within the solidification front. This is based on the work of Langmuir (1989) who derived equations demonstrating the

behaviour of trace elements with different compatibilities become more similar as the efficiency of crystal/liquid fractionation decreases. Effective crystal/liquid fractionation also allows for effective crystallization of interstitial liquid and may result in a relatively thin crystal mush (Morse, 1986b; 2002; 2011). In the case of magnetitite, two compatible elements are compared with differing compatibilities, namely Cr with a crystal/liquid partition coefficient in magnetite that varies from 60-600 in basaltic melts (Irving, 1978; Toplis and Corgne, 2002; Castle and Herd, 2017), and V that ranges from about 10 to 30 (Irving, 1978; Toplis and Corgne, 2002). Effective crystal/liquid exchange would ensure maximum depletion of Cr and V during magnetite fractionation. If crystal/liquid exchange is less effective, the depletion of Cr and V will slow down as magnetite crystals will be in contact with more evolved, Cr and V depleted melt. This limits the amount of these trace elements that the crystals can extract from the surrounding liquid. The effect is more pronounced for Cr because of its higher partition coefficient in magnetite compared to V. The more dissimilar the behaviour of Cr and V, the more effective the interstitial liquid crystallizes due to effective liquid exchange, providing a qualitative indication of the thickness of the crystal mush.

1.3.3 Determining the means of the accumulation of crystals in magnetitite layers

An attempt will be made to test for the existence of "growth nodes" that were predicted by Cawthorn (1994) as explained above. By reducing the minimum sample spacing employed by Cawthorn (1994) of 50 cm to just 1.5 cm, and by geochemically mapping outcrops in two dimensions, Cr-contour maps will be constructed to test if growth nodes can be visualized. If so, this can serve as powerful evidence for the *in situ* crystallization of massive magnetitite. Mapping will also be performed in sections where the contact between magnetite and anorthosite is sub-vertical. *In situ* crystallization would predict crystallization directly onto the sub-vertical contact, while this would not be possible for crystal settling. In some cases, magnetitite may also contain inclusions of anorthosite (e.g. Scoon & Mitchell, 2012). It can be expected that magnetite would nucleate and grow all over their outer surfaces if *in situ* crystallization predominates, and should be indicated by higher Cr contents in the vicinity of such inclusions.

1.3.4 Constraining the mechanisms of differentiation during the crystallization of magnetitite

By establishing the thickness of the crystal mush and the means of accumulation of magnetite, strict constraints can be placed on the mechanism of magmatic differentiation during magnetitite crystallization. For example, if the evidence is in favour of *in situ* crystallization,

crystal settling can be disproven, the latter can be excluded as a means of magmatic differentiation. If the crystal mush within magnetitite is found to be thin or non-existent, we can exclude models like compaction or compositional convection with a thick crystal-liquid pile. A prediction of the hypothesis that magmatic evolution occurs by the convective removal of a thin (a few mm) compositional boundary layers from *in situ* growing crystals is that effective liquid exchange would still be able to occur in extremely confined spaces. This can be tested by checking if adcumulus growth and liquid exchange still occur in such confined spaces, such as underneath inclusions or within small magnetite-bearing veins.

1.3.5 Unravelling the origin of massive magnetitite layers

The answers provided to the above questions can already help resolve the first polarizing aspect of magnetitite petrogenesis, namely whether or not magnetite crystals accumulate *in situ*, are deposited on the chamber floor by gravity, or both. Clues regarding whether or not magmatic recharge occurred may be obtained by studying the variation in Cr contents across sequences containing both magnetitite layers and silicate rocks. Because Cr contents are rapidly depleted during massive magnetitite crystallization (Cawthorn and McCarthy, 1980), this trace element could prove much more sensitive to detect any chemical reversals that may have occurred compared to, say, An contents in plagioclase. Field evidence, such as the presence of potholes within the footwalls of magnetitite layers may also provide further clues on this debate, as such structures underneath chromitite layers and the Merensky Reef have been interpreted as the products of thermochemical erosion following a magmatic recharge event (e.g. Campbell, 1986; Latypov *et al*., 2016; Latypov *et al*., 2017a; Pebane and Latypov, 2017).

By combining all the above observations, an attempt will be made to come up with a model that can potentially explain how magnetitite layers formed in the Bushveld magma chamber, why anorthositic footwalls are so common underneath this rock type, and why massive magnetitite possess gradational contacts into overlying anorthosite layers.

1.4 Thesis outline

Because this thesis follows the article format, the following chapters that form the body of the thesis represent journal articles that have already been published, and/or will soon be submitted for publication (with the exception of Chapter 2). They are as follow:

1.4.1 Chapter 2

An overview is provided of the methods employed to accomplish the goals stated above.

1.4.2 Chapter 3

This chapter shows the results obtained by the two-dimensional geochemical mapping of the MML in the Magnet Heights locality from the Eastern Limb of the Bushveld Complex and has been published in Nature Communications. The results obtained allow for the visualization of fossilized solidification fronts and are used to constrain the mechanism by which crystals accumulate within magma chambers (crystal settling versus *in situ* crystallization), the thickness of the crystal mush during magnetitite crystallization, and the potential mechanisms by which crystal/liquid fractionation occurs within magmatic systems.

1.4.3 Chapter 4

Results are presented following the two-dimensional mapping of an outcrop of the lowermost magnetitite layer from the Western Limb of the Bushveld Complex that contains several curious field relationships, such as depressions in the footwall anorthosite and the presence of various anorthositic inclusions within the magnetitite layer. By studying the propagation pattern of the solidification front, it is possible to finally unravel the origin of such anorthositic inclusions in Bushveld magnetitite. A new petrological concept is introduced that is referred to as magmatic karst, where previously deposited cumulates are partially destroyed by thermochemical erosion following a magmatic recharge event resulting in an undercut-embayed chamber floor. By studying the crystallization of magnetite within such an environment provides unique insights into and how, where, and why magma chambers crystallize and differentiate. This work has been submitted for publication.

1.4.4 Chapter 5

This chapter presents variations in Cr contents in magnetite across a 180 m thick section containing both the bottom seam and the MML, as well as several smaller magnetitite layers. The field characteristics of magnetite layers are also documented. Thereafter follows a review of previous literature dealing with magnetitite petrogenesis that is tested against the new findings made in this study, including those from Chapter 3 and 4. Aspects of old models that are not consistent with the data are discarded, while potential strong points are incorporated into a new model that attempts to explain the origin of massive magnetitite, the origin of the gradation into overlying magnetite anorthosite, and the origin of underlying anorthositic footwalls. Other aspects of magnetitite petrogenesis discussed in previous chapters (such as the mechanisms by which magmatic evolution occurs during magnetitite crystallization) are discussed in more depth. As of writing this work is yet to be submitted for publication.

1.4.5 Chapter 6

The main findings of the study are summarized.

CHAPTER 2

METHODOLOGY

2.1 Chemical analysis with the portable XRF and quantification of data.

We have analysed an exposure of the MML located in the Magnet Heights area, Eastern Bushveld Complex (24°50'14.83"S, 29°58'18.55"E), and the bottom seam from the Rhovan open pit mine, Western Bushveld Complex (25°34'56.76"S, 27°34'37.59"E) on grid patterns using a portable Niton XL3t XRF analyser. The instrument analyses an area with a diameter of 8 mm. The MML is coarse grained, with grain sizes in excess of 2 cm (Cawthorn *et al*., 1983), but grains are originally thought to be extremely small (0.2 mm) and have grown to their present size possibly due to post-cumulus annealing. Therefore, a single analysis represents the average Cr composition of potentially thousands of magnetite grains. A grid spacing was employed of 4 cm for the profiles in Figure 3.3a, 3.4a, 3.5a, 4.1 and 1.5 cm for the profile in Figure 3.3c. Each spot of the grid was screened with the portable XRF (pXRF) for approximately 60 seconds. The instrument was calibrated after every few hours of its use by means of its own built-in standards. To obtain quantitative data from the pXRF, we have performed the following recalculations. First, the Cr/V ratio of each analysis was determined. This is because the surface of the magnetitite layers is not perfectly planar and it is not always possible to obtain proper contact with the pXRF for every analysis. As a result, the instrument underestimates the actual elemental concentration in nearly all cases. However, the analysis provides accurate measurements for elemental ratios as long as a fair amount of contact is maintained. This can be seen in terms of the constant V/Ti ratios recorded by our data (V/Ti ratios are also near-constant for in-house XRF analysis on pure magnetite separates from the MML, despite the fact that some deviation occurs from the ideal V/Ti ratio if grains of ilmenite are also included in the spot analysed). Spots with anomalous V/Ti ratios were omitted from the geochemical contour map. After calculation of the Cr/V ratios, the values are multiplied by 9.757 for the MML and 20.29 for the bottom seam to obtain a quantitative Cr concentration in weight percent. For the MML and the bottom seam, this gives a fit with a linear function f(x)=x between the in-house and portable XRF data and an R-squared correlation coefficient of 0.97 (Figure 2.1 and 2; Appendix A). Geochemical contour maps were then constructed using Surfer Version 9.2.397. The average 2σ analytical uncertainty is 575 ppm, with the highest analytical uncertainty being 2350 ppm for the MML. For the bottom seam the average is 405 ppm with a maximum recorded as 1073 ppm. To account for this uncertainty, geochemical contours on

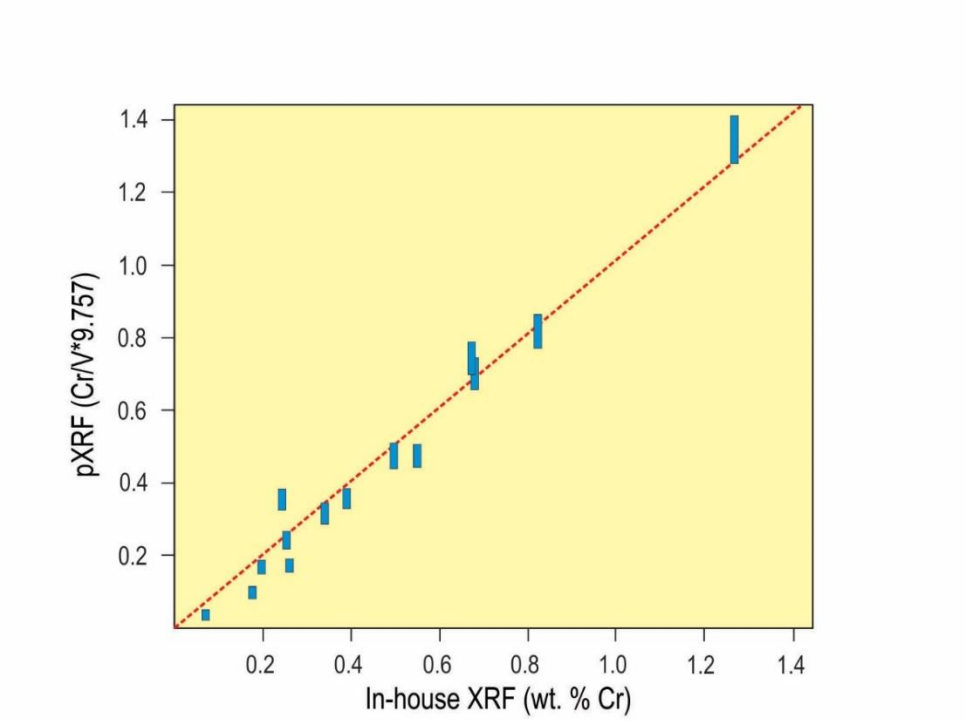

Figure 2.1 Calibration curve for the portable X-ray fluorescence spectrometer. Hand samples collected from the MML were analysed via the pXRF except for the sample with the highest Cr concentration which was pulverised prior to analysis (high Cr concentration gradients are present in samples with very high Cr concentrations and the sample needs to be homogenized before any chemical analysis can be performed). The vertical spacing of the blue bars represents the 2σ analytical uncertainty of the pXRF analysis. In-house XRF data (Maila, 2015) were obtained from pure magnetite separates. Because the pXRF data does not come from pure magnetite separates, some difference between the pXRF and XRF data is to be expected.

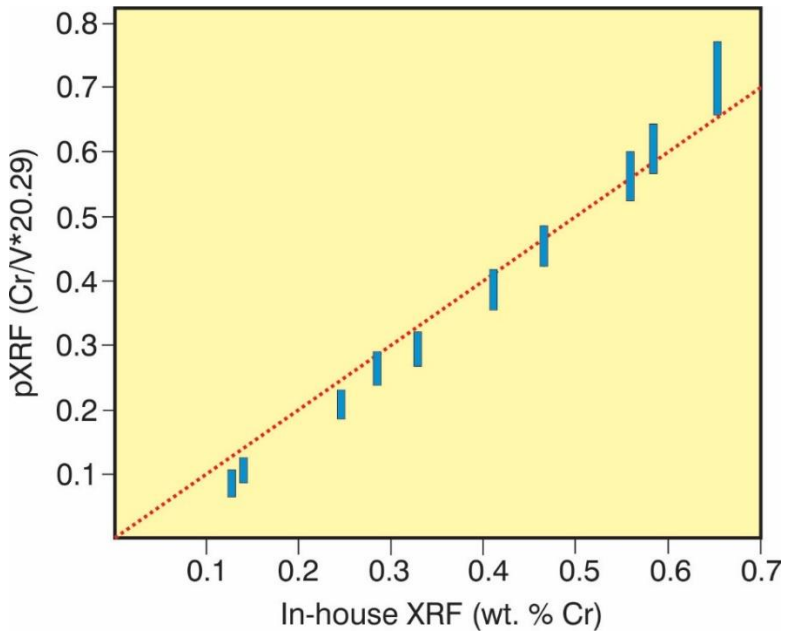

Figure 2.2 Calibration curve for the portable XRF (pXRF) against in-house XRF data for the bottom seam. Hand samples collected from the bottom seam were analysed via the pXRF. The vertical spacing of the blue bars represents the 2Θ analytical uncertainty of the pXRF analysis. In-house XRF data were obtained from pure magnetite separates.

geochemical contour maps were spaced accordingly to ensure they are further apart than the maximum 2σ measured within each region. All pXRF data used in this study can be found in Appendix B, C D, and F.

2.2 Procedures for geochemical modelling for the Main Magnetite Layer in Chapter 3.

2.2.1 Equations employed and two-dimensional modelling

A modified version (Rollinson, 1993) of Langmuir's (1989) equation for *in situ* crystallisation is employed to model the variation of both Cr and V in the MML:

$$C_L/C_O = (M_L/M_O)^{(f(D-1)/[D(1-f)+f])} \quad (1)$$

Where C_L is the concentration of a trace element in the liquid, C_O is the initial concentration of the trace element in the liquid, M_L is the amount of liquid in the chamber, M_O is the initial amount of liquid, f is the fraction of liquid that is ejected from the solidification front into the interior of the magma chamber, and D refers to the partition coefficient for the trace element in question. This equation assumes that there is no trapped liquid in the solidification front. The equation also ignores the trapped liquid shift effect which is negligible considering the small amount of trapped liquid (zero to three percent) present in our modelling. A further assumption of the equation is that the melt in the basal melt layer surrounding magnetite crystals is homogeneous throughout. This is a simplification to some extent as the composition does change within the compositional boundary layer prior to its convective removal from the crystal. We assume the convective removal of the boundary layer occurs at a sufficiently rapid rate and mixes quickly with the overlying liquid that true values do not deviate significantly from those predicted by equation (1).

To perform modelling in two dimensions, the amount of magnetite contained within each contour on the geochemical contour map is measured. This measurement can then be used to calculate M_L/M_O for equation (1) which is then used to determine the concentration at different coordinate positions on the contour map.

In an open system, changes in the Cr and V concentration due to melt addition is calculated using the following equation:

$$C_L = (M_i/M_t)(C_i) + (M_a/M_t)(C_a) \quad (2)$$

Where C_L is the liquid composition after melt addition, M_i is the amount of melt in the basal layer before melt addition, M_t is the total amount of melt in the basal layer after melt addition, C_i is the concentration of the liquid before melt addition, M_a is the amount of melt added to the

basal layer, and C_a is the composition of the incoming melt. The latter value is calculated by dividing the highest Cr concentration measured (Cawthorn, 1994) in the MML (4.8 wt. %) by the partition coefficient of Cr into magnetite. A spreadsheet used for the purpose of this modelling can be found in Supplementary Data 2 available online at https://www.nature.com/articles/s41467-020-16723-6#Sec11.

In the final modelling (Figure 3.6c and 7b), the initial thickness of the basal melt layer is 20 metres. After every 100 cm^2 of magnetite crystallized in this part of the profile, a certain quantity of melt is added to the basal layer. For the first 1600 cm^2 of crystallization (or after the deposition of 16 cm of magnetite considering the section is 100 cm wide), 1.0 metres of melt is added to the system, then 0.8 metres of melt for the next 800 cm^2 of crystallization, followed by 0.54 metres of melt for the next 800 cm^2 of crystallization, and finally 0.38 metres of melt for the final 500 cm^2 centimetres of crystallization in the profile. A gradual decrease in the amount of melt added is necessary to explain the inflections observed in the Cr content (Figure 3.7). At the top of the 40 cm high profile, the basal layer has grown to a thickness of 48 metres. After 1 m of magnetitite crystallization, it would have reached a height of 58 metres.

2.2.2 Choice of partition coefficients.

Because the V concentration of the melt parental to the Upper Zone of the Bushveld Complex is not known, we rely on experimental work to select a partition coefficient. The D values for V into magnetite ranges from 10 to 30 and is highly dependent on the oxygen fugacity of the melt. Based on theoretical work, previous researchers have estimated the D of V for magnetite from the Bushveld to vary from 20 to 30 (Toplis and Corgne, 2002). We use a D value of 20 because it reproduces the near-consistency of V as observed in vertical profiles through the MML (Maila, 2015) more accurately compared to higher values. A D value of 20 implies that the melt had a V concentration of about 600 ppm.

Estimating the actual thickness of the basal layer is highly dependent on the partition coefficient used for Cr. The very rapid depletion of Cr at the base of the MML (up to more than 200 ppm/mm towards the top of growth nodes) requires an initially very thin basal layer of liquid. Based on experimental results, the D for Cr appears to be poorly constrained and varies from 100 to 620 in basaltic melt (Irving, 1978). Finding further constraints on the D value for Cr can be accomplished by studying the change in V in the layer. In vertical profiles across the

MML in the Magnet Heights area, it was found that the V concentration may reach a maximum of 1.23 wt. %. The V concentration within the MML rarely drops below 0.90 wt. %[60]. Using a starting V concentration of 1.23 wt. % in magnetite, the V concentration should be kept above 0.90 wt. % during modelling. Using a low D value for Cr requires an initially thinner basal layer to describe the rapid rate of Cr depletion around growth nodes (Supplementary Figure 3.1). In addition, a lower D value for Cr implies that the incoming melt has a higher concentration. This is because the incoming melt composition is calculated by dividing the maximum Cr recorded in the MML by the partition coefficient for Cr. A smaller amount of melt is thus required to model the retardation in Cr depletion upwards if Cr has a lower partition coefficient. Both the thinner basal layer and the smaller quantity of incoming melt leads to a more rapid depletion in V and a lower V concentration results at the top of the profile (Supplementary Figure 3.1). Modelling is based on analysis selected from the dotted line in Figure 3.3b but the profile has been extended to 100 cm high. At this height, the Cr concentration usually levels off at around 700 ppm[1], and the rate of melt addition is adjusted to mimic this effect in the modelling. Above 100 cm in the MML, an approximately 30 cm thick feldspar parting is present. No modelling is performed above the base of the parting. Under these conditions, only if a D value for Cr is used of more than 525 can V be kept above 0.9 wt. % assuming a D of 20 for V. By dividing the D for Cr in magnetite by the highest Cr content recorded in the MML, a Cr concentration of 91 ppm is obtained for the liquid prior to its formation. These parameters put a constraint on the minimum initial thickness of the basal layer of 20 metres and are the parameters used in the final modelling (Figure 3.6c and 3.7b).

2.3 Properties of a compositional boundary layer.

In Chapter 3, the conclusion is reached that during the *in situ* crystallization of a high density phase on the floor of a magma chamber, a thin boundary layer of liquid with a relatively low density develops around a growing crystal. This boundary layer progressively increases in thickness and decreases in density as the crystal grows until the boundary layer exceeds the critical Rayleigh number for convection. At this point the boundary layer breaks away from the growing crystal. Equations 3 and 4 below (Martin *et al*., 1987) allow the calculation of the compositional change across and the thickness of the boundary layer, respectively, at the very moment when the boundary layer becomes unstable and convection commences:

$$d_s = \left[\frac{pvk_s^2}{C^3 \mathbf{g}\beta q}\left(L + C_p \frac{dT}{dS}\right)\right]^{1/4} \quad (3)$$

$$\Delta S = \left(\frac{v}{\mathbf{g}\beta k_s^2}\right)^{1/4}\left[\frac{q}{pC\left(L+C_p\frac{dT}{dS}\right)}\right]^{3/4} \quad (4)$$

Where ds is the compositional change across the boundary layer in weight fraction, ΔS is the boundary layer thickness, p is the density of the melt, v is the kinematic viscosity of the melt, k_s is the diffusivity of the solute, C is a dimensionless constant with a value of 0.1, **g** is acceleration due to gravity, β is the compositional expansion coefficient, q is the heat flux out of the chamber, L is the latent heat of crystallization, Cp refers to the specific heat capacity of the melt, and dT/dS is the liquidus slope in temperature-solute space. The p, v, Cp, and dT/dS were all calculated from using alphaMELTS software, version 1.4.1. An Fe-rich liquid composition that is considered to be parental for the Upper Zone (Tegner *et al*., 2006) and which was slightly modified to have magnetite as the first liquidus phase was used in the MELTS run. The diffusivity of Fe in magma (Zhang *et al*., 2010) (K_s) is taken as 10^{-11} m^2 s^{-1} and the average Cp of gabbro (Lesher and Spera, 2015) (396 000 J kg^{-1}) is used. The compositional expansion coefficient (β) of magnetite is 0.36 (weight $fraction^{-1}$) (Koyaguchi, 1990). A value for the heat loss through the basal layer (q) is taken so as to allow a crystallization rate of 1 cm per year. The density change across the boundary layer was obtained from the MELTS run by choosing a composition that corresponds to the compositional change given by Equation 4 above. The calculations performed to obtain the properties of the boundary layer can be found in Supplementary Data 3 as well as the MELTS run in Supplementary Data 4 available online at https://www.nature.com/articles/s41467-020-16723-6#Sec11.

2.4 Sample collection, chemical analysis, and field observations for Chapter 5

Chapter 5 generally focusses on the geochemical and field characteristics of massive magnetitite layers from a section of Subzone A and B that is exposed in the open pits of the Rhovan and Vametco mines and drill cores, as well as field outcrops in the Magnet Heights locality from the Eastern Limb (Figure 5.1). Field observations regarding the nature of the contact of massive magnetitite layers to their over- and underlying lithologies were conducted both in the field and in drill core. Samples for whole-rock X-ray fluorescence (XRF) analysis and petrographic investigation were taken from two composite Rhovan drill cores that together intercepts the lowermost magnetitite layer (henceforth referred to as the Bottom seam) and the Main Magnetite Layer (MML). The two drill cores join at a height of 6 metres above the lowermost sample collected.

Samples selected for bulk-rock major and trace element analysis were sent to Genalysis Intertek Laboratory in Australia. Silicate rock samples were cut into approximately 8 by 4 by 2 cm large blocks while smaller, 4 by 2 by 1 cm blocks were cut for magnetitite samples because of their large Cr gradients. Compressed powder pellets were prepared for XRF analysis for major elements using the AMIS0368 standards in addition to in-house controls for calibration. Less than 1-6% percent of deviation occurs from recommended values. For trace element analysis, samples were prepared with four acid digests and analysed via inductively coupled plasma mass spectrometry (ICP-MS) using control standards GTS-2a, AMIS0167, and AMIS0013. Selected samples were doubly analysed to check for anomalous results and standard deviations are found to be less than 10%. All whole-rock data is available in Appendix E.

CHAPTER 3

FOSSILIZED SOLIDIFICATION FRONTS IN THE BUSHVELD COMPLEX ARGUE FOR LIQUID-DOMINATED MAGMATIC SYSTEMS

Reference to paper:

Kruger, W. and Latypov, R. Fossilized solidification fronts in the Bushveld Complex argue for liquid-dominated magmatic systems. Nature Communications, DOI: 10.1038/s41467-020-16723-6. Impact factor: 12.1.

Author contributions

Kruger: 65% (Geochemically analysed field outcrops, performed quantification of geochemical data, performed geochemical modelling, wrote the first draft of the manuscript, and contributed to ideas presented in the paper);

Latypov: 35% (Supervisor, contributed to ideas presented in the manuscript, assisted with editing and reviewing the manuscript).

Abstract

Chemical differentiation of magma on Earth occurs through physical separation of liquids and crystals. The mechanisms of this separation still remain elusive due to the lack of information on solidification fronts in plutonic magmatic systems. Here, we present records of fossilized solidification fronts from massive magnetitites of the Bushveld Complex in South Africa, obtained by two-dimensional geochemical mapping on field outcrops. The chemical zoning patterns of solidification fronts indicate that nucleation and crystallization occur directly at the chamber floor and result in near-perfect fractionation due to convective removal of a compositional boundary layer from in situ growing crystals. Our data precludes the existence of thick crystal mushes during the formation of massive magnetitites, thus providing no support for the recent paradigm that envisages only crystal-rich and liquid-poor mushy reservoirs in the Earth's crust.

3.1 Introduction

At the heart of magma differentiation on Earth and other terrestrial planets, irrespective of whether this occurs in shallow magma chambers (Wager and Brown, 1968; Cawthorn and McCarthy, 1980; 1981; Jackson, Campbell, 1996; Cawthorn, 1996a; Marsh, 1996; Latypov and Egorova, 2012; Charlier *et al*., 2015), magma oceans/impact melt sheets (Vaughan *et al*., 2013; Latypov *et al*., 2019b) or planetary cores (Fearn and Loper, 1981; Morse, 2002) is a physical separation of chemically distinct crystals and liquids. Exactly how this separation takes place to cause chemical differentiation of magmas is a central question of modern volcanology and igneous petrology (Figure 3.1). Three major physical mechanisms are commonly considered for this role in magmatic systems: gravity settling/floating of crystals on the chamber floor/roof that leaves behind an evolved liquid (Jackson, 1961; Wager and Brown, 1968; Cawthorn, 1996a; Charlier *et al*., 2015) (Figure 3.1c), compaction of a mushy cumulate pile that squeezes the evolved liquid into the overlying magma reservoir (Shirley, 1986; Tegner *et al*., 2006; McKenzie, 2011: Cashmann *et al.,* 2017) (Figure 3.1d), and compositional convection in a mushy cumulate pile that drives out the buoyant evolved liquid into the overlying magma body (Tait *et al.*, 1984; Namur and Charlier, 2012) (Figure 3.1e). These processes are well-established theoretically and experimentally, but what role they play in driving chemical differentiation of magmas in nature is still far from being fully understood.

Critical information necessary to address this issue is locked in the internal structure of solidification fronts; the partially crystalline zones of magma that occur along the margins of magmatic systems (Marsh, 1996; 2013). Drilling into historic Hawaiian lava lakes back in 60's-80's of the last century allowed the first documentation of the textural and chemical features of the solidification fronts in volcanic environments (Helz, 1987; Marsh, 2013). However, the solidification fronts in deep-seated, slow-cooling magma chambers is still poorly explored, and their physical and chemical dynamics are largely unknown because of their inaccessibility for direct petrological observations. Inferring chemical and physical properties of solidification fronts from fossilized magma chambers is extremely difficult, with only a few prominent attempts being undertaken to overcome this challenge (Campbell, 1977; McBirney & Noyes, 1979; Cawthorn and McCarthy, 1980; 1981). A major problem is that distribution coefficients (D) for compatible trace elements, such as Ni, Cr, and Sr, are not particularly high – they normally range from 2 to 15 for most rock-forming minerals (GERM partition coefficient database). As a result, these minerals are not chemically sensitive enough to record the evolution and propagation of solidification fronts in magmatic systems.

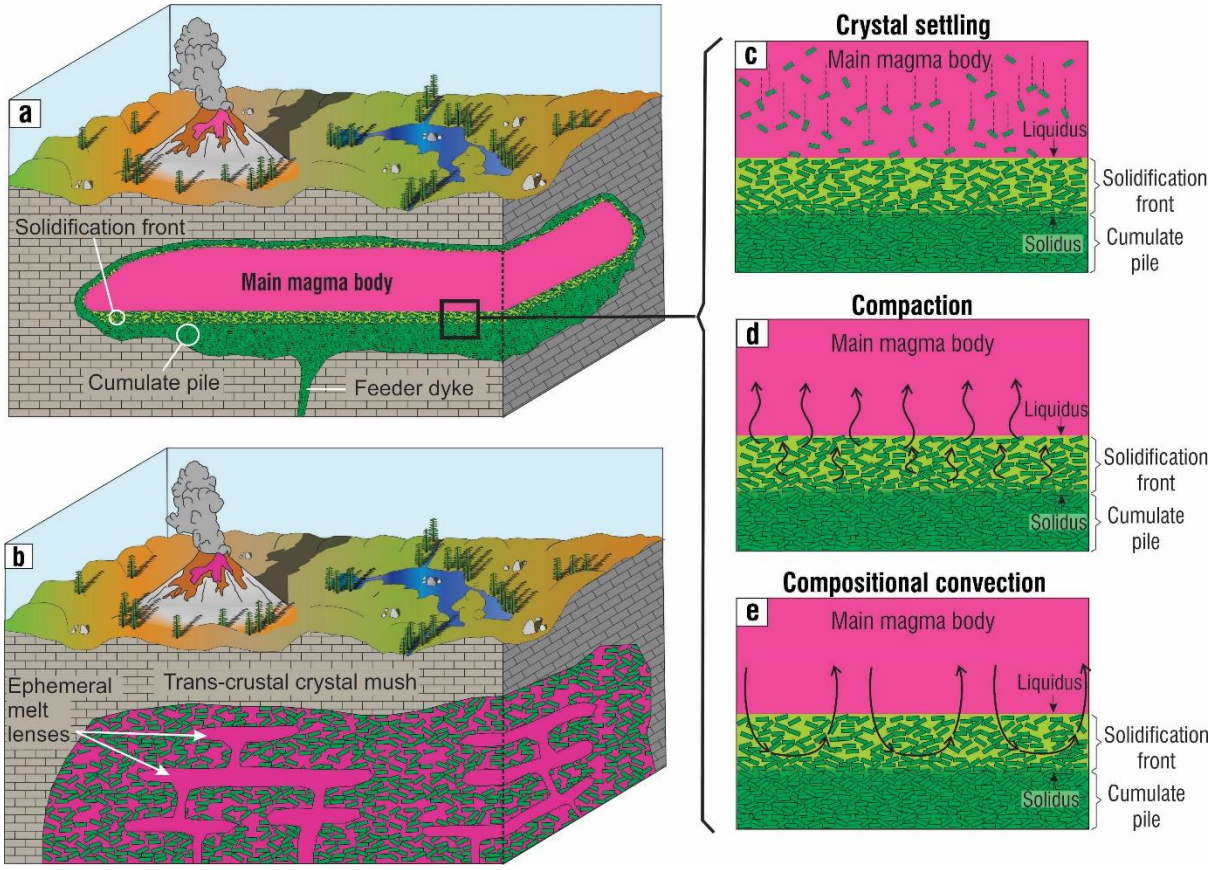

Figure 3.1 Potential magma reservoirs geometries and mechanisms for their evolution a, The classical view of a melt-dominated, long-lived magmatic chamber situated underneath a volcano (Cawthorn and McCarthy, 1980; Jackson, 1961; Wager and Brown, 1968; Campbell, 1996; Cawthorn, 1996a; Marsh, 1996; Latypov & Egorova, 2012; Charlier et al., 2015, compared to b, a new concept that considers trans-crustal magmatic systems as composed of crystal-rich mushes with only small, short-lived melt lenses (Cashmann et al., 2017). Differentiation of the magma can occur in several different ways: c, crystal settling (Jackson, 1961; Wager & Brown, 1968; Cawthorn, 1996a; Charlier, 2015) whereby crystals grow in the interior of the magma chamber and settle towards the floor; d, compaction of the cumulate pile (Shirley, 1986; Tegner et al., 2009; McKenzie, 2011; Cashmann et al., 2017), and e, compositional convection within the cumulate pile (Tait et al., 1984; Tait and Juapart, 1992; Namur and Charlier, 2012) which forces a light evolved liquid out of mushy solidification fronts into the main magma body.

In addition, the minerals are susceptible to re-equilibration with trapped liquid (Barnes, 1986; Cawthorn, 1996a; Lundgaard *et al*., 2006) which tends to obliterate the primary chemical patterns in solidification fronts of plutonic complexes.

Fortunately, there is one notable exception from this rule: the partitioning of Cr into magnetite, a rock-forming mineral that is common in the uppermost parts of mafic layered intrusions. A compilation of D values for Cr in magnetite in silicate liquids shows that they may range from 20 to 300 (Dare *et al.*, 2012). A few experimental studies indicate that even higher values, from 69 to 620 (Irving, 1978; Toplis and Corgne, 2002; Castle and Herd, 2017), are possible in basaltic systems. In more evolved melts, D values may rise up to 1290 (Bachmann *et al*., 2004).

In addition, geochemical modelling shows that D values need to be at least as high as 275 to 400 to reproduce the vertical variations in Cr across massive magnetitites of the Bushveld Complex (Cawthorn and McCarthy, 1980; Wright *et al*., 1983; Kruger and Smart, 1987). The crystallization of magnetite is thus expected to cause a rapid depletion of basaltic melt in Cr which must be recorded in decreasing Cr abundance in massive magnetitites at the scale of solidification fronts. This principle was first used by Cawthorn and McCarthy (1980; 1981) and resulted in a discovery of steep gradients in Cr concentrations in vertical profiles across magnetitite layers and even individual magnetite crystals (Cawthorn and McCarthy, 1983) from the Bushveld Complex in South Africa. This finding led to an important realization that these layers are likely formed by *in situ* crystallization directly at the chamber floor (Cawthorn and McCarthy, 1980; 1981; Wright *et al*., 1983; Cawthorn *et al*., 1983). Here, we build upon this pioneering work by undertaking a geochemical study of magnetitite layers in two dimensions using a handheld X-ray fluorescence spectrometer (pXRF). The study was motivated by an idea that the two-dimensional contours of the Cr decrease can be interpreted as Cr-isopleths that depict successive steps in the development of inward-growing solidification fronts in magma chambers. If so, the chemical patterns in magnetitite solidification fronts may provide a clue to the physical mechanisms that cause chemical differentiation of magmas in plutonic systems. Our two-dimensional geochemical study has confirmed a remarkable prediction by Cawthorn (1994) that layers of magnetitite start forming via *in situ* growth nodes emerging at the contact with the footwall rocks. We show that during the growth of these nodes all rejected liquid components are effectively removed by compositional convection from the *in situ* growing crystals and transported into the main magma body. This results in effective adcumulus growth and inhibits the formation of crystal-rich mushes. We hypothesize that such compositional convection is induced by the instability of a chemical boundary layer around *in situ* growing crystals at the chamber floor and is one of the most effective mechanisms for melt fractionation in magmatic systems.

3.2 Results

3.2.1 Geochemical maps.

We have explored the local-scale variations in Cr distribution in massive magnetitite layers of the Bushveld Complex, the largest basaltic magma chamber in the Earth's crust (Cawthorn, 2015), by two-dimensional geochemical mapping (Appendix A and B) directly on field outcrops. Here we present geochemical maps from the basal part of the most prominent

magnetitite layer referred to as the Main Magnetite Layer (MML). The near-monomineralic nature of this layer (Figure 3.2) implies that its chemical composition has been practically unaffected by a reaction with trapped liquid (Cawthorn *et al*., 1983; Barnes, 1986). This implies that primary chemical patterns are likely preserved in solidification fronts of the MML. The layer was analysed in four separate areas, two of which show a planar basal contact (Figure 3.3), one that contains a sub-rounded anorthosite autolith (Figure 3.4), and another with a subvertical basal contact (Figure 3.5). The irregularities in the floor (Figs. 3.4-5) are thought to result from thermo-chemical erosion of the anorthositic footwall during magma

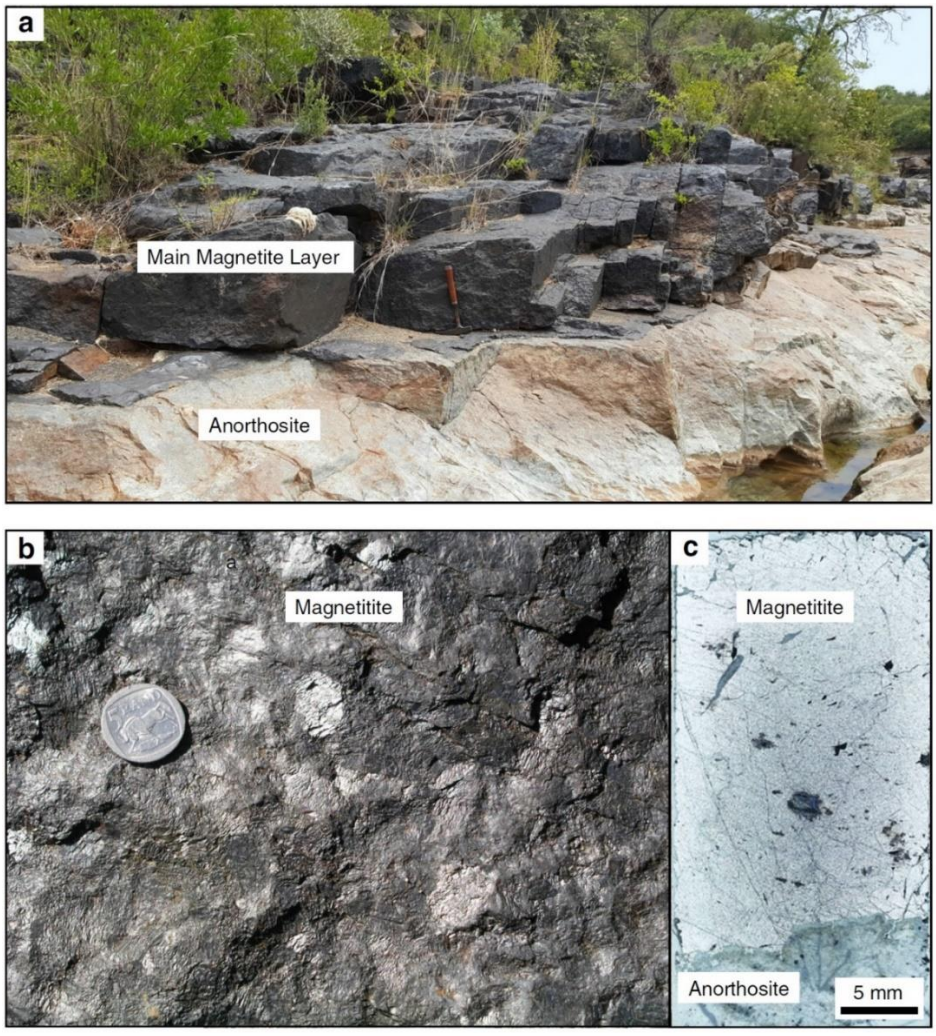

Figure 3.2 The Main Magnetite Layer at Magnet Heights from the Eastern Bushveld Complex. (a) Field photograph of an outcrop of the MML with footwall anorthosites. The length of a hammer shaft is about 40 cm. (b) Field photograph of massive magnetitite from the MML. Sunlight reflected off individual titano-magnetite grains reveal the large grain size (typically more than 1 cm in size) and generally planar to slightly curved grain boundaries. Grains are typically polygonal with 120° triple-point grain boundary junctions, typical of monomineralic rocks in which textural equilibrium has been obtained. The coin has a diameter of 26 mm. (c) Photomicrograph in reflected light of the base of the MML including a portion of its underlying anorthositic footwall. Notice the near-perfect adcumulate and massive nature of the magnetite with virtually no intercumulus phases present.

replenishment of the chamber by basal flows as has been documented for other layers of the Bushveld Complex (Latypov *et al*., 2016; 2017a), including magnetitite (Scoon and Mitchell, 2012). A key result of our study is the documentation of fine-scale domical structures with steep chemical gradients in Cr-content. These appear to be randomly distributed along the base of the MML and are characterized by a planar bottom with the highest Cr-content (up to 1.8-

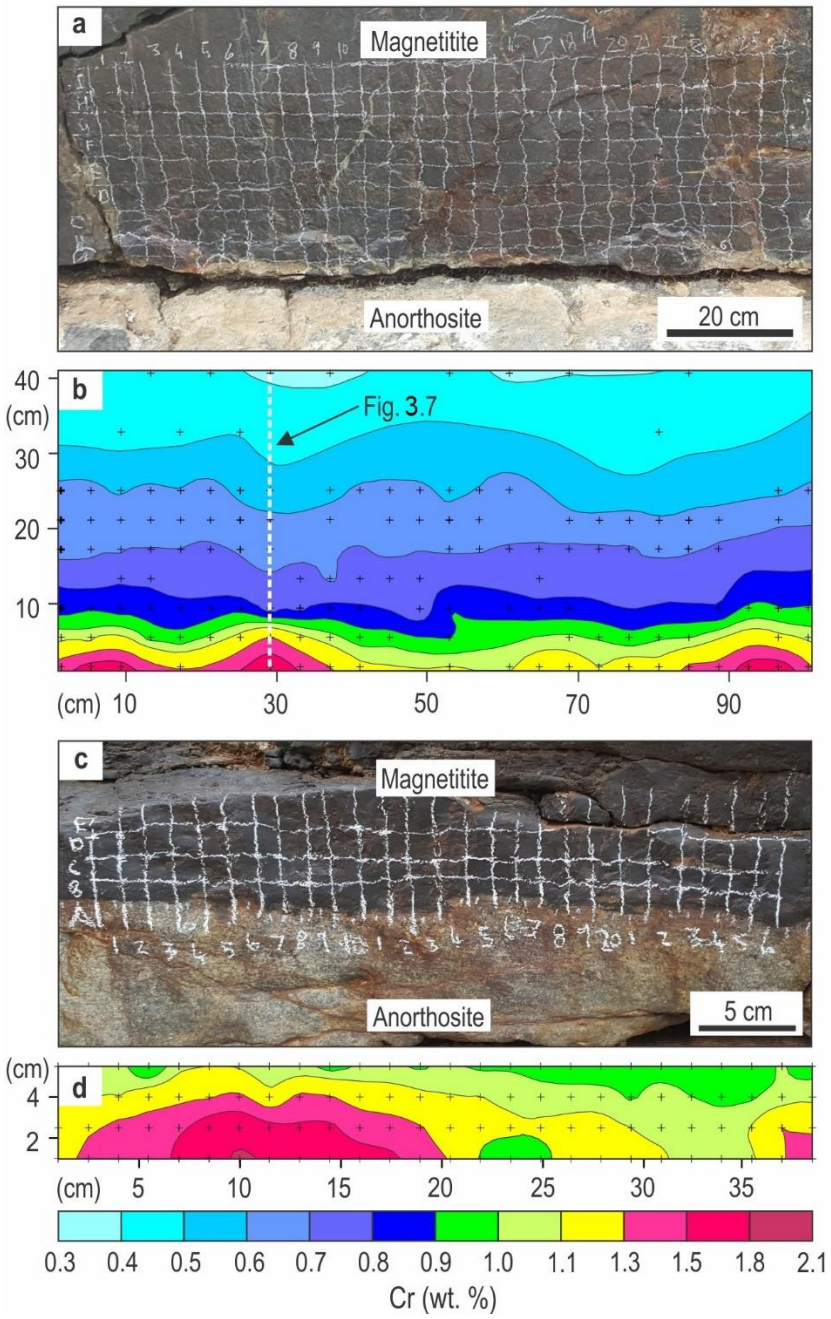

Figure 3.3 Two-dimensional geochemical maps of basal part of the Main Magnetite Layer with a planar basal contact. Field photographs of studied areas in (a) and (c) are supplemented with their corresponding geochemical contour maps in (b) and (d), respectively. Black crosses indicate the positions of individual data points. Some data points were omitted because the analysis was not of sufficient quality for proper quantification. The maps reveal basal nodes showing a steep upwards and outwards depletion in Cr over short distances. These nodes represent places where magnetite starts to nucleate and grow providing evidence for the in situ crystallization of the MML. The vertical dotted line in (b) indicates the section used for modelling in Figure 3.7. The outcrop is located at Magnet Heights, Eastern Bushveld Complex.

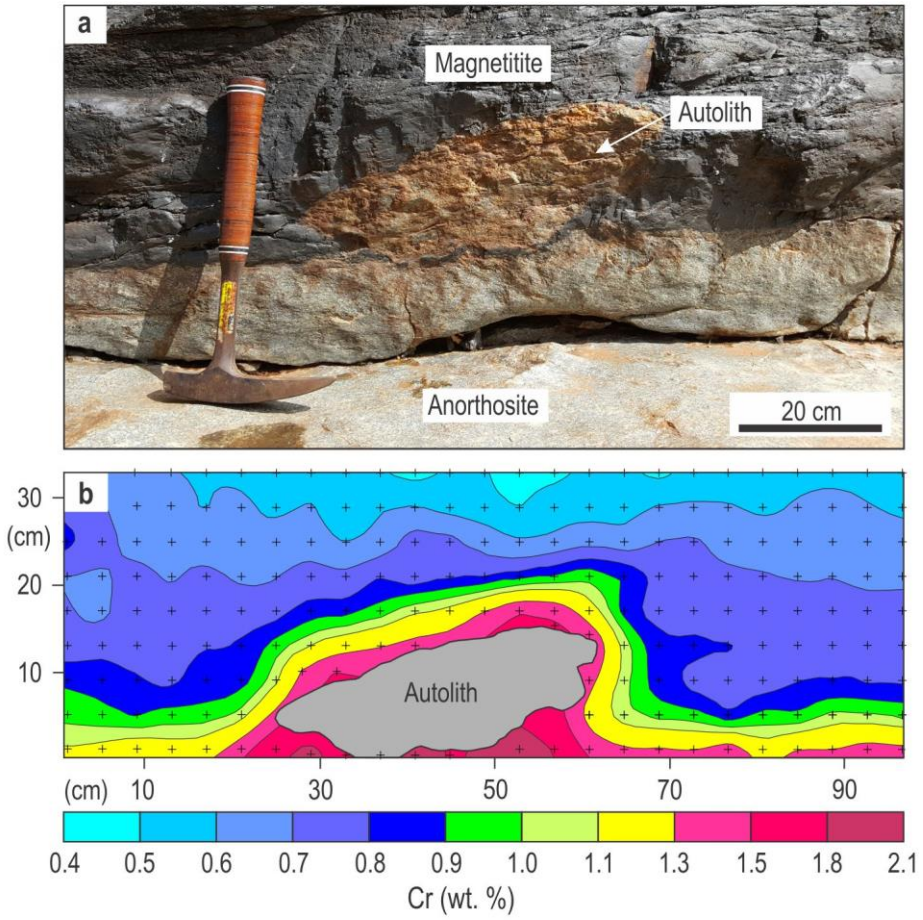

Figure 3.4 Geochemical map of basal part of the Main Magnetite Layer that contains a sub-rounded anorthosite autolith. Field photograph of the section and the corresponding geochemical contour map are shown in (a) and (b)**,** respectively. Black crosses indicate the positions of individual data points. Notice how the geochemical contours drape over the autolith, indicating in situ growth all along its outer surface. Several growth nodes appear directly underneath the autolith as well. The outcrop is located at Magnet Heights, Eastern Bushveld Complex.

2.1 wt.%) that passes outwards in a concentric manner towards much lower Cr-contents (down to 1.0 wt.%) across a distance of only a few cm (Figure 3.3b and d). Importantly, the structures with high Cr-content even occur below the anorthosite autolith (Figure 3.4b). Moving upwards from the nodes, Cr-contours in magnetite turn into continuous sublayers with roughly planar contours. These sublayers tend to drape over the autolith (Figure 3.4b) and develop roughly parallel to subvertical portions of a basal contact (Figure 3.5b).

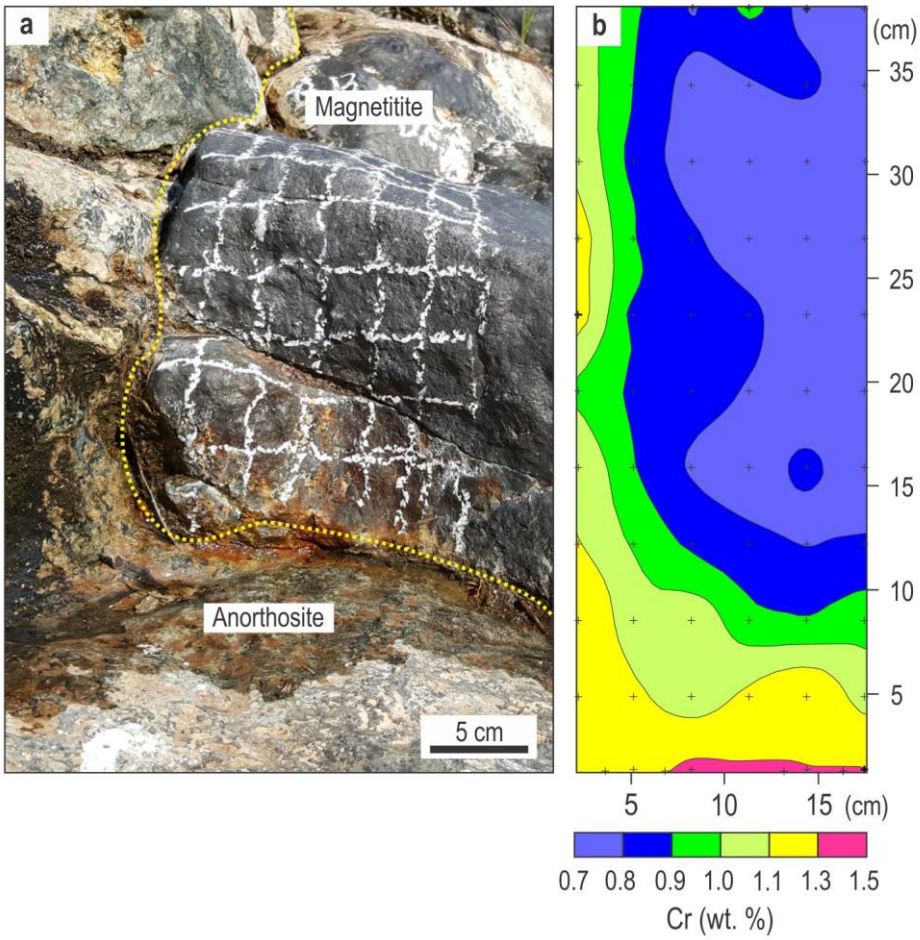

Figure 3.5 Geochemical map of basal part of the Main Magnetite Layer with a sub-vertical footwall contact. Field photograph of the section and the corresponding geochemical contour map are shown in (a) and (b), respectively. Black crosses indicate the positions of individual data points. Geochemical contours remain subparallel with the footwall contact, indicating in situ nucleation and growth directly on the subvertical contact. The outcrop is located at Magnet Heights, Eastern Bushveld Complex.

The first question to address is whether the high-Cr structures (Figs. 2.3-5) are primary magmatic features, or products of some secondary, non-magmatic processes superimposed on early-formed, internally homogeneous magnetitites. One of the most common secondary processes is the action of late-stage hydrothermal fluids and/or melts that migrate upwards from the underlying cumulates and can potentially affect the distribution of Cr within massive magnetitite (Boudreau and McCallum, 1992). However, such fluids or melts are expected to be highly depleted in Cr because of its partitioning into pyroxenes and magnetite in the underlying cumulate rocks. Therefore, the upward percolation of such fluids/melts and their reaction with magnetite may only cause its depletion in Cr, rather than the enrichment that is required to produce the high-Cr structures. Cr gradient in a single magnetite crystal also excludes the possible influence from late-stage interstitial fluids (Cawthorn *et al.*, 1983). An

alternative idea, namely the differential leaching of Cr from a magnetite layer by migrating fluids/melts, is also problematic because it would require a very peculiar flow pattern to form the domical high-Cr structures. It is also worth pointing out that a detailed geochemical study performed at our locality (Cawthorn and Street, 1994) failed to detect any change in Cr in magnetitite that could be ascribed to the activity of fluids coming from the underlying cumulate pile.

It seems, therefore, much more likely that the discovered high-Cr structures (Figs. 2.3-5) are of primary magmatic origin. The simplest explanation appears to be that they represent areas on the chamber floor where magnetite first starts nucleating and crystallizing outwards in a concentric manner. In this interpretation, we thus follow Cawthorn (1994) who predicted the existence of such high-Cr structures in the Bushveld's massive magnetitites and referred to them as *in situ* growth nodes. With further cooling, *in situ* growth nodes continue to spread laterally to cover the entire floor and eventually coalesce to form a layer with a planar surface (Supplementary Movie 1 available at https://www.nature.com/articles/s41467-020-16723-6#Sec11). Our results suggest that a planar solidification front may form after just 10-20 cm of crystallization, which explains why all magnetitite layers, including the thinnest ones (~10 cm), show planar top contacts. This tendency for the solidification front to become planar is also easily observed above the autolith (Figure 3.4b). If our interpretation is correct, then these chemical structures (Figs. 2.3-5) are arguably the first ever records of the morphology of fossilized solidification fronts in deep-seated plutonic systems on Earth. The successive stages in *in situ* generation and subsequent upward propagation of these fronts are clearly indicated by Cr-isolines.

The internal structure of the solidification fronts in the MML (Figs. 3.3-5) provides a unique opportunity to rigorously test the competing concepts of magma differentiation (Figure 3.1). *In situ* growth nodes are clearly not compatible with gravity settling (Figure 3.1c) as the latter implies a deposition of crystals from the overlying melt on the chamber floor to form a continuous layer, rather than a few small and highly localized Cr-rich nodes. The gravity concept is also at odds with the occurrence of the Cr-rich growth nodes below an autolith (Figure 3.4) as well as the development of layers along the subvertical sidewalls (Figure 3.5). These places are not appropriate for gravity-controlled accumulation of settling crystals. Similarly, *in situ* growth nodes are not consistent with compaction (Figure 3.1d). The steep Cr-concentration gradients (>200 ppm/mm) in these nodes imply that chemical differentiation of melt became highly efficient almost immediately after the onset of magnetite crystallization.

This dictates that rejected solute from every mm-thick 'shell' on *in situ* growing nodes must have been almost instantaneously transferred into the overlying melt to ensure its chemical evolution. Because compaction requires at least a few dozens to hundreds of metres of mush to operate (Shirley, 1986; Tait *et al*., 1984; Boudreau and McCallum, 1992), it cannot work in a magnetitite growth node less than a couple of centimetres thick. One may, perhaps, argue that compaction may squeeze interstitial liquid from a crystal mush below the magnetitite layer. However, recent work suggests that crystal mushes in layered intrusions are less than 4 metres thick (Holness *et al*., 2017a), and igneous cumulates are notably void of textural features indicating compaction (Holness *et al*., 2017b). In addition, deposition of a couple of centimetres of magnetite cannot provide sufficient loading to compact the underlying mush, thus precluding the transfer of the evolved liquid from below. The above objections can be equally well applied to compositional convection within a mush (Figure 3.1e) because it has been estimated to require at least a 90 m thick mushy layer on the chamber floor for the onset of its operation (Tait and Juapart, 1989). The conventional models (Figure 3.1c-e) thus fail to explain the chemical features of magnetitite solidification fronts.

3.2.2 Geochemical modelling.

Further constraints on a mechanism of magma differentiation during the formation of massive magnetite come from geochemical modelling. To explain the rapid upward depletion in Cr, previous studies (Cawthorn and McCarthy, 1980; Kruger and Smart, 1987) have indicated that the magnetitite could not have crystallized from the entire, ~1.5 km-thick column of resident melt in the chamber (Cawthorn and McCarthy, 1980). Instead, it was concluded that the magnetitites must have been crystallizing from a relatively thin isolated layer of melt at the chamber floor (Cawthorn and McCarthy, 1980; Kruger and Smart, 1987). At issue is to understand which process is responsible for the formation of this basal layer of melt. In a closed system, it can be potentially produced by double-diffusive convection (Kruger & Smart, 1987; Tegner *et al*., 2006), liquid immiscibility (VanTongeren and Mathez, 2012; Fischer *et al*., 2016; Scoon *et al*., 2017), *in situ* fractionation of abundant plagioclase (Reynolds, 1985a) or melt stagnation at the chamber floor (Cawthorn and McCarthy, 1980; Jaupart and Brandeis, 1986). In an open system, it can be most easily formed by a new pulse of a melt replenishing the chamber as a basal flow (Huppert and Sparks, 1980; Snyder and Tait, 1995). The dilemma can be addressed by referring to the recent work on the Upper Zone of the Bushveld Complex that revealed a few prominent reversals in terms of Cr content in magnetite (Yuan *et al*., 2017) and pyroxene (Tanner *et al*., 2014) as well as in An-content in plagioclase and magnesium

number of mafic silicates in the proximity of magnetite layers (Scoon and Mitchell, 2012; Yuan *et al*., 2017). It has also been earlier reported that the basal part of the MML contains up to 240 times more Cr than pure magnetite separates from the underlying rocks (Cawthorn and McCarthy, 1980). These reversals in composition of cumulus minerals are clearly not consistent with the above-mentioned closed system models. The reversals are more compatible with the interpretation of the Upper Zone as an open system, with the magma additions into the chamber contributing to the formation of massive magnetitites (Yuan *et al*., 2017; Tanner *et al*., 2014; Scoon and Mitchell, 2012). Following these studies, we argue that the replenishments of the chamber by new magma pulses are likely responsible for the generation of a thin basal layer that crystallized the MML. To crystallize monomineralic magnetitite, the melt needs to be saturated in magnetite-alone for some period of its crystallization history. One possible way to produce such a melt is to allow a deep staging chamber to fractionate silicates, causing Fe-enrichment and forcing the melt towards magnetite saturation (e.g. Scoon and Mitchell, 2012). When the melt is close to or at magnetite saturation, a pulse of melt is released upwards and ascends towards the Bushveld Chamber. This process results in a drop in pressure, shifting phase boundaries in such a manner that magnetite may be the sole crystallizing phase upon entry in the shallow level chamber (Latypov, *et al*., 2018). A more in-depth description of this model is given in sections 5.5.12 and 5.6.5 of this thesis.

Upon emplacement into the chamber, the basal melt layer will cool until magnetite starts to crystallize. To gain further insights into this process, previous studies have attempted to model the distribution of Cr in magnetitite in one dimension. One study (Cawthorn and McCarthy, 1980) considers growth of magnetite in a stagnant layer of melt. In this model, growth of magnetitite is controlled by diffusion, leading to a profile of melt depleted in Cr directly at the crystal-liquid interface. In addition, occasional convective currents are involved to assist in supplying Cr to the growing magnetitite to prevent Cr from being depleted too rapidly (Cawthorn and McCarthy, 1980). However, later theoretical (Martin *et al*., 1987) and experimental (Seedhouse and Donaldson, 1996) studies have shown that such a stagnant layer will experience vigorous convection from the very onset of crystallization, and the above process may therefore be physically unrealistic. Another study (Kruger and Smart, 1987) envisages the crystallization of magnetite in a magma chamber stratified by double-diffusive convection. In this case, magnetite crystallizes in situ on the chamber floor, rapidly depleting the lowermost layer in terms of its Cr content. This causes Cr to diffuse from the overlying layers into the crystallizing basal layer, generally slowing the rate of Cr depletion.

However, the presence of growth nodes show that the MML did not simply grow in one direction (upwards), rendering a one-dimensional approach inaccurate. Our geochemical maps (Figure 2.3-5) provide an opportunity to improve on these previous attempts (Cawthorn and McCarthy, 1980; Kruger & Smart, 1987) by performing modelling in two dimensions. We base our modelling on the two-dimensional distribution of Cr on the geochemical map of Fig 2.3b. Our results reveal that the initial depletion around the growth nodes is much too fast, with the rate of depletion slowing down too strongly to be explained by the above models (Cawthorn and McCarthy, 1980; Kruger & Smart, 1987) or by the Rayleigh law alone. Although it is possible to produce the extremely rapid initial depletion by assuming a very thin basal melt layer (40 metres) and simple Rayleigh fractionation, the depletion becomes much too rapid further upwards (Figure 3.6a). In contrast, while it is possible to accurately reproduce the Cr concentration in the upper part of the profile by assuming a thick basal melt layer (130 metres), this results in the Cr concentration that is too high around the nodes (Figure 3.6b). This issue can be resolved, however, if the basal melt layer is treated as an open system that develops incrementally via multiple magma additions that effectively mix with a melt in a basal layer. The incoming melt supplies Cr to the crystallizing layer, and, as it grows in thickness, the depletion rate of Cr gradually slows down. In contrast to what has been done before (Kruger and Smart, 1987), this model accurately reproduces the two-dimensional distribution of Cr in magnetitite (Figure 3.6c).

Yet another important outcome of the above modelling is that a combination of a steep chemical gradient of Cr depletion with much more constant V contents (Maila, 2015) (Figure 3.7) is only reproducible if all rejected liquid from *in situ* growth nodes is returned into the overlying melt (Figure 3.7; Methods). If this is not the case, then the rate at which the magma differentiates slows down dramatically (Langmuir, 1989). The effect is much more pronounced on trace elements with very large partition coefficients (Figure 3.8). If only as little as 3% of melt fails to return from *in situ* growth nodes to the overlying melt, a much thinner basal melt layer would be required to reproduce the Cr concentration in the MML compared to the case where fractionation is perfect (Figure 3.7). Imperfect fractionation also causes trace elements with different compatibilities to behave more similarly. In such a thin boundary layer, V would also be rapidly depleted (Figure 3.7a), while data from the MML shows no consistent increase or decrease in terms of the V concentration (Langmuir, 1989). Perfect fractionation with a much thicker basal melt layer more accurately reproduces both the Cr and V concentrations

(Supplementary Data 2). Since all liquid is returned from the solidification front to the liquid interior, no crystal mush would be able to develop at the chamber floor.

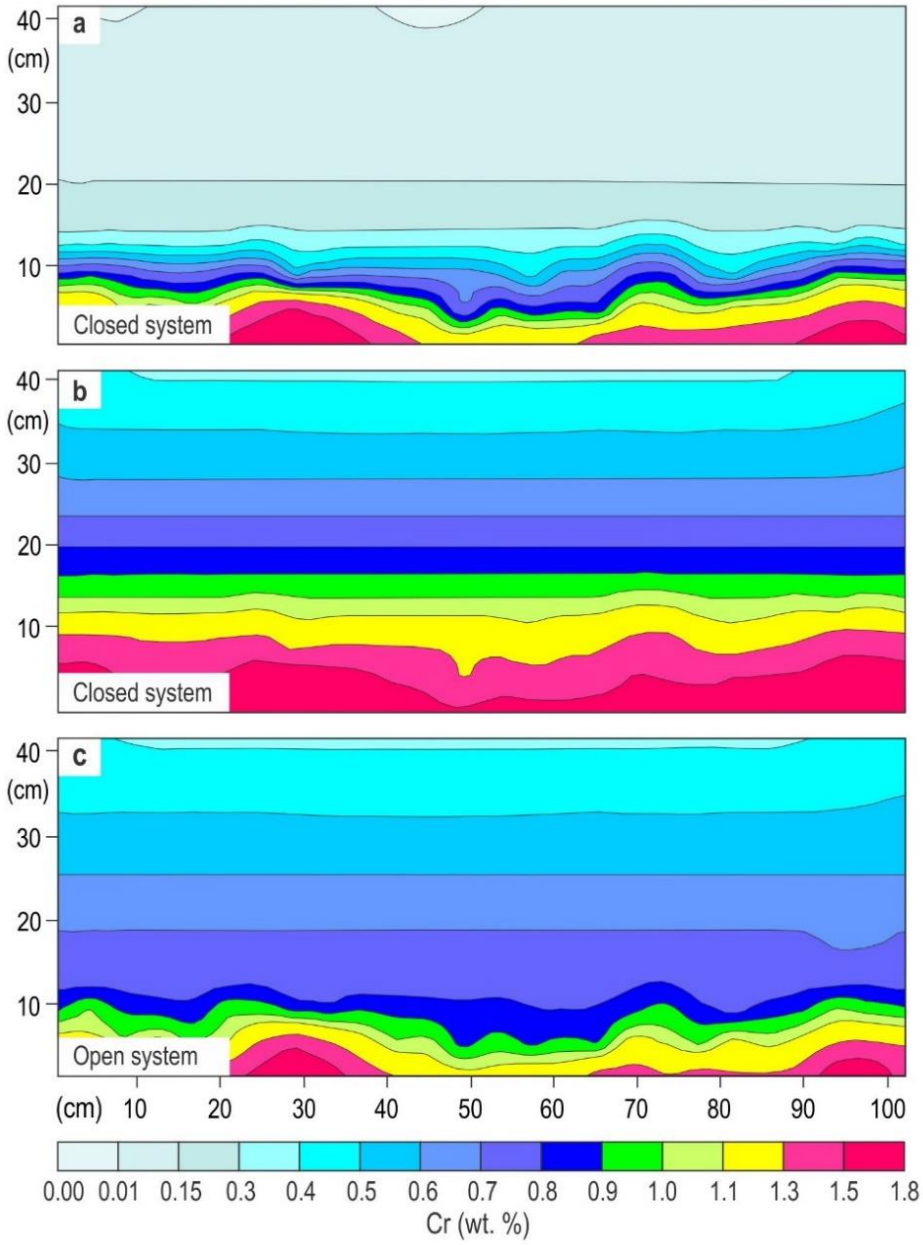

Figure 3.6 Two-dimensional geochemical modelling of Cr in the Main Magnetite Layer. The two-dimensional modelling is based on the results shown in Figure 4.3b and clearly illustrates the need for an open system to accurately describe the change in the Cr concentration (D=525) in the MML. In (a) a closed system is assumed and a relatively thin basal layer is chosen (40 metres) to accurately reproduce the Cr concentration around the growth nodes. However, higher up in the profile Cr is depleted much too rapidly compared to Figure 3b. In (b) a thicker basal layer (130 metres) more accurately reproduces the Cr concentration towards the top of the profile but the Cr concentration around the growth nodes is far too high. Only in an open system (c) in which the basal layer grows incrementally from initially 20 metre to beyond 57 metres thick due to frequent magma addition, can the Cr-concentration accurately be reproduced in two-dimensions (Methods). Because undulations observed in the solidification front in the chemical map (Figure 2.3b) are not statistically significant after about 20 cm of crystallization, a planar solidification front is assumed above this point in our modelling.

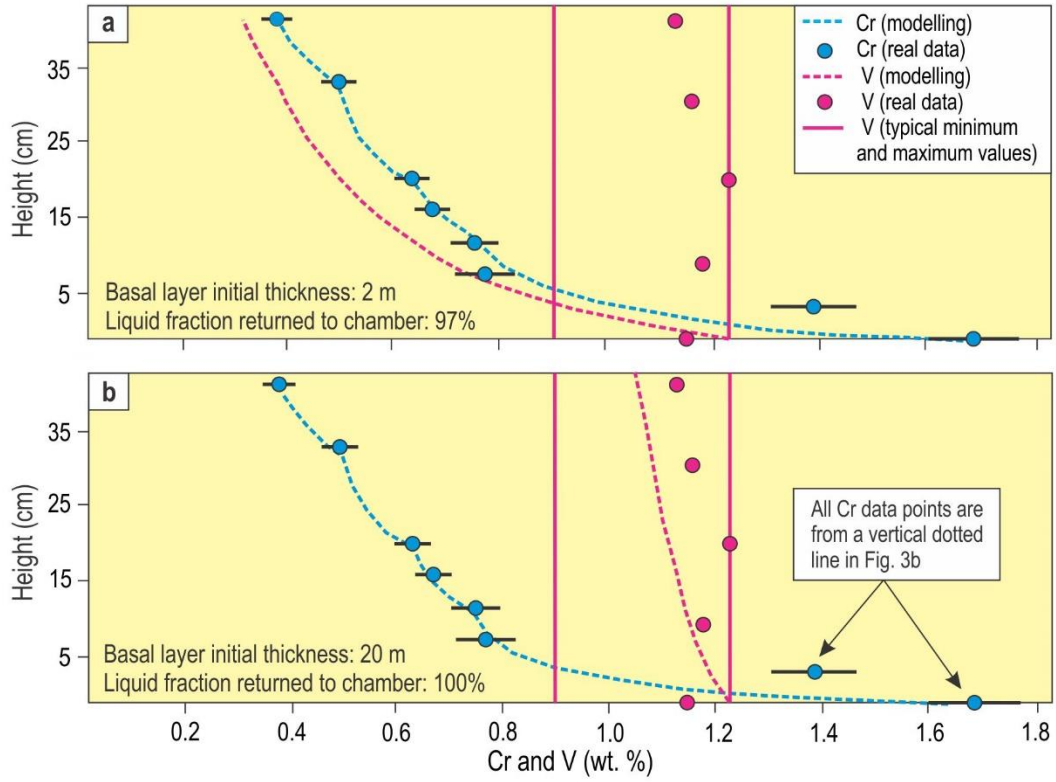

Figure 3.7 One dimensional geochemical modelling of Cr and V in the Main Magnetite Layer. (a) One dimensional modelling of Cr and V in magnetite along a vertical dotted line in Fig 3.3b. It is assumed that 97% of rejected melt is removed from the solidification front and returned to the main magma body. The basal melt layer grows incrementally due to frequent melt additions (Methods). Because fractionation is not perfect, the rate of Cr depletion is much slower, and a relatively thin (2 m) basal melt layer is needed to reproduce the depletion in Cr. In this case the behaviour of Cr and V are similar to each other, with both trace elements being rapidly depleted. However, while the Cr modelling curve matches reality, the modelled V concentration deviates dramatically from typical minimum and maximum values reported in the MML (Maila, 2015). This approach is clearly not compatible with what is observed in reality. (b) In this case, it is assumed that perfect fractionation occurs so that 100% of rejected melt is immediately returned to the main magma body from the solidification front. It is now possible to reproduce the Cr concentration while the V concentration is much closer to reality using a 20 m thick basal melt layer. During the crystallization of massive magnetitite, near-perfect crystal-liquid fractionation must occur (Methods). V concentration data plotted on this diagram are from Maila (2015) as it was not possible to properly quantify V concentrations from our pXRF data. Horizontal black lines indicate the 2σ analytical uncertainty and are calculated by the instrument during analysis. However, because the Cr concentration is calculated from a Cr/V ratio (Methods), the Cr and V analytical uncertainties are compounded to obtain the final 2σ analytical uncertainty shown on the figure. Analytical errors for V are too small to show but standard deviation following the analysis of several samples are approximately 0.01 wt.% (Maila, 2015).

A good match with real chemical data can be produced when magnetite starts crystallising from a 6 to 27 m thick basal melt layer (assuming no interaction with the overlying resident melt) and with a D value of 100 to 600 for Cr and 10 to 25 for V (Supplementary Figure 3.2). Our final modelling (Figure 3.6c and 3.7b) assumes a 20 m thick basal layer using a D value of 525 for Cr and 20 for V. To reproduce the data, this basal melt layer is taken to grow in thickness incrementally to more than 59 m thick via the replenishment by Cr and V undepleted melt

(Supplementary Figure 3.1; Supplementary Data 2 available online at https://www.nature.com/articles/s41467-020-16723-6#Sec11). In the modelling, we assume that a new pulse of melt enters the chamber after every centimetre of crystallization. Because the deposition of a centimetre-thick layer of crystals from a basal layer would barely affect its major element composition, it remains compositionally similar to the new pulses of melt entering the chamber. This will ensure effective mixing between the melt in the basal layer and the incoming melt from the very onset of magmatic recharge. The additional heat input from this process will temporarily halt the crystallization of magnetite, giving time for the compositional effects of magmatic recharge to spread evenly throughout the entire chamber before crystallization resumes.

3.3 Discussion

There appears to be only one, hitherto largely neglected petrological process that can be reconciled with our geochemical data (Figs. 3.3-5) and modelling (Figs. 3.6-8). This is compositional convection caused by the gravitational instability of a thin liquid boundary layer around *in situ* growing crystals (Martin *et al.*, 1987; Campbell, 1996; Seedhouse and Donaldson, 1996) (Figure 3.9). Note that this process differs from the "convection within a crystal mush" model proposed by Tait and Juapart (1989) mentioned earlier as this requires a very thick crystal mush before the onset of convection. During magnetite crystallization, Fe diffuses towards the crystal resulting in a thin boundary layer of a light rejected liquid. As crystallization proceeds, the boundary layer gradually increases in thickness and decreases in density as it loses Fe to the crystallizing magnetite growth nodes. Because our results suggest that magmatic differentiation starts operating after a magnetite node grows to only a couple of centimetres thick, the boundary layer must reach sufficient buoyancy to convect away close to the very beginning of crystallization. To validate this inference, we performed calculations based on equations derived by Martin *et al.* (1987) that allows the examination of the properties of a compositional boundary layer. These calculations suggest the boundary layer around a crystallizing magnetite exceeds the critical Rayleigh number for the onset of vigorous convection when it reaches a thickness of only 1.74 mm, with a compositional change across the boundary layer of about 3.02 wt.%. This corresponds to a density change across the boundary layer of 14.5 kg/m^3 (Methods; Supplementary Data 3 and 4 available at https://www.nature.com/articles/s41467-020-16723-6#Sec11). At this stage, the boundary layer will obtain sufficient buoyancy to be released upwards into the main magma body, either as a constant stream of melt or as a series of plumes (Martin *et al.*, 1987; Campbell, 1996;

Seedhouse and Donaldson, 1996). Their mixing with the overlying melt of the basal layer causes its chemical differentiation which is recorded in subsequently forming mm-thick shells of magnetite. When growth nodes eventually coalesce to form a planar solidification front, multiple plumes are released from random points on the front. Intermingling of the plumes results in vigorous convection and chemical differentiation of the basal layer (Langmuir, 1961) (Figure 3.9). This rejection of unwanted chemical components causes such effective adcumulus

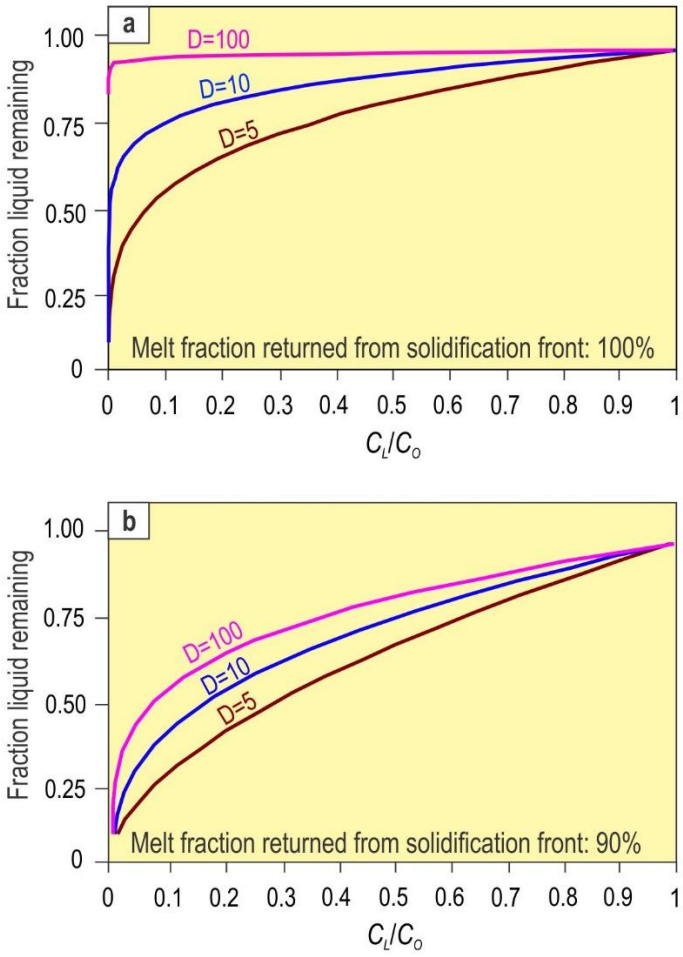

Figure 3.8 The comparative behaviour of compatible trace elements in magmatic systems with perfect and imperfect liquid fractionation. During the crystallization of magma, compatible trace elements are rapidly depleted as the fraction liquid remaining decreases. (a) If perfect crystal-liquid occurs, the rate at which trace elements are depleted are most rapid, and magmatic differentiation is most effective. The varying rates of depletion is shown for three trace elements with varying values of D (5, 10, and 100). (b) In this case, the fractionation of crystals and liquid is imperfect and 10% of the rejected liquid remains within the solidification front. This dramatically slows the rate of depletion of compatible elements with the effect being more dramatic for elements with higher compatibilities. This causes different trace elements with different compatibilities to behave more similar. Thus, to best describe the more constant V concentration compared to the extremely rapid depletion of Cr in magnetitite from the Bushveld Complex (Fig 2.7), the crystal-liquid fractionation needs to be near-perfect (Methods). C_L: Concentration of a particular trace element in the liquid. C_O: Initial concentration of a particular trace element in the liquid.

growth of magnetite that the floor cumulates become totally solid directly at the crystal-liquid interface. Crystal growth is likely to be relatively rapid compared to average crystallization rates in magma chambers of 1 to 2 cm a year (Morse, 1986) as the magnetite crystals are constantly being brought into contact with magnetite-saturated melt due to effective composition convection.

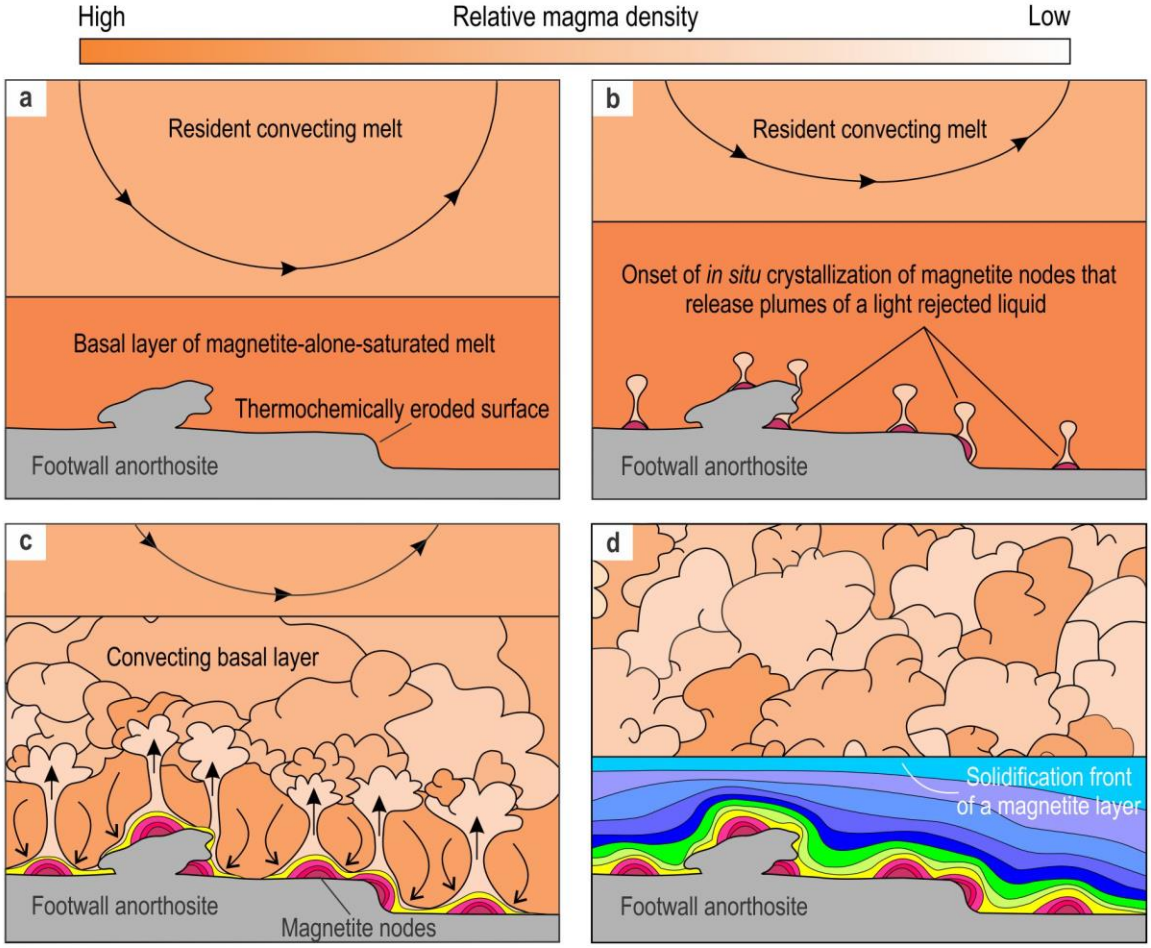

Figure 3.9 A physical model for chemical differentiation of the Main Magnetite Layer in the Bushveld Complex (not to scale). (a) A magnetite-alone-saturated melt is emplaced as a basal layer along the chamber floor causing erosion of pre-existing footwall rocks. (b) On cooling, magnetite starts nucleating on the irregular surface of the anorthositic footwall. (c) Self-nucleation and crystal growth result in the formation of growth nodes. A residual, buoyant layer of liquid is produced around crystallizing nodes that migrates towards their top and is released into the overlying melt. (d) Nodes coalesce to form a planar solid floor; multiple plumes are released which leads to vigorous mixing in the basal layer. In each progressive step, the basal layer increases in thickness due to further addition of magnetite-alone-saturated melt into the chamber as indicated by geochemical modelling (Methods).

We thus conclude that three conventional processes of magmatic differentiation (Figure 2.1) are not necessarily the dominant mechanisms of chemical differentiation in magmatic systems as deeply entrenched in most petrogenetic concepts (Jackson, 1961; Wager and Brown, 1968; Cawthorn, 1996a; Charlier *et al*., 2015). A viable alternative is compositional convection caused by an unstable chemical boundary layer around *in situ* growing crystals at the chamber floor (Martin *et al*., 1987; Campbell, 1996; Seedhouse and Donaldson, 1996). This process is unlikely to be unique to magnetitite layers. For example, field evidence for other cumulates of the Bushveld Complex, such as development of chromitite and orthopyroxenite layers along overturned portions of the chamber floor, attests to their *in situ* crystallization as well (Latypov *et al*., 2016; 2017a; 2017b; Chistyakova *et al*., 2019). Similar to magnetitite, any other oxide-rich or mafic-ultramafic lithologies are expected to produce a buoyant boundary layer around the crystal liquid interface as has been demonstrated experimentally for *in situ* growing olivine (Seedhouse and Donaldson, 1996). *In situ* growth nodes may occur in these lithologies as well but cannot be detected due to the lack of sufficiently sensitive trace-element indicators of chemical differentiation in their minerals. We speculate therefore that this type of compositional convection may represent a very effective mechanism of magma evolution on Earth. Importantly, because of the very high buoyancy of a compositional boundary layer produced by crystallizing magnetite, a crystal mush is virtually absent in these oxide rocks, while it may only be a few metres thick in silicate rocks (Latypov *et al*., 2017a; Holness *et al*., 2017b; Hess, 1960; Irvine *et al*., 1998). A lack of a thick mushy zone provides strong support for a classical 'magma chamber' paradigm (Figure 2.1a) that has been underpinning models of the Earth's magmatism for over a century (Jackson, 1961; Wager and Brown, 1968; Cawthorn and McCarthy, 1980; Campbell, 1996; Cawthorn, 1996a; Marsh, 1996; Latypov & Egorova, 2012; Charlier *et al*., 2015), magma oceans/impact melt sheets (Vaughan *et al*., 2013; Latypov *et al*., 2019b).

One important implication of our study is that it casts doubt on the universal validity of a recently advanced mushy reservoir paradigm (Cashman *et al*., 2017; Jackson *et al*., 2018) (Figure 2.1b) that denies the existence of large and long-lived magma chambers in the Earth's crust and suggests that all magmatic systems, including layered intrusions, are predominantly composed of crystal-rich mushes. This concept is at odds with our data on solidification fronts in magnetite layers of the Bushveld Complex; the largest layered intrusion that is so widely employed for constraining petrological concepts. In addition, melt segregation and chemical

differentiation in this novel paradigm is thought to be dominated by compaction (Cashman *et al*., 2017; Jackson *et al*., 2018). However, the most recent petrographic studies indicate a notable lack of textural evidence for compaction in cumulate rocks of layered intrusions, including the Bushveld Complex (Holness *et al*., 2017b). This is perfectly reasonable since a very thin to nearly absent crystal mush in this (Holness *et al*., 2017a) and other layered complexes (Hess, 1960; Irvine *et al*., 1998) implies essentially nothing to compact. We hypothesize, therefore, that the mere existence of the Bushveld Complex with its spectacular phase, modal and cryptic layering and giant mineral deposits (Cawthorn, 2015), such as magnetitite layers up to hundreds of kilometres in length, is evidence that large, long-lived and largely molten magma chambers existed in the past, may operate right now and will likely emerge in the future life of our restless Earth.

3.4 Acknowledgements

The original manuscript benefited from the constructive peer reviews by James Day, Brian O'Driscoll, Tim Ivanic, Sofya Chistyakova, Spike McCarthy, Olivier Namur, Ed Mathez, Tony Naldrett, Ed Ripley, Chris Hawkesworth, and Jean Bédard. We would like to thank Merrily Tau for his assistance in performing pXRF measurements in the field, Grant Cawthorn for providing us with magnetite samples and in-house XRF data for the construction of a calibration curve for the pXRF analysis, and Grant Bybee and Gelu Costin for their assistance with MELTS modelling. Sofya Chistyakova is thanked for helping us substantially improve the quality of our figures. The study was supported by research grants to R. L. from the National Research foundation (NRF) and Department of Science and Technology (DST)–NRF Centre of Excellence for Integrated Mineral and Energy Resource Analysis (CIMERA) of South Africa. Any opinion, finding and conclusion or recommendation expressed in this contribution is that of the authors and the DST-NRF CIMERA and NRF do not accept any liability in this regard. The clarity of the final version of this manuscript has been increased by comments of two official reviewers.

3.5 Supplementary information

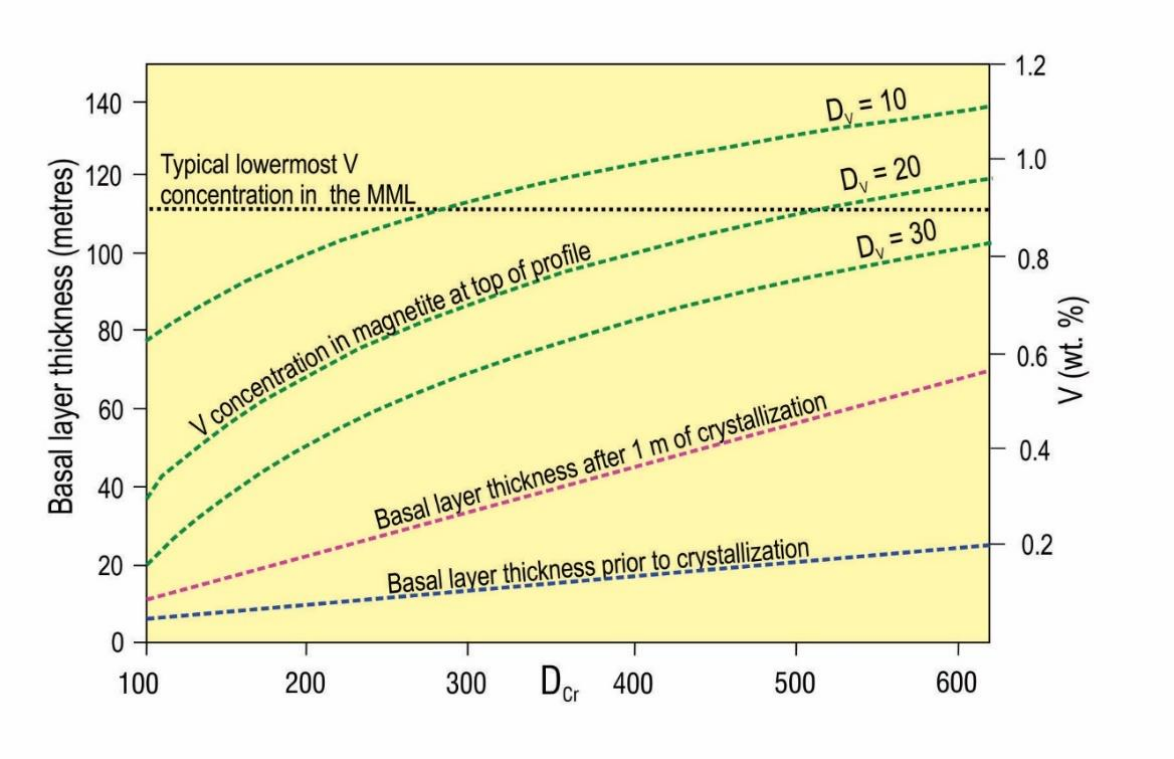

Supplementary Information Figure 3.1 Constraints on the basal melt layer thickness depending on the selected D value for Cr. The diagram should be read in the following way: first select a partition coefficient for Cr in magnetitite on the x-axis. Trace a line directly upwards until the blue line is intercepted. From this point the initial basal layer thickness before crystallization can be read off on the y-axis on the left. Trace the line further upwards until in intercepts the purple line. This allows the final thickness of the basal melt layer to be read off the y-axis after the deposition of 1 metre of magnetitite assuming the basal melt layer grows incrementally due to continued magma addition. Continue tracing the line upwards to intercept one of the green curves depending on the preferred D value for V (10, 20, or 30). This allows the determination of the final V concentration of the MML based on a starting V concentration that can be read off on the y-axis on the right (Methods). By using the entire range of experimentally determined D values for Cr in magnetite in basaltic melt (Irving, 1978), the initial basal layer thickness is unlikely to be more than 6 metres and less than 27 metres thick to accurately describe the distribution of Cr in the MML. After 1 m of magnetitite crystallization, the basal layer has grown to a thickness of between 12 and 71 metres thick due to the addition of melt to the basal layer. The upper curves (green) indicate V concentration at the upper part of the MML assuming a starting V concentration in magnetite of 1.23 wt. % compared to the typical lowermost V concentration recorded in this layer (Maila, 2015) (the typical lowermost V concentration is indicated by the black horizontal stippled line). To prevent the V concentration from dropping below the typical lowermost value, and assuming a D for V in magnetite of about 20, a D value of 525 is needed for Cr in magnetite. This requires an initial basal melt layer thickness to be of about 20 metres. These are the final modelling parameters used (Figure 3.6c and 7b) (Methods).

CHAPTER 4

MAGMATIC KARST REVEALS DYNAMICS OF CRYSTALLIZATION AND DIFFERENTIATION IN EARTH'S MAGMA CHAMBERS

Reference to paper:

Kruger, W. and Latypov, R. Magmatic karst reveals dynamics of crystallization and differentiation in Earth's magma chambers. Submitted to Nature Geoscience. Impact factor: 13.6.

Author contributions

Kruger: 65% (Geochemically analysed field outcrops, performed quantification of geochemical data, wrote the first draft of the manuscript, and contributed to ideas presented in the paper);

Latypov: 35% (Supervisor, contributed to ideas presented in the manuscript, assisted with editing and reviewing the manuscript).

Abstract

A deep understanding of magma chamber dynamics is the key to many natural phenomena, from chemical patterns in crystals to an internal structure of terrestrial planets. Where, why and how magma crystallizes and differentiates in crustal magma chambers are three fundamental questions, all highly controversial. Here we report on our discovery of a new natural phenomenon – the undercut-embayed chamber floor in the Bushveld Complex – which allows us to address these questions. The undercut-embayed floor is produced by magmatic karstification (i.e. erosion by dissolution) of the basal cumulates by replenishing magmas. This results in a few metres thick three-dimensional framework of spatially interconnected erosional remnants that separate the floor cumulates from the overlying resident melt. The resident melt in this environment is effectively cooled through the floor inducing heterogeneous nucleation and *in situ* growth against much of its three-dimensional framework. The solidification front thus propagates in multiple directions from the surfaces of erosional remnants. Fractional crystallization occurs there by convective removal of a compositional boundary layer from *in situ* growing crystals and it is remarkably efficient even in very confined spaces. We propose that the way magma crystallizes and differentiates in the undercut-embayed chamber floor is likely common for the evolution of most magma chambers in Earth's crust.

4.1 Introduction

Gaining deeper insights into how natural magmas crystallize and differentiate in crustal magma chambers is crucial for scientific investigations in almost all fields of volcanology and igneous petrology, from highly detailed studies at the scale of individual crystals (Humphreys, 2009; Namur and Humphreys, 2018) to global tectonic reconstructions concerning the evolution of Earth and other terrestrial planets (Solomon, 1980; Fearn and Loper, 1981; Latypov *et al*., 2019b). A complete understanding of the inner workings of magma chambers relies on answering three fundamental questions: Where do crystallization and differentiation occur? Why do crystallization and differentiation occur within this particular environment? What processes are responsible for crystallization and differentiation? A plethora of opinions exist on each of these questions. For instance, in regards to the first question, models may portray magma chambers as melt pools in which crystals either grow on pre-existing crystals along the chamber margins (Campbell, 1978; Martin *et al*., 1987; Campbell, 1996), form within the melt and then settle on the chamber floor (Wager, 1963; Wager and Brown, 1968; Irvine, 1970; Morse, 1986a; 2015), or are kept suspended in a convecting melt until the formation of crystal-rich mush that is unable to flow (Bachmann and Bergantz, 2004; Bea, 2010). Critical information necessary to resolve these and many other contrasting interpretations is difficult to obtain because evolving magma chambers are hidden from our direct observation. One way to address this problem is by studying the internal structure of solidification fronts in mafic-ultramafic layered intrusions – 'fossilized' natural laboratories that constrain many fundamental principles of igneous petrology (Wager and Brown, 1968; Cawthorn, 1996a; Charlier *et al*., 2015). However, not even this approach is always fruitful. The intrusions primarily developed via the inward propagation of a planar solidification front that provides little constraints on magma chamber processes. Moreover, most rock-forming minerals are not chemically able to record and/or preserve the properties of a solidification front (Kruger and Latypov, 2020a). Here we report on intricate chemical patterns in massive magnetitites of the Bushveld Complex in South Africa (Cawthorn, 2015) that enables the recognition of a new petrological phenomenon in magma chambers – the undercutting and embayment of the temporary chamber floor. The 'undercut-embayed floor' is unique in providing definitive constraints on magma crystallization and differentiation processes, thereby providing explicit solutions to the above fundamental questions.

4.2 Chemical patterns in massive magnetitite

We have examined a spectacular outcrop of the lowermost magnetitite layer (also termed as the bottom seam) in the Bushveld Complex – the largest preserved layered intrusion in Earth's crust (Cawthorn, 2015). This layer shows peculiar field relationships with the underlying anorthosite (Figure 4.1a) such as depressions and undulations, while its most striking feature is the presence of several elongated anorthositic inclusions trapped within the magnetitite. In layered intrusions, such inclusions can be viewed as transported fragments that have either been brought into the chamber with inflowing magmas (Sparks *et al*., 1977) or fallen from the roof sequence onto the chamber floor (Irvine, 1987; Irvine *et al*., 1998; Namur *et al*., 2015; Latypov *et al*., 2019b).They may also be interpreted as *in situ* remnants of originally continuous layers that were partially dissolved by thermochemical erosion associated with magma chamber replenishment (Latypov *et al*., 2016; Pebane and Latypov, 2017). A commonality for these interpretations is that they imply that after mechanical deposition (Sparks *et al*., 1977; Irvine, 1987; Irvine *et al*., 1998; Namur *et al*., 2015; Latypov *et al*., 2019b) or *in situ* formation (Latypov *et al*., 2016; Pebane and Latypov, 2017) the fragments are supposed to lie directly on the chamber floor, with no open space filled with resident melt below them.

We have examined this outcrop following a procedure from our recent study of trace element (e.g. Cr) distributions in magnetitites in two dimensions by a handheld X-ray fluorescence spectrometer (pXRF) (Kruger and Latypov, 2020a) (Appendix C). Special attention has been given to Cr due to its exceptionally high magnetite-liquid partition coefficients in basaltic melts that may range from 300 to beyond 600 (Irving, 1978; Cawthorn and McCarthy, 1980; Toplis and Corgne, 2002; Dare *et al*., 2012). This, along with inferences that massive magnetitites in the Bushveld Complex crystallized from basal melt layers less than a few tens of metres thick (Cawthorn and McCarthy, 1980; Kruger and Smart, 1987; Kruger and Latypov, 2020), allows for a rapid depletion of the basal melt layer in Cr. During crystallization, the melt's depletion in Cr is recorded in decreasing Cr-isolines in massive magnetitites at the scale of solidification fronts (Cawthorn and McCarthy, 1980; Kruger and Latypov, 2020a). This feature makes Cr in magnetite a very powerful tracer of magmatic differentiation processes (Cawthorn and McCarthy, 1980), with two-dimensional Cr geochemical maps of field outcrops allowing an unparalleled visualization of the solidification front's step-wise propagation (Kruger and Latypov, 2020a). Results of our geochemical mapping of the bottom seam (Methods; Appendix

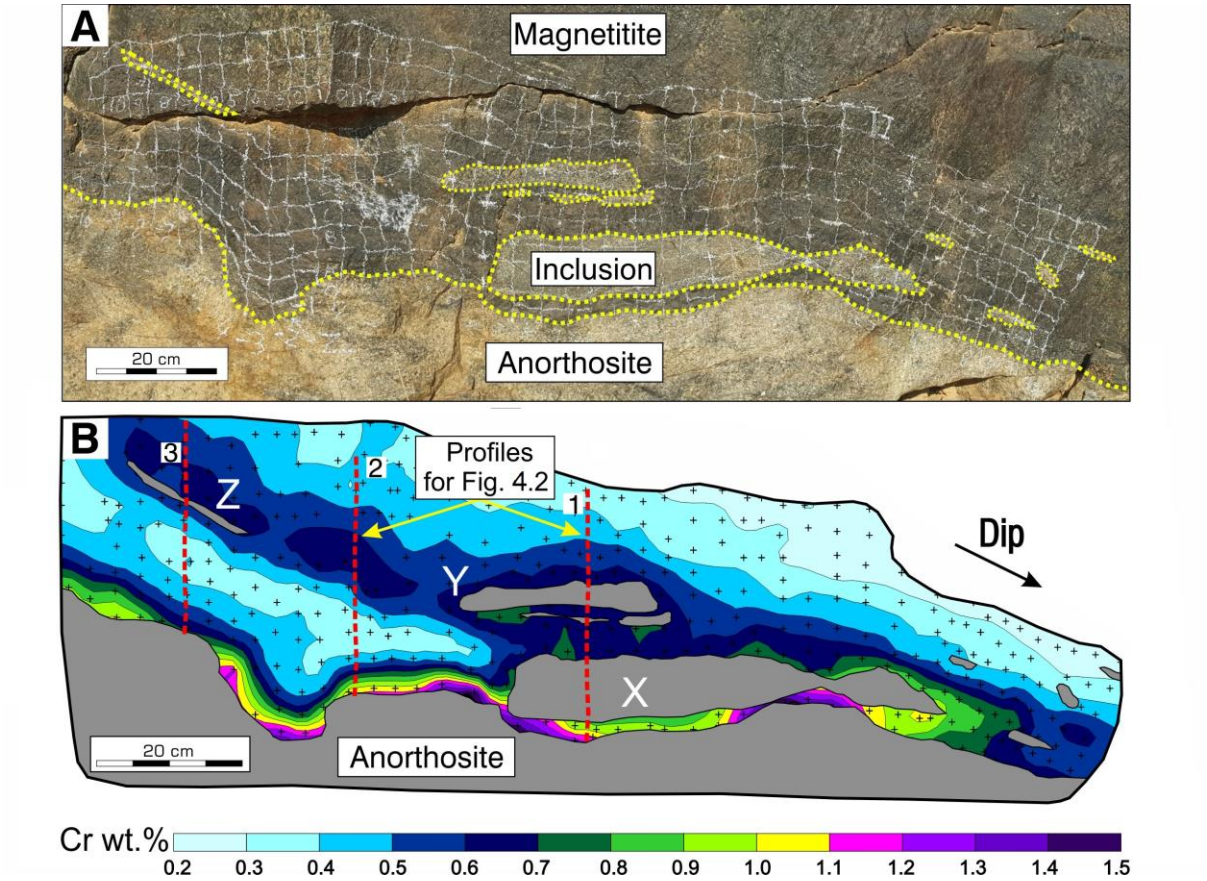

Figure 4.1 Massive magnetitite with two-dimensional Cr chemical patterns. (a) Field photograph of an outcrop of the bottom seam of massive magnetitite showing undulated footwall contact and several anorthositic inclusions; (b) Geochemical contour map showing the distribution of Cr within the layer. Overall, the Cr concentration decreases rapidly upwards in the layer. Higher Cr contents were recorded at the basal contact and around anorthositic inclusions, including a cryptic zone with higher Cr contents connecting the central inclusion Y and a smaller one Z to the left. A converging chemical pattern is observed between this cryptic zone and the floor. Several dome-shaped high Cr growth nodes on the bottom contact of the layer indicate incipient in situ nucleation and growth of magnetitite (Cawthorn, 1994; Kruger and Latypov, 2020a). Black crosses indicate positions of individual data points. The outcrop is located at the Rhovan Mine, Western Bushveld Complex, South Africa.

C, Supplementary information Figure 4.1) reveals the two-dimensional distribution of Cr within the layer (Figure 4.1b). Chromium contents generally decreases rapidly upwards from the base of the magnetitite layer while Cr contents appear elevated in the vicinity of anorthositic fragments. We have also discovered a cryptic zone of magnetite with an elevated Cr concentration (blue in colour) that connects a small anorthositic slither to the left (Z) and a larger inclusion (Y) towards the centre of the outcrop. In selected one-dimensional profiles, three distinct compositional trends are observed: a continuous upward depletion in Cr across fragments (Figure 4.2a), a gradual reversal in Cr where no fragments are present (Figure 4.2b), and an inward decrease in Cr away from the footwall and a fragment (Figure 4.2c). Two more

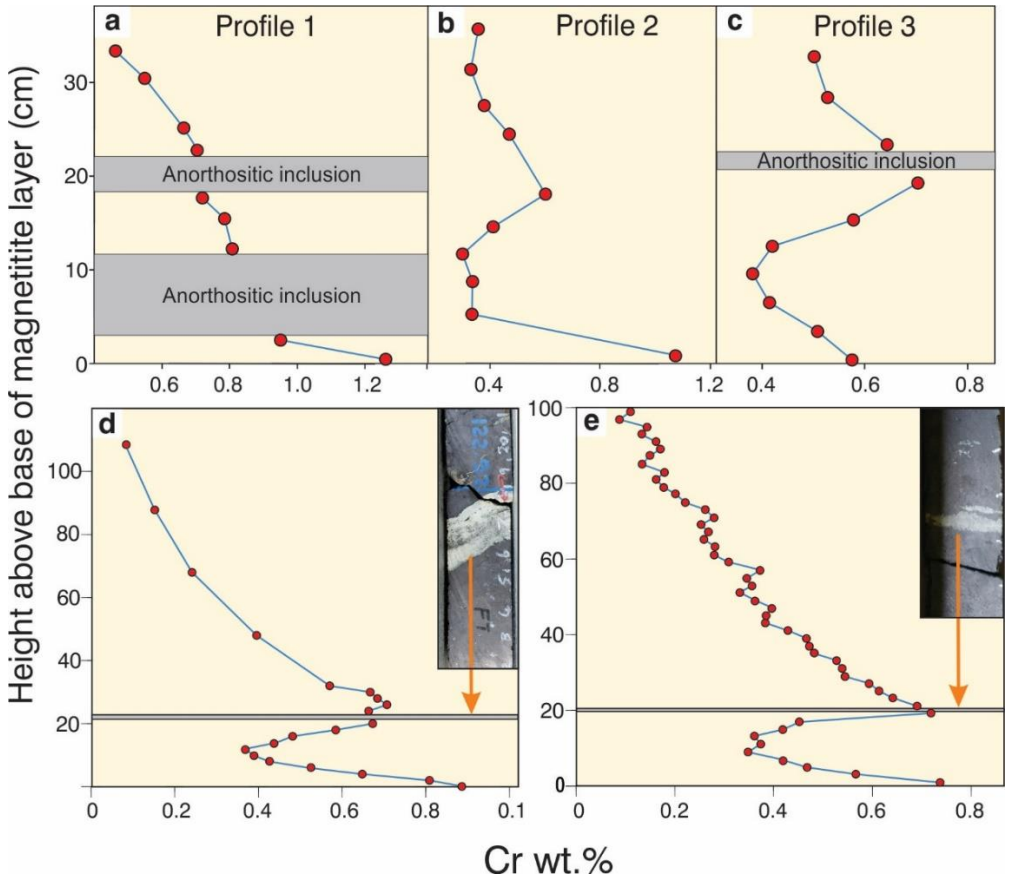

Figure 4.2 One-dimensional vertical profiles in Cr content across a massive magnetitite. Position of these three profiles across the bottom seam of massive magnetitite is indicated on Figure 4.1b. **a,** A rapid continuous decrease in Cr content upwards with no chemical changes/breaks at anorthositic inclusions; **b,** A gradual reversal in Cr content in a level where no anorthositic inclusions are visible; **c,** An initially rapid decrease in Cr content followed by its gradual increase towards an anorthositic inclusion. Cr content again declines upwards from the top of the anorthositic inclusion. d and e, Additional examples of vertical profiles in Cr content across the bottom seam that contains anorthosite inclusions from drill cores in a different locality (Vametco mine, Western Bushveld Complex). Insets show anorthositic inclusions (light in colour) trapped within the massive magnetitite (dark in colour). The distribution of the Cr in these two examples are similar to that in (c).

examples with an inward decrease in Cr through the bottom seam are additionally shown from other areas (Figure 4.2d, e) (Appendix D).

4.3 The phenomenon of the undercut-embayed floor

In line with some previous studies (Cawthorn, 19994; Kruger and Latypov, 2020), we have recorded high Cr structures (purple in colour; Figure 4.1b) that indicate sites of incipient nucleation of magnetitite at the very base of the profile. This was followed by self-nucleation on the pre-existing nuclei, causing outward concentric growth to produce dome-shaped structures that are referred to as *in situ* growth nodes. Magnetite growth at the base proceeded

until most of the footwall was covered. Shortly thereafter, magnetite must have started nucleating and growing directly on the surfaces of anorthositic inclusions as indicated by the elevated Cr contents of magnetite in their vicinity. Locally, solidification fronts growing from the floor upwards and from the inclusions downwards converged, resulting in cryptic layers that are depleted in Cr relative to the magnetitite directly above and below. This omnidirectional growth of magnetite around anorthositic inclusions leads to the most intriguing conclusion: these fragments must have been present in their current positions and entirely surrounded by the melt prior to onset of its crystallization. This finding precludes the models that imply that fragments had to be resting directly on a solid floor (Sparks *et al*., 1977; Irvine, 1987; Irvine *et al*., 1998; Namur *et al*., 2015; Latypov *et al*., 2019b). Clearly, these fragments could not remain suspended in the melt near to the floor; they would either settle or float depending on their density relationships with the resident melt. Even in the unlikely case that these fragments were initially neutrally buoyant, they would sink to the floor rapidly the moment magnetite started crystallizing on their outer surfaces. If this were the case a gradual increase in the Cr contents towards the bottom of the fragments would not be observed over a distance of a few cm (Figure. 4.2). To prevent their movement, the inclusions must somehow have been anchored in their current positions. The cryptic zone of magnetite enriched in Cr that connects two inclusions (Z and Y, Figure 4.1b) provides an important clue to this issue. The continuous nature of this zone as well as the fact that the reversal appears to be gradual (Figure 4.1b and 4.2b) suggests that magnetite was growing on some septum that is now either hidden behind the current face of the outcrop or has already been removed by mining. This septum is most likely composed of a continuous anorthosite body that interconnects these two and likely many other obscured inclusion-like bodies. All the seemingly separate anorthositic inclusions in this outcrop are thus likely interlinked with each other and firmly attached to the footwall in three dimensions. We refer to this three-dimensional framework of spatially interconnected bodies at the bottom of the chamber as the ‘undercut-embayed floor’.

4.4 Magmatic karstification of the floor cumulates

The undercut-embayed floor can be best explained as a result of thermochemical erosion of the basal cumulates by highly reactive and likely superheated melts replenishing the evolving Bushveld chamber (Latypov *et al*., 2016; Latypov *et al*., 2017a; 2017b). Replenishing melts may possess high erosive power due to their chemical and thermal disequilibrium with the pre-existing floor cumulates. Thermal disequilibrium results from melt superheating that can be up

to 90°C for basaltic melts rising near adiabatically from the deep-seated magmatic reservoir (Latypov *et al*., 2020). Even if some cooling of the ascending melt takes place so that it arrives into the chamber at a much lower degree of superheating (say, 10-15°C), a few tens of metres' thick column of such a melt can still erode a few metres of footwall rocks (Latypov *et al*., 2017a; 2017b) (Methods). This is because a major agent of magmatic erosion is not the heat itself (causing melting) but rather chemical disequilibrium (causing dissolution) between the new melts and floor cumulates (Kerr, 1994; Latypov *et al*., 2020). Melt superheating is still, however, essential in preventing the onset of melt crystallization. The reason is that the formation of a new basal layer of rocks may immediately terminate the dissolution of the floor cumulates (Latypov *et al*., 2016). Geochemical evidence suggests that magmatic recharge of the chamber preceded the formation of massive magnetitite layers in the Bushveld Complex (Scoon and Mitchell, 2012). If these new pulses are not in chemical and thermal equilibrium with the floor rocks, the melt may cause their whole-sale thermochemical erosion. With time, the intensity of erosion will wane to become only partial – mostly occurring along fractures and planes of weakness (Figure 4.3) – and will result in the complex, undercut-embayed morphology of the floor cumulates. We suggest referring to this phenomenon as magmatic 'karstification' of the chamber floor cumulates as it is similar in both morphology and origin to karst landforms in surface sedimentary rocks produced by infiltrating acidic water (Waele *et al*., 2011).

4.5 Challenging the fundamentals of magma chamber dynamics

The chemical patterns in the magnetitite layer (Figure 4.1) challenge the universal validity of several fundamental principles of magma chamber dynamics which are deeply entrenched, although not always explicitly formulated, in modern petrological concepts. The first postulate that requires attention is that the temporary floor of a magma chamber is planar so that the cumulate pile is always in direct contact with the overlying resident melt (Wager and Brown, 1968; Campbell, 1978; 1996; McBirney and Noyes, 1979; Charlier *et al*., 2015; Cawthorn, 1996a; Latypov *et al*., 2016). Our data show that this may not be true for magma chambers undergoing repeated replenishments. In this case, the solid floor may be separated from the overlying melt by a few metres thick undercut-embayed floor (Figs. 4.3-4). This transitional zone consists of a three-dimensional framework of *in situ* bodies (i.e. non-transported erosional remnants) that are spatially interconnected with each other and the floor rocks. Revisiting our field observations indicates that the undercut-embayed floor is, in fact, a quite common

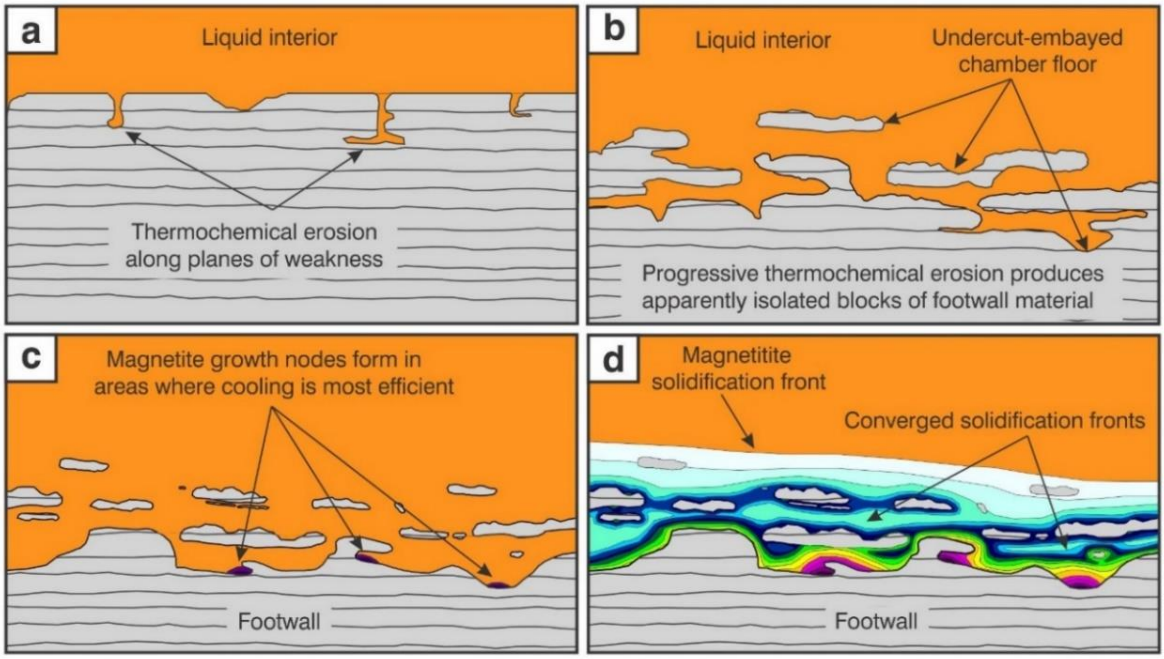

Figure 4.3 Physical model for the origin of the undercut-embayed chamber floor and propagation of a solidification front therein. (a) Floor cumulates with an initial planar surface undergo thermochemical erosion along points/planes of weakness by a newly-emplaced reactive melt; (b) As erosion progresses, blocks that appear isolated in two dimensions but still connected with the floor in three dimensions may form, eventually resulting in the undercut-embayed chamber floor. (c) With time, thermochemical erosion comes to a halt and, after some degree of cooling, magnetite starts to nucleate and grow in areas where heat loss is most rapid, such as in depressions or underneath fragments partly attached to the floor. (d) Crystal nucleation and growth from the floor and fragments results in omnidirectional propagation patterns of the solidification front, with some converging solidification patterns in the vicinity of the chamber floor.

phenomenon in the Bushveld Complex which has so far escaped our attention. Field evidence for such a floor is abundant at all stratigraphic levels of this complex in the form of erosional remnants that are still partly attached to their footwall (Figure 4.4b, c; Supplementary information Figure 4.2a-d). More commonly, the erosional remnants occur as isolated fragments that are seemingly 'suspended' among host rocks (Figure 4.4d; Supplementary information Figure 4.1e-f). Regrettably, to prove the non-transported nature of these fragments using geochemical mapping does not seem possible because, unlike magnetite, all silicate minerals (e.g. plagioclase, olivine, pyroxenes) and chromite are not chemically sensitive enough to record the evolution and propagation of solidification fronts in magmatic systems in sufficient detail (Kruger and Latypov, 2020a).

Another tenet to be reconsidered is that the resident melt in large basaltic chambers is only cooled by losing heat through the roof rocks once crystallization is underway (Irvine, 1970; Morse, 1988; Hess, 1972). This view stems from a well-known fact that in large layered

intrusions heat loss through the chamber floor becomes negligible once a thick cumulate pile has accumulated, insulating the resident melt from the cold country rock below (Morse, 1988; Hess, 1972). For this reason, after the formation of only ~100 m of floor cumulates, *in situ* nucleation and growth of crystals due to cooling through the chamber floor is considered to be impossible (Holness *et al*., 2020). However, our results suggest otherwise (Figure 3.1).

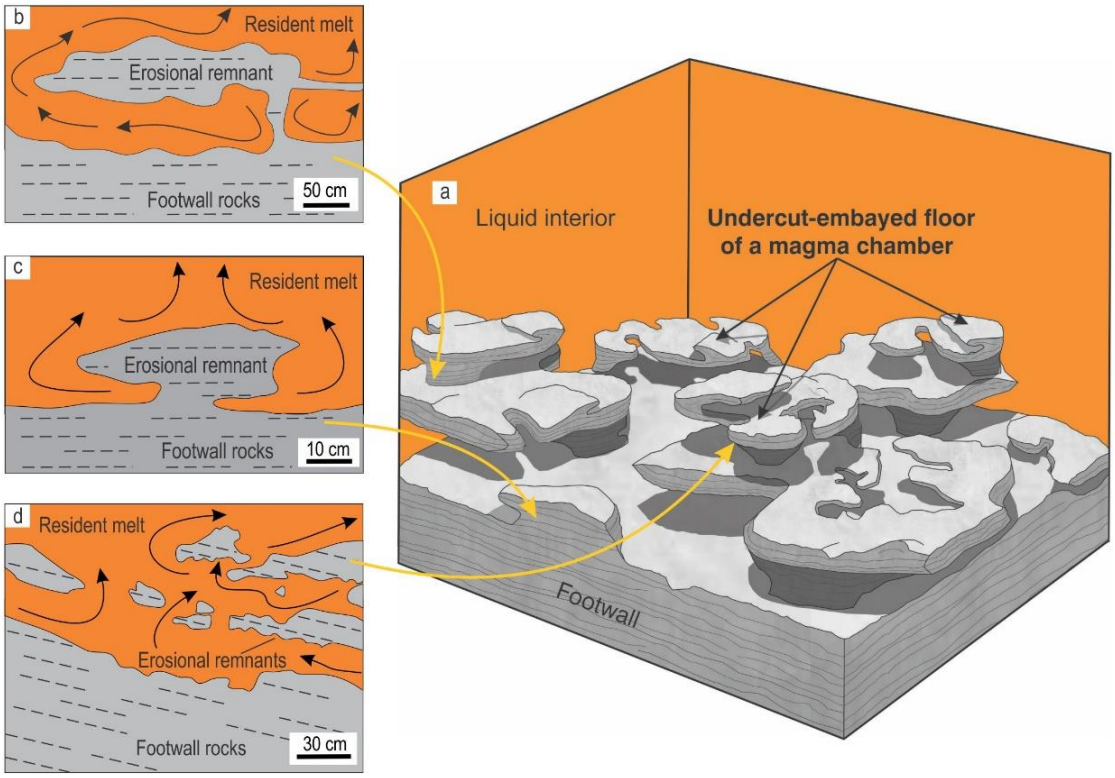

Figure 4.4 Artistic impression of the undercut-embayed chamber floor in an evolving magma chamber along with interpretive sketches of relevant exposures. (a) When the undercut-embayed floor is observed in three dimensions, it becomes obvious that most seemingly isolated 'inclusions' in two dimensions are actually connected with each other to produce an intricate in three-dimensional framework of partially eroded floor cumulates. The process responsible for the formation of such a floor is referred to as here as magmatic 'karstification'. The undercut-embayed floor is expected to be common in open magma chambers. The artistic design of the figure is by an artist Inna Laur (Finland). (b) Interpretive sketch of an erosional remnant of anorthosite that is hosted by the Main Magnetite Layer and is still attached to the footwall rocks. Vametco Vanadium Mine, Upper Zone of the Western Bushveld Complex (Supplementary information Figure 4.2a). (c) Interpretive sketch of an erosional remnant of orthopyroxenite that is hosted by the LG6 chromitite and is still attached to the footwall rocks. Jagdlust area, Lower Critical Zone of the Eastern Bushveld Complex (Supplementary information Figure 4.2b). (d) Interpretive sketch of in situ erosional remnants of anorthosite that are hosted by the Merensky Reef orthopyroxenite and seemingly not attached to the footwall rocks in this section. Rustenburg Platinum Mine, Upper Critical Zone of the Western Bushveld Complex (Supplementary information Figure 4.2e). Black arrowed curves in (b-d) show compositional convection. Yellow arrowed curves indicate possible positions of these 2D exposures in the 3D space of the undercut-embayed chamber floor.

Magnetite growth nodes detected in the profile are not randomly distributed but rather tend to be concentrated in the vicinity the largest inclusion X and in a small depression (Figure 4.1b). In our previous study (Kruger and Latypov, 2020a), the highest Cr concentration recorded in the Main Magnetite Layer from the Bushveld Complex was also located underneath an anorthositic inclusion. Growth nodes of a similar Cr content are never found directly on the surfaces of the inclusions. Such distribution of the growth nodes can be most logically explained by cooling directly through the floor, while the anorthositic inclusions serve as heat sinks that further aid cooling of the surrounding melt. Where anorthositic inclusions are located close to the floor cooling would be most efficient, explaining why nucleation and the formation of growth nodes are more favourable here. Cooling would also be more efficient within a depression, and magnetite nucleation is more probable here than on a flat surface. The reason why growth nodes with high Cr contents are not located directly on the outer surfaces of inclusions is likely because of their inability to cool the melt as effectively as the thick cumulate pile below. Cooling of melt through the floor in open magma chambers likely becomes important because magmatic karstification excavates the deep and already cold cumulates. It should be noted, however, that cooling through the floor provides only a partial solution to an *in situ* crystallization mechanism. A major reason why crystals prefer to form on the 3D framework of the undercut-embayed floor is because heterogeneous and self-nucleation on pre-existing crystals is much more favourable due to energy considerations compared to homogenous nucleation in the main magma body (Campbell, 1978; 1996).

Yet another dogma to be reassessed is that, with progressive cooling, basal solidification fronts in magma chambers invariably propagate unidirectionally upwards until the chamber is completely solidified (Wager and Brown, 1968; Irvine, 1970; Campbell, 1978; 1996; Morse, 1988; Cawthorn, 1996a; Marsh, 2006; 2013; Charlier *et al*., 2015; Latypov *et al*., 2015; 2016; 2019). This postulate is invalid for the undercut-embayed floor (Figs. 4.3-4) because its three-dimensional framework has multiple cooling surfaces on which crystals may nucleate and grow. As a result, solidification fronts may simultaneously advance in nearly all directions (Figure 4.3) causing them to converge underneath some inclusions (Figure 4.3c-e). This realization provides a distinctly different interpretation for Cr reversals that are so common in Bushveld magnetitite layers (Cawthorn and McCarthy. 1980) (Figure 4.2). Because these reversals were found to be laterally discontinuous, they could not be explained by replenishment of the chamber by new Cr-undepleted melts. They also cannot be attributed to convective Cr-undepleted eddies descending from the interior of the magma chamber

(Cawthorn and McCarthy, 1980) because these can hardly penetrate through a three-dimensional framework of the undercut-embayed floor. In contrast, we suggest that these reversals are due to the omnidirectional propagation of solidification fronts from the outer surfaces of anorthositic fragments (Figure 4.3). Although such fragments were not reported to be associated with Cr reversals (Cawthorn and McCarthy, 1980), the reversal in a cryptic zone of magnetite that connects inclusions (Z and Y in Figure 4.1b) clearly shows that the fragments may simply not be visible. It is also important to note that not all fragments may be associated with Cr reversals. The reversals may be absent if cooling through the floor is very efficient, so that an upward-propagating solidification front captures the lowermost inclusions before crystals start nucleating and growing on their outer surfaces (Figs. 4.1 & 4.2a).

4.6 Most profound implications for magma chamber dynamics

A key advantage of the undercut-embayed floor – as a newly recognized petrological realm – is that it provides clear-cut constraints on where, why and how magma crystallizes and differentiates in basaltic magma chambers. The following solutions to these fundamental questions can be proposed: (1) *where:* magma crystallizes *in situ* on the floor of the chamber, i.e. directly on all surfaces of three-dimensional framework of the undercut-embayed floor; (2) *why: in situ* crystallization occurs on these surfaces because heterogeneous and self-nucleation on pre-existing crystals of the floor cumulates has the lowest activation energy; in addition, cooling through these surfaces favours crystal nucleation on the undercut-embayed floor. This leaves the final question; (3) *how* do these processes occur within this environment? It is generally accepted that a planar chamber floor is crucial for magmatic differentiation because it allows effective mass transfer between the overlying resident liquid and floor cumulates, such as compaction compaction (McKenzie, 2011) or compositional convection within mushy cumulates (Tait and Jaupart, 1992). Following this logic, the three-dimensional framework of the undercut-embayed floor would serve as a serious obstacle for magmatic differentiation. In this respect, it is noteworthy that even in extremely confined spaces, such as those below the largest fragment X or where solidification fronts converge (Figure 4.1), the mass exchange still occurs extremely effectively to produce a pure magnetite adcumulate. This means that the undercut-embayed floor presents no physical barriers whatsoever for the chemical exchange between the resident melt and the melt in a three-dimensional framework. We can envisage only one mechanism of magma differentiation that is able to operate in such extremely confined spaces. This is compositional convection governed by a gravitational instability of a thin liquid

boundary layer around *in situ* growing magnetite crystals (Martin *et al*., 1987; Campbell, 1996; Seedhouse and Donaldson, 1996; Kruger and Latypov, 2020a). During magnetite crystallization, the boundary layer obtains sufficient buoyancy to be released upwards into the main magma body (Kruger and Latypov, 2020a), either as a constant stream of melt or as a series of plumes (Campbell, 1996). Their mixing with the overlying resident melt causes its chemical differentiation which is recorded in subsequently forming magnetite nodes and layers (Kruger and Latypov, 2020a).

Magma chamber evolution via *in situ* crystallization and differentiation in the undercut-embayed floor may be quite common in nature because almost all large plutonic complexes grow by multiple magma replenishments (Wager and Brown, 1968; Jackson, 1970; Irvine, 1970; Campbell, 1996; Cawthorn, 1996a; Kruger, 2005; Charlier *et al*., 2015;) which are prone to induce karstification of the floor cumulates (Latypov *et al*., 2016; 2017a; 2017b; 2020). We predict that many more examples of the undercut-embayed floor will be documented with time in intrusions that show large scale erosional unconformities (Stillwater, Penikat, Windimurra, etc.) such as circular excavations in the chamber floor in which parts of cumulate rocks are missing. However, in between karstification events, the growth of the magma chamber would still likely occur predominantly by a planar solidification front, and a pertinent question is whether a physical mechanism of crystallization and differentiation would be different from that inferred from the undercut-embayed floor. At present, we see no obvious reason as to why a transition from the undercut-embayed floor to the planar floor and vice versa may somehow change the magma chamber dynamics (e.g. replace *in situ* growth by crystal settling or crystal mush formation). We argue, therefore, that the evolution of magma in the chamber would likely be governed by convective removal of a compositional boundary layer from *in situ* growing crystals irrespective of whether they form along the planar or undercut-embayed chamber floor. Whether or not *in situ* crystallization via a planar floor or the undercut-embayed floor will have a different effect on the chemical evolution of a resident melt remains an open question to be addressed in future research. However, as of now it is clear that the undercut-embayed floor is an extremely promising environment for unravelling new fundamentals of igneous petrology which may bring us closer to the ultimate goal of geosciences – understanding how our home planet was formed.

4.7 Acknowledgements

The original manuscript benefited from the constructive peer reviews by Olivier Namur, Spike McCarthy, Chris Ballhaus and Chris Hawkesworth. We would like to thank the staff at the Rhovan Vanadium mine for their assistance with field work in the open pit without whom this research would not be possible. Sofya Chistyakova is greatly thanked for her help in preparing Supplementary material figures and substantially improve the quality of figures in the manuscript. The study was supported by research grants to R.L. from the National Research Foundation (NRF) and Department of Science and Technology (DST)-NRF Centre of Excellence for Integrated Mineral and Energy Resource Analysis (CIMERA) of South Africa. Any opinion, finding and conclusion or recommendation expressed in this contribution is that of the authors and the DST-NRF CIMERA and NRF do not accept any liability in this regard. We thank an artist Inna Laur (Finland) for helping us artistically depict the undercut-embayed chamber floor in Figure 4.4.

4.8 Supplementary material

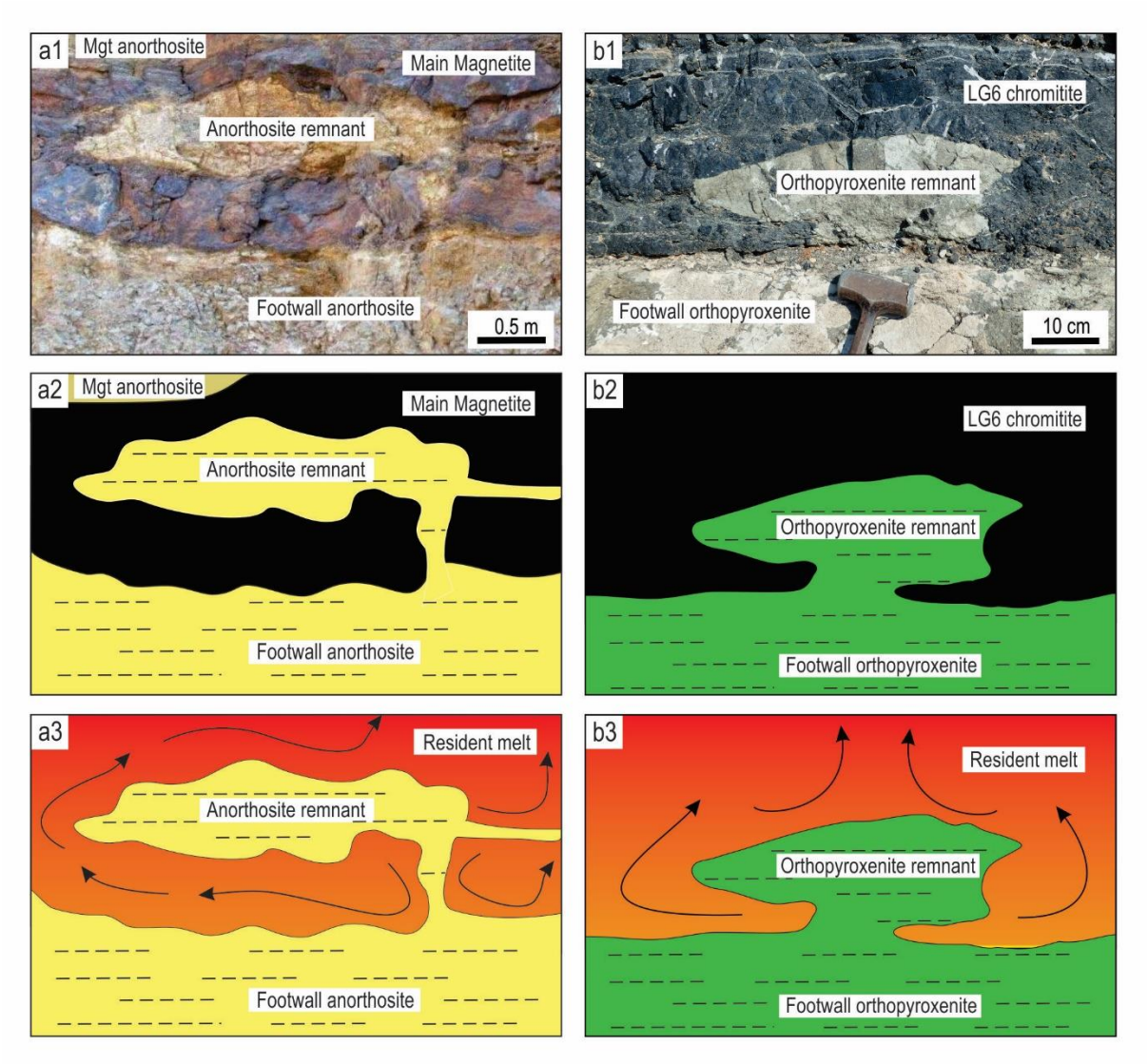

Supplementary information Figure 4.1 The morphology of the undercut-embayed chamber floor from different localities of the Bushveld Complex, South Africa. (a1, a2, a3), Photo, sketch and reconstruction of an erosional remnant of anorthosite that is hosted by the Main Magnetite Layer and is still attached to the footwall rocks. Vametco Vanadium Mine, Upper Zone of the Western Bushveld Complex. Photo courtesy of Dirk Venter; (b1, b2, c3), Photo, sketch and reconstruction of an erosional remnant of orthopyroxenite that is hosted by the LG6 chromitite and is still attached to the footwall rocks. Jagdlust area, Lower Critical Zone of the Eastern Bushveld Complex.

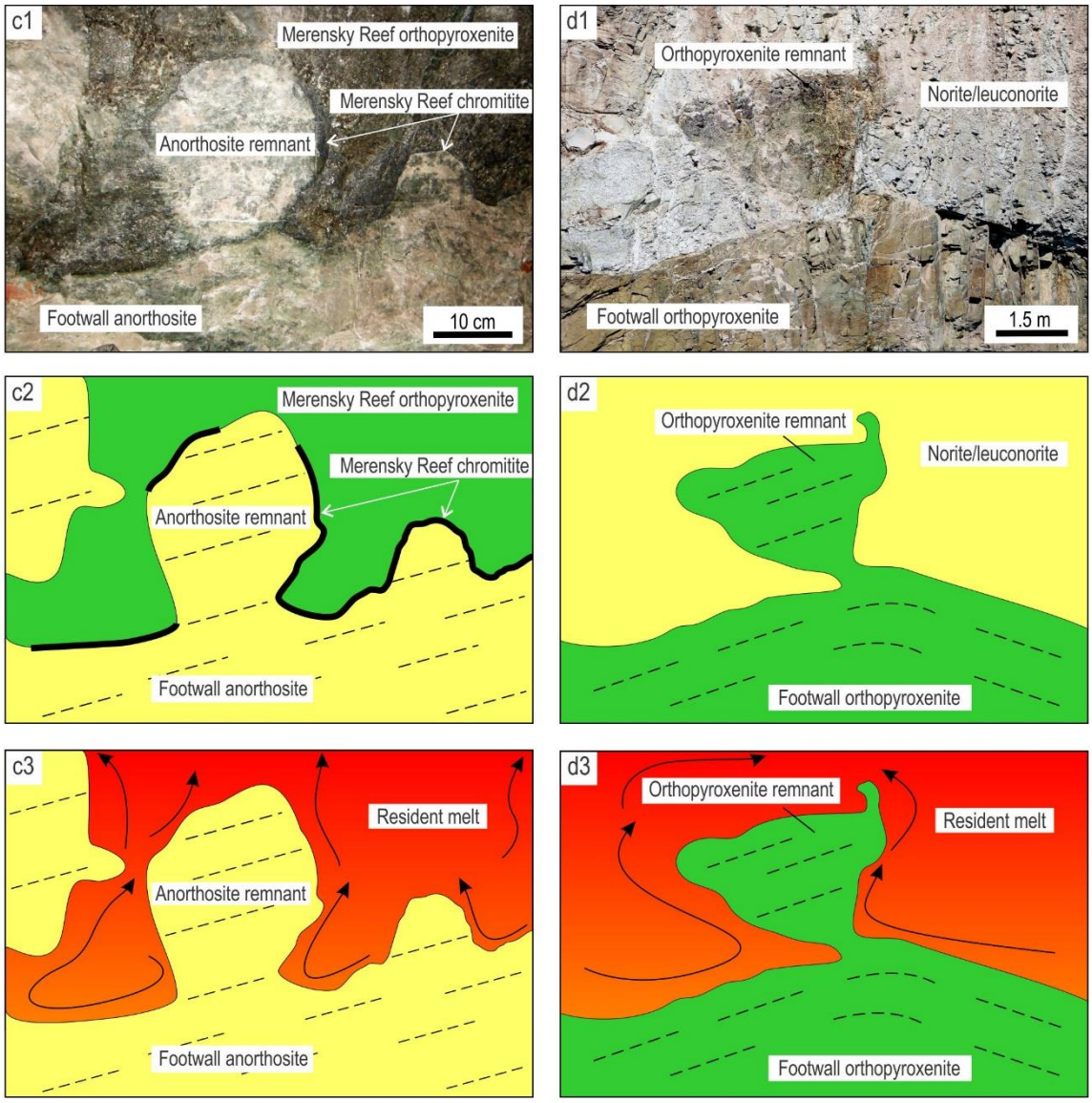

Supplementary information Figure 4.1 (continued). The morphology of the undercut-embayed chamber floor from different localities of the Bushveld Complex, South Africa. (c1, c2, c3), Photo, sketch and reconstruction of erosional remnants of anorthosite that are hosted by the Merensky Reef orthopyroxenite and are still attached to the footwall rocks. Karee Platinum Mine, Upper Critical Zone of the Western Bushveld Complex. Photo courtesy of Colleen Meissner; **(**d1, d2, d3), Photo, sketch and reconstruction of an erosional remnant of orthopyroxenite that is hosted by the overlying norite/anorthosite and is still attached to the footwall rocks. Modikwa Platinum Mine, Upper Critical Zone of the Eastern Bushveld Complex.

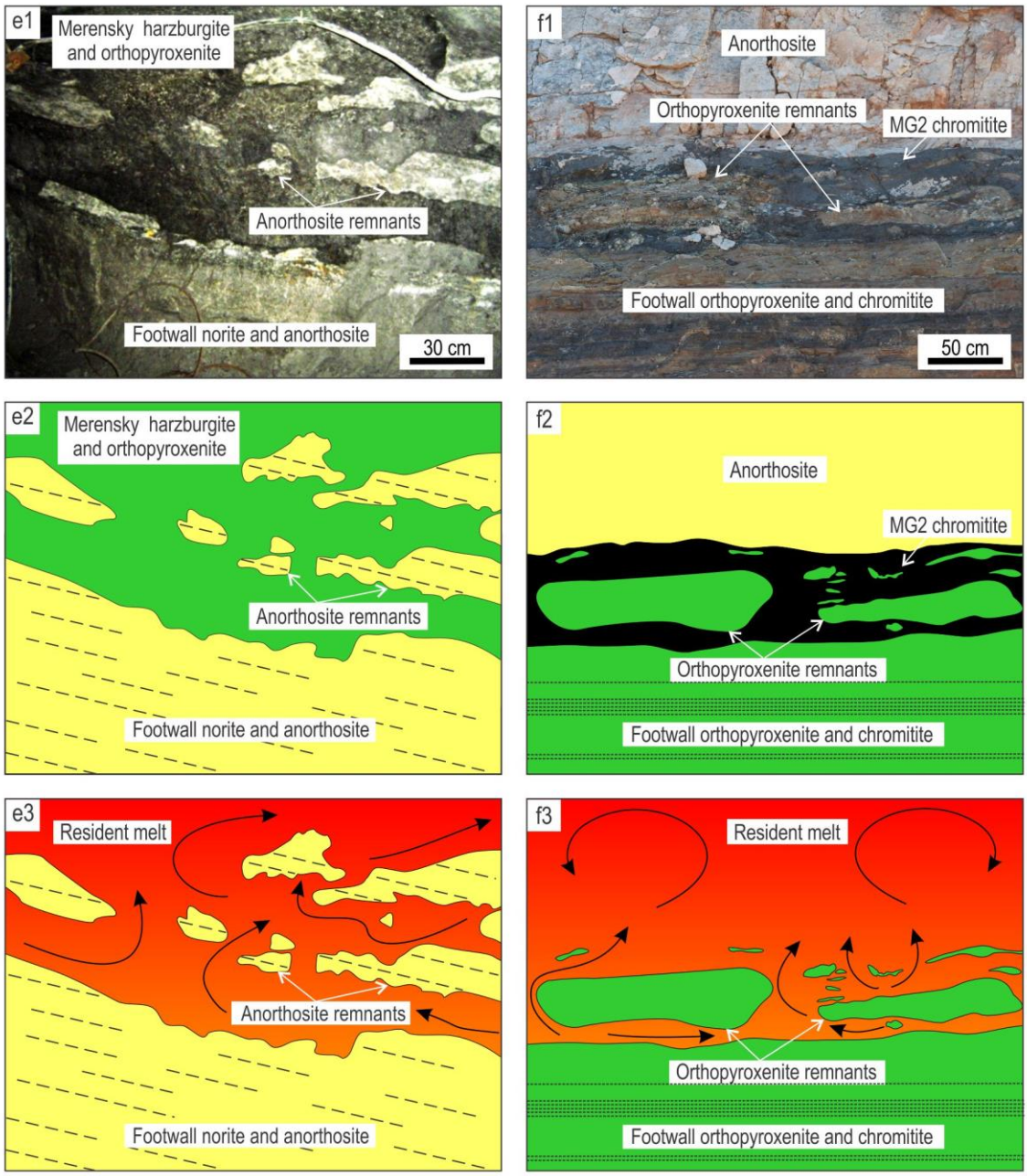

Supplementary information Figure 4.1 (continued) The morphology of the undercut-embayed chamber floor from different localities of the Bushveld Complex, South Africa. (e1, e2, e3), Photo, sketch and reconstruction of in situ erosional remnants of anorthosite that are hosted by the Merensky Reef orthopyroxenite and seemingly not attached to the footwall rocks in this section. Remnants appear to have retained their original positions and orientations. Brakspruit Pothole, Rustenburg Platinum Mine, Upper Critical Zone of the Western Bushveld Complex. Modified from Figure 7a from Latypov et al. (2016); (f1, f2, f3), Photo, sketch and reconstruction of *in situ* erosional remnants of orthopyroxenite that are hosted by the MG2 chromitite and seemingly not attached to the footwall rocks in this section. Remnants appear to have retained their original positions and orientations. Hoggenoeg Chrome Mine, Upper Critical Zone of the Eastern Bushveld Complex. In all the above examples, the morphology of the undercut-embayed floor is attributed to magmatic karstification (i.e. erosion by dissolution) of the chamber floor cumulates by new magma pulses that replenish the chamber.

CHAPTER 5

FIELD AND GEOCHEMICAL CONSTRAINTS ON THE ORIGIN OF THE LOWERMOST MASSIVE MAGNETITITE LAYERS OF THE BUSHVELD COMPLEX, SOUTH AFRICA

Reference to paper:

Kruger, W. and Latypov, R. Field and geochemical constraints on the origin of the lowermost massive magnetitite layers of the Bushveld Complex, South Africa. To be submitted to Ore Geology Reviews. Impact factor: 3.86.

Author contributions

Kruger: 75% (Geochemically analysed field outcrops, performed quantification of geochemical data, wrote the first draft of the manuscript, and contributed to ideas presented in the paper);

Latypov: 25% (Supervisor, contributed to ideas presented in the manuscript, assisted with editing and reviewing the manuscript).

Abstract

Massive magnetitite layers of the Busvheld Complex in South Africa remains a petrological enigma even after many decades of research. Here an attempt is made to vigorously constrain the origin of the lowermost massive magnetitite layers by studying their field and geochemical characterstics in detail. Rock samples are collected from drill core that covers a 174 m interval of stratigraphy from the lowermost portion of the Upper Zone of the Western Bushveld Complex. Whole-rock geochemistry was obtained via XRF and ICP-MS analysis. Special attention is given to the variation in Cr in magnetite across these layers and intervening silicate-rich rocks due to the extreme sensitivity of this trace element to magmatic differentation and recharge events. Several intersections of two prominent magnetitite layers, called the Main Magnetite Layer and the bottom seam, were analyzed in great detail using a portable XRF spectrometer from several drill cores from the Rhovan and Vametco vanadium mines. Our results reveal intricate depressions in the typically anorthositic footwalls of magnetitite layers, interconnected fragments of anorthositic inclusions, and prominent Cr reversals at their bases that strongly suggest that magmatic recharge occurred prior to the formation of massive magnetitite layers. Extreme lateral variations in the Cr contents along the bases of magnetitite

layers indicate their *in situ* crystallization, implying the incoming melt was free of crystals and, after a period of thermochemical erosion and cooling, saturated in magnetite-alone. The latter is possibly due to a reduction in pressure associated with magmatic ascent from depth and assimilation of crustal material. Gradual magmatic recharge allowed for intermittent mixing, cooling, and crystallization, producing a layer of anorthosite prior to the crystallization of magnetitite. During magnetitite crystallization, magmatic differentiation occurred by the convective removal of a thin compositional boundary layer surrounding magnetite crystals. Random nucleation of plagioclase within this boundary layer that becomes increasingly more probable as magmatic differentiation proceeds is responsible for the *in situ* production of non-cotectic magnetite-plagioclase cumulates that led to the formation of a gradational contact with the overlying magnetite anorthosite as observed atop massive magnetitite layers.

5.1 Introduction

Layered intrusions are the ancient fossilized remains of magma chambers and their study has proven invaluable for our understanding of magmatic systems (Wager and Brown, 1968; Parson, 1987; Cawthorn, 1996a; Charlier *et al*., 2015; O'Driscoll and VanTongeren, 2017). However, one aspect of layered intrusions has provided igneous petrologists with one of their greatest challenges: explaining the origin of stratiform monomineralic rocks within these geological features. Many experimental studies have shown that basaltic magmas originating from the mantle will predominantly evolve along multi-phase cotectics to produce igneous rocks with well-defined mineral proportions (e.g. Bowen, 1928; Roeder and Osborn, 1966; Kushiro, 1969; Latypov and Chistyakova, 2001). The occasional occurrence of monomineralic layers clearly indicates that some event occurs within the magma chamber that causes a deviation from this expected crystallization trend. Exactly what this process (or processes) may be has eluded igneous petrologists for decades with very little consensus among experts on the subject (Charlier *et al*., 2015).

This study aims to focus on a particularly puzzling monomineralic rock type: the massive magnetitite layers of the Bushveld Complex, South Africa. In the case of magmas that follow a tholeiitic differentiation trend, like those responsible for the formation of the Bushveld, the magma needs to undergo a significant amount of Fe-enrichment and/or an increase in oxygen fugacity by fractional crystallization before magnetite will start to crystallize (Hunter and Sparks, 1987; Berndt and Koepke, 2005; Tatsumi and Suzuki, 2009). By that time, magnetite should crystallize with several silicate mineral phases that have reached saturation in the

magma long before. For example, in the Skaergaard intrusion in Greenland, plagioclase appears as the first primocryst followed by clinopyroxene after a stratigraphic thickness of 200 m of crystals have formed. Only after an additional ±500 m thick pile of crystals have formed does magnetite appear as a primocryst, crystallizing in conjunction with the former two minerals in proportions that rarely exceed 25 vol.% (Namur and Humphreys, 2018). Some process must have been able to concentrate magnetite into the monomineralic reefs we observe today in the crystallized remnants of the Bushveld Complex.

Attempts by previous investigators to discover the nature of the above process has proven to be highly contentious. In particular, there exists two polarizing aspects when it comes to unravelling the petrogenesis of this rock type. The first deals with the manner of accumulation of the magnetite crystals in the chamber. While some researchers argue for *in situ* crystallization (e.g. Cawthorn and McCarthy, 1980; McCarthy *et al*., 1985; Reynolds, 1985a; Cawthorn, 1994), many others favour a model that involves crystal settling or sorting (e.g. Scoon and Mitchell, 2012; Maier *et al*., 2013; Bilenker *et al*., 2017; Yuan *et al*., 2017; Knipping *et al*., 2019; Vukmanovic *et al*., 2019). The second issue considers whether massive magnetitite formed by some mechanism involving magmatic recharge (e.g. Maier *et al*. 2013; Yuan *et al*., 2017; Lesher *et al*., 2019), or whether it came about in a closed magmatic system (e.g. Cawthorn, 1980; Tegner *et* al., 2006).

In an attempt to resolve these issues, we document the geochemical and field characteristics of Bushveld magnetitite layers from three different localities; Magnet Heights from the Eastern Bushveld Complex, and the Rhovan and Vametco vanadium mines from the Western Bushveld Complex (Figure 5.1). The field characteristics of magnetitite layers have mostly been neglected by models that attempt to resolve their petrogenesis. An approach that relies predominantly on field characteristics have successfully been applied in several recent studies to gain deeper insights into the origin of the Bushveld's chromitite layers and the Merensky Reef (Latypov *et al*., 2016; Latypov *et al*., 2017a; Mukherjee *et al*., 2017; Pebane and Latypov, 2017; Hunt, *et al*., 2018; Chistyakova *et al*., 2019). Based on our results we test multiple hypotheses from the literature that addressed the petrogenesis of massive magnetitite. By extracting and building on the strengths of previous models, whilst discarding potentially weaker points, we construct a new petrogenetic model to explain their formation. Thereafter, we address several questions that are fundamental to arrive at a complete understanding of the formation of this rock type, such as how magmatic differentiation occurs and what factors affect the propagation of the solidification front during magnetitite crystallization. These, in

turn, might provide an understanding of some other characteristics of magnetitite layers, such as the gradational contacts into overlying magnetite anorthosite. Finally, we attempt to provide a unique solution to one of the most puzzling features of magnetitite layers, namely that they commonly contain anorthositic footwalls.

Without a doubt the mere existence of massive magnetitite layers holds an important clue to some of the processes that operate within magma chambers. Not only that, but these layers also serve as economically important reserves of V in South Africa (Cawthorn and Molyneux, 1986;

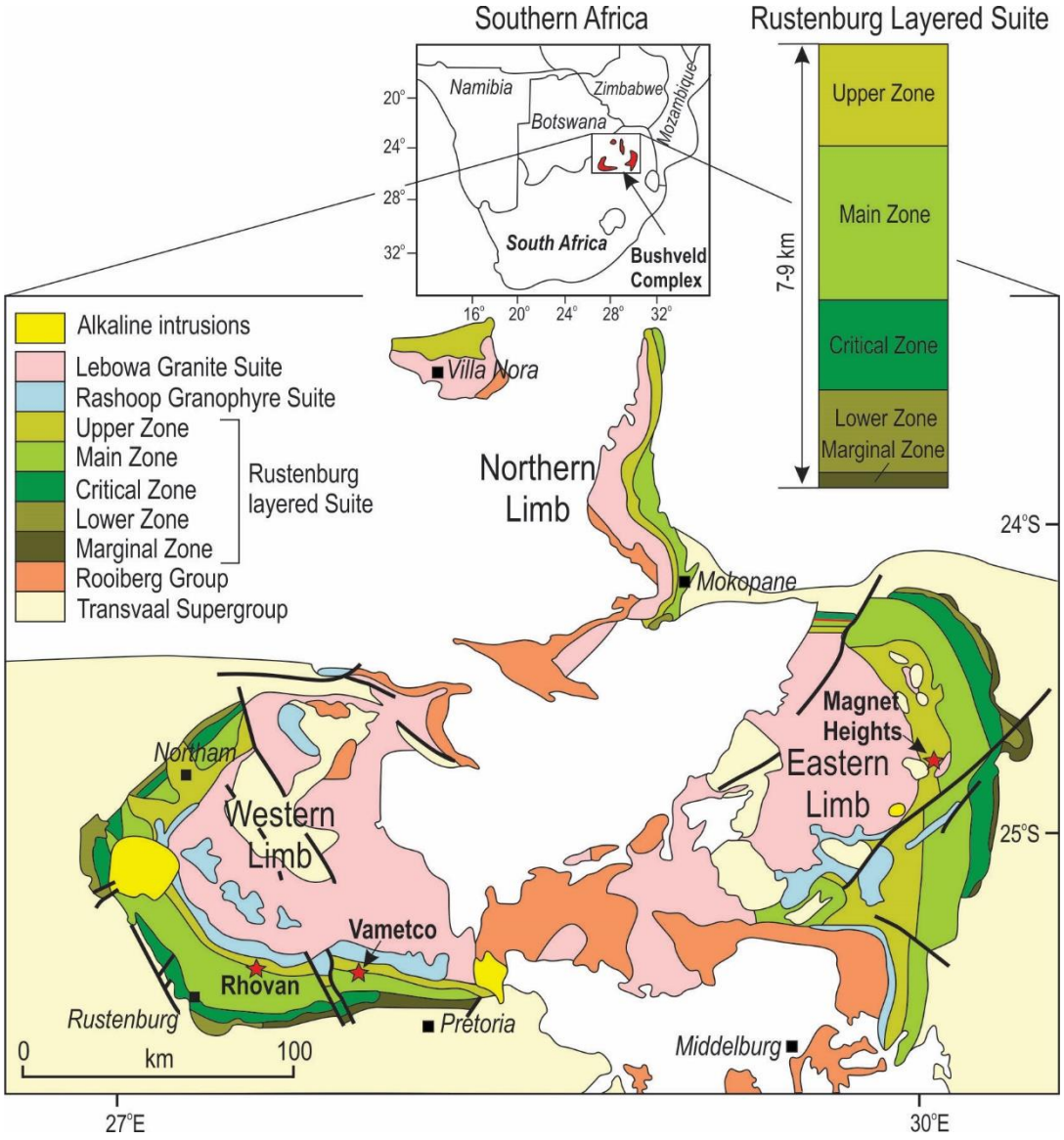

Figure 5.1 Geological map of the Bushveld Complex. Study sites for this project are indicated by red stars for the Rhovan and Vametco vanadium mines in the Western Limb and Magnet Heights in the Eastern Limb.

Viljoen, 2016). It is up to us as petrologists to figure out what their origin might be. In turn, we will gain a better perspective of magma chamber dynamics, while potentially improving our capabilities to find and extract the valuable metals bounded within this enigmatic rock type in the future.

5.2 Regional geology

There are many well-constructed reviews on the Bushveld Complex of South Africa (Cawthorn, 1996a; Cawthorn, 2015; Viljoen, 2016). A short overview is given here. The layered, primarily ultramafic to dioritic part of the complex (called the Rustenburg Layered Suite) originated when an enormous amount of basaltic magma (in excess of 1,000,000 km^3) (Cawthorn and Walvaren, 1998) was emplaced in multiple pulses (Kruger, 1994; Eales, 2002) between about 2060-2055 Ma ago (Scoates and Friedman, 2008; Scoates *et al*., 2021) over a time period of 75,000 (Cawthorn and Walraven, 1998) to 10^6 (Zeh *et al*., 2015) years, to form what is today known as the largest layered intrusion on Earth. Subsequent erosion (and later deposition of younger sedimentary rocks) created an outcrop pattern of four different limbs of the Bushveld Complex. The larger limbs are called the Western and Eastern Limbs (Figure 5.1) which may (Cawthorn *et al*., 1998; Webb *et al*., 2011) or may not (Cousins, 1959; Du Plessis and Kleywegt, 1987) be connected at depth.

In total, the Rustenburg Layered Suite (RLS) ranges from 7-9 km in thickness (Cawthorn, 2015). At its lowermost section it contains ultramafic cumulates referred to as the Basal Ultramafic Sequence (Wilson, 2015) which is overlain by a noritic Marginal Zone. This is followed by a sequence of ultramafic rocks (mostly harzburgite and orthopyroxenite) called the Lower Zone which is in turn overlain by the Critical Zone (consisting of chromitite, orthopyroxenite, norite, and anorthosite). Above the Critical Zone occurs the Main Zone, a sequence of mostly norite, gabbronorite, and gabbro that is generally poorly layered compared to the rest of the intrusion. About 200 m metres below the top of the Main Zone occurs an orthopyroxenite layer that is referred to as the Pyroxenite Marker. The Pyroxenite Marker is thought by many to represent the final influx of magma into the RLS magma chamber (Kruger *et al*., 1987; Cawthorn, 1991; Tegner *et al*., 2006; VanTongeren *et al*., 2010; VanTongeren and Mathez, 2013). Differentiation of this magma is thought to have eventually led to the appearance of cumulus magnetite that represents the base of the Upper Zone (Molyneux, 1974). Relative thicknesses of the different zones are indicated on Figure 5.1. Shortly after the appearance of cumulus magnetite, the first massive magnetitite layers appear. The Bushveld's

Upper Zone is further subdivided into several subzones, with the base of Subzone A being marked by the first appearance of cumulus magnetite, Subzone B the appearance of cumulus olivine, and Subzone C by the appearance of cumulus apatite (Tegner *et al*., 2006).

In total, 26 magnetitite layers have been identified in the Bierkraal drill cores from the Western Limb of the Bushveld Complex, along with 6 nelsonite layers towards the very top of the intrusion (Tegner *et al*., 2006). Layers may range from just 10 cm in thickness, while the so-called Main Magnetite Layer (MML) measures up to 2 m in thickness. The uppermost magnetitite layer in the Eastern Limb of the complex, referred to as magnetite layer 21, is the thickest oxide layer within the complex with an average thickness of about 10 meters (Molyneux, 1974) and a maximum thickness of up to 22 meters (Scoon and Mitchell, 2012). A remarkable feature of these magnetitite layers are their extreme lateral extent. For example, the MML can be found in all three major limbs (Western, Eastern, and Northern) of the complex and can be traced for hundreds of kilometres.

5.3 Methods

This study generally focusses on the geochemical and field characteristics of massive magnetitite layers from a section of Subzone A and B that is exposed in the open pits of the Rhovan and Vametco mines and drill cores, as well as field outcrops in the Magnet Heights locality from the Eastern Limb (Figure 5.1). More details are provided in the Methodology chapter.

5.4 Results

5.4.1 Field relations

In terms of field relations, magnetitite layers of the Bushveld Complex are characterised by three common features: they contain a massive part of nearly pure titano-magnetite (Figure 5.2a and b), a sharp basal contact with underlying anorthosite (Figure 5.2a and c), and a gradational contact into the overlying rock type, typically magnetite anorthosite (Figure 5.2 c and d; Fig 5.3a and c).

On closer expection, the contact between the magnetitite and anorthosite is characterized by many intricacies. Small depressions, occasionally no more than a centimetre across, is commonly observed within the anorthosite (Figure 5.4a). Less commonly, such depressions also occur on a much larger scale, from a few cm (Figure 5.4b) to more than a metre wide (Fig 5.4c). Several other irregularities are detected at the boundary between the magnetitite and the

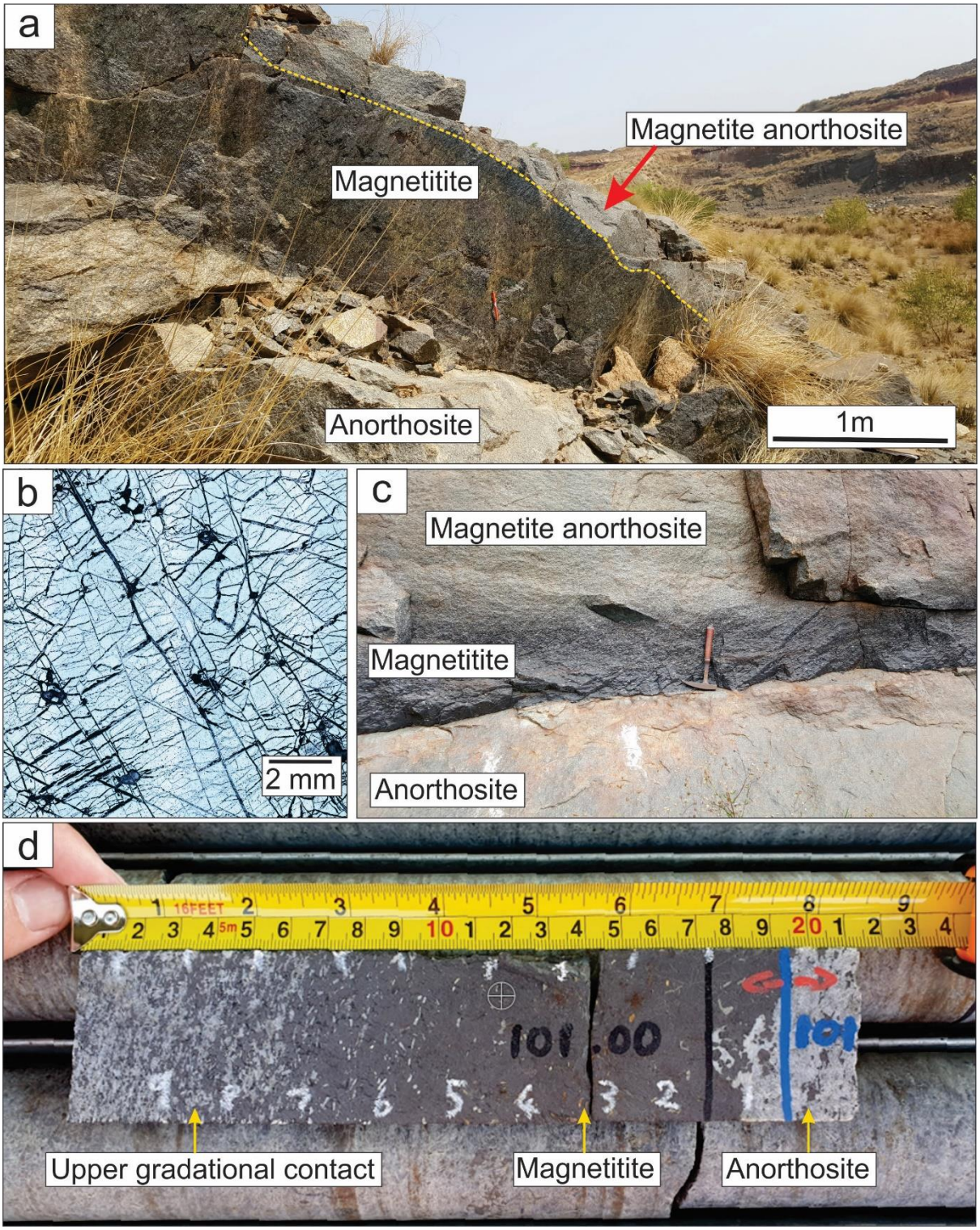

Figure 5.2 Typical appearance of magnetitite from the Bushveld Complex. (a) The lowermost massive magnetitite layer of the Upper Zone from the Western Limb, Rhovan vanadium mine. It is underlain by anorthosite and overlain by magnetite anorthosite. (b) Photomicrograph of the MML from the Western Bushveld Complex in reflected light. The layer consists almost entirely of titano-magnetite with little to no interstitial phases. (c) Magnetite Layer 1 from Magnet Heights, Eastern Bushveld Complex. Notice the gradational upper contact into the overlying magnetite anorthosite and the sharp basal contact with its anorthositic footwall. (d) A thin magnetitite layer from the Western Bushveld Complex obtained from drill core. It also displays an upper gradational contact to magnetite anorthosite and an intricate bottom contact with anorthosite. The formation of these three features (anorthosite, massive magnetitite, and the upper gradational contact) is central to this study.

anorthosite, such as off-shoots and fingers of magnetite penetrating the footwall (Figure 5.4a and 5.5e), and interconnected frameworks of plagioclase grains that appear to be connected to each other and the floor in cross-section (Figure 5.4b).

Another common feature of magnetitite layers is that they contain numerous inclusions of anorthosite (Figure 5.3b and 5.5). These inclusions are typically oval in shape and taper out towards their margins (Figure 5.5a, c). Some angular inclusions are also observed (Figure 4.5b), while some may be highly irregular in shape (Figure 5.5d). These inclusions vary significantly in size, from more than a metre wide (Figure 5.5c) to only a few cm across (Figure 5.4a). Larger inclusions appear to be more common closer to the bottom of the layer. An interesting observation is that, in some instances, the inclusions may appear to be connected to the footwall in some manner (Figure 5.5e and f).

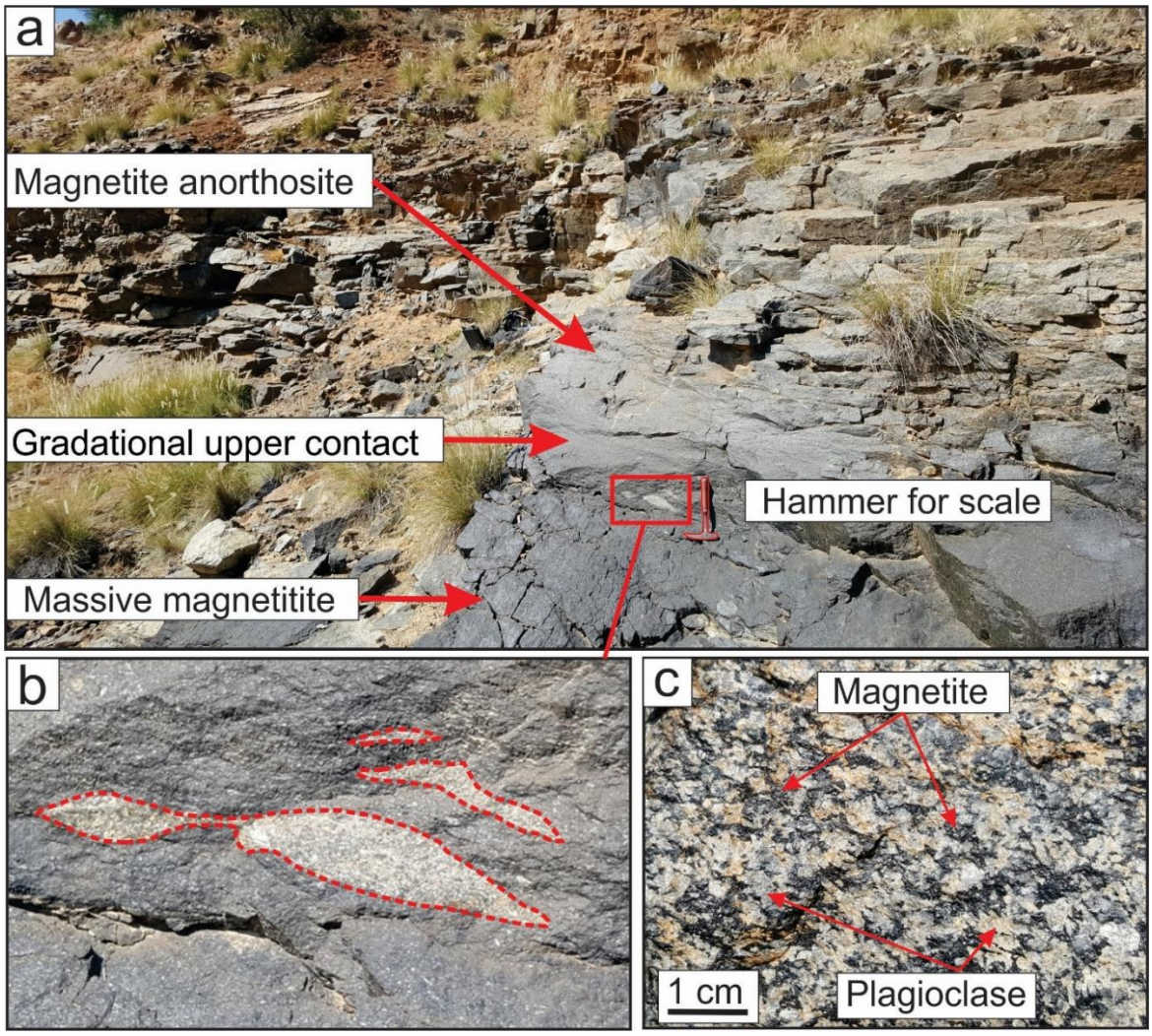

Fig 5.3 Appearance of the upper portion of the Bottom seam from the Western Bushveld Complex. (a) Massive magnetitite contains a gradational contact into magnetite anorthosite. (b) Inclusions of anorthosite present within the magnetitite layer. (c) The appearance of the magnetite anorthosite containing cumulates of both magnetite and plagioclase. Hammer for scale is about 40 cm in length.

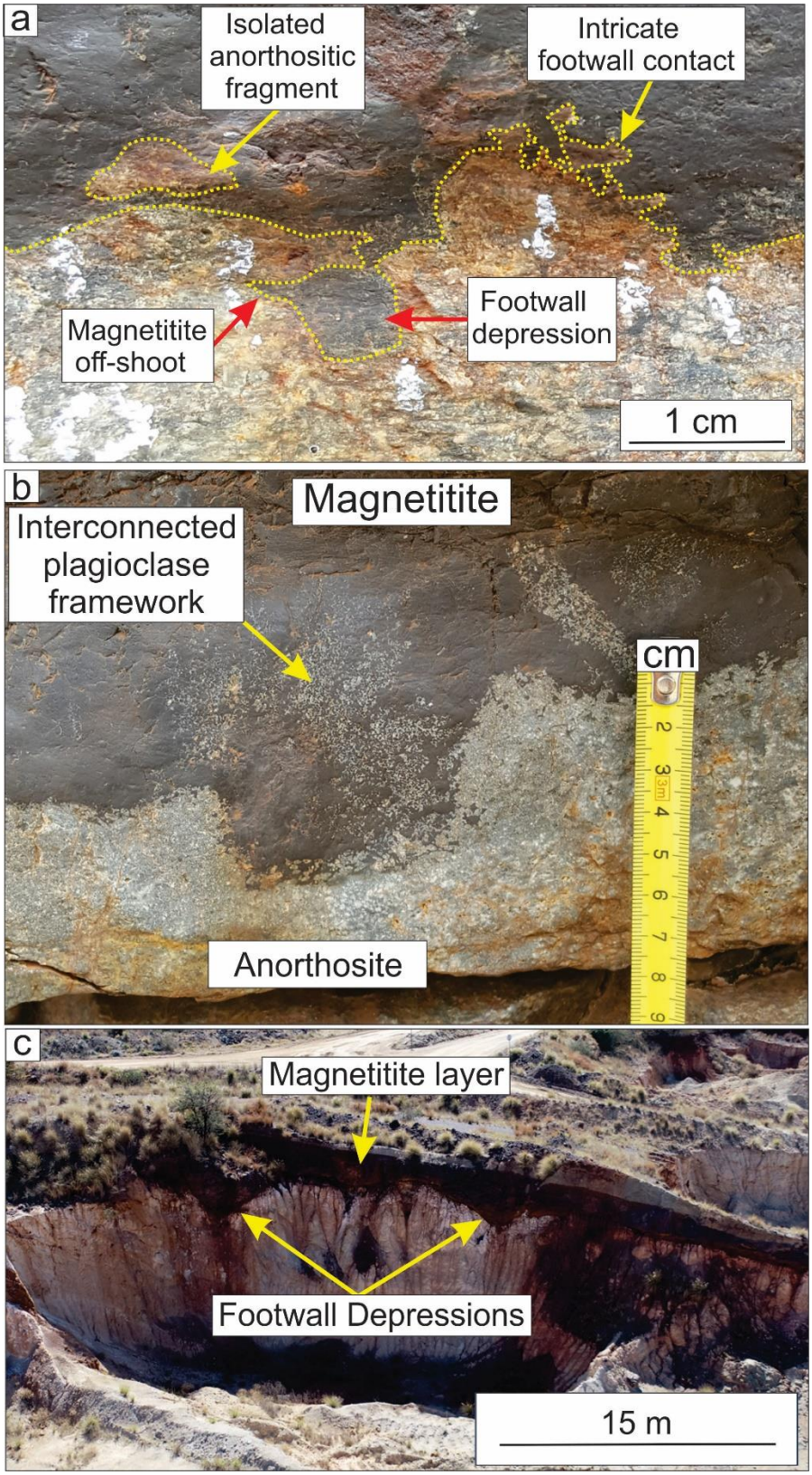

Figure 5.4 Irregularities observed in the footwall contact between magnetitite and anorthosite. (a) Main Magnetite Layer from Magnet Heights, Eastern Bushveld Complex.Various intricate features are observed when examining the contact in detail, such as a small depression, an off-shoot of magnetitite, and a small anorthositic inclusion. (b) A slightly larger footwall depression that is partially filled by a delicate interconnected framework of plagioclase crystals. (c) Larger footwall depressions observed in the anorthosite underlying the Main Magnetite Layer from the Rhovan vanadium mine, Western Bushveld Complex.

In one particular outcrop from Rhovan, fragments of Magnetite Layer 1 (so labelled as it is the first magnetitite layer present above the MML) appear to be scattered in the overlying magnetite anorthosite (Figure 5.6a). In most cases, their upper gradational contacts are still attached, making it possible to determine the orientation of the fragments that varies from sub-vertical (Figure 5.6b and d) to completely upside-down (Figure 5.6c and e).

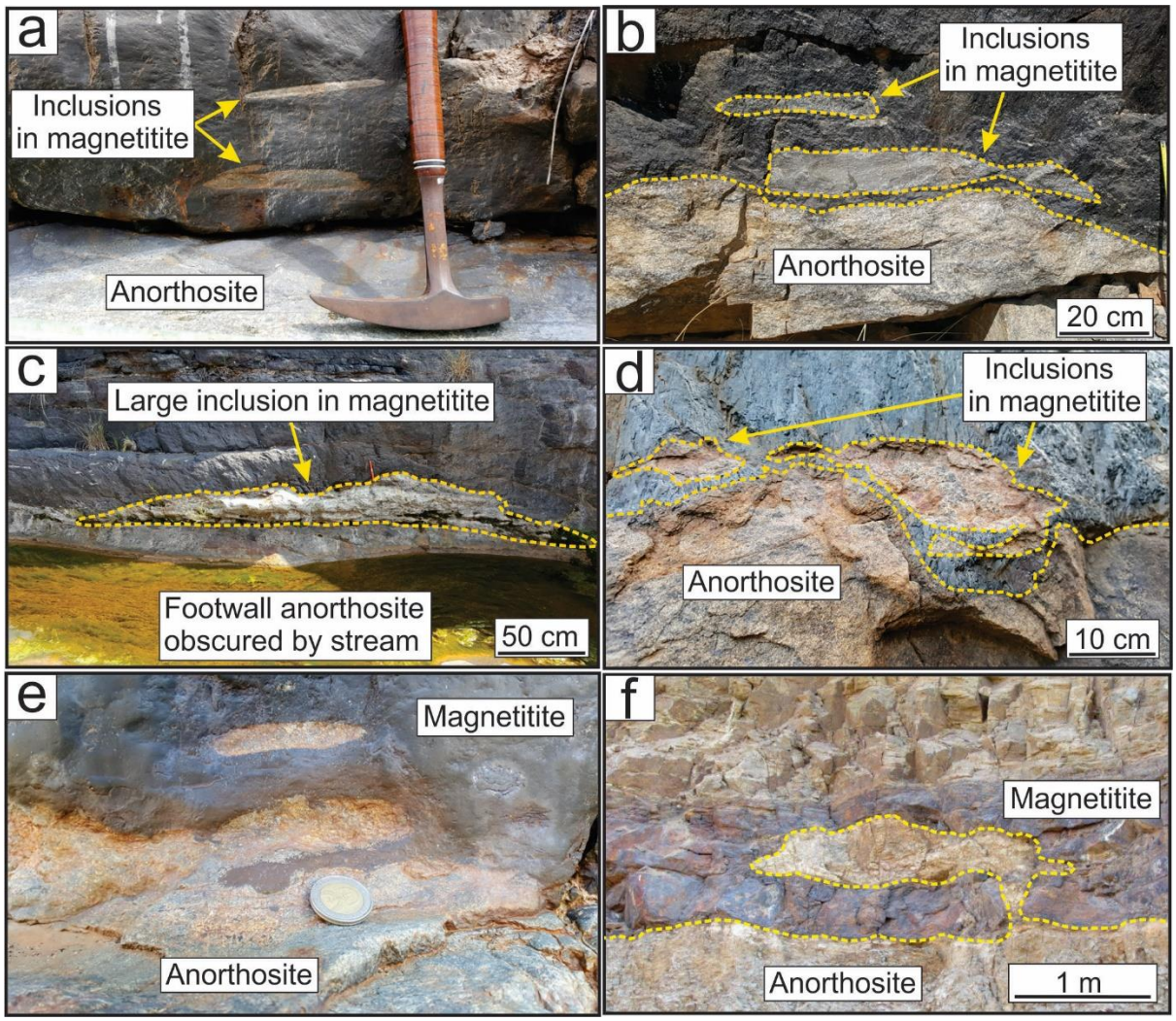

Figure 5.5 Anorthositic inclusions in magnetitite layers from the Bushveld Compex. (a) Two relatively small, elongated inclusions in the Main Magnetite Layer from Magnet Heights. (b) Inlcusions in the Bottom seam from the Rhovan vanadium mine. Notice the angular shape of the largest inclusion in the section. (c) A large inclusion of anorthosite in the Main Magnetite Layer from Magnet Heights that tapers our towards its edges. (d) Inclusions with highly irregular shapes enclosed in a magnetitite layer from Magnet Heights. (e) A small elongated inclusion trapped in the Main Magnetite Layer from Magnet Heights. A finger protrusion of magnetite can be seen in the underlying layer, forming a partially isolated anorthositic fragment that is similar in shape to the inclusion above. (f) A large inclusion in the Main Magnetite Layer from the Vametco vanadium mine that is connected to the footwall. Photo courtesy of Dirk Venter.

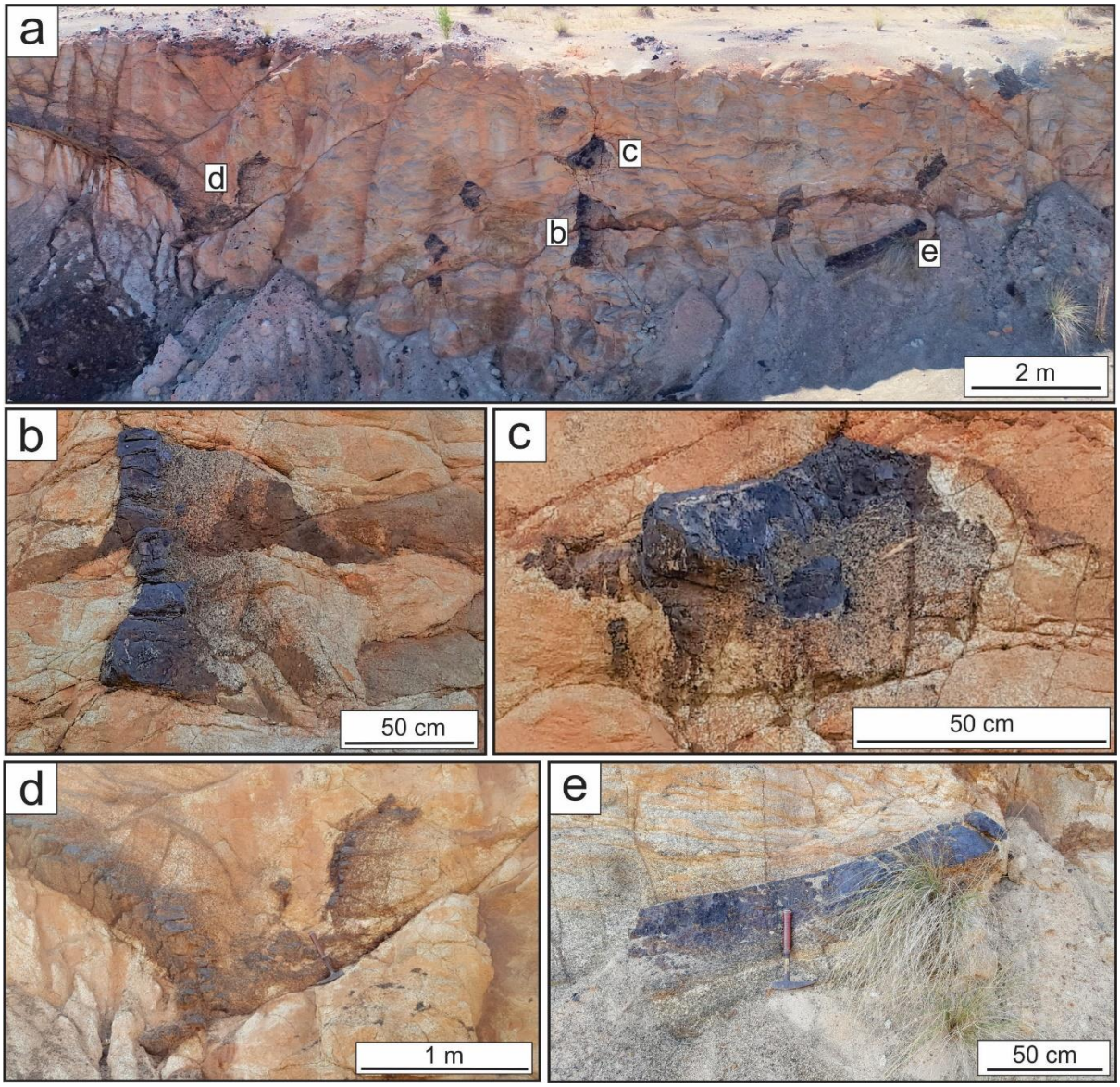

Figure 5.6 Fragments of magnetitite layer 1 scattered in overlying magnetite anorthosite. (a) An overview of an outcrop containing several fragmented and rotated pieces of Magnetitite Layer 1. (b) A piece of magnetitite that has been rotated by at least 90° as indicated by the orientation of the gradational upper contact. (c) This fragment has been rotated by at least 180° while its gradational upper contact remained in tact. (d) A portion of magnetitite layer 1 that appears to be plunging downwards and is cut off by faulting. A sub-vertical fragment of this layer is also present. (e) An upside-down fragemt of magnetitite layer 1.

5.4.2 Petrography

As mentioned before, the section of the Upper Zone from Rhovan drill cores contains two prominent massive magnetitite layers called the Bottom seam and the MML. Both these layers are underlain by anorthosite and possess gradational upper contacts into magnetite anorthosite. Underneath the anorthosite occurs gabbro. The petrography and mineralogy of each of these rock types are discussed below in stratigraphic order.

The gabbro (Figure 5.7a) contains very little (<3%) magnetite and, when present, occurs only as an interstitial phase. Plagioclase is moderately to well-foliated. Pyroxene is typically occurs as inverted pigeonite. The abundance of pyroxene and plagioclase suggests that they are primocrysts while the lower abundance and scarcity of magnetite may suggest it crystallized during the post-cumulus stages.

Further up in the stratigraphy above the gabbro, pyroxene dissapears as a primocryst to give way to the anorthosite that underlies the massive magnetitite (Figure 5.7b). Plagioclase may be poorly to well-foliated, while magnetitite and pyroxene sometimes appear as large oikocrysts, occasionally giving the anorthosite a mottled appearance (Figure 5.7j). Oikocrysts of this nature appear to be more common underneath the MML compared to the Bottom seam.

Microscopically the irregularity of the contact between the anorthosite and the massive magnetitite is abundantly clear, with the magnetitite seemingly penetratiting into its footwall, preferentially along grain boundaries (Figure 5.7c). *In situ* fragments of plagioclase may appear scattered within the massive magnetitite close to the contact with the underlying anorthosite (Figure 5.7c). While most massive magnetitite layers are underlain by anorthosite free of cumulus magnetite or pyroxene, two ±30 cm thick magnetitite layers from Rhovan deviate from this general observation. One of these magnetitie layers is underlain by a very thin layer of clinopyroxenite (Figure 5.7g), while another is underlain by magnetite anorthosite (Figure 5.7h).

The petrography and mineralogy of the magnetitite layers themselves have received attention in numerous other publications (Willemse, 1969; Molyneux, 1970; Molyneux, 1972; Molyneux, 1974; Butcher and Merkle, 1987; Reynolds, 1985a). Magnetitite layers are composed of titano-magnetite that shows fine-scale exsolution of ülvospinel, typically too fine to observe with typical magnifications used on the petrographic microscope. Oxy-exsolution also produces ilmenite that may appear to decorate magnetite grain boundaries. Granular ilmenite may occasionally be present and is generally considered to result from protacted exsolution of ilmenite from the magnetite host (Figure 5.7d). Magnetite grains are generally very coarse grained (up to 2 cm across) (Willemse, 1969) and may display triple-point 120° grain boundary junctions. Interstitial silicates within magnetitite layers are scarce and typically include magnetite crystals of a much smaller size (typically 0.2 mm). However, in some patches, magnetitite layers may contain relatively well-formed grains of plagioclase that also show a good foliation (Figure 5.7i).

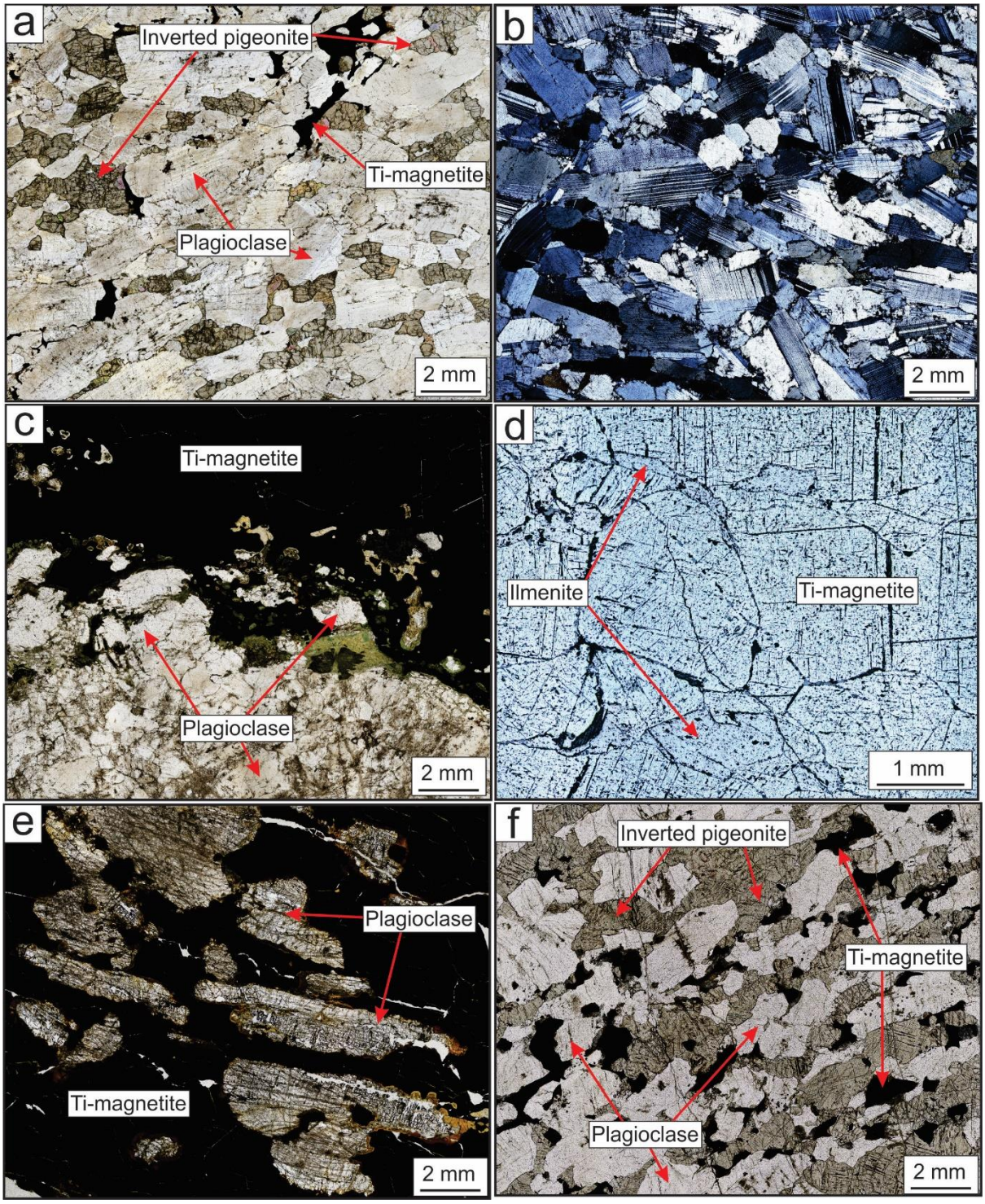

Figure 5.7 Textural and mineralogical features of massive magnetitite layers and adjacent rock types of the Bushveld Complex. (a) Gabbro that occurs below the first layer of magnetitite (Bottom seam) of the Bushveld's Upper Zone from Rhovan viewed in plane polarized light (PPL). The rock contains primocrysts of plagioclase, inverted pigeonite and titano-magnetite. (b) Anorthosite located directly below the Bottom seam that consists of almost pure plagioclase with orthopyroxene present as a minor phase in cross polarized light. (c) The contact between the Bottom seam and its footwall anorthosite (PPL). The irregularity of the contact is clear under the microscope and various anorthositic fragments appear scattered in the massive magnetitite. (d) The Bottom seam in reflected light showing titano-magnetite and grains of ilmenite (e) The upper gradational contact of the Main Magnetite Layer from Rhovan (PPL). Plagioclase appear as primocrysts and are generally well foliated. (f) Magnetite gabbro from Rhovan (PPL).

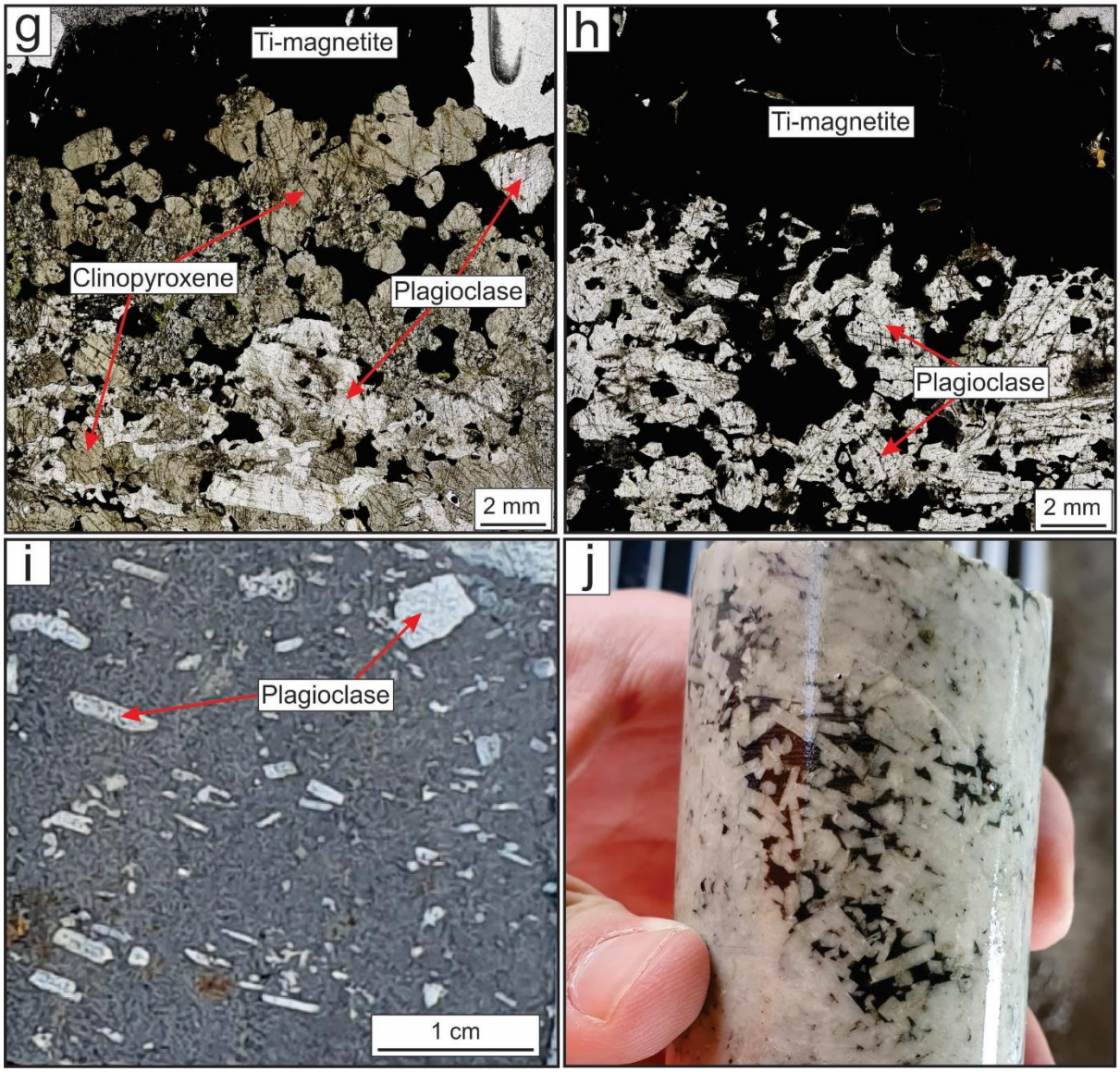

Figure 5.7. continued. (g) Photomicrograph of a magnetitite layer overlying clinopyroxene cumulates that in turn overlie cumulates of clinopyroxene, plagioclase, and magnetite from Rhovan (PPL). (h) A magnetitite layer overlying magnetite anorthosite from Rhovan (PPL). (i) Well-formed, euhedral and foliated grains of plagioclase located within the Bottom seam, Vametco. (j) Anorthosite underlying magnetitite containing a magnetite oikocryst from Vametco.

The upper gradational contact of magnetitite layers contain elongated laths of plagioclase (Figure 5.7e), once again characterized by a well-developed foliation. The same texture is observed in the overlying magnetite anorthosite, but with plagioclase being more abundant. In the case of the Bottom seam, priomocrysts of pyroxene eventually joins the assemblage further upwards, forming a magnetite gabbro (Figure 5.7f).

5.4.3 Geochemistry

Massive magnetitite layers are truly exceptional from a geochemical perspective. This is because of the extremely high crystal/liquid partition coefficient of Cr into magnetite, that ranges from 30 to 1200 (Irving, 1978; Toplis and Corgne, 2002; Castle and Herd, 2017; Cawthorn and McCarthy, 1980; Kruger and Smart, 1987; Dare, 2012) making magnetitite layers very useful to study magmatic processes such as differentiation or magmatic recharge (Cawthorn and McCarthy, 1980), perhaps more so than any other rock type (Kruger and Latypov, 2020a). We thus focus our attention on the distribution of Cr in magnetite from both magnetitite layers and disseminated ore.

The work performed here builds on numerous other publications that focussed on the Cr contents of massive magnetitite layers. Cawthorn and McCarthy (1980; 1981) and McCarthy and Cawthorn (1983) collected closely spaced samples across the MML from various localities and found dramatic decreases in the Cr content upwards within these layers. Later on, a similar gradient was recorded within a single magnetite grain from the MML that showed a vertical, instead of the more typical concentric, zonation pattern with a rapid decrease in Cr upwards (Cawthorn *et al*., 1983). In the following decade, Cawthorn (1994) noticed extreme lateral variations in the Cr contents at the base of the MML. In our own recent work we examined the two-dimensional distribution pattern of Cr in the MML from the same locality (Kruger and Latypov, 2020).

In this study we attempt to improve upon previous work by performing a detialed investigation of the variation of Cr in magnetitite across a 180 m thick section of the base of the Upper Zone from the Western Bushveld Complex in great detail. The section includes two thick massive magnetitite layers (the Bottom seam and MML), and three smaller (5 to 35 cm thick) magnetitite layers. Cr in magnetite is determined by first calculating the modal abundances of all minerals present (Figure 5.8 a). For the modal calculations, a Mg# of 40 is attributed to pyroxenes and olivine that is typical of this section of the Bushveld Complex (Tegner *et al*., 2006). The remaining Fe is then assigned to magnetite. All Cr determined by whole-rock chemical analysis are assumed to be located within magnetite. For example, if a rock contains 100 ppm Cr and 10% magnetite, the concentration of Cr in magnetite is assumed to be 1000 ppm. Because some Cr would also partition into pyroxene, the amount of Cr in magnetite would therefore be slightly overestimated in rocks with an abundance of this mineral. However, this

overestimation does not have any effect on the conclusions made in this study as rocks with a high modal abundance of pyroxene contain very low concentrations of Cr anyway.

By tracing the variation in Cr contents of magnetite from the bottom of the drill core upwards, a relatively high Cr concentration is observed at the base of Bottom seam (Figure 5.8 b and d). The Cr concentration then dramatically drops off towards the top of the layer and progresses smoothly into the overyling magnetite anorthosite. For the next ±140 m the Cr content of magnetite stays comparatively low except for three small reversals associated with thin massive magnetitite layers (Figure 5.8b and Figure 5.9). At about 150 m another Cr reversal is recorded that also coincides with the dissapearance of olivine from the cumulus assemblage. An extremely large reversal is recorded at the base of the MML to such an extent that it contains even more Cr than the Bottom seam below it (Figure 5.8b and c). Similar to the Bottom seam, the Cr content rapidly decreases upwards within the MML, leaving the overlying magnetite anorthosite with a very low Cr concentration. Despite being located higher up in the stratigraphy, the MML is not depleted in Cr relative to the Bottom seam. In contrast, it appears to have a slightly higher Cr concentration overall (Figure 5.10).

Another Cr reversal is also recorded at 82 metres where there is a relatively high modal abundance of magnetite. However, in terms of its field relations it is uncharacteristic of magnetitite layers as it lacks both a very sharp bottom contact and upper gradational contact into a magnetite-plagioclase cumulate. It also contains cumulus olivine that are not found within the other magnetitite layers. We propose that this layer crystallized from a magma with a different chemical signature compared to the melt responsible for the formation of the massive magnetitite layers, perhaps similar to iron-rich ultramafic pegmatites frequently observed in the Bushveld Complex (Molyneux, 1974; Viljoen and Scoon, 1985; Scoon *et al*., 2017; Cawthorn *et al*., 2018).

Several examples of the bottom seam and MML were analyzed in drill core from Rhovan and Vametco using the pXRF to study the variations Cr across these layers in detail (Figure 5.11). An attempt was made to focus on samples that contain anorthositic inclusions like those shown in Figure 5.5 to gain further clues on their origin. In some cases, Cr contents seem to pass smoothly through inclusions (Figure 5.11a). In others, a typical rapid depletion in Cr is observed upwards from the base of the layer, but this trend reverses as one approaches an inclusion (Figure 5.11b, c, and d). Above the inclusions the rapid decrease in Cr continues upwards.

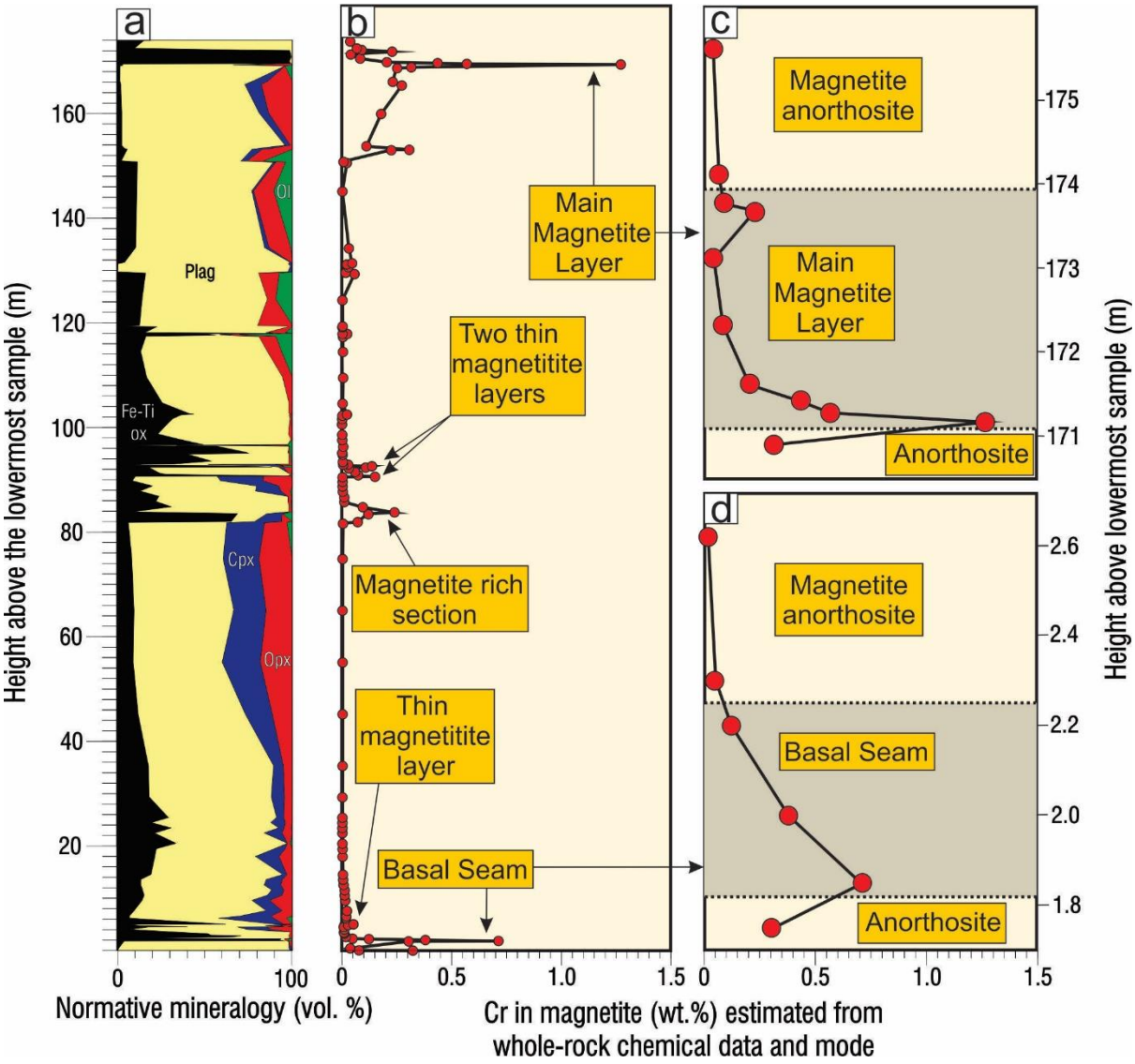

Figure 5.8 Variation in Cr in magnetite across a section of the base of the Upper Zone of the Bushveld Complex, Western Limb, Rhovan vanadium mine. (a) Normative mineralogy of the section. (b) Variation in Cr in magnetite across the entire drill core. Higher Cr contents are generally recorded within massive magnetitite layers, while magnetite grains from the Main Magnetite Layer and Bottom seam are also richer in V compared to adjacent lithologies. (c) A closer look at the Cr variation within the Main Magnetite Layer and the (d) Bottom seam as well as adjacent rock type. Cr reversals are recorded at the bases of both layers, followed by a rapid depletion of the Cr content upwards.

One abnormally thick inclusion in the bottom seam contained a small vein of magnetite (Figure 5.11a). When this vein was analyzed with the pXRF, a singificantly higher Cr concentration (0.34 wt.%) was recorded compared to magnetite from the massive layer immediately adjacent to the inclusion (0.22 wt.%).

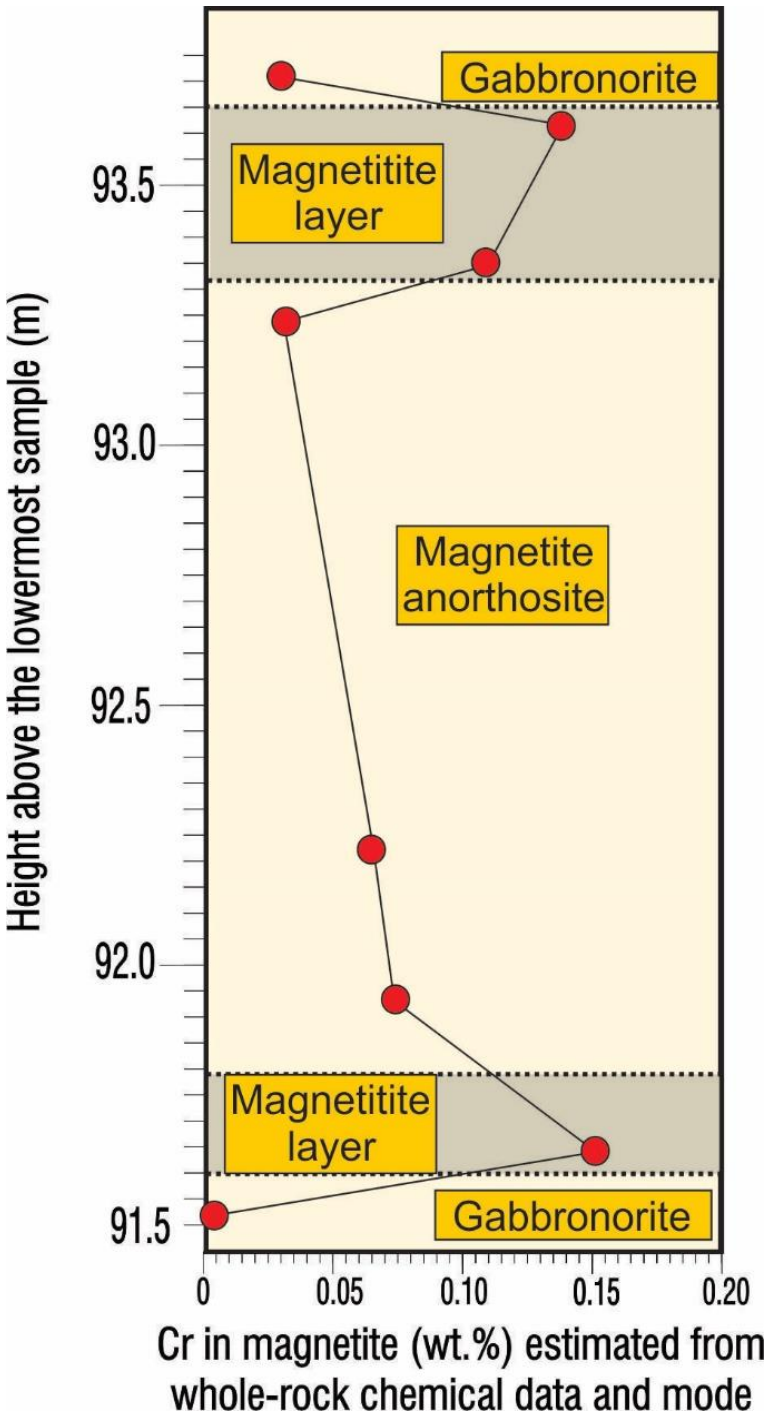

Figure 5.9 Variation in Cr and V in magnetite across two thin magnetitite layers from the Rhovan drill core. (a) Magnetite in magnetitite layers are enriched in Cr relative to the surrounding rock types.

The two MML profiles from Vametco shows a dramatic decrease in Cr identical to that observed by Cawthorn and McCarthy (1980; 1981). A gradual reversal is present near the top of the layer similar to the reversal from Rhovan shown in Figure 5.8c. Cawthorn and McCarthy (1981) also documented such a reversal in the MML near the town of Brits in the same area.

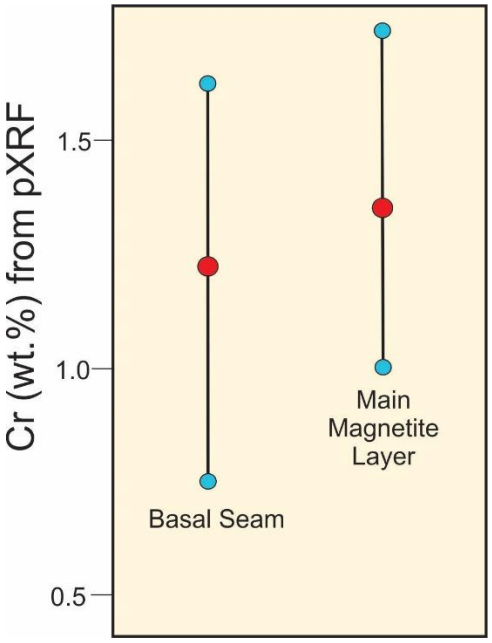

Figure 5.10 Average, minimum, and maximum Cr contents measured at the very bases of the Main Magnetite Layer and the Bottom seam with a portable XRF spectrometer from the Western Bushveld Complex. The bases of the Bottom seam and the Main Magnetite Layer largely overlap in terms of Cr contents, although the Main Magnetite layer appears to be slightly richer in Cr overall. Six analysis for the Bottom seam and three analysis for the MML were used in the construction of the Figure. Analysis for both magnetitite layers come from both Rhovan and Vametco, covering a strike length of about 30 km.

An attempt is also made to improve on Cawthorn's (1994) lateral sampling along the base of the MML in the Magnet Heights area by decreasing the minimum sample spacing of 50 cm of Cawthorn (1994) to just 4 cm using the pXRF. The improved sample spacing reveals a chemical pattern that is significantly less erratic than that documented by Cawthorn (1994). Similar to Cawthorn (1994), our results also show a dramatic lateral variation in Cr contents (Figure 5.12). With the greater sample spacing, peaks of high Cr concentration are observed that may be spaced closely together, forming a crest and trough pattern, while individual peaks may be separated by a plateau of a relatively low and constant Cr concentration in some cases. The Cr concentration gradient across the largest peaks may be very steep (up to 3200 ppm cm^{-1}). Despite the great lateral variability of Cr within the MML, its concentration never seems to drop below 1.0 wt. %, while the a maximum recorded is 4.5 wt. % Cr.

5.5 Review of previous models on magnetitite petrogenesis

The above geochemical, textural and field evidence places strict constraints on the formation of massive magnetitite layers. Here follows a review of previous models that attempt to explain the genesis of massive magnetitite. Each model is critically evaluated for its ability to explain the geochemical and field observations provided above.

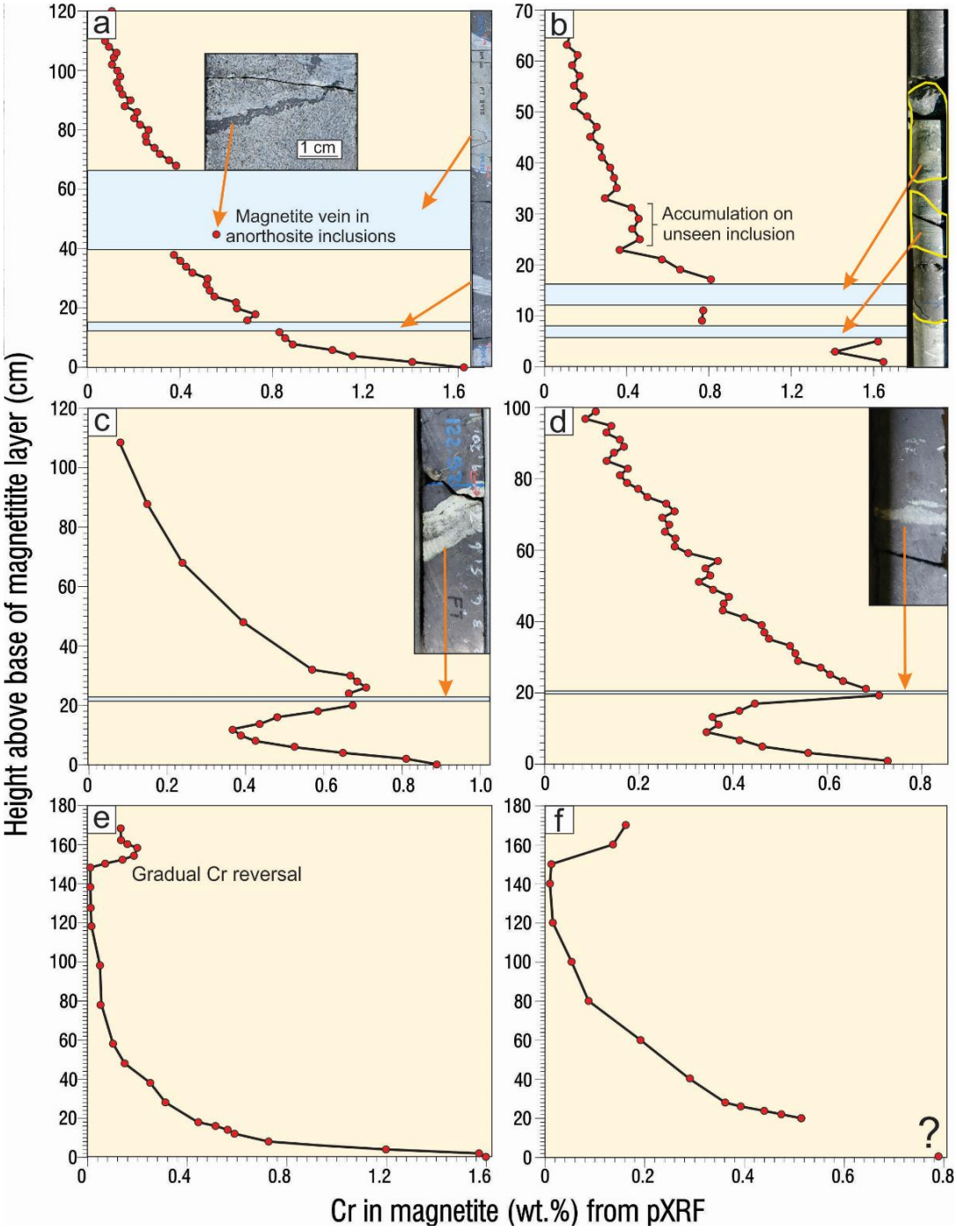

Figure 5.11 Vertical profiles through the Bottom seam and the Main Magnetite Layer from the Western Limb of the Bushveld Complex. (a) Bottom seam from the Vametco vanadium mine. The Cr concentration appears to be unnaffected by two inclusions (inset) in the profile. A vein of magnetite within one inclusion has a higher Cr concentration that the magnetite directly adjacent to the inclusion. (b) Bottom seam from the Rhovan vanadium mine. Two inclusions are also present (inset). Underneath the lowermost inclusion, Cr contents initially decrease then start to increase again. A reversal in Cr about 10 cm above the uppermost inclusion potentially indicated accumulation of magnetite on an inclusion not visible in the drill core. (c) Bottom seam from the Vametco vanadium mine that shows an initial rapid decrease followed by an increase in Cr contents underneath an anorthositic inclusion (inset). (d) Bottom seam from Rhovan with a single inclusion (inset) that shows a similar Cr distribution pattern compared to (c). (e) and (f) shows two examples of the Cr distribution in the Main Magnetite Layer from the Vametco vanadium mine. Notice the gradual reversal in Cr contents towards the top of the layers that is comparable to the reversal observed in the Main Magnetite Layer from Rhovan (Figure 5.8c). Question mark in (f) indicates that it is not known if this sample represents the true base of the layer because the drill core was fragmented in this section.

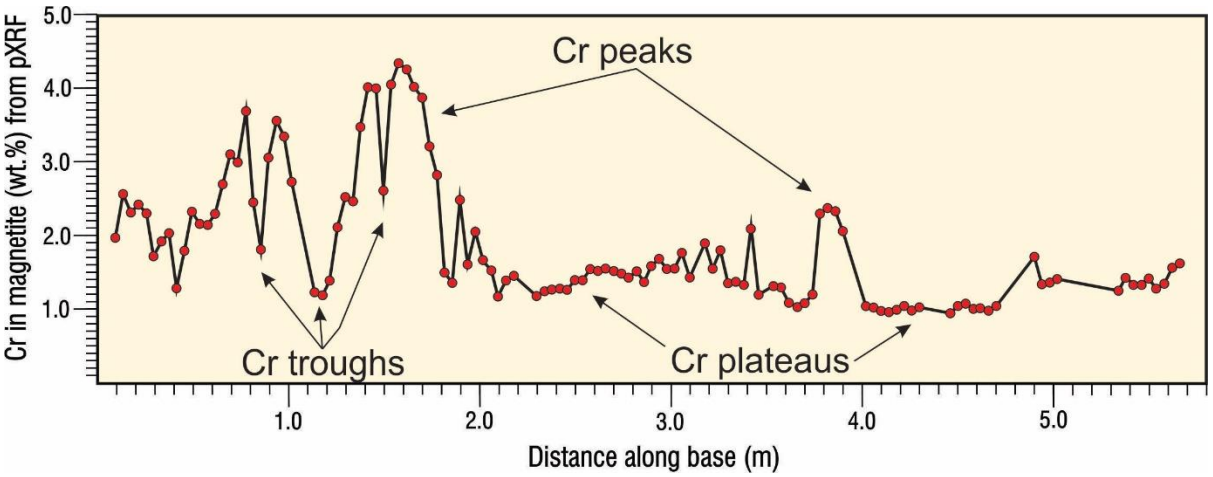

Figure 5.12 Lateral variation in the Cr contents along the base of the Main Magnetite Layer, Eastern Bushveld Complex, Magnet Heights. Cr contents vary dramatically along the lateral profile.

5.5.1 Late gravitative liquid accumulation by Bateman (1951)

During most of the 20th century, petrologists greatly favoured the idea of crystal settling to produce oxide ore deposits in layered intrusions, primarily because of the experimental work performed by Bowen (1915). A good example of this was considered to be the magnetitite layers of the Bushveld Complex. However, Bateman (1951) realized that this theory faced a great challenge when applied to magnetitite layers. Tholeiitic magmas, like those responsible for the formation of the Bushveld, only reaches magnetite saturation closer to their final stages of differentiation. Oxide deposits thus could not form simply by settling of early-formed magnetite crystals. Instead of crystal settling, Bateman (1951) suggested the idea of "late gravitative liquid accumulation". In this model, it is first necessary to produce a thick crystal mush of silicate minerals. As crystallization proceeds within the mush, Fe, Ti, and Cr contents increase, and the liquid progressively becomes denser. Eventually, the liquid may reach a sufficient density to start percolating downwards while simultaneously forcing the less dense silicates upwards. The liquid finally accumulates on top of a previously deposited ultramafic layer which would be more resistant to floating in the Fe-rich liquid. When the liquid then crystallizes, a magnetitite layer may form. Magnetite anorthosites commonly found atop magnetitite layers are then ascribed to imperfect separation of the Fe-enriched liquid and plagioclase grains (Figure 5.13).

However, if Bateman's (1951) model holds true, disseminated magnetite found in gabbroic rocks in the Upper Zone should be representative of the liquid that eventually formed the massive magnetitite. In all our results presented here, massive magnetitite layers are

significantly richer in Cr compared to the disseminated rocks. Significant Cr enrichment for the interstitial liquid therefore does not seem to occur. Another issue that requires attention is that magnetitite layers of the Bushveld are commonly underlain by anorthosite, not ultramafic rocks as suggested by Bateman (1951). An anorthositic mush would not be resistant to the gravitative liquid accumulation to form the sharp contact observed between magnetitite and anorthosite layers. The interstitial liquid would also have to be able to jump across any cotectics and into the field of magnetite for it to be able to crystallize massive magnetitite. No explanation is given as to how this can occur.

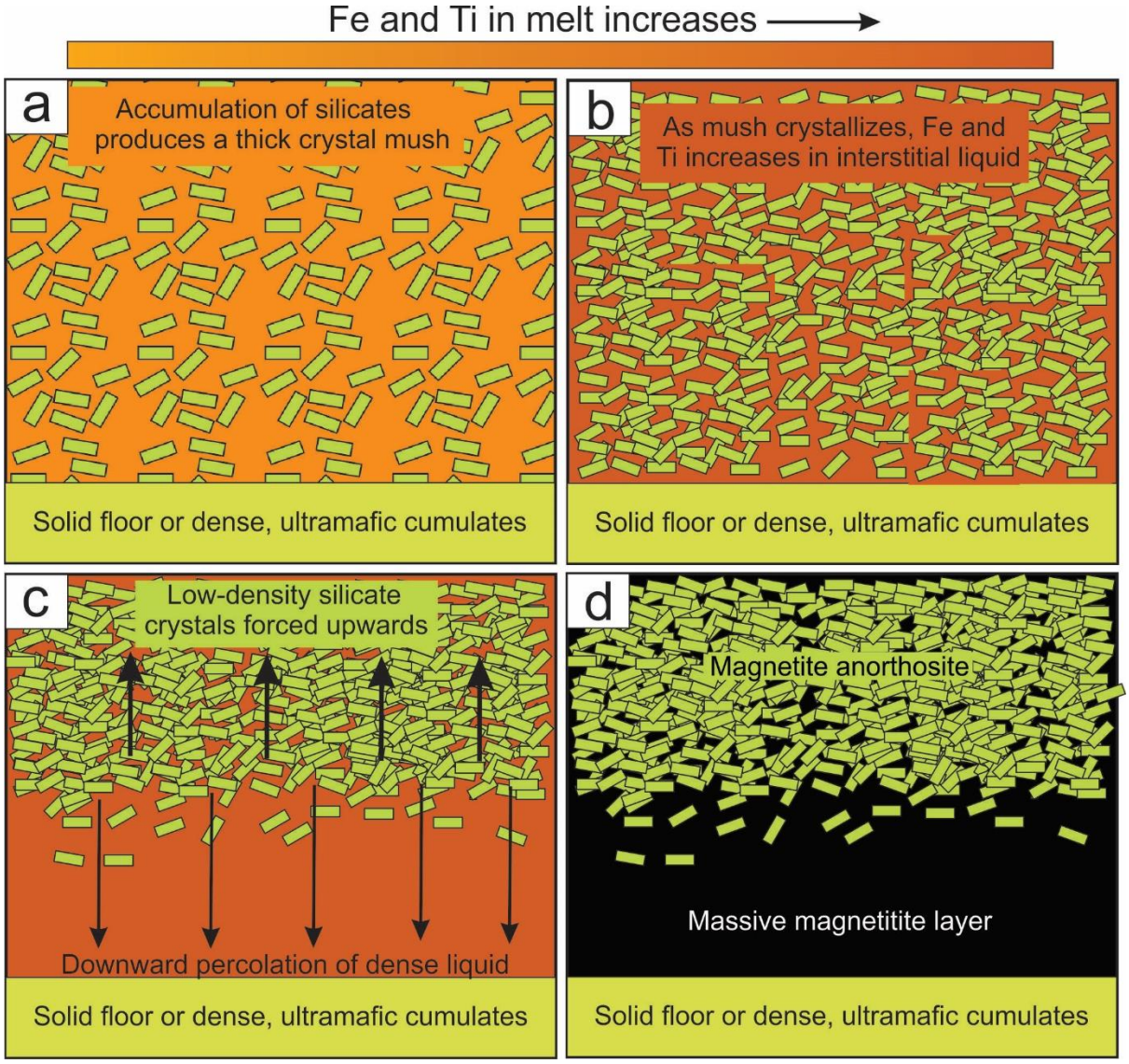

Figure 5.13 Late gravitative liquid accumulation model of Bateman (1951). (a) Low density silicates (such as plagioclase) accumulate on top of a dense or solid floor of previously deposited cumulates, forming a thick crystal mush. (b) As the interstitial liquid in the mush crystallizes, it is gradually enriched in Fe and Ti. (c) Crystallization of the mush proceeds until the interstitial liquid obtains sufficient density to start percolating downwards, forcing the less dense silicates upwards. (d) Eventually the liquid crystallizes, forming a massive magnetitite layer with a magnetite-anorthosite layer on top where crystal-liquid seperation was incomplete.

5.5.2 Contamination by granitic melt of Irvine (1975)

Some igneous intrusions, like the Muskox intrusion and Bushveld Complex, contain granitic rocks at their roofs. Irvine (1975) argued that partial melting of such roof rocks can cause contamination of the basaltic melt by the felsic liquid. This process may then alter the crystallization sequence within the magma chamber. One particular effect of contaminating a basaltic melt by a felsic liquid could be to raise its fO_2, a process that has been established to enlarge the stability field of magnetite (Roeder and Osborn, 1966). It was thus proposed that such a contamination event can lead to the crystallization of massive magnetitite layers in layered intrusions (Figure 5.14). However, Irvine (1975) himself pointed out that the model is too simple to explain the association of magnetitite layers with their footwall anorthosites and the problem deserved a more in-depth study. Another issue with the above model is that granitic rocks typically contain much lower Cr concentrations that basaltic liquid. In light of our new data, this model also faces the challenge to explain why Cr is elevated in magnetitite layers.

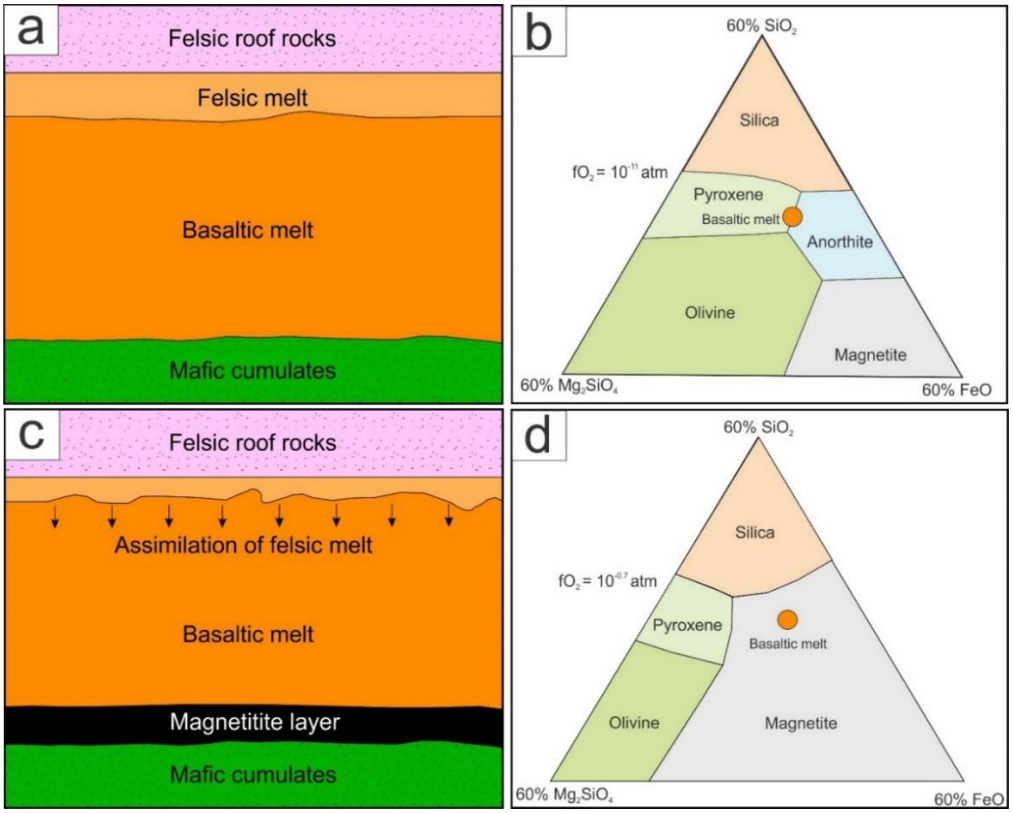

Figure 5.14 Origin of massive magnetitite layers by the contamination of granitic roof rocks by Irvine (1975) (not to scale). (a) A basaltic melt crystallizes mainly silicate minerals whilst partially melting granitic roof rocks. The basaltic melt may initially be characterized by a low fO_2 (b). As the granitic melt is assimilated (c), the fO_2 in the basaltic melt is raised and the field of magnetite is enlarged (d), leading to the crystallization of a massive magnetitite layer on the floor of the intrusion (c). The increase in fO_2 shown here is perhaps more dramatic than what can be expected from this process in reality, but serves to illustrate the point that a change in fO_2 can possible favour the crystallization of massive magnetitite. Phase diagrams in (b) and (d) are sections through the system Mg_2SiO_4-FeO-Fe_2O_3-$CaAl_2Si_2O_8$-SiO_2 with a constant $CaAl_2Si_2O_8$ of 40 wt. % (Roeder and Osborn, 1966).

5.5.3 Pressure increase and latent heat build-up of Cawthorn and McCarthy (1980; 1981; 1983), McCarthy et al. (1985), Cawthorn (1994), and Cawthorn and Ashwal (2009)

As mentioned before, Cawthorn and McCarthy (1980; 1981) first realized the great potential of Cr in magnetite as an extremely sensitive tracer of magmatic differentiation. This prompted them to set out and collect samples along vertical profiles through the MML in the Eastern Limb of the Bushveld Complex. They found an extremely rapid but regular depletion in Cr in magnetite upwards within this magnetitite layer similar to the results shown here (Figure 5.11). Only crystal settling over very small distances or *in situ* crystallization was deemed possible with such a smooth depletion in Cr content. Later on, Cawthorn (1994) also noted extreme lateral variation in the Cr content of the MML along the base of the layer. It was proposed that high-Cr areas indicate areas where magnetite started nucleating and growing on the chamber floor. Cawthorn (1994) predicted that the growth of magnetitite may proceed radially outwards to produce dome-shaped high Cr structures. Such dome-shaped structures have since been observed in our recent studies (Kruger and Latypov, 2020a; 2020b) and by our more detailed analysis of the lateral variation in Cr content as the base of the MML (Figure 5.12). Models involving crystal settling or sorting would most likely produce a blanket of crystals with a much more constant composition and is not be compatible with the dramatic horizontal variation in Cr content.

When Cawthorn and McCarthy (1980) examined a portion from Subzone A of the Upper Zone, they failed to find any reversals in Cr across relatively thin layers of massive magnetitite. When studying the variation in An contents of plagioclase grains in the Bellevue drill core from the Northern Limb, Cawthorn and Ashwal (2009) also failed to detect any significant reversal across most magnetitite layers. They therefore made the conclusion that some physical process must be responsible for the formation of massive magnetitite that excluded the introduction of new magma into the chamber (Cawthorn and McCarthy, 1980; Cawthorn and Ahwal, 2009). Following the work by Cameron (1978), Cawthorn and McCarthy (1980) therefore proposed that perhaps a change in pressure in the magma chamber caused the phase boundaries in such a manner that only magnetite crystallized (Figure 5.15a).

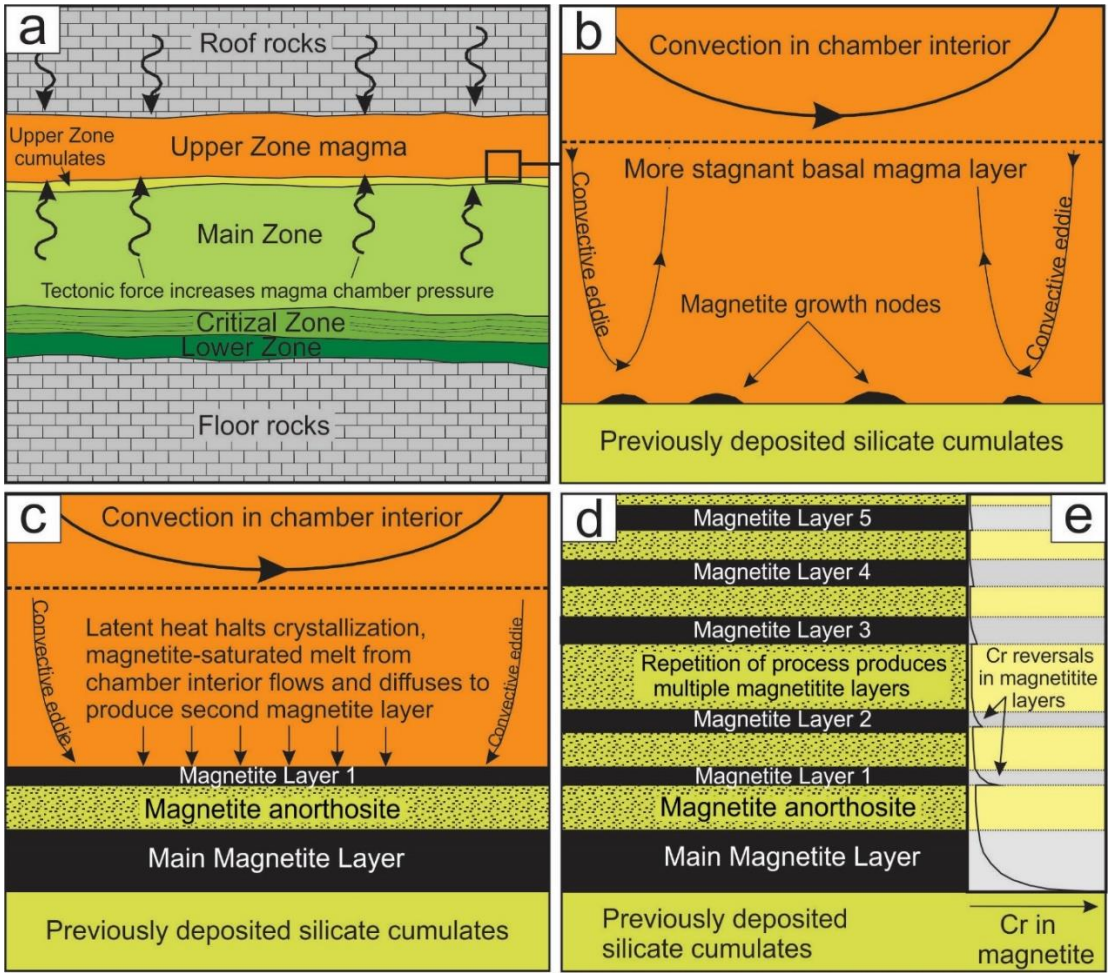

Figure 5.15 Model for the origin of magnetitite based on a compilation of work from Cawthorn and McCarthy (1980; 1981; 1983), McCarthy et al. (1985), and Cawthorn (1994) (not to scale). (a) Some tectonic event causes an increase in pressure in the Bushveld magma chamber. (b) This pressure increase shifts phase boundaries in such a manner that the entire magma chamber ends up in the magnetite stability field. Magnetite then starts crystallizing in situ at the base of the magma chamber to produce magnetite growth nodes in a stagnant basal layer of melt, free of the more interior. Crystallization of magnetite proceeds under the influence of diffusion that is partly aided by secondary convective eddies. (c) Continued crystallization eventually produces the Main Magnetite Layer. As the stagnant basal layer evolves, magnetite anorthosite eventually crystallizes. Crystallization then stops due to the accumulation of latent heat. This allows time for magnetite components to diffuse and flow towards the solidification front. When crystallization resumes, a second (Magnetite Layer 1) is produced. (d) Repetition of this process eventually produces several magnetitite layers of intervening silicate-rich layers. (e) Somewhat simplified variation in the Cr contents of magnetitite layers. A Cr reversal is associated with each magnetitite layer as Cr-undepleted magma is transported from the chamber interior towards the floor cumulates prior to the crystallization of each magnetitite layer.

A few years later McCarthy *et al*. (1985) extended their vertical profiles through the MML further upwards to include Magnetite Layer 1. A Cr reversal was found within this layer similar to what is observed in the first magnetitite layer above the Bottom seam in data from this study (Figure 5.8b). This observation is clearly at odds with the previous proposal that magnetitite layers formed by pressure increase only as this process cannot enrich the chamber in Cr. While maintaning that the MML formed after a pressure increase, McCarthy *et al*. (1985) proposed a

different mechanism to explain the origin of Magnetite Layer 1. The MML was considered to have crystallized from a relatively stagnant, isolated layer of melt at the base of the chamber approximately 120 m thick. Crystallization would occur largely through diffusion in this stagnant layer which is partially supplemented by secondary convective eddies coming from the chamber interior (Cawthorn and McCarthy, 1981). During the crystallization of the magnetite anorthosite atop the MML, significant amounts of latent heat would accumulate at the solidification front, eventually inhibiting crystallization. This would give time for fresh magma, still located within the field of magnetite due to the earlier pressure increase, to migrate downwards into the stagnant layer by diffusive and convective processes. When crystallization resumes, a new layer of magnetite (Magnetite Layer 1) would form. This process would also record a Cr reversal at the base of this magnetitite layer (Figure 5.15).

This model faces two significant challenges in light of our new data. The first is the very large Cr reversal at the base of the MML. A pressure increase within the chamber alone cannot explain how the melt got saturated in magnetite only, as this process cannot produce a Cr reversal. Secondly, the diffusion of heat is 10^4 to 10^7 times faster than the diffusion of matter (Barnes and Robertson, 2019). The build-up of latent heat during crystallization thus cannot halt the crystallization process, as the diffusion of matter towards the solidification front, and not heat away from it, would be the determining factor that controls crystallization.

5.5.4 In situ fractionation of plagioclase to produce massive magnetitite of Reynolds (1985b)

Following the work by petrologists such as Jackson (1961), Campbell (1978), and Cawthorn and McCarthy (1980), Reynolds (1985b) favoured the idea of *in situ* crystallization of magnetitite from the Bushveld Complex. His model is also one of the few that attempts to explain the association of magnetitite with anorthosite. Reynolds believed that the underlying anorthosite layer was directly responsible for the formation of the magnetitite. During the *in situ* crystallization of an anorthositic layer, the overlying melt would become enriched in Fe as the chemical components necessary to construct plagioclase are preferentially removed, forming a dense basal layer of melt overlying the anorthosite. The fractionation of plagioclase would increase the OH^- content of the overlying liquid, which in turn has the effect of increasing the oxygen fugacity of the melt. Extraction of alkalis by plagioclase from the basal layer would also decrease the solubility of Fe^{3+} (Reynolds, 1985b). All of these factors may eventually favour the crystallization of massive magnetitite (Figure 5.16).

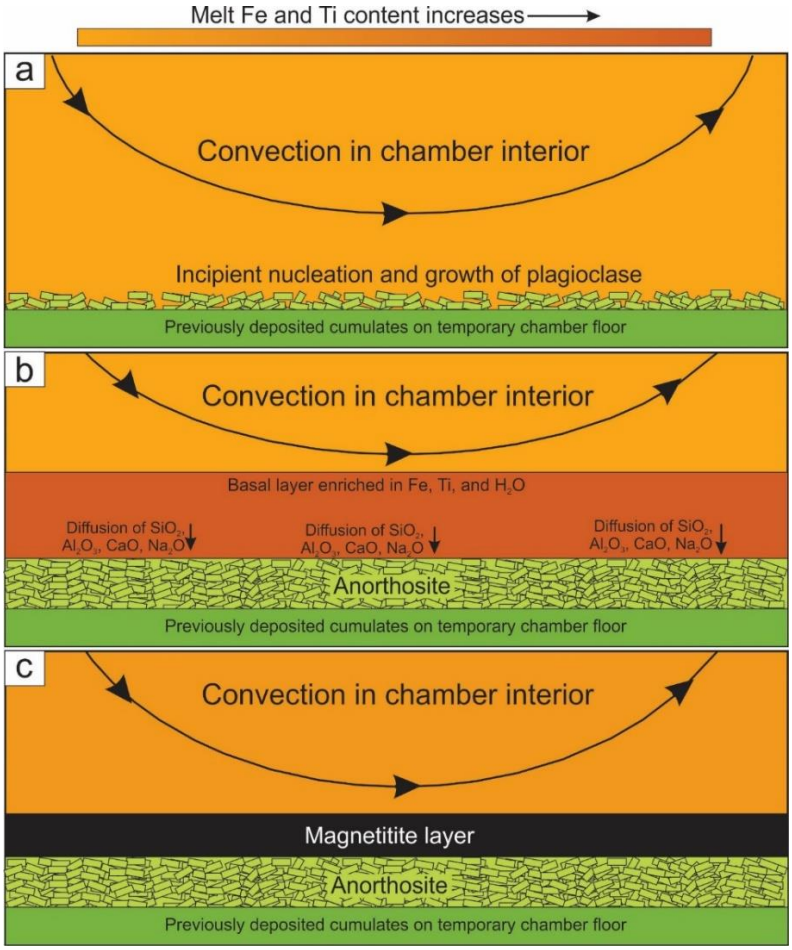

Figure 5.16 A model involving the *in situ* fractionation of plagioclase by Reynolds (1985b) for the origin of massive magnetitite. (a) Plagioclase starts crystallization on the bottom of the magma chamber. (b) As the anorthosite layer grows, the components necessary to construct plagioclase moves downwards, leading to the formation of a basal layer enriched in Fe, Ti, and H_2O that favours magnetite crystallization. The basal melt layer is unable to convect with the chamber interior due to its high density. (c) Eventually a magnetitite layer crystalizes from the dense basal melt layer which is destroyed by convective overturn.

A problem with this model is the extremely large Cr reversal recorded at the base of the MML. The uppermost sample with cumulus magnetite underneath the anorthosite layer below the MML from the Rhovan drill core has a Cr in magnetite content of 225 ppm. The concentration recorded at the base of the MML is about 12,712 ppm, i.e. a 56 fold increase. Assuming the partition coefficient of Cr into plagioclase is essentially zero, the melt would have to fractionate approximately 98 wt.% of plagioclase to produce such an increase in the Cr content. A melt capable of producing >98% plagioclase cumulates will need to have an extraordinary composition. Only <2% of the melt will then remain to crystallize massive magnetitite and it should only be about 2% of the thickness of the anorthosite layer, i.e. the anorthosite layer underneath the 2 m thick MML is supposed to be 100 m thick for the model to work. This is certainly not observed in drill core (Figure 5.8a). In addition, one magnetitite layer was found

atop magnetite anorthosite and another on a pyroxenite layer as mentioned previously (Figure 5.7g and h). The *in situ* fractionation of these rock types are even more unlikely to lead to the formation of the magnetitite layers with pronounced Cr reversals.

5.5.5 Variation in oxygen fugacity of Klemm et al. (1985)

It has long been known that an increase in the oxygen fugacity of silicate melts significantly enlarges the magnetite stability field (Roeder and Osborn, 1966). Another consequence of such an increase in oxygen fugacity is that V becomes less compatible in magnetite due to the increase of its oxidation state (Toplis *et al*., 2002). Klemm *et al*. (1985) undertook a study to examine the difference in the geochemistry of pure magnetite separates from disseminated and massive ore across the entire Upper Zone in the Eastern Limb. What they found is that massive magnetitite typically contains a lower V concentration on average than the disseminated magnetite. Similar to Irvine (1975), Klemm *et al*. (1985) therefore suggested that massive magnetitite formed due to a sudden increase in the oxygen fugacity in the magma chamber. However, their proposed source for the higher oxygen content was not contamination by granitic melt (Irvine, 1975), but instead intercumulus liquid migrating upwards through a mushy cumulus pile below. This intercumulus liquid would be enriched in H_2O due to the accumulation of largely anhydrous primocrysts, and dissociation of the H_2O molecule would produce the necessary oxygen for the crystallization of magnetite. Convection above the cumulus pile was applied as a mechanism to spread out the oxygen-enriched melt across the chamber, ensuring the crystallization of magnetite across hundreds of kilometres (Figure 5.17).

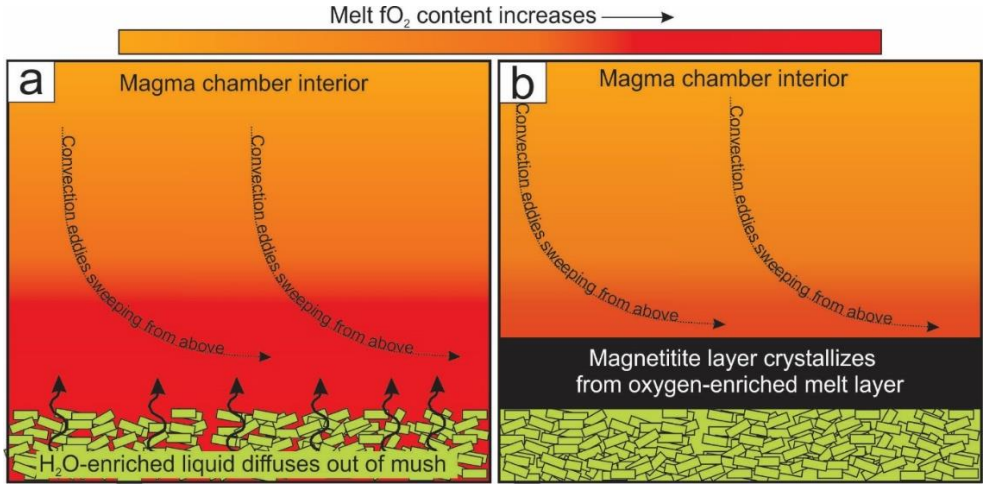

Figure 5.17 Increase in the melt's oxygen fugacity to crystallize magnetitite of Klemm et al. (1985). (a) The crystallization of anhydrous minerals on the floor of the magma chambers results in an interstitial liquid that is enriched in H_2O. As this liquid diffuses upwards towards the magma interior, a layer of melt forms with an elevated oxygen fugacity due to the dissociation of the H_2O molecule. Convection from above aids to distribute the oxygen-enriched melt chamber wide. (b) The elevated oxygen oxygen fugacity in the basal melt layer favours the crystallization of magnetitite across the entire floor of the magma chamber.

However, in our own data from Rhovan we failed to detect any significant difference between the V contents of massive and disseminated magnetite (Figure 5.18), although the highest V concentration was measured in massive magnetitite. As with the previous models, a sudden change in oxygen fugacity cannot explain the extremely large Cr reversal observed at the base of the MML. This is especially true considering that Cr behaves as a compatible element in both magnetite and clinopyroxene, and an intercumulus liquid coming from mostly plagioclase-pyoxene-magnetite cumulates below will be greatly depleted in Cr.

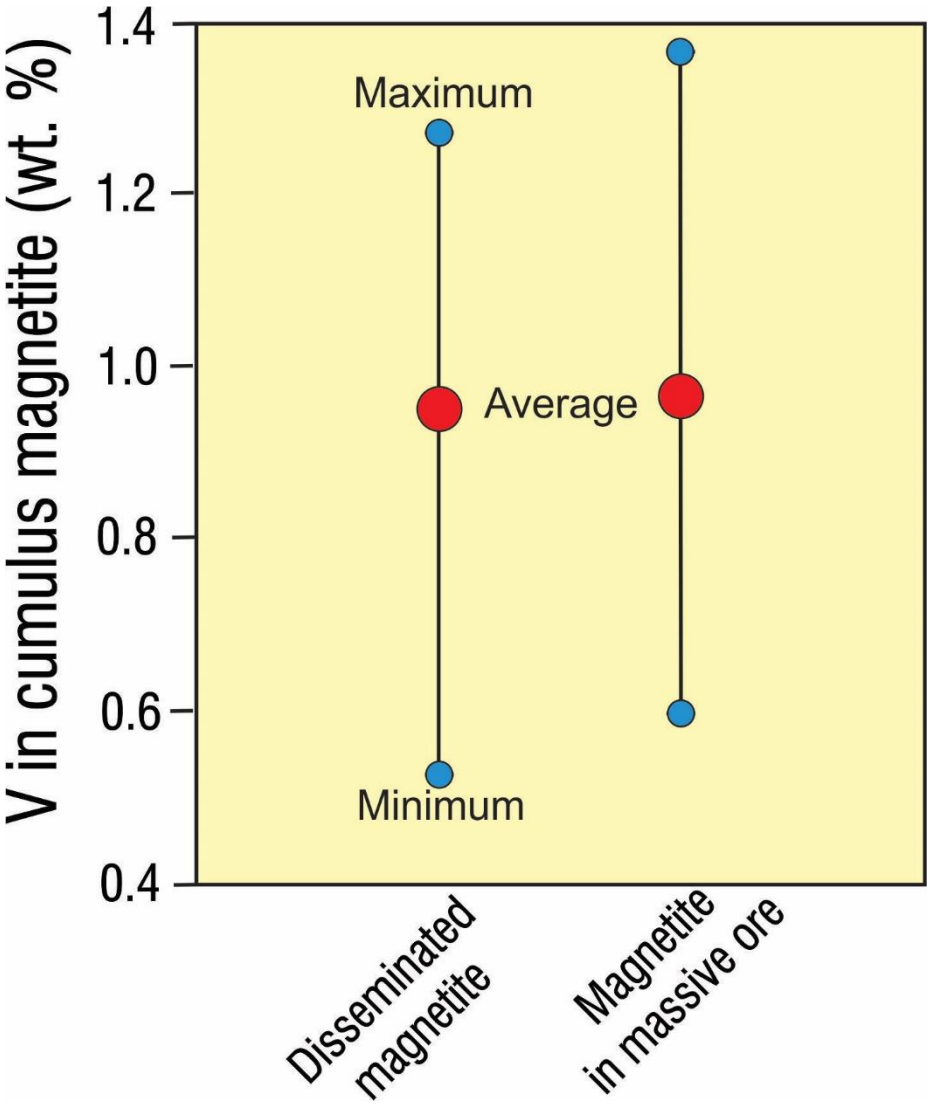

Fig 5.18 Average, minimum, and maximum V contents of titano-magnetite in disseminated and massive ore from the Rhovan vanadium mine, Western Bushveld Complex. The two types of magnetite deposits cannot be distinguished in terms of their V contents.

5.5.6 Magma addition and thermal erosion of Butcher and Merkle (1991)

Butcher and Merkle (1991) made a noteworthy discovery at the Vametco vanadium mine when studying the anorthosite that underlies the Bottom seam. Within it occurred several layers of magnetite, only one grain in thickness and only a couple of mm apart. This locality thus differs from others where cumulus magnetite is typically absent in the anorthosite beaneath the Bottom seam. The intermittent depostion of these magnetite grains seems to have recorded the morphology of the solidification front of the anorthosite at different stages during its propagation. Interestingly, discordant relationships were recorded between these magnetite layers, with some layers cutting across others. In some instances, magnetite grains were depsosited in small transgressive depressions and resemble potholes that are frequently observed on a larger scale underneath the Merensky Reef and Upper Group chromitites (Schmidt, 1952; Carr *et al*., 1999; Lomberg *et al*., 1999; Latypov *et al*., 2016 Latypov *et al*., 2017a).

The lack of modal grading within the anorthosite led Butcher and Merkle (1991) to the conclusion that, if the magnetite had accumulated by crystal settling, it could only have occurred over very short distances or at a very rapid rate. Alternatively, *in situ* crystallization was also considered a possibility. To explain the field relations observed, Bucther and Merkle (1991) invoked periodic and frequent magmatic recharge events. During each event, some thermal erosion of the footwall may occur, leading to the observed cross-cutting relationships. After the erosional event a layer of magnetite may then be deposited, and the morphology of the floor is intermittently preserved (Figure 5.19).

Although Butcher and Merkle's (1991) study does not directly deal with the origin of massive magnetitite, their idea that the thin magnetite layers formed after a magmatic recharge event is compatible with the Cr reversal we have recorded at the base of the MML. Many of the intricate field relationships documented in this study (Figure 5.4-5) may also be explained by thermal erosion as discussed later on.

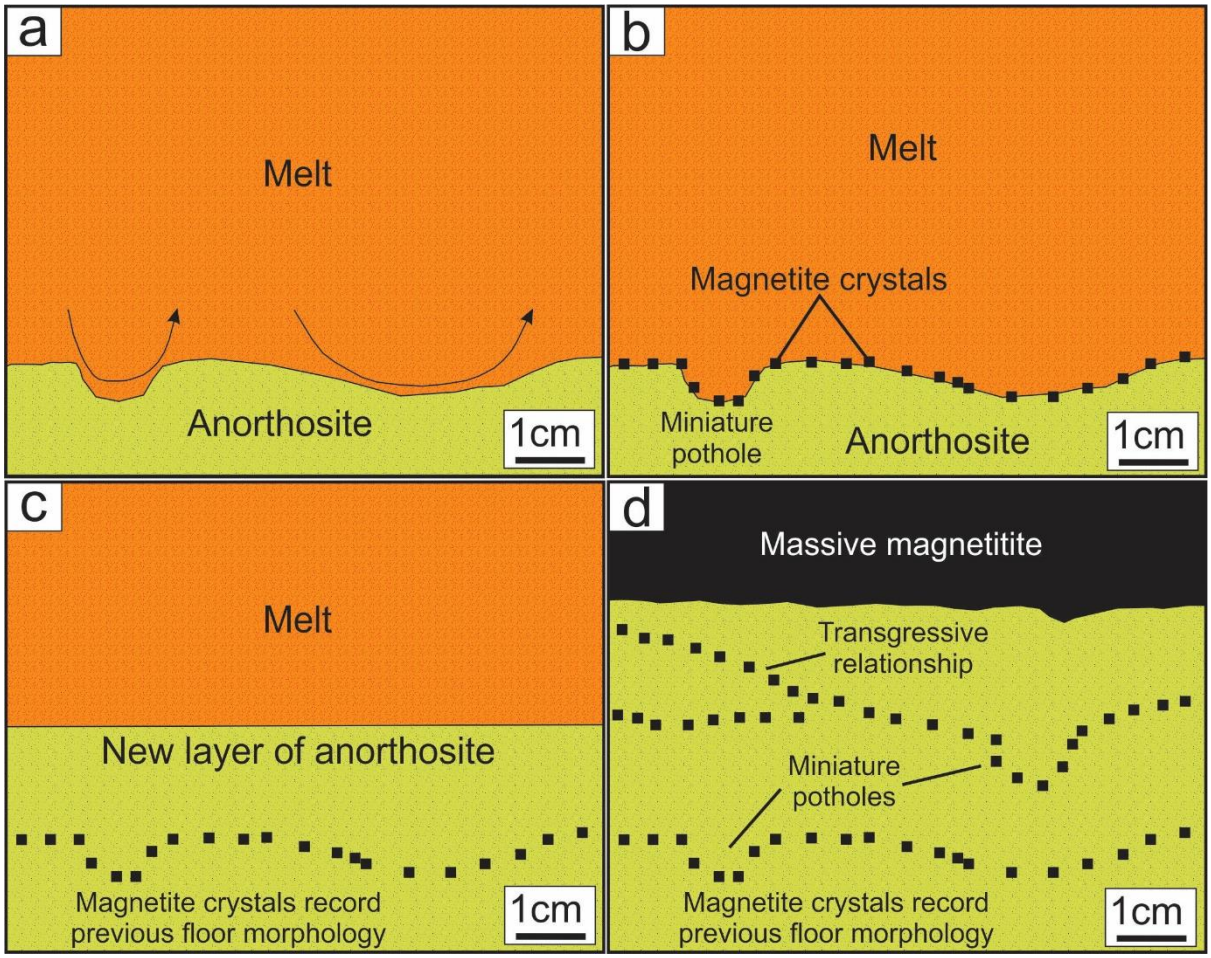

Figure 5.19 Intermittent thermal erosion and crystallization model of Butcher and Merkle (1991). (a) A layer of anorthosite undergoes partial destruction by thermochemical erosion due to magmatic recharge. (b) Upon cooling, a one-crystal-thick layer of magnetite is deposited on the eroded surface by *in situ* crystallization. (c) When plagioclase crystallization resumes, the older floor morphology can still be observed by studying the distribution of the magnetite crystals. (d) Repitition of the above process preserves complex structural relationships between anorthosite layers, such as miniature potholes and transgressive layers. Everntually, for reasons that are so far unknown, a massive magnetitite layer crystallizes atop the anorthosite.

5.5.7 Breakdown of density stratified liquid layers by Harney and Von Gruenewaldt (1995)

Several lines of evidence led Harney and Von Greunewaldt (1995) to conclude that the MML forms the base of a geochemical cycle. Although no reversal in terms of the An content of plagioclase could be detected, they did find a shift in the Sr/Al ratios of plagioclase to slightly higher values across the MML. A change in the shape of a chondrite-normalized PGE pattern was also detected by Harney *et al*. (1990) a few years earlier. The base of a geochemical cycle is commonly interpreted as a horizon where magmatic recharge occurred. However, Harney and Von Gruenewaldt (1995) realized that such a model would be in conflict with the Sr-isotope data from Kruger (1987; 1994) that suggests the Upper Zone of the Bushveld Complex crystallized as a closed system. As an alternative they proposed that the Upper Zone may be

stratified by density. The collapse of such density-stratified layers would lead to magma mixing. Since it has been demonstrated that magma mixing may cause the crystallization of chromite (Irvine, 1977), the same process was deemed responsible for the crystallization of the massive magnetitite (Figure 5.20). On the other hand, they proposed that perhaps the MML formed due to a relatively small influx of magma which could not cause any significant deviation from the relatively constant intitial Sr-isotopic ratios as observed across the Bushveld's Upper Zone (Kruger, 1987).

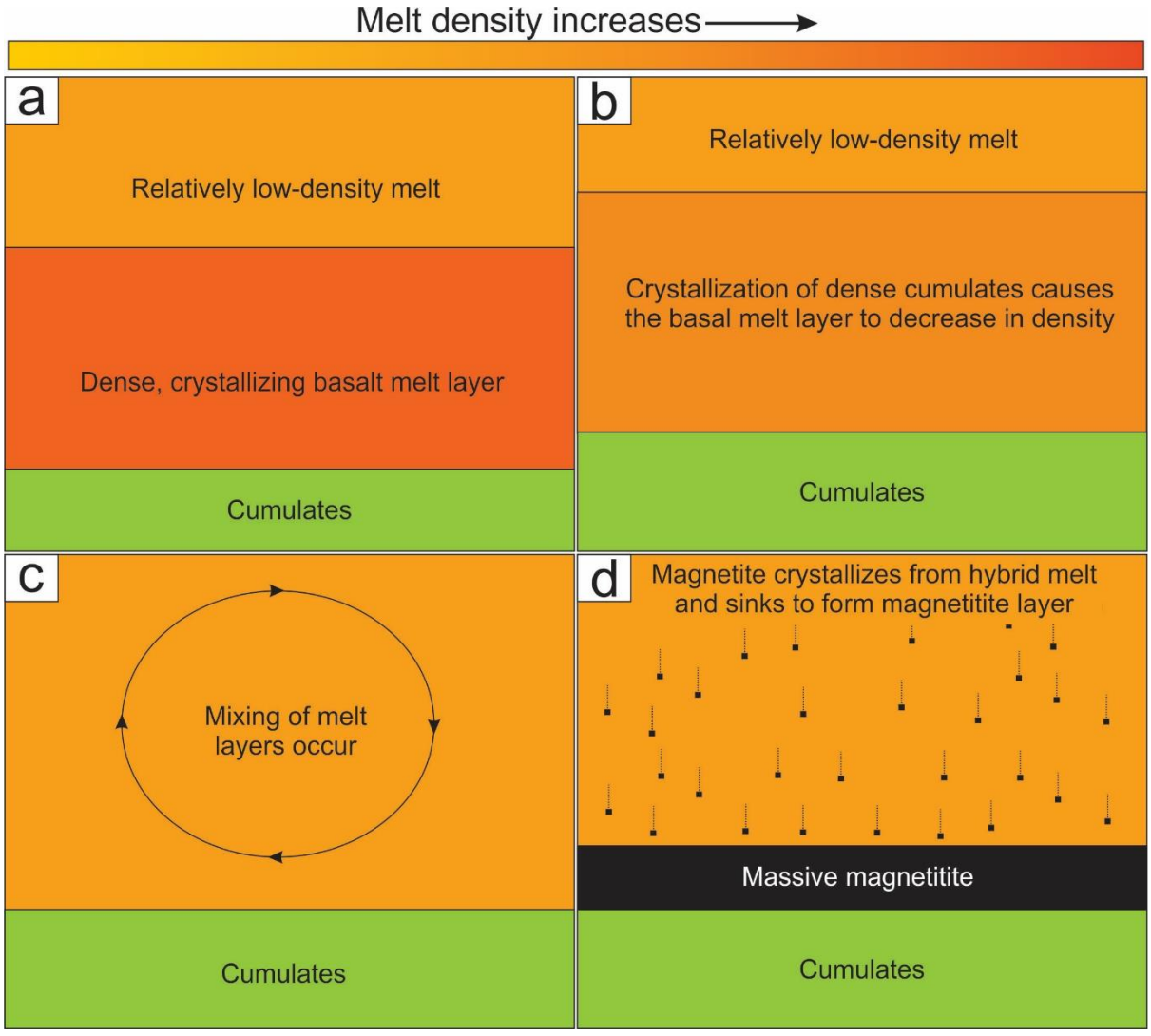

Figure 5.20 Model for the origin of massive magnetitite layers of Harney and Von Gruenewaldt. (a) In this model the Bushveld magma chamber is stratified according to density. (b) During crystallization, the lowermost layer decreases in density. (c) When the basal melt layer matches the upper melt layer in density, the interface between the two liquid layers start to break down and mixing ensues. (d) The mixing process ensures the sole crystallization of magnetite crystals that may then sink out and accumulate on the floor to produce a massive magnetitite layer.

A model that involves the collapse of density stratified layers has the potential to produce Cr reversals as observed in magnetitite layers in this study. An intriguing question is if such a process can produce the MML with its higher Cr abundance compared to the Bottom seam which is located further down in the stratigraphy. The MML seems to have crystallized from a magma that is richer in Cr than the Bottom seam and could not have been resident in the chamber during the Bottom seam's crystallization. Therefore Harney and Von Greunewaldt's suggestion that the MML formed by the introduction of a new pulse of magma into the chamber seems more reasonable, and is discussed in more depth later. However, a proper assessment of phase diagrams is still required to test the magma mixing hypothesis for the origin of massive magnetitite.

5.5.8 Crystallization of magnetitite in a double-diffusive-convective system by Tegner et al. 2006

During their study of Bierkraal drill cores from the Western Limb of the Bushveld Complex, Tegner *et al*. (2006) recognized several geochemical cycles in the Upper Zone identified by plagioclase An contents, Mg# of olivine, clinopyroxene, and orthopyroxene, bulk-rock P_2O_5 contents and V contents of magnetite. These base of these cycles were attributed to the convective overturn of double-diffusive convecting layers caused by a density inversion brought on by the fractionation of magnetite during bottom crystallization. While some magnetitite layers were found clustered across the boundaries of these geochemical cycles, others were found to occur within cycles (including the MML). No significant changes in the silicate mineral chemistry was detected across magnetitite layers. This observation led Tegner *et al*. (2006) to conclude that magnetitite layers did not form due to a magmatic recharge event, or even convective overturn, as suggested by Harney and Von Greunewaldt (1995). Instead, they argued that "simple fractional crystallization led to the formation of the magnetitite layers".

The above model does not, however, deal with the difficulty in explaining how magnetite may accumulate in monomineralic layers. Tegner *et al*. (2006) also does not report on the Cr contents of magnetitite layers for which large reversals were reported at the bases of magnetitite layers in this study. The latter may suggest magnetitite layers do indeed represent the bases of geochemical cycles. This matter is addressed in more detail later.

5.5.9 Magmatic recharge and crystal settling of Scoon and Mitchell (2012)

In contrast to Kruger (1987) and Tegner *et al*. (2006) who proposed that the UZ intruded as a single pulse of magma, Scoon and Mitchell (2012) used several lines of evidence to suggest that the Upper Zone intruded incrementally in the form of numerous sheets of magma originating from deeper-seated staging chambers. These include the highly transgressive nature of the UZ to underlying zones of the Bushveld in a northern section of the Eastern Limb, the so called gap-areas in the Western Limb where the UZ appears to have intruded into the Lower, Critical and Main Zones of the Bushveld Complex, and the appearance of outliers of UZ rocks in the Transvaal Supergroup near the town of Marble Hall. In their geochemical data from five different boreholes in the Roossenekal area in the Eatern Limb, Scoon and Mitchell (2012) noticed a great amount of scatter in the whole-rock Mg#, which they believed are incompatible with the idea that the UZ crystallized as a closed system. Following Zhang *et al*'s (2012) work on the Baima Intrusion in China, Scoon and Mitchell (2012) proposed the following sequence of events that led to the formation of massive magnetitite layers of the Bushveld Complex: fractional crystallization in a deep staging chamber under low fO2 conditions forces the melt along a tholeiitic differentiation trend of Fe-enrichment. When a pulse of melt is released from the staging chamber upwards, magnetite may crystallize as an early phase on the liquidus within magmatic conduits or upon entry in the Bushveld magma chamber. Because of the high density of the magnetite crystals, they may then rapidly settle out once the melt enters the Bushveld magma chamber, forming a massive magnetitite layer on its floor (Figure 5.21). The idea of magmatic recharge is also promising to explain the origin of anorthositic inclusions found within magnetitite layers (Fig 5.5) that Scoon and Mitchell (2012) referred to as "partially resorbed xenoliths" as discussed in more detail later.

In light of the data presented in this paper, this model has one great advantage and one significant disadvantage. While magmatic recharge in the UZ can readily explain Cr reversals associated with massive magnetitite layers, density sorting of magnetitite crystals within the chamber probably cannot explain the extreme lateral variability of Cr along the base of the MML. Scoon and Mitchell (2012) also does not provide a mechanism to explain how exactly magnetite becomes an early liquidus phase in the magma during magmatic ascent or upon entry of the magma in the Bushveld magma chamber.

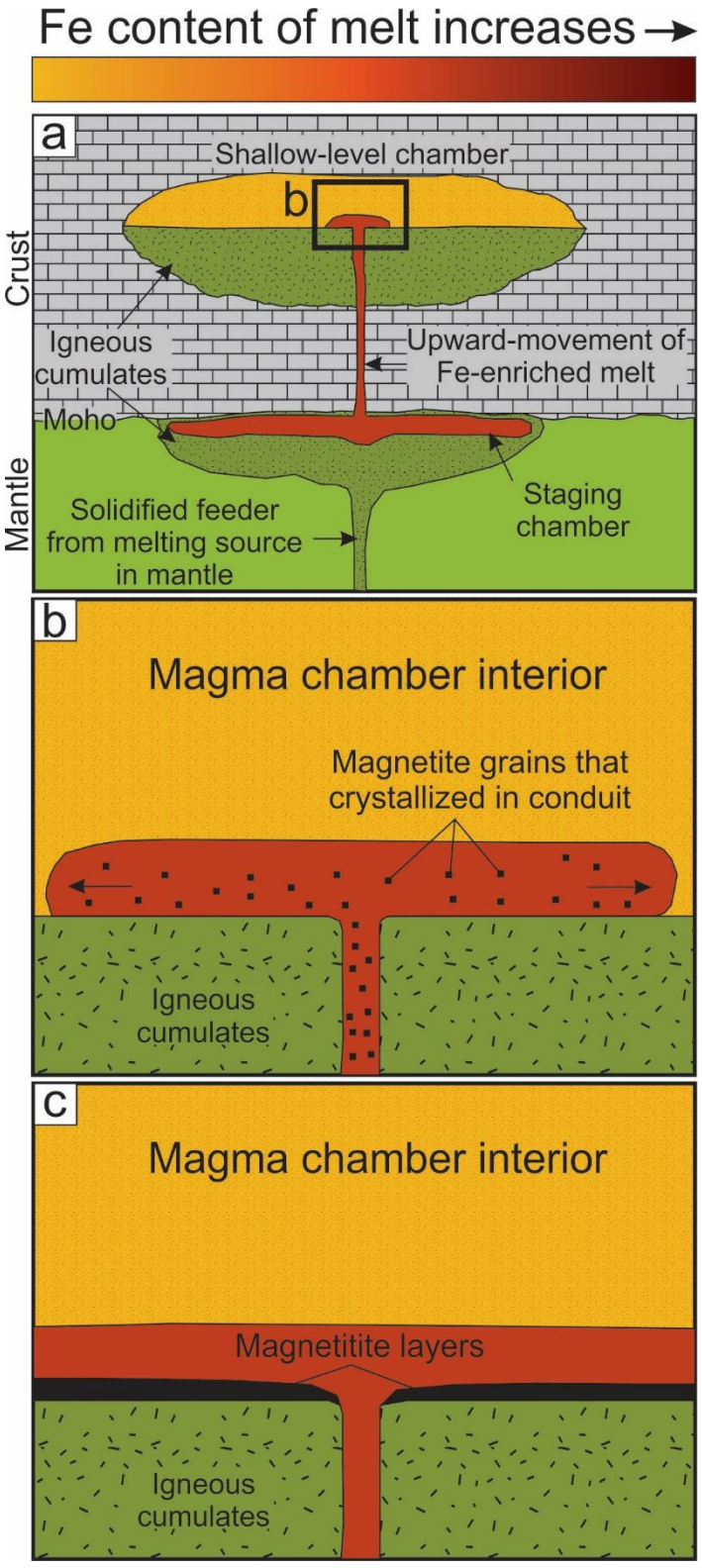

Figure 5.21 Model for the origin of magnetitite layers of Scoon and Mitchell (2012). (a) Crystallization in a deep staging chamber under low fO_2 conditions causes the melt to become enriched in Fe. A pulse of this Fe-enriched liquid is expelled upwards towards a shallow level chamber (i.e. the Bushveld Complex). (b) The melt may crystallize magnetite en-route to the chamber, and the subsequent deposition of these magnetite crystals on the chamber floor may result in the formation of magnetitite layers (c).

5.5.10 Hydrodynamic sorting of cumulate slurries by Maier et al. (2013)

Because of the great challenges in explaining how monominerallic rocks are produced from crystallizing magmas, Maier *et al*. (2013) suggested that layering in the Bushveld Complex only formed by hydrodynamic sorting only after minerals were crystallized in their expected cotectic proportions. The process involves the generation of thick crystal mushes and the subsidence of the Bushveld chamber floor, either due to loading or devolatilization of the underlying carbonate sedimentary rocks. When the subsidence occurs, the crystal mushes are forced to flow under the force of gravity towards the centre of the intrusion, and minerals become sorted according to their densities. In the Bushveld's Upper Zone, such a process may be able to separate dense magnetite crystals from the less dense silicates, leading to the formation of magnetitite layers (Figure 5.22). In this model, every single magnetitite layer is believed to have formed due to an individual subsiding event.

The above model could potentially explain some of the intriguing field observations in the footwall of magnetitite layers (Figure 5.5) as Maier *et al*. (2016) later proposed that the injection of moving slurries into the temporary floor of the chamber may lead to transgressive relationships. However, it may be exceedingly difficult to explain the distribution of Cr in magnetite because of such a process. The extremely regular depletion of Cr upwards in the MML and the Bottom seam recorded from several localities seems incompatible with a model than involves any movement of crystals in a chamber. Dramatic lateral variability in the Cr concentration along the bottom contacts of magnetitite layers (Figure 5.12) (Cawthorn, 1994; Kruger and Latypov, 2020a) are also not to be expected from such a process; entropy dictates that such a process should produce a much more uniform Cr concentration along the layer's base. This is especially true considering the original cumulus size of magnetite crystals may have been less than 1 mm while the size of Cr troughs and peaks may exceed severals tens of centimetres. Another problem is that this model cannot explain why pyroxene only appears as a primocryst after plagioclase above magnetitite layers since its density is intermediate between plagioclase and magnetite.

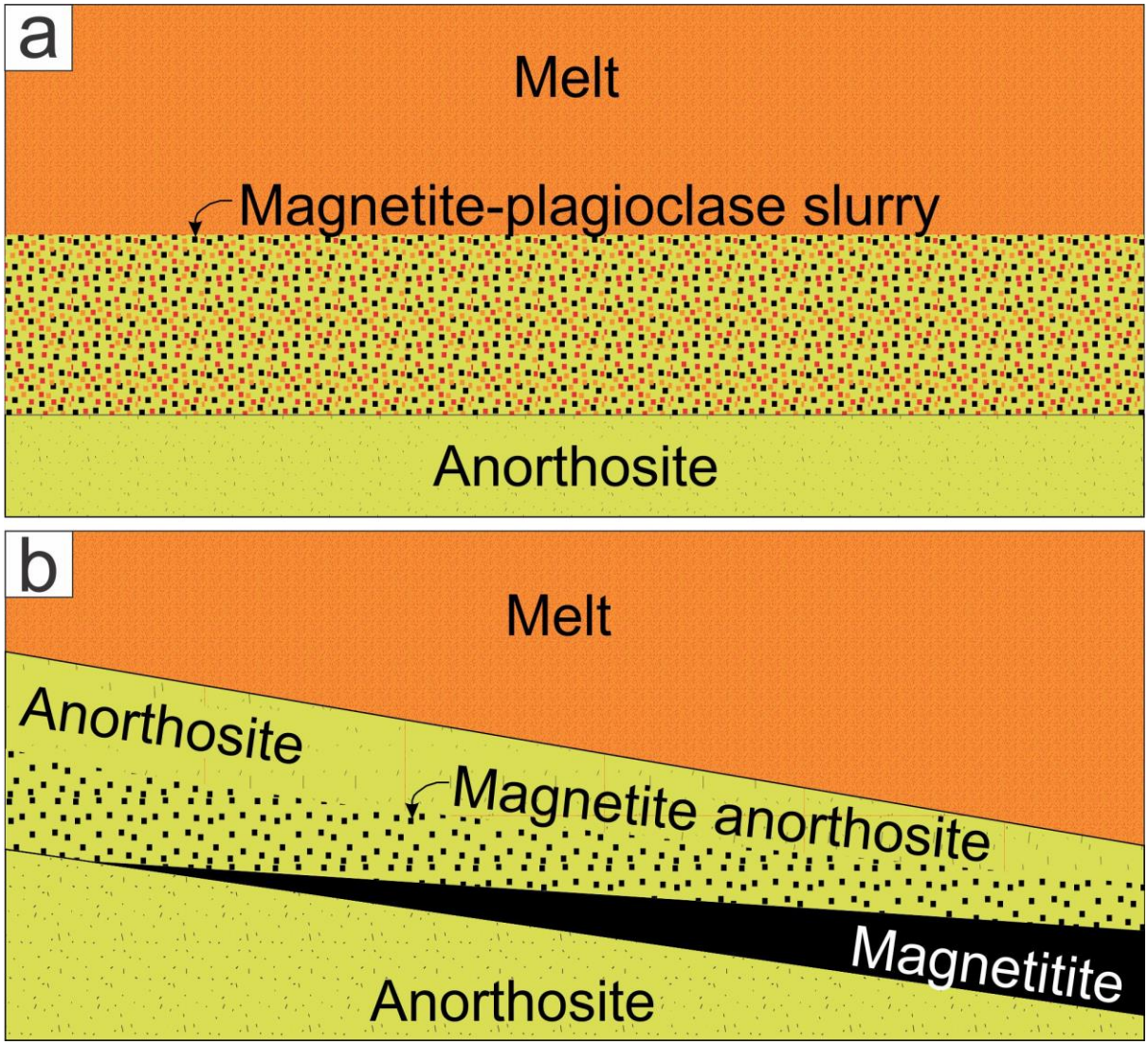

Figure 5.22 Model for the origin of massive magnetitite layers by Maier et al., (2013). (a) Magma crystallizes to produce cotectic proportions of, for example, magnetite and plagioclase, forming a thick crystal-rich mush. (b) Due to the overlying weight of the cumulates or possibly because of devolatilization of underlying carbonate rocks, the crust subsides, and subsequent flow of the crystal results in hydrodynamic sorting. The densent mineral grains (in this case magnetite) ends up on the bottom of the cumulate pile, potentially forming a magnetitite layer.

5.5.11 Magma mixing model of Yuan et al. (2017)

Yuan *et al*. (2017) found reversals in the An content of plagioclase in anorthosite layers beneath magnetitite layers from the Bierkraal drill cores in the Western Limb of the Bushveld Complex. This prompted them to suggest that magmatic recharge occurred prior to the formation of the anorthosite layers. Similar to what is commonly suggested for the formation of massive anorthosite complexes, they proposed that the anorthosite layers of the Bushveld are due to the injection of a plagioclase crystal slurry. The incoming magma would then mix with the resident

magma, potentially favouring the crystallization of magnetite. Magnetite crystals would then settle out from the hybrid melt to form a massive magnetitite layer (Figure 5.23).

The injection of new magma as a mechanism to explain the origin of the anorthosite is promising, as such a model may produce magnetitite layers with Cr reversals. However, a problem arises with the idea of magma mixing as it requires crystal settling (Yuan *et al*., 2017). Any movement of crystals is considered unlikely to produce the delicate Cr profiles as documented by Cawthorn and McCarthy (1980; 1981; 1983), Cawthorn (1994), Kruger and Latypov (2020a), and the results shown here (Figures 5.11-12). It is also improbable that simple settling of magnetite crystals can produce the various field relationships documented between massive magnetitite crystals and the underlying anorthosite layer (Figure 5.4-6).

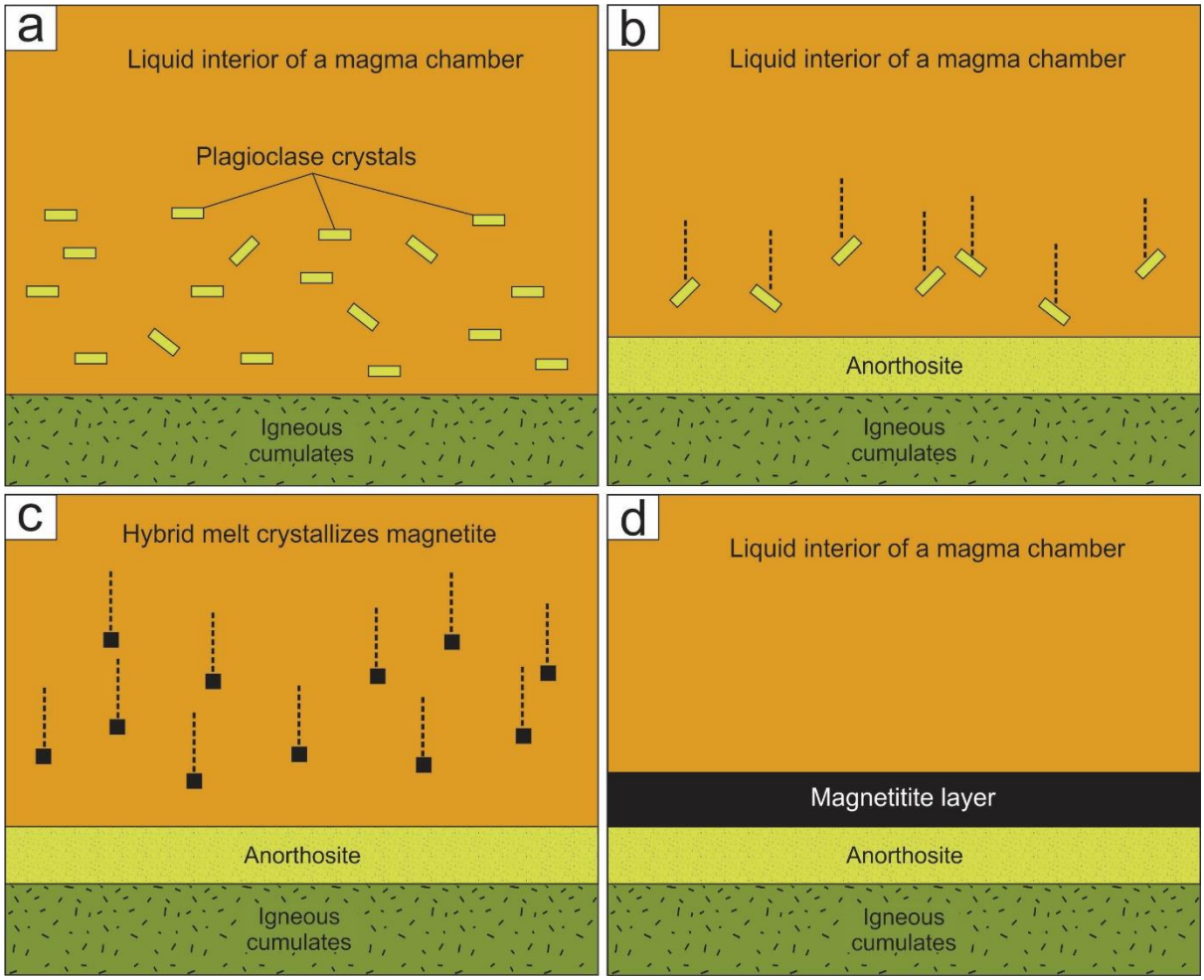

Fig 5.23 Model for the origin of massive magnetitite layers by Yuan et al. (2017). (a) Magmatic recharge occurs with a magma carrying a crystal load of plagioclase that crystallized in a staging chamber at depth. (b) These crystals settle out on the previously formed igneous cumulates to form an anorthosite layer. (c) Mixing between the incoming melt and the resident melt, possibly leading to the saturation of magnetite in the hybrid liquid. (d) As the magnetite crystals settle out, a magnetitite layer forms atop an anorthosite layer.

5.5.12 Pressure reduction during magmatic ascent by Latypov et al. (2018)

This model was proposed to explain the origin of stratiform chromitite deposits in layered intrusions (Latypov *et al*. 2018). The idea requires a staging chamber at great depth (for example at the Moho) that fractionates silicates, pushing the magma towards chromite saturation. Shortly before (or during) the crystallization of chromite in the staging chamber, a pulse of magma is released upwards that rises adiabatically, causing it to become superheated before it intrudes into a shallow level magma reservior (e.g. the Bushveld chamber). The reduction in pressure associated with magmatic ascent causes the phase boundaries to shift in such a manner that the magma ends up within the stability field of chromite. All that is now required is for the superheated magma to undergo some degree of cooling that results in the crystallization of a layer of pure chromitite. The model has also been proposed to be applicable to the crystallization of monomineralic magnetitite layers (Figure 5.24) (Latypov *et al*., 2018; Kruger and Latypov, 2020a), although proper modelling has yet to be performed to test its applicability to massive magnetitite.

Unlike most other models, this model may have the potential to explain Cr reversals associated with magnetitite layers (Figure 5.8). Because it involves the intrusion of a superheated magma, this idea can be a powerful tool to understand some field characteristics of Bushveld magnetitite, as explained later.

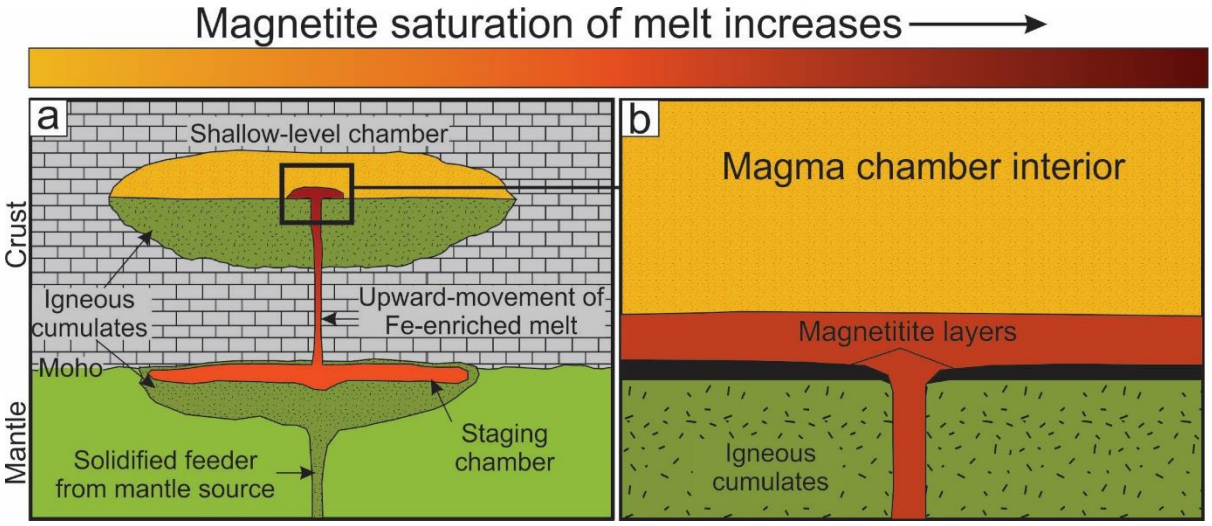

Figure 5.24 Model for the origin of massive magnetitite layers by Latypov et al. (2018). (a) Fractional crystallization in a deep staging chamber forces the melt towards magnetite saturation. A pulse of magma is then released upwards, and the drop in pressure during magmatic ascent shifts the phase boundaries in such a way that the melt finds itself within the field of magnetite upon entry into the chamber. (b) As the melt enters the chamber, it forms a basal flow that crystallizes only magnetite upon cooling.

5.5.13 Magnetite accumulation by flotation on bubbles by Knipping et al. (2019)

Knipping *et al*. (2019) made an interesting proposition to explain why dense magnetite crystals may be found atop lense dense cumulates such as plagioclase where, considering a regime where crystals accumulate by crystal settling, the most dense phases are expected to accumulate first on the floor of the magma chamber. The potential solution of this problem was proposed to involve the exsolution of fluids during magmatic decompression. Because there is a tendency for the fluid to nucleate on surfaces of oxides (such as magnetite or chromite), their settling rates will dramatically decrease because of the relatively low density of the fluid (Figure 5.25). This model is perhaps too simple to explain the accumulation of magnetitite layers in the Bushveld however, as it does not account for the absence of pyroxene in the cumulate assemblage surrounding, for example, the bottom seam of the MML. As with all models that deal with crystal settling, it is difficult to explain the very sharp contacts between magnetitite and anorthosite layers (Figure 5.2), as well as the dramatic lateral variations in Cr along the bases of the layers.

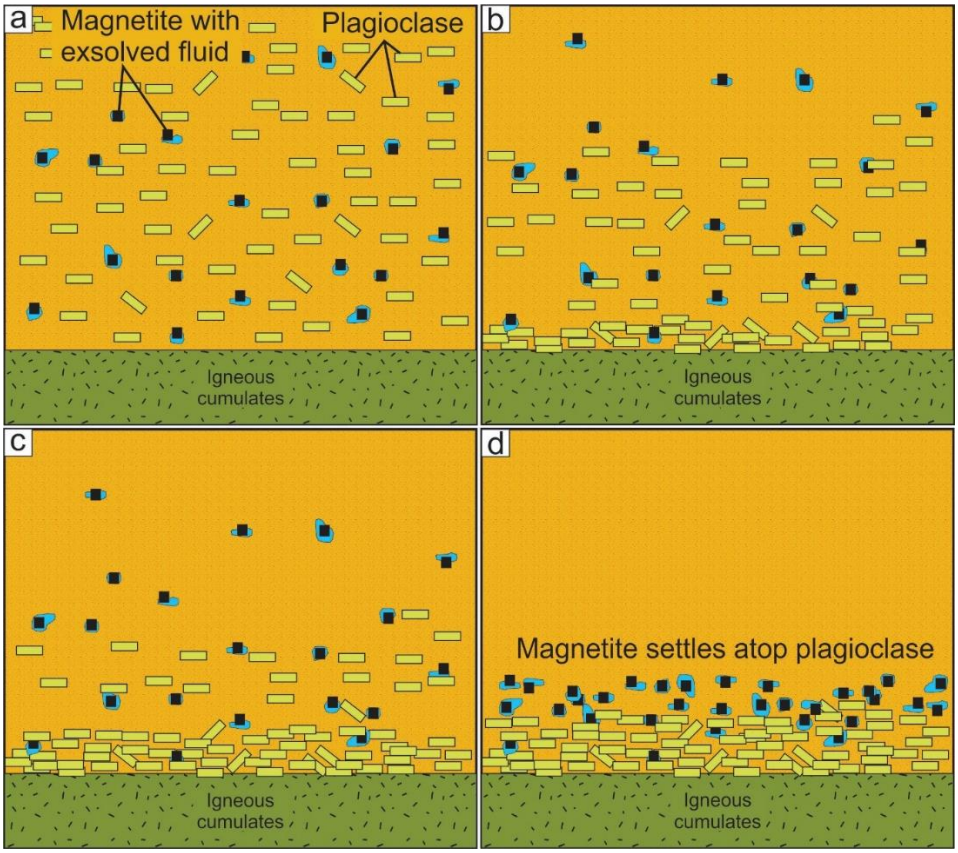

Figure 5.25 Model for the origin of magnetitite atop anorthosite by Knipping et al. (2019). (a) Fluids that are exsolved from magmatic systems tend to nucleate on magnetite crystals. (b) and (c) This causes the magnetite to sink more slowly towards the chamber floor compared to typically lense dense plagioclase crystals. (d) This may cause a suspension of plagioclase and magnetite crystals to settle out to form an anorthosite layer overlain by magnetitite.

5.5.14 Liquid immiscibility of Vukmanovic et al. 2019

While most studies that attempt to resolve the petrogenesis of massive magnetitite mainly focusses on the geochemistry of these layers, Vukmanovic *et al*. (2019) relied largely on textural evidence to seek out clues for their origin. During their study, they noticed a difference in the appearance of isolated grains of plagioclase compared to those that are clustered together in magnetitite layers. Whilst the latter would show signs of recrystallization, the former shows very little signs of deformation. This led them to the conlcusion that magnetitite layers had to form in a liquid-rich environment containing a small crystal load of magnetite and plagioclase. In this enviroment, isolated plagioclase crystals could move around freely, while clustering of plagioclase crystals would inhibit free movement, causing jamming and lattice distortions. The liquid was deemed to be the Fe-rich conjugate of an unmixed magma, possibly like those observed in experimental studies (e.g. Philpotts, 1967) or as fluid inclusions (Fischer *et al*., 2016). Deposition of magnetite crystals carried by this liquid on the chamber floor would be responsible for the formation of the magnetitite layer (Figure 5.26). Cawthorn and Ashwal (2009) previously made the argument against the liquid immiscibility hypothesis for the origin of Bushveld magnetitite that a dense, Fe-rich liquid should percolate into the underlying mush if such a process has occurred. The latter is generally not observed with the contact between anorthosite and magnetitite generally being sharp. Following the work of Holness *et al*. (2017a), Vukmanovic *et al*. (2019) countered this argument by suggesting that the underlying anorthositic mush were only a couple of centimetres thick, restricting the depth to which the Fe-rich melt could percolate in between the underlying cumulates. The presence of symplectites partially replacing plagioclase grains were presented as evidence for the existence of an immiscible Fe-rich liquid.

From a geochemical perspective, liquid immiscibility is more sensible to explain the origin of the uppermost magnetitite/nelsonite layers of the Bushveld Complex due to their high P_2O_5 contents (Reynolds, 1985a; 1985b; Harney and Von Greunewaldt, 1995). This is because P is observed to strongly partitioned into the Fe-rich conjugate of the immiscible liquid in experimental studies (Philpotts, 1967). Magnetitite layers from the lowermost portion of the Bushveld Complex contains only very low concentrations of P (Cawthorn and Ashwal, 2009; data from this study). Cawthorn and Ashwal (2009) further argued against the liquid immiscibility hypothesis by stating that experimental melts typically contain very low concentrations of Ti, while even the lowermost Bushveld magnetitite layers are rich in Ti (>10 wt. %). As with many of the models outlined above, a liquid immiscibility model may also face

a challenge in the Cr reversals recorded in magnetitite layers. If liquid immiscibility was indeed responsible for the formation of massive magnetitite layers, Cr should also strongly partition into the Fe-rich liquid of the conjugate. Veksler *et al*. (2006) performed experiments to study the paritioning behaviour of numerous trace elements during liquid immiscibility. The element with the highest partition coefficient in their experiments were Zn with a value of 3.59. At its base, the MML contains up to 56 times more Cr than cumulus magnetite crystals above or below it. Unforunately, Cr was not used in Veksler *et al*.,'s experiments, and further experimental work is needed to test if Cr would partition so strongly into the Fe-rich conjugate before the hypothesis can be accepted. At present it appears unlikely that such a process is responsible for the formation of Bushveld magnetitite. The delicate chemical patterns observed at the base of the MML (Cawthorn, 1994; Figure 5.12) is also not compatible with random deposition of thousands of magnetite crystals from a crystal slurry.

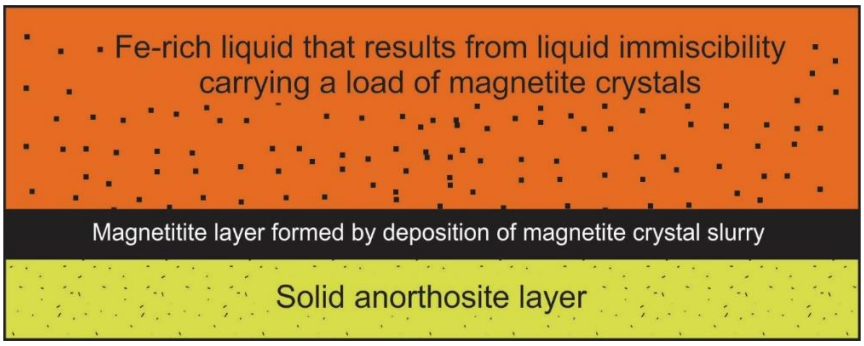

Figure 5.26 Model for the origin of massive magnetitite from Vuknamovic et al. (2019). A Fe-rich liquid that results from liquid immiscibility carries a load of magnetite crystals that are deposited on the chamber floor to produce a massive magnetitite layer.

5.6 Formation of massive magnetitite layers

Based on the results in this paper and work published before, any model that deals with the origin of massive magnetitite needs to be able to explain their curious field relationships (such as depressions in the chamber floor, interconnected frameworks of plagioclase crystals, and inclusions of anorthositic and gabbroic inclusions), the large Cr reversals associated with magnetitite layers such as the MML, the extreme lateral variability of Cr along the chamber floor, the regular depletion of Cr upwards in the MML and Bottom seam, while also having some explanatory power for the existence for their anorthositic footwalls. All the models presented above singularly fail in some or another way to simultaneously explain all these observations. In the next section, we attempt to construct a single model that can explain all these observations by combining and adding to the ideas from the models outlined above.

5.6.1 In situ crystallization versus crystal settling/sorting

The extremely regular depletion of Cr upwards detected by Cawthorn and McCarthy (1980; 1981) was presented as strong evidence for the *in situ* crystallization of magnetite. Our findings here (Figure 5.11) perfectly matches the results from these authors, providing additional support for the *in situ* crystallization of magnetite. This was later supported by the discovery of growth nodes as predicted by Cawthorn (1994), once again supported by our findings here (Figure 5.12). Such growth nodes were also detected during our recent two-dimensional geochemical mapping of the MML in the same locality (Kruger and Latypov, 2020a) and from the Bottom seam in the Western Limb (Kruger and Latypov, 2020b). These geochemical maps also provided additional support for the *in situ* crystallization of magnetitite, such as magnetite crystals nucleating and growing directly on subvertical footwall contacts with the underlying anorthosite. We thus strongly favour the *in situ* crystallization of massive magnetite, and exclude all models that attempt to explain the origin of this rock type from the Bushveld Complex by any process that involves movement or transport of crystals (Scoon and Mitchell, 2012; Maier *et al*., 2013; Bilenker *et al*., 2017; Yuan *et al*., 2017; Knipping *et al*., 2019; Vukmanovic *et al*., 2019).

5.6.2 Possible origins for the Cr reversal associated with massive magnetitite

The origin of Cr reversals associated with magnetite now deserve attention and, as explained above, have proven effective to potentially disprove many other models that deal with the formation of massive magnetitite. Models that remain are those that allow some mechanism that can explain the Cr reversal, such as magma mixing due to the collapse of melt layers within a stratified magma chamber (Harney and Von Greunewaldt, 1995; Tegner *et al*., 2006) or by magmatic recharge prior to the formation of the magnetitite. An attempt will now be made to differentiate between the two processes based on the available data.

Kruger and Smart (1987) studied the chemical evolution of magnetite considering crystallization in a double-diffusive convective system (e.g. Huppert and Turner, 1981; Huppert and Sparks, 1984; Tegner *et al*., 2006). In their model, magnetite is crystallizing *in situ* from the bottom of the lowermost layer in the magma chamber, rapidly depleting that layer in Cr. The depletion in Cr is partly balanced by the diffusion of Cr from the overlying layer downwards, causing the upper layers to become progressively depleted in Cr. Occasionally, as the density of the lowermost layer decreases due to the extraction of magnetite, convective overturn occurs and a Cr reversal is recorded within the layer, a mechanism similar to what

was proposed by Jackson (1961) for the origin of cyclic units in the Stillwater intrusion. This process should have the effect that subequent magnetitite layers contain less Cr than the very first magnetitite layer that formed. This is, however, clearly not the case, as the MML typically has a comparable or higher Cr concentration compared to that of the Bottom seam (Figure 5.8 and 10). It seems more likely at present that the relative Cr-rich magma responsible for the MML's formation came from an outside source.

Another potential clue to the puzzle is the Cr reversal presistently recorded near the top of the MML from both Rhovan (Figure 5.9c) and Vametco (Figure 5.11e and f). In previous studies, some Cr reversals within the MML were shown to be of very limited lateral extent (Cawthorn and McCarthy, 1980), and were explianed by Cr-undepleted convective eddies descending downwards from the chamber's liquid interior (McCarthy and Cawthorn, 1983). However, this particular reversal appears to be continuous over a lateral extent of at least 30 km. It may be unlikely that the above processes can produce a reversal over such a large area in the magma chamber. Alternatively, such a reversal can originate by magmatic recharge as a basal flow of incoming melt can spread quickly across large areas of the chamber's floor (Huppert and Sparks, 1980; Huppert *et al*., 1982). While the geochemistry appears to indicate that magmatic recharge occurred to produce Cr reversals associated with magnetitite layers, attention is now turned to the field relationships for additional clues.

5.6.3 Origin of magnetitite footwall depressions and anorthositic inclusions

In Figure 5.4 and the paper by Butcher and Merkle (1991), it was shown that magnetitite layers may contain depressions of various sizes in their footwalls. These depressions may be similar to large, semi-circular depressions called potholes observed in the footwall of the famous Merensky Reef (e.g. Carr *et al*., 1999; Latypov *et al*., 2016; Latypov *et al*., 2019a) and chromitite layers (e.g. Lomberg *et al*., 1999; Latypov *et al*., 2017a) of the Bushveld Complex. Although the depressions so far identified in the footwall of Bushveld magnetitites are not quite of the same magnitude (Merensky Reef potholes may be up to 200 m wide), models considered for their origin may also be applied to magnetitite.

One of the earlier ideas for pothole formation associated with the Merensky Reef comes from Schmidt (1952). Schmidt (1952) considered destruction of the footwall by physical erosion whereby magma currents carrying a crystal load would physically dig out the footwall before depostion of the Merensky Reef. However, geochemical evidence strongly suggest the *in situ* crystallization of magnetite. If Schmidt's (1952) model were true, this observation begs the

question of what happened to the crystals that served as the eroding agent since only massive magnetitite crystallized on the chamber floor. It also seems unlikely that the delicate and intricate structures preserved in the footwall contact (Figure 5.4a) would survive the onslaught of a crystal slurry. An interconnected framework of plagioclase crystals (Figure 5.4b) would surely also fail to remain in tact if such a process did occur. Furthermore, magnetite also appears to penetrate in between grain boundaries of the underlying anorthosite (Figure 5.7c). Such an erosional feature that is of a much finer scale than the crystals themselves cannot be produced by this process.

Maier *et al*. (2013; 2016) proposed a different model compared to the one above where, instead of scouring, cumulates are forcefully injected into the footwall during subsidence of the chamber as mentioned earlier. The same objection to this model provided previously applies here: the intricate distribution of Cr in massive magnetitite (Cawthorn and McCarthy, 1980; Cawthorn, 1994; Kruger and Latypov, 2020; Figure 5.11 and 12) cannot be produced by the random sorting of millions of magnetite grains.

Remaining models include the those from Ballhaus (1988) that considers the upward migration of hydrothermal fluids from below, preventing the deposition of plagioclase crystals in certain areas; the model from Boudreau (1992) that involves an explosion caused by excessive fluid pressure build-up from below, leading to plagioclase resporption; the extensional model of Carr *et al*. (1999), where Merensky Reef cumulates are deposited in pull-apart structures. All the above models may have some explanatory power for the depressions observed in the footwalls of magnetitite layers. However, these models have no place for the anorthositic inclusions trapped within these layers. There remains one model that can simultaneously provide an elegant explanation to all the above features.

The origin of anorthositic inclusions in massive magnetitite have received very little attention in the literature. One exception is Scoon and Mitchell (2012) who referred to these inclusions are “resobred xenoliths” that formed after magma addition, but no further information is given. Similar inclusions have, however, been observed in other rock types of the Bushveld Complex, such as the Merensky Reef and notably the UG1 chromitite layer. Models derived from field oberservations on these layers can be directly applied to magnetitite layers. However, since Cr in magnetite is such a powerful tracer of magmatic differentiation, these models can finally be tested geochemically in magnetitite to great effect. For example, consider one of the most simple explanations for the origin of such inclusions, namely, that they are transported

fragments of anorthosite that were deposited on and captured by the advancing magnetitite solidification front. If that is the case, the Cr concentration should proceed smoothly through the inclusions (Figure 5.27a to d)). The same chemical pattern will apply to the eruption model of Nex (2004) or the depositional model by Cawthorn (2003; 2015) as applied to chromitite layers. Such a geochemical pattern is apparently observed in one of the drill cores analyzed (Figure 5.11a) but none of the others. Any model that may attempt to explain the origin of such inclusions by crystal mushes (e.g. Voordouw *et al*., 2009; Maier *et al*., 2013) are discredited based on the evidence for the *in situ* crystallization of massive magnetitite.

When studying the UG1 chromitite, Pebane and Latypov (2017) proposed an idea that involves alternating pulses of magma entering the chamber that are in turn either saturated in plagioclase or chromite. For example, a first pulse of magma may crystallize a layer of chromite, while a second pulse of magma would crystallize a layer of anorthosite on top of the chromite. When a third pulse of magma enters the chamber, it thermochemically erodes the previously deposited layer of anorthosite, leaving only fragments of it behind (Figure 5.27e-g). If we apply this model to magnetitite, we should expect to see large Cr reversals at the levels that define the bases of the anorthositic inclusions (Figure 5.27h). However, this is not observed in any of the profiles analyzed (Figure 5.11). Instead, we either see no reversal (Figure 5.11a) or a gradual reversal underneath the inclusions (Figure 5.11c, and d).

Since the above models cannot explain all the Cr profiles that are observed in the vicinity of anorthositic inclusions, another model is clearly needed. The gradual reversals underneath the inclusions does resemble another chemical feature that are sometimes observed in igneous intrusions called a “Sandwich Horizon”. Perhaps the most famous example of a Sandwich Horizon comes from the Skaergaard intrusion in Greenland (e.g. McBirney, 1995). Here, the propagation of the solidification front from the floor upwards and from the roof downwards results in a layer where the two fronts meet that bears the most evolved rocks within the intrusion. If the same principle is applied to the gradual reversal in magnetitite, it becomes clear that magnetite had to grow on the bottom contact of the inclusion downwards as well as from the floor upwards. When the two solidification fronts meet, a chemical structure results that resembles a mini Sandwich Horizon, bearing a lower Cr concentration that the adjacent magnetite. The structure is, of course, not a true Sandwich Horizon as it does not contain abundant trapped liquid. However, the implication of this observation is that the inclusions were already present in their current positions prior to the crystallization of the magnetite.

While the inclusions may appear isolated in two-dimensional field outcrtops, it is significant to note that some of these inclusions appear to be connected to the floor in some outcrops (Figure 5.5e and f). In our recent work (Kruger and Latypov, 2020b) we proposed that these inclusions form a three-dimensional network of interconnected anorthositic fragments. The formation of such a framework can be explained by thermochemical erosion; a process where superheated magma that is in chemical dissequilibrium with the cumulates below causes partial destruction of the footwall (Campbell, 1986; Scoon and Mitchell, 2012; Latypov *et al*., 2016; Latypov, 2017; Pebane and Latypov, 2017). Field observations reveal that anorthosite underlying massive magnetitite tends to fracture to produce elongated, rectangular blocks. If thermochemical erosion advances along these planes of weakness, "inclusions" may form that appear to be isolated in two-dimensions. This process has previously been termed "magmatic karsification" (Kruger and Latypov, 2020b), as it produces a topography that resembles karst environments (Waele *et al*., 2011). As erosion progresses deeper into the footwall cumulates, upper anorthosite fragments will grow smaller until they are completely consumed by the magma. When erosion finally comes to a halt, larger fragments will generally be concentrated near the bottom, while smaller inclusions will be present higher upwards. When the originally superheated melt finally starts crystallizing, a protective layer of magnetite will cover the floor of the intrusion, preventing any further magmatic erosion.

The above model applies well to the chemical profiles observed in Figure 5.12c and d. However, if the above were true, then why are not all inclusions associated with a gradual "reversal" (Figure 5.11a) and instead produce a chemical pattern that seems more compatible with Model 1 (Figure 5.27a-d)? The most likely answer lies in the exact propagation pattern of the magnetitite's solidification front. If there is a growth node underneath an inclusion, the solidification front growing from the bottom upwards may intercept the inclusion before magnetite had a chance to start growing on its outer surface (Figure 5.28). This topic is explored in more detail below in the section titled "Controls on the magnetitite solidification front propagation pattern**."**

Thermochemical erosion (i.e. magmatic karsification) can also be applied to explain depressions in the footwall (Figure 5.4) or fine-scale erosion along grain boundaries. In some cases it may even leave a framework of interconnected silicates behind (Figure 5.4b) or produce other fine-scale intricacies in the footwall contact (Figure 5.4a). None of the other models proposed so far have the same explanatory power for all the different features we observe.

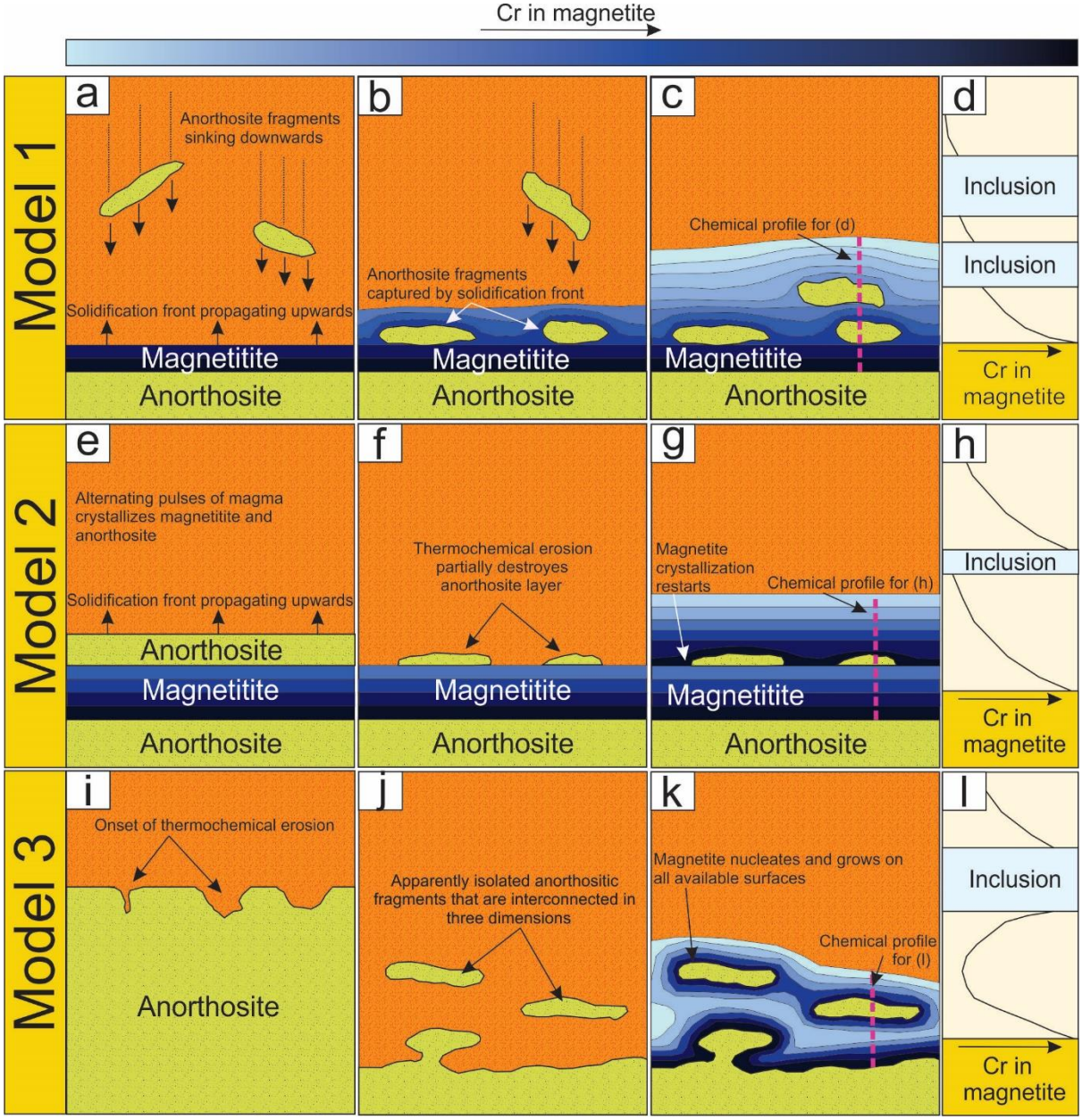

Figure 5.27 Potential models to explain the origin of anorthosite inclusions in massive magnetitite. (a) In the first model, anorthosite fragments are transported from a different source and are deposited on and (b and c) captured by the advancing magnetitite solidification front. (d) In such a model no reversals are recorded at the level of the inclusions. (e) In the second model, a layer of magnetitite crystallizes from a magnetite saturated melt, followed by the intrusion of a plagioclase-saturated melt, producing a layer of anorthosite on the pre-existing magnetitite layer. (f) Another pulse of magnetite-saturated melt enters the chamber which causes thermochemical erosion of the previously deposited anorthosite layer. (g) Magnetite crystallization then resumes, and the anorthosite fragments are completely encapsulated by magnetite. (h) Because the second layer of magnetitite crystallizes from a fresh batch of magma, a reversal can be expected at the level of the anorthositic inclusions. (i) In the third model, a layer of anorthosite is thermochemically eroded by a superheated magma. (j) As thermochemical erosion proceeds along fractures and planes of weakness, a three-dimensional framework of interconnected anorthositic fragments are left behind, apparently disconnected in two dimensions. (k) In this model, a gradual Cr reversal will be documented beneath anorthositic inclusions as the solidification front grows from the floor upwards and from the inclusion downwards.

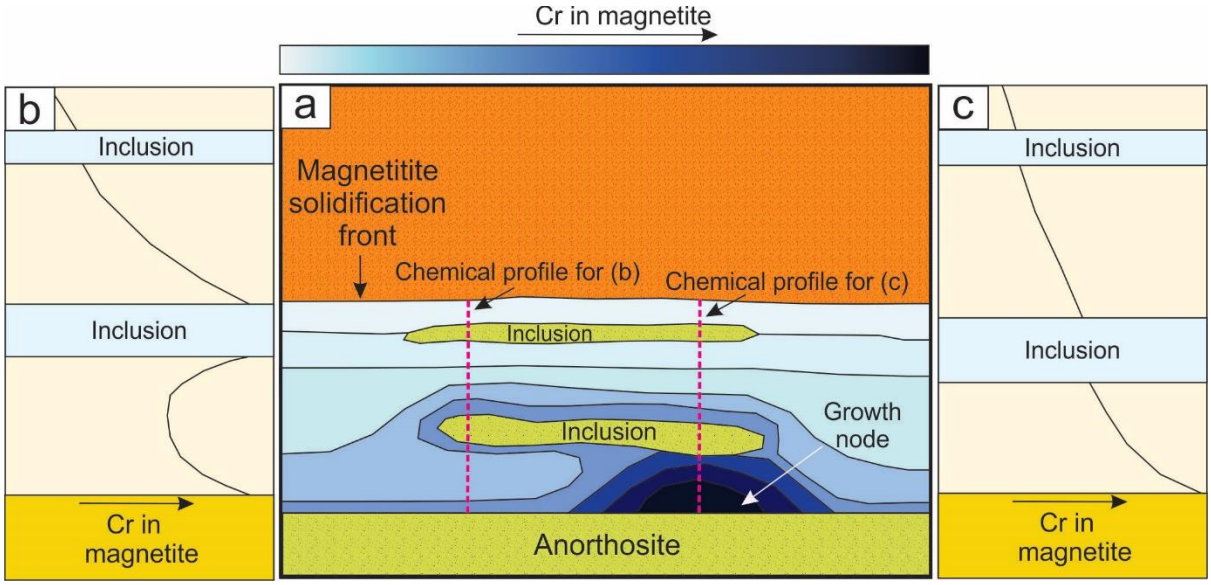

Figure 5.28 The origin of diverse one-dimensional Cr profiles across a magnetitite layer with inclusions. (a) Theoretical distribution of Cr within a magnetitite layer that grew in the presence of anorthosite inclusions. A dome-shaped growth node is present underneath one of the inclusions. (b) Appearance of the Cr distribution in a one dimensional profile. Here, a gradual "reversal" is observed underneath an as two solidification fronts meet; one growing from the floor upwards and the other from the inclusion downwards. No reversal is associated with the upper inclusion because it is intercepted by the solidification front before nucleation starts on its outer surface. This is attributed to the high temperature of the inclusion suspended higher up in the magma column. (b) Where a growth node is present underneath an inclusion on the floor, no gradual "reversal" may be observed.

The inference that thermochemical erosion occurred prior to the crystallization of magnetitite is significant to understand the processes that led up to the formation of this enigmatic rock type. What is especially important is that the melt must be superheated for thermochemical erosion to occur. If this is not the case, the melt will immediately crystallize magnetite on the footwall, forming a protective layer and preventing any significant thermochemical erosion. It is not clear how such a superheated melt can be produced in a closed system. An internal process that may favour the crystallization of magnetite (such as magma mixing due to the breakdown of strafied melt layers) will likely cause the magma to become supercooled with respect to the liquidus as the melt moves from a cotectic into the field of magnetite. However, an effective way to obtain a superheated melt is the near-adiabitic rise of magma from a deep-seated staging chamber (Latypov *et al.*, 2018). Such a superheated melt may be capable of destroying several dozens of metres of cumulates on the chamber floor prior to its crystallization (Latypov *et al.*, 2020). We would thus argue that both the nature of the footwall contact and the Cr reversals associated with magnetitite may be easily explained by the addition of new magma into the chamber. However, as mentioned before, several other investigators that have worked on the Upper Zone have argued that this section of the Bushveld Complex differentiated as a closed system. This issue is addressed next.

5.6.4 Upper Zone of the Bushveld Complex: open or closed system?

Evidence for a closed system is primarily based on the variation of Sr-isotopes throughout the uppermost portion of the Bushveld Complex. Within the Main Zone of the intrusion, there lies a thin layer of pyroxenite that has been identified in both the Western and Eastern Limbs, called the Pyroxenite Marker (Cawthorn, 1991). Across a couple of hundreds of meters beneath the Pyroxenite Marker there is a gradual upward increase in the mg# and plagioclase An-content, as well as a gradual decrease in the initial Sr^{87}/Sr^{86} isotope ratios (Sr_0) (Cawthorn, 1991). This gradual variation in these values have been interpreted as a magma mixing event. Above the Pyroxenite Marker, the S_0 remains more or less constant (Figure 5.29), with all values plotting within error of a proposed parental magma with an S_0 ratio of 0.7073 ± 1 (Kruger *et al*., 1987; Kruger, 1994). It was concluded that no further magma addition occurred after the formation of the Pyroxenite Marker, and that the entire, approximately 2 km-thick Upper Zone was emplaced as a single pulse of magma. Because this magma is a hybrid between the liquid remaining after the formation of the Main Zone and the new pulse of magma responsible for the mixing event, any addition of magma should cause a deviation in the Sr_0 values. This prompted Kruger's (2005, page 16) statement that magnetitite layers "appear to be strictly internally generated".

Despite these findings, there are several lines of evidence (in addition to those presented by our new data here) to suggest that magma addition may have occurred in the Upper Zone of the Bushveld Complex, some of which are associated with massive magnetitite layers. For example, differentiation cycles were identified with magnetitite layers at their bases in terms of pentlandite and olivine chemistry, with Ni being more abundant at the base of these cycles (Merkle and Von Greunewaldt, 1986). Tanner (2014) also found a reversal in the Cr-content of pyroxenes at the base of the Upper Zone, and suggested that further magma addition occurred here. In their in-depth study of the Bellevue drill core located in the Bushveld's Northen Limb, Ashwal *et al*. (2005) identified numerous reversals in mineral chemistry in the Upper Zone that they ascribed to magmatic recharge. As mentioned above, different chondrite-normalized PGE patterns were also identified above and below the 2 metre-thick MML, as well as differing Sr/Al ratios in plagioclase (Harney and Von Gruenewaldt, 1995). Yuan et al. (2017) found An-reversals in anorthosite layers below magnetitite layers and suggested that magma addition was responsible for both the formation of the underlying anorthosite and the magnetitite itself.

Yuan *et al*. (2017) stated that the Sr-isotopic data may not necessarily preclude addition of magma into the chamber if new pulses of magma has an identical Sr-isotopic character (i.e. they are sourced from the same staging chamber). An issue with this suggestion is that there must have been a significant amount of liquid present in the magma chamber prior to the magma recharge event that formed the Pyroxenite Marker. This is based on the fact that cumulates of plagioclase and pyroxene have not evolved all the way to their low-temperature end-members (Cawthorn, 2015). In fact, the resident melt column present prior to magmatic recharge has been estimated by VanTongeren and Mathez (2013) to be about 2000 to 2380 metres thick while the total sum of the incoming melt amounts to about 1200 metres. Mixing must therefore have occurred between the resident and incoming melt (Cawthorn *et al*., 1991) and, since the hybrid liquid would have a unique isotopic composition, any further injection of magma will cause a deviation from the hybrid liquid's Sr-isotopic ratios. Unless the Main Zone formed by the injection of crystal slurries (e.g. Roelofse and Ashwal, 2012) with very little liquid present, Yuan *et al*.'s (2017) suggestion appears invalid. This is likely the case, as work by Holness *et al*. (2017a) seems to preclude the existence of crystal mushes in the Bushveld Complex that are more than a few metres thick.

On close inspection on the isotopic data (Figure 5.29), it is, however, clear that two samples (one from Kruger *et al*., 1987 and another from Cawthorn, 1991) was collected within a cluster of magnetitite layers close to the base of the Upper Zone. Both these samples show an increase in the initial Sr-isotopic ratios that is statistically significant compared to the samples taken directly from above and below. This is also true of one sample collected by Tegner *et al*. (2006) from a different cluster of magnetitite layers that also show a significant deviation in the Sr-isotopic character from their adjacent samples. This could possibly indicate that magma addition occurred within these zones to produce magnetitite layers. A more detailed isotopic study across zones that bear clusters of magnetitite layers can shed some light on this question.

Another obstacle for the magma addition hypothesis for the origin of massive magnetitite is the absence of significant An reversals associated with these layers. When comparing plagioclase chemistry from hangingwall and footwall lithologies of massive magnetitite, Cawthorn and Ashwal (2009) were only able to detect An reversals across four magnetitite layers in the Northern Limb that ranged from 2 to 6% An in size, while one layer recorded a 2% lower An content it its hangingwall. They stated that the remaining 15 magnetitite layers showed no statistically significant difference in the An contents of their footwalls and hangingwalls and that "magma addtion is not likely to be the common mechanism for layer

formation". The problem may be that An contents of plagioclase is not sensitive enough to record magmatic recharge events, while Cr with its extremely large crystal/liquid partition coefficient in magnetite is. Suppose that the Upper Zone is occasionally recharged from the

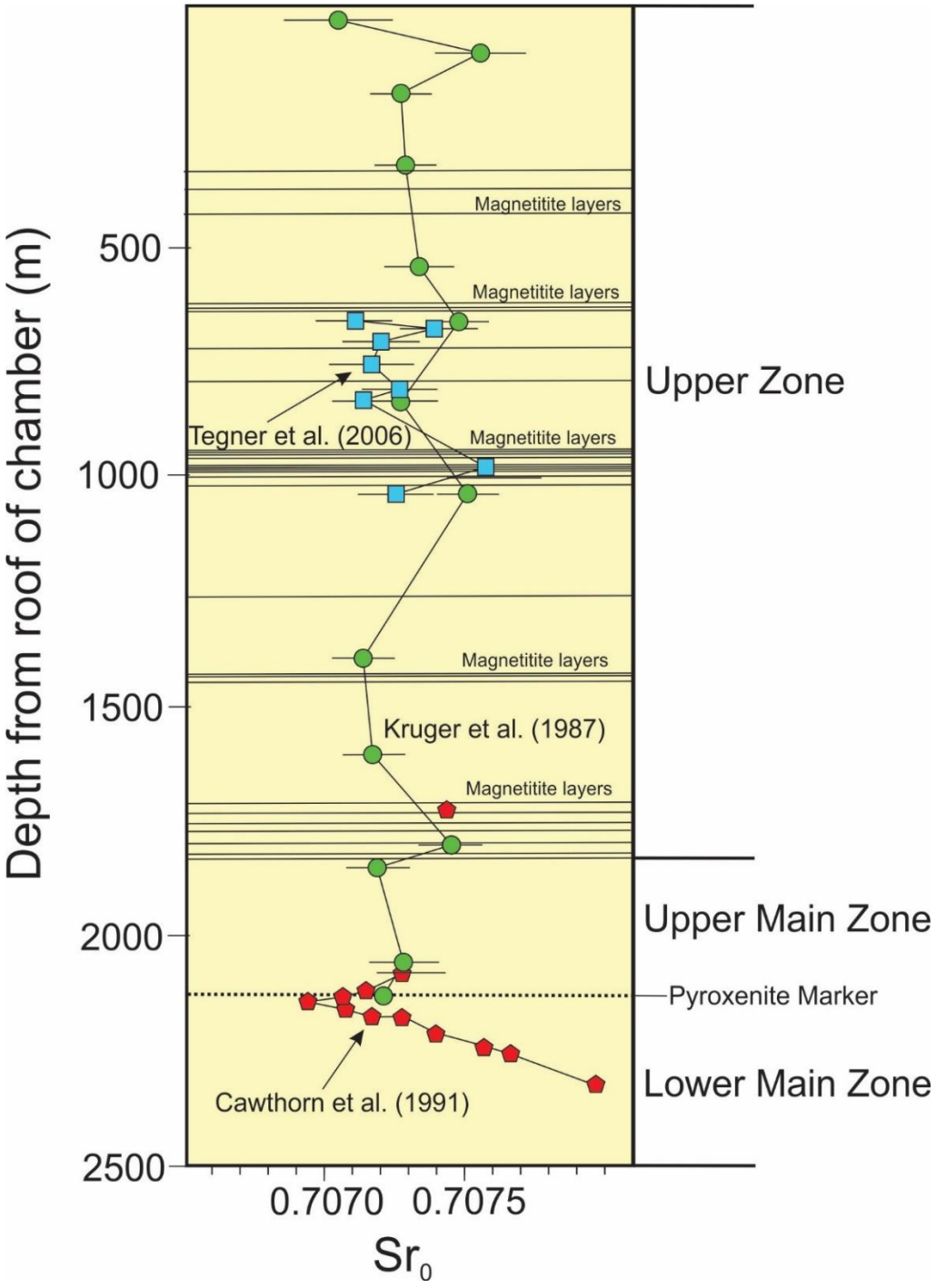

Figure 5.29 Compilation of strontium isotopic data across a section of the Lower Main Zone, Upper Main Zone, and the Upper Zone from the Western Bushveld Complex (modified from Tegner et al., 2006). Notice how one sample from Kruger et al. (1987) shown a higher Sr_0 were present within the lower cluster of magnetitite layers. The same is true for one sample colleted by Tegner et al. (2006) in a cluster of magnetitite layers towards the centre of the Upper Zone.

same source that is also responsible for the reversal leading up to the Pyroxenite Marker. If an injection of melt from this source crystallizes magnetite in the Bushveld Chamber, Cr will be rapidly depleted, while An contents will change at a much slower rate. If magmatic recharge occurs, it will be much easier to detect a reversal by studying the variations in Cr in magnetite than An in plagioclase. As explained later, we also consider that footwall anorthosites crystallize from the same magma source that eventually crystallizes massive magnetitite. Little variation can therefore be expected in the An contents between the immediate footwall and hangingwall of magnetitite layers.

5.6.5 Origin of a magnetite-alone saturated melt

Based on the above analysis and the work by previous investigators, we argue that magmatic recharge occurred prior to the crystallization of massive magnetitite, causing thermochemical erosion of the footwall and a Cr reversal. Upon cooling magnetite crystallized *in situ*, forming a nearly pure layer of massive magnetitite. The latter implies that the melt must have been saturated in magnetite alone for this to occur. How to produce such a melt is a question that sits at the heart of the problem to solve the petrogenesis of massive magnetitite layers. It appears unlikely that such a melt becomes saturated in magnetite alone due to a pressure increase, variations in fO_2 within the chamber, liquid immiscibility, or magma mixing, as explained above. At this stage a pressure decrease associated with magmatic ascent (Latypov *et al*. 2018) (Figure 5.24) from some staging chamber is the only viable way to produce such a melt. Recent geophysical evidence for the existence of a staging chamber has recently been documented by Cole (2018). It appears to be located at the base of the Moho and is about 10 km thick. By combining Latypov *et al*.'s (2018) model with that of Scoon and Mitchell's (2012) (Figure 5.21), we can argue that a deep-seated staging chamber fractionates mainly silicates due to a low fO_2 of the melt. When a pulse of magma is released upwards from the staging chamber and traverses the crust, the resulting drop in pressure may favour the crystallization of magnetite once the magma enter the Bushveld magma chamber. In addition, the melt may also assimilate some crustal material during its ascent, raising its fO_2 contents. The model is somewhat similar to that proposed by Irvine (1975) for the origin of massive magnetitite with the excpetion that crustal contamination occurs en-route to the chamber and not within the chamber itself. This process ensures that the Upper Zone of the Bushveld as a whole crystallizes with a higher fO_2 content compared to the staging chamber. The model therefore does not require disseminated magnetite to be enriched in V as other that typically envoke an increase in fO_2 within the chamber as they both form from the same fO_2 enriched melt (Irvine, 1975;

Klemm *et al*. 1985). The superheated melt initially crystallizes only magnetite, while plagioclase is the first phase to join magnetite on the liquidus, possibly because the pressure reduction associated with magmatic ascent will delay the crystallization of mafic minerals. Only with further differentiation does pyroxene joins plagioclase and magnetite as a crystallizing phase to produce a magnetite gabbro/norite/gabbronorite. While this is our preferred model at present, it is essential that this model be tested further using proper phase diagrams in the future.

5.7 Magmatic differentiation during magnetitite crystallization

Now that the processes that led up to the formation of massive magnetitite layer has been discussed, focus shifts to how magmatic differentiation occurs during the crystallization of this rock type. Interest in the topic was sparked by the extremely rapid but regular depletion of Cr upwards in the MML as detected by Cawthorn and McCarthy (1980). It was abundantly clear that fractional crystallizationg models were not compatible if the magnetitite was crystallizing from the entirety of the Upper Zones's 1.5 km-thick column of magma. A diffusive controlled model was proposed with magnetite crystallizing in a relatively stagnant layer of melt at the bottom of the chamber. However, it was quickly realized that diffusion alone is a too slow process to account for the depletion in Cr, as the depletion in Cr is much too fast when modelling diffusion alone (Cawthorn and McCarthy, 1980; Wright *et al*., 1983). Secondary convection cells were thus proposed that occasionally intrude the more stagnant layer at the chamber floor to aid the supply of Cr to the crystallizing magnetite (Cawthorn and McCarthy, 1981; McCarthy and Cawthorn, 1983).

A couple of years after the work cited above, theoretical work was performed to demostrate the concept of the convection of thin compositional boundary layers around *in situ* growing crystals in mafic magma chambers (Martin *et al*., 1987). These boundary layers would form due to diffusion of material towards the growing crystal that, in the case of mafic minerals, would have a lower density that the surrounding melt. Once the boundary layer reaches some critical density and thickness, it will convectively break away from the growing crystal, possibly as a constant stream of melt or as a series of plumes (Figure 5.30). Using olivine crystallizing in the Great Dyke of Zimbabwe, it was calculated that convection of a thin boundary layer would occur shortly after the start of crystallization when the boundary layer was no more than 3.5 mm thick (Campbell, 1996). Later, the convection of such a thin boundary layer was observed experimentally with olivine crystallizing in a tank of synthetic magma

(Seedhouse and Donaldson, 1996). This process would cause vigorous compositional convection in the basal parts of magma chambers, and suggests that the model originally proposed by Cawthorn and McCarthy (1980) may not be physically realistic. Recently we have proposed that the compositional convection of thin boundary layers are responsible for driving magmatic evolution during magnetitite fractionation (Kruger and Latypov, 2020). We expand on our findings here to provide additional support for the existence of such boundary layers.

By comparing the geochemistry of magnetite seperates from massive magnetitite layers and disseminated magnetite from the Bushveld Complex, Klemm *et al*. (1985) found that magnetite from massive ore is significantly richer in MgO, Al_2O_3, and SiO_2 compared to disseminated ore. Klemm *et al*. (1985) attributed this finding to rapid growth of magnetite, where rejected components such as SiO_2 are rapidly enriched. This finding can, however, also be explained by magnetite that share compositional boundary layers with silicates in disseminated ore, where the silicates will tend to consume oxides such as MgO, Al_2O_3 and SiO_2, causing magnetite to be more depleted in these elements. Klemm *et al*. (1985) noted that Cr does not follow the predicted behaviour in light of this model as it is dramatically enriched in massive magnetitite than in the disseminated ore. This observation is easily attributed to the fact that massive magnetitite formed after magma recharge from a melt still rich in Cr while the disseminated ore formed from melt depleted in terms of its Cr content as discussed above.

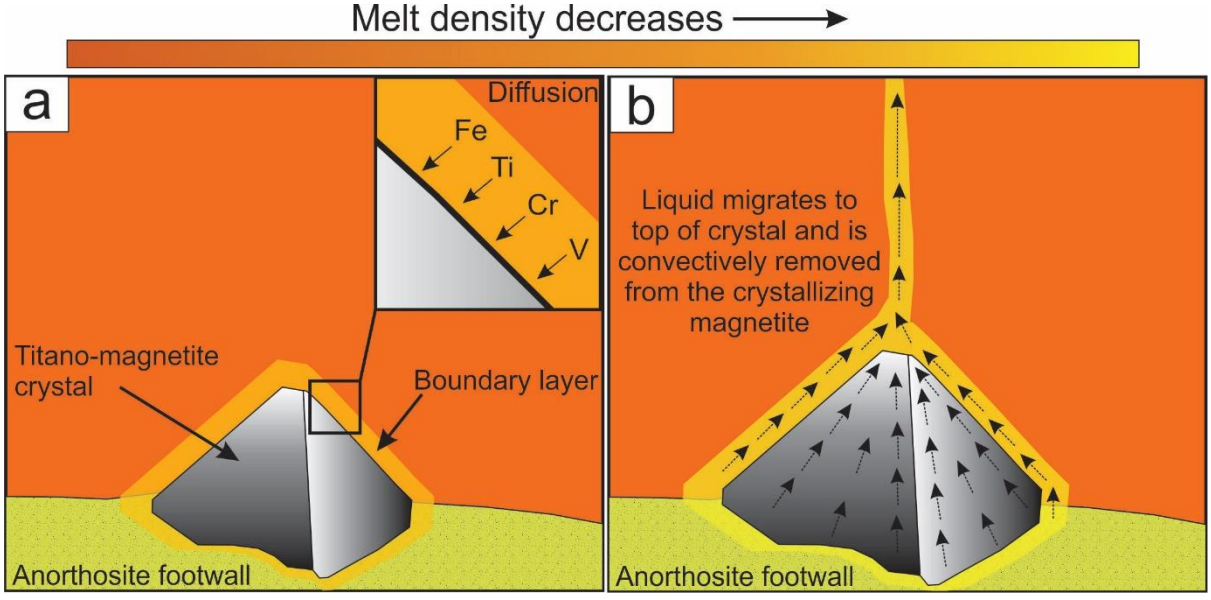

Figure 5.30 Magmatic differentiation during the crystallization of magnetite. (a) During crystallization, the components necessary to construct titano-magnetite diffuse toward the growing crystal. Because of the relatively high nuclear density of these elements, the boundary layer becomes lighter. (b) As crystal growth continues, the boundary layer thickens and decreases in density until it obtains sufficient buoyancy to be released upwards into the overlying melt. Mixing of the rejected liquid from the crystal with the surrounding melt drives magmatic differentiation.

Other lines of evidence come from detailed microprobe analysis of magnetite grains. Butcher and Merkle (1987) noticed that magnetite grains show a lower Al_2O_3 and a higher Cr content when crystallizing adjacent to plagioclase. This may be because plagioclase is consuming Al_2O_3 from a shared boundary layer, causing magnetite to be depleted in this element. Likewise, crystallization of magnetite from a shared boundary layer with plagioclase would mean less competition for the magnetite crystal to incorporate Cr compared to crystallization adjacent another magnetite crystal.

If the above model is true, then it should be theoretically possible for magmatic differentiation to occur in extremely confined spaces due to the very small size of the boundary layer. With this in mind the magnetite vein shown in Figure 5.11a allows to further test this hypothesis. The vein may have formed because of superheated magma penetrating into the inclusion, followed by the crystallization of magnetite when the magma cooled down. It is remarkable to note that the vein posesses a relatively high Cr concentration (5507 ppm). This concentration far exceeds estimates for the liquid Cr contents of the upper zone that range from 100 to 280 (Davies and Cawthorn, 1984; Van Tongeren and Mathez, 2013; Kruger and Latypov 2020a). The latter implies that crystal/liquid fractionation still occurred within the vein. It is not reasonable to assume this occurred via diffusion, as Cr would be far to rapidly depleted in such a small volume of melt. Convective eddies (Cawthorn and McCarthy, 1981; McCarthy and Cawthorn, 1983) from the outside are unlikely to penetrate the vein and will be unable to transport Cr to the growing crystals. Instead, convection had to be produced from within the vein itself by the removal of thin boundary layers around the growing crystals. This would ensure effective liquid exchange with the liquid outside the chamber.

The existence of thin compositional boundary layers that break away convectively from *in situ* growing crystals seem to have great explanatory power for several puzzling features of magnetitite. This is discussed in the next two sections.

5.8 Controls on the magnetitite solidification front propagation pattern

Due to their inaccessability, very little is known about the propagation patterns of solidification fronts in magma chambers and how it may influence our understanding of igneous processes. Luckily, because of the high partition coefficient of Cr into magnetite, it is possible to gain some insights into this largely unexplored aspect of igneous petrology. An understanding of the factors controlling solidification front propagation may be important to better understand

some fundamental aspects of the magma chamber dynamics, such as the mechanisms that drive magmatic evolution and crystallization.

Information on how the solidification front propagates comes mainly from our recent two-dimensional geochemical mapping of magnetitite layers and Figure 5.12 here. As always, crystallization starts with the formation of a single nuclei of magnetite directly on the chamber floor as heterogenous nucleation is far more favourable than homogeneous nucleation (Campbell, 1978; Vernon, 2018). The first nuclei of magnetite will appear where heat loss is most significant, possibly within a depression in the footwall or underneath an inclusion (Kruger and Latypov, 2020b). Because the melt is supercooled relative to the liquidus, rapid growth occurs on the first nucleation point. Growth proceeds radially outwards to produce a dome-like structure that Cawthorn (1994) referred to as a growth node. In some cases, closely-spaced growth nodes may converge to produce the trough and peak pattern in terms of the Cr distribution. However, growth nodes are also commonly seperated by a plateau of fairly constant Cr concentration (Figure 5.12; results from Kruger and Latypov, 2020). This shows that, if growth nodes are spaced sufficiently far apart, radial outwards growth does not persist until very large domes are produced that converge. Instead, it appears as though radial growth is quickly replaced by lateral growth of the magnetite until the entire floor is covered. As Cawthorn (1994) rightly pointed out, a similar growth pattern was observed by Tait and Juapart (1992). Whilst growing crystals in the laboratory, Tait and Juapart (1992) noticed that heterogenous nucleation occurred on various spots on the bottom of the tank. Growth proceeded laterally until the entire floor of the tank was covered. Why, however, does this tendency exist for initial radial outwards growth to be replaced by rapid lateral growth? Other structures in nature, like stromatolites, do seem to grow radially outwards until they converge to produce a planar growth front. Why should this be any different for the crystallization of massive magnetitite?

The existence of compositional boundary layers around magnetitite growth nodes may have great explanatory power in this regard. As the dome-shaped growth node starts to take shape, there may be a tendency for the liquid within the boundary layer to migrate upwards towards the top of the growth node due to its lower density. This process was illustrated by Campbell (1996) for a single crystal and is reproduced here (Figure 5.30). The lighter liquid would tend to collect on top of the growth node until enough liquid accumulates to exceed the critical Rayliegh number for convection. The liquid is then released in a convective fashion upwards. This has the effect that the growth node is not fed with magnetite-building components from

the top, but is prefernatially fed from the sides as fresh liquid is dragged towards the growing crystals (Figure 5.31). New nuclei and crystal growth would thus preferentially occur at the margins of the growth node. This causes the solidification front to grow laterally outwards, quickly covering the floor of the intrusion. Once a planar solidification front has formed growth will proceed vertically.

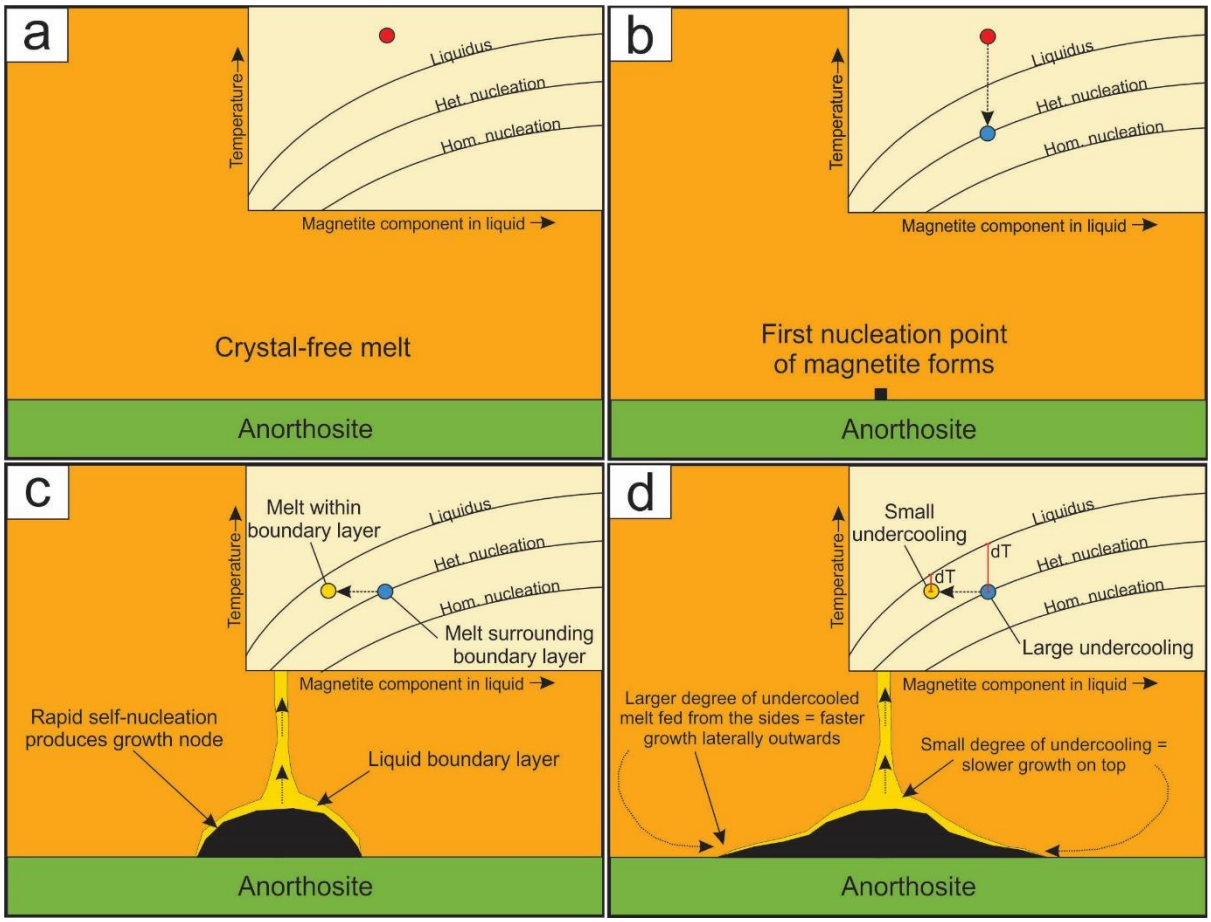

Figure 5.31 The formation of a magnetitite growth node and the transition from intially radial outwards growth to lateral growth. (a) Melt overlying anorthosite at the temporary floor of the magma chamber is initially superheated relative to the magnetite liquidus (inset). (b) Cooling occurs until the magma reaches the required amount of undercooling for heterogeneous nucleation to occur directly on the underlying anorthosite. (c) Once the first nuclei has formed, the magma is supercooled relative to the required amount of undercooling for self-nucleation to occur, assuming the latter process is more favourable than simple heterogeneous nucleation. This causes rapid self-nucleation on the pre-existing magnetite nuclei and growth proceeds radially outwards to produce a dome-shaped growth node. A liquid boundary layer forms around the growth node similar to what is shown in Figure 5.30. (d) Because of its lower density, the liquid within the boundary layer will tend to migrate towards the top of the growth node. Because some magnetite-building components have been extracted from this boundary layer, it has a relatively smaller undercooling than the surrounding melt. Fresh magma is primarily supplied from the sides to the growth node, causing more rapid growth outwards. Growth will proceed until the entire footwall is covered and a planar solidification front results.

The above process will have a strong tendency to erradicate any irregularity in the solidification front as rejected liquid will tend to flow to higher areas. For example, if a depression is present within the solidification front, rejected components will tend to flow upwards along the solid interface of the solidification front and out of the depression. The depression would thus be constantly fed by fresh liquid and growth would preferentially occur within until it is eliminated. The same principle applies to the case where inclusions are present. Rejected liquid components may migrate and accumulate on the upper parts of inclusions, slowing down growth on their tops. Growth will be more favourable in low lying areas until a planar solidification front is produced once more. The latter may explain why we never see a hump in the top of a magnetitite layer directly above inclusions (Figure 5.32) even if growth proceeds *in situ*. The above process may also explain why even very thin magnetitite layers possess planar tops even through growth initially occurs to produce dome-shaped growth nodes.

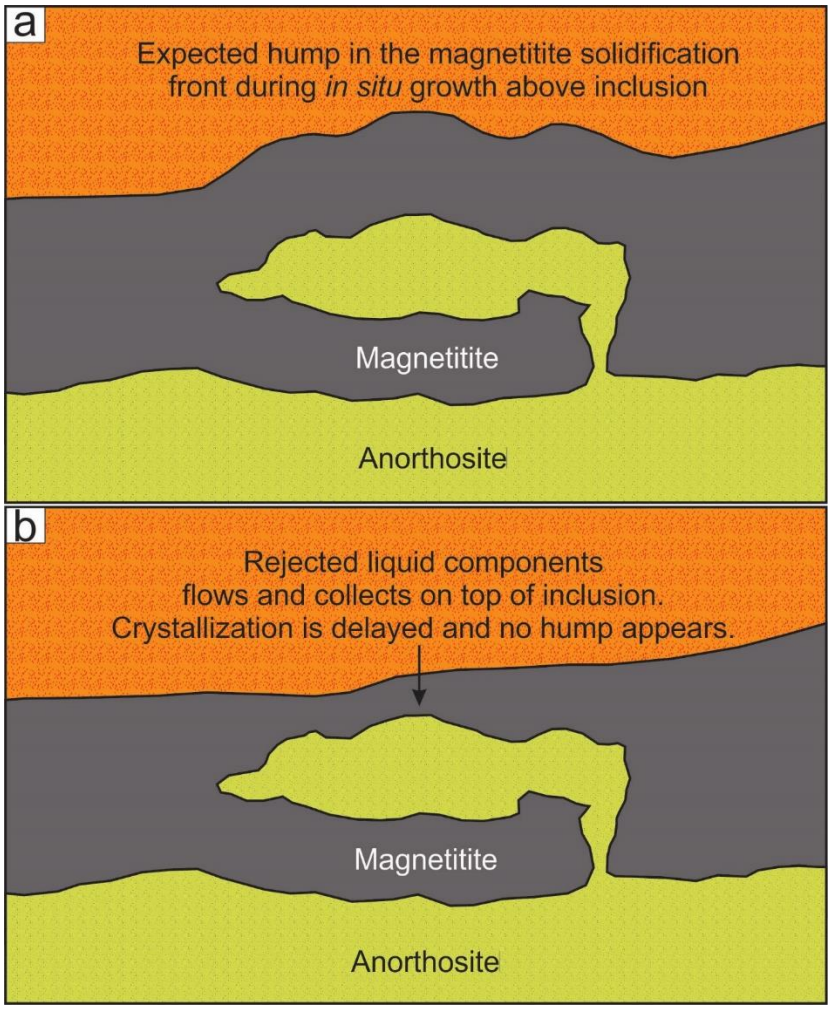

Figure 5.32 Morphology of the solidification front above an inclusion in magnetitite. (a) If *in situ* growth occurs around an inclusion, one may expect a hump to be produced in the upper boundary of a magnetitite layer. (b) In reality, no hump is observed. This may be because low density boundary layers will tend to flow to topographic highs of the solidification front. If they accumulate on top of inclusions, magnetitite growth would be retarded, and the upper contact of the layer appears flat. Section in (b) is based on the outcrop shown in Figure 5.5f.

Another control on the propagation pattern of the solidification front has to do with cooling. In our recent work (Kruger and Latypov, 2020b) we came to the conclusion that heat must be lost through the floor of the magma chamber before the onset of magnetitite crystallization. This is possible because of thermochemical erosion that ensures the melt comes into contact with deeper and cooler cumulates further down. Both the floor and inclusions serve as cooling surfaces for the melt. Heat loss is most sufficient directly through the floor and less so for inclusions located higher up in the profile. The latter is indicated by the lower Cr concentration on inclusions located higher up in the magnetitite layer, meaning that magnetite only starts nucleating on the inclusions after some amount of growth has occurred on the solid footwall, i.e. the inclusions are initially too hot for nucleation to take place on their outer surfaces.

5.9 Origin of gradational upper contact and non-massive portions of magnetitite layers

The above section dealt with the processes that occurred just prior and during the crystallization of massive magnetitite. The next challenging aspect of magnetitite petrogenesis; namely the origin of the gradational contact into the overlying magnetite anorthosite layer, can now be discussed. Nearly all massive magnetitite layers of the Bushveld Complex are characterized by such a gradational contact into overlying magnetite anorthosite. Similar gradational contacts are also observed in magnetitite layers from the Sept Iles layered intrusion in Canada while these layers also have sharp bases (Namur *et al*., 2015). In Bushveld magnetitites, pyroxene is notably absent in this transition above the Bottom seam and the Main Magnetite Layer. Plagioclase grain shapes reveal they are clearly of cumulus status and show some degree of foliation. Any petrogenetic model proposed for the origin of such a layer must be compatible with the above observations.

5.9.1 Previous work

The great challenge with the gradational contact is that its mineral proportions cannot be found on a phase diagram. Theoretically, it is at least possible for a melt to be located within the magnetite or plagioclase field on a phase diagram to crystallize either magnetitite or anorthosite, respectively. The proportions of magnetite and plagioclase that should co-crystallize along cotectics are supposed to be fixed at relatively constant pressures and oxygen fugacities. In the transition from magnetitite to anorthosite, all possible proportions between the two minerals are observed. It is for this reason that such kind of non-cotectic rocks are usually explained by a process involving crystal settling or sorting rather than *in situ* crystallization.

At first the problem may appear simple. Magnetite is more dense that plagioclase and should therefore sink more rapidly from suspension in the magma. When the two minerals accumulate on the floor, a gradational contact is produced that is characterized by a density-inversion upwards. This mechanism has been invoked by Cawthorn and Ashwal (2009) to explain such density inversions in the Bushveld's Upper Zone. However, for this process to be feasible one would need to be able to explain why initial *in situ* crystallization (to produce the massive magnetitite) was replaced by crystal settling. Another significant drawback is that cumulus magnetite grains are generally considered to be extremely small in size. Because crystal size is the most important factor when calculating settling velocities, plagioclase may in reality accumulate much faster than magnetite. In some cases there is also a size gradation across the upper contact of magnetitite layers with plagioclase grains getting progressively larger (Figure 5.33). This observation is also at odds with Stoke's Law as the largest grains are expected to lie at the bottom.

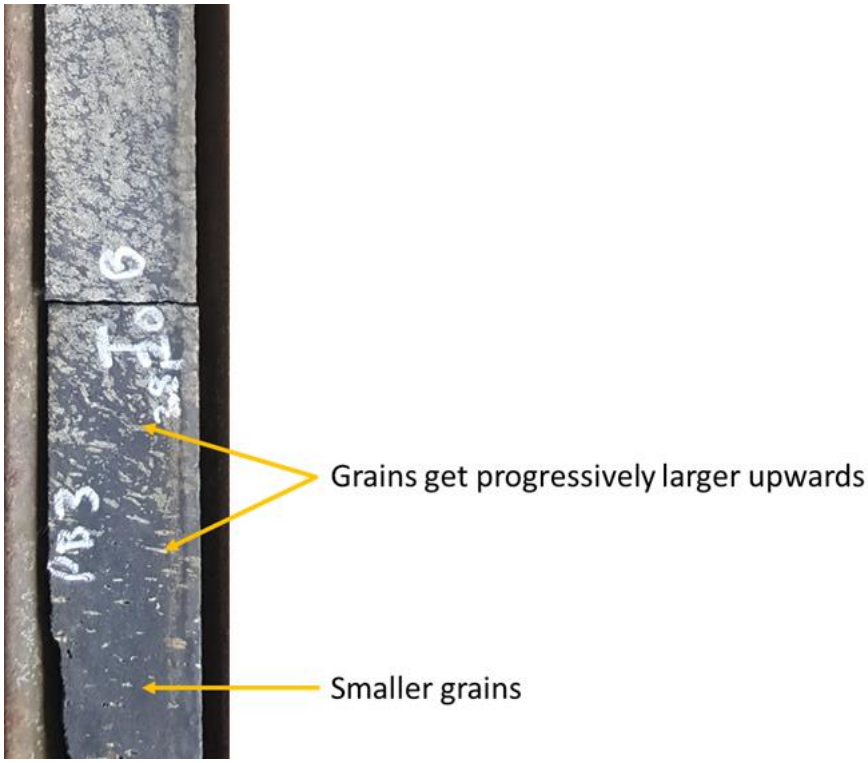

Figure 5.33 Upper gradational contact of the Bottom seam from Rhovan. Notice a general tendency for plagioclase grains to get larger upwards. Drill core measures 4.5 cm across.

Latypov and Chistyakova (2020) came up with a new approach to potentially explain the origin of non-cotectic rocks bearing chromite and plagioclase. Similar to Latypov *et al.*'s (2018) model discussed previously, the process involves a pressure reduction due to magma ascending

from a deeper staging chamber. Contrary to the formation of monomineralic chromitite layers, in Latypov and Chistyakova's (2020) model some crystallization of chromite occurs while the magma is ascending en-route to, say, the Bushveld magma chamber. A certain proportion of these chromite crystals are then deposited on the chamber floor, followed by crystallization of the melt to fill up all the pore spaces. Crystallization within the pore spaces occurs along cotectic proportions but, depending on the amount of chromite that was initially deposited by the incoming magma, rocks may be produced with varying proportions of chromite to plagioclase. If the model is applied to massive magnetitite, it would require that an injection of a magnetite slurry occurred right after the crystallization of just about every magnetitite layer in the complex. At no point would magnetitite be allowed to crystallize until the melt naturally becomes saturated in another mineral phase (such as plagioclase). In addition, no Cr reversal has been detected in the overlying magnetite anorthosite of either the Bottom seam or the MML. Instead, one dimensional curves of the Cr content in magnetite generally seems to pass smoothly into the overlying rock type (Figure 5.8c and d). The upper gradational contact of massive magnetitite is probably a natural consequence of the processes that occur within the chamber without external input.

Another alternative explanation could be that plagioclase crystals may co-crystallize with magnetite at the solidification front but, because of the relative lower density of plagioclase, the crystals may float upwards, potentially forming the overlying anorthosite layer. There are two issues associated with this hypothesis, however. Crystallization of plagioclase along with magnetite would significantly slow down the rate of both Cr and V depletion. Because Cr has a much higher D value in magnetite than V, the effect is more pronounced for Cr, causing the behaviour of the two trace elements to become more similar. This makes is impossible to produce the rapid depletion of Cr compared to V as documented by Kruger and Latypov (2020a) in Chapter 2 of this thesis. Secondly, nucleation of plagioclase at the solidification front is much more likely to occur heterogeneously than homogeneously as the former is kinetically favourable. Nuclei of plagioclase would therefore be stuck to magnetite crystals. It is for the same reason that crystals can grow on the sides or roof of a container from solution without sinking to the bottom.

5.9.2 Geochemical constraints on the formation of non-cotectic cumulates

An important clue to resolve this petrologic enigma may come from a source that has so far been neglected in this study: the incompatible element contents of rocks from the Rhovan drill

core. Whole-rock incompatible element contents are controlled by two factors; the crystal/liquid partition coefficients of the primocrysts that are present and the amount of liquid that becomes trapped within the rock as it crystallizes (Bédard, 1994; Cawthorn, 1996b; Cawthorn, 2013). If the first of these factors solely controls the distribution of incompatible trace elements (i.e. the amount of trapped liquid is kept constant) we can expect a linear curve when plotting the concentration of incompatible elements against the ratio of magnetite to plagioclase. A potential incompatible trace element to use would be Ce. Reported D values for Ce in magnetite are extremely variable. For example, D'Orazio *et al*., (1998) reports on a D value of 0.005 in hawaiite but can be as high as 4.3 in mafic rocks (Schock, 1979). Massive magnetitite layers analysed in this study are extremely poor in Ce (as low as 0.12 ppm). Based on data and literature from VanTongeren and Mathez (2013) the liquid that intruded to form the Bushveld's Upper Zone probably contained between 14 and 52 ppm Ce, resulting in a partition coefficient in magnetite of the Bushveld Complex between 0.002 and 0.008. These values encapsulates the D value reported by D'Ozario *et al*., (1998). For Ce in plagioclase the D value is typically around 0.1 (Bedard, 2006). The typically lowest concentration of Ce in anorthosite samples collected for my thesis is approximately 3.0 ppm. This would imply a liquid composition of about 30 ppm Ce, well within reported values in the literature (VanTongeren and Mathez, 2013). It therefore seems that Ce is much more compatible in plagioclase than magnetite and a linear enrichment trend can thus be expected as the abundance of plagioclase over magnetite (Figure 5.34a).

If crystal settling (or potentially floating) predominates, we can expect the initial porosity of the rock to contribute mostly to the incompatible element contents as it will also detemine the amount of trapped liquid present. In sedimentary petrology, it is common knowledge that sorting determines the porosity of the rock in question. Primocrysts of magnetite and plagioclase differ greatly in terms of their grain sizes and, if a rock contains only one of these minerals, sorting will be at its greatest. In this case the rock should contain more trapped liquid. This results in a parabolic curve when plotting Ce contents against the magnetite to plagioclase ratio (Figure 5.34b).

To understand what type of curve we may expect for *in situ* crystallization, it is essential to consider how crystal-liquid fractionation will take place for both magnetite and plagioclase. As explained above, for magnetite this process occurs by the convective removal of a thin boundary layer of melt surrounding the crystals (Figure 5.30). In the case of plagioclase, the liquid components required to construct plagioclase crystals are less dense compared to the

melt. It is generally assumed that for plagioclase crystals that grow *in situ*, crystal liquid seperation can only occur by diffusion (Morse, 1986b). Because convection is much faster than diffusion, it is expected that interstitial liquid would be much more effectively removed during the crystallization of magnetite than for plagioclase. As the modal abundance of plagioclase increases at the solidification front, the longer it takes for a boundary layer to reach the required density to break away convectively. This would also allow more time for the enrichment of incompatible elements within the boundary layer and the crystals would also record a higher incompatible element abundance. Along with the added effect that Ce is more compatible in plagioclase, the concentration of Ce would thus be expected to increase exponentially as the plagioclase contents increase (Figure 5.34c).

When plotting a selection of rocks that contain only primocrystic magnetite and plagioclase from the Rhovan drill core, the *in situ* crystallization curve best matches what is observed in reality. As the plagioclase content increases, the whole-rock Ce content increases exponentially. This shows that the mineralogy has a direct effect on the trace element abundance in the rock that cannot be explained by just crystal/liquid partition coefficients. If the above explanation holds true, this serves as evidence that non-cotectic cumulates are indeed being produced by *in situ* crystallization. A similar curve results when plotting any other incompatible element. More examples are given in Figure 5.35.

Additional evidence in support of the above comes from the variation in Cr across the Bottom seam from Vametco (Figure 5.36). Within one example of the Bottom seam intercepted by drill core occurs a section that contains well-formed plagioclase primocrysts. The depletion of Cr upwards across this section generally follows a very regular pattern. This very regular depletion upwards is much more likely produced by *in situ* crystallization than from a more random process such as crystal settling (e.g. Cawthorn and McCarthy, 1980).

5.9.3 Field constraints on the formation of the gradational upper contact

Support for the above inference coming from the geochemical data may be found within the field relations that show various fragments of a magnetitite layer scattered in the overlying anorthosite (Figure 5.6). Similar fragments of chromitite have been observed in the UG1 chromitite from the Dwarsriver locatlity (Pebane and Latypov, 2017). In the latter case, chromite fragments appear to have undergone brittle deformation and fragmentation, and are scattered in the surrounding plagioclase-chromite cumulates (chromite-bearing anorthosite). After deformation, large orthopyroxene oikocrysts crystallized across both the chromite-

bearing anorthosite and the chromitite fragments. This suggests that the chromite-bearing anorthosite surrounding the chromitite was still in a partially liquid state while the chromitite layer itself was rigid when the deformation occurred (Pebane and Latypov, 2017). The same model involving brittle deformation in a crystal mush can be applied to the magnetitite fragments.

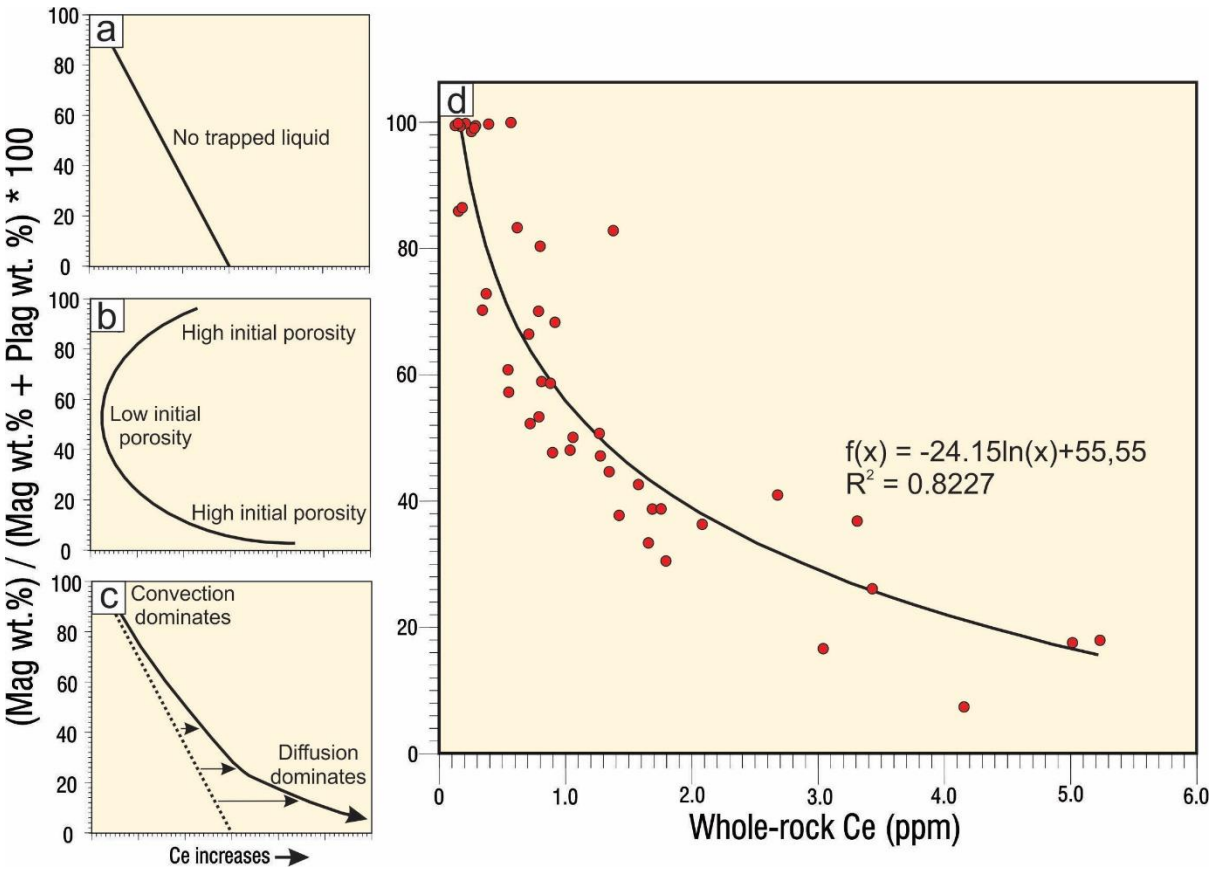

Figure 5.34 Variations in whole-rock Ce contents depending on the magnetite content of rocks containing only plagioclase and titano-magnetite primocrysts. (a) Theoretical varitation in Ce if its distribution of only affected by crystal-liquid partition coefficients. Because Ce is more compatible in plagioclase than in magnetite, its concentration increases linearly as the plagioclase contents increase. (b) Theoretical distribution of Ce if its concentration depends upon the initial porosity of the rock. If a rock contains only plagioclase or magnetite, intitial porosity is at its highest due to the greater sorting. (c) Theoretical distribution of Ce if magnetite and plagioclase co-crystallize within a solidification front. As the abundance of plagioclase increases, the effectiveness of compositional convection diminishes, and the Ce concentration increases. (d) True distribution of whole-rock Ce for selected samples from the Rhovan drill core than contain only primocrystic magnetite and plagioclase. A trendline that produces the closest fit to the data best matches the theoretical curve shown in (c).

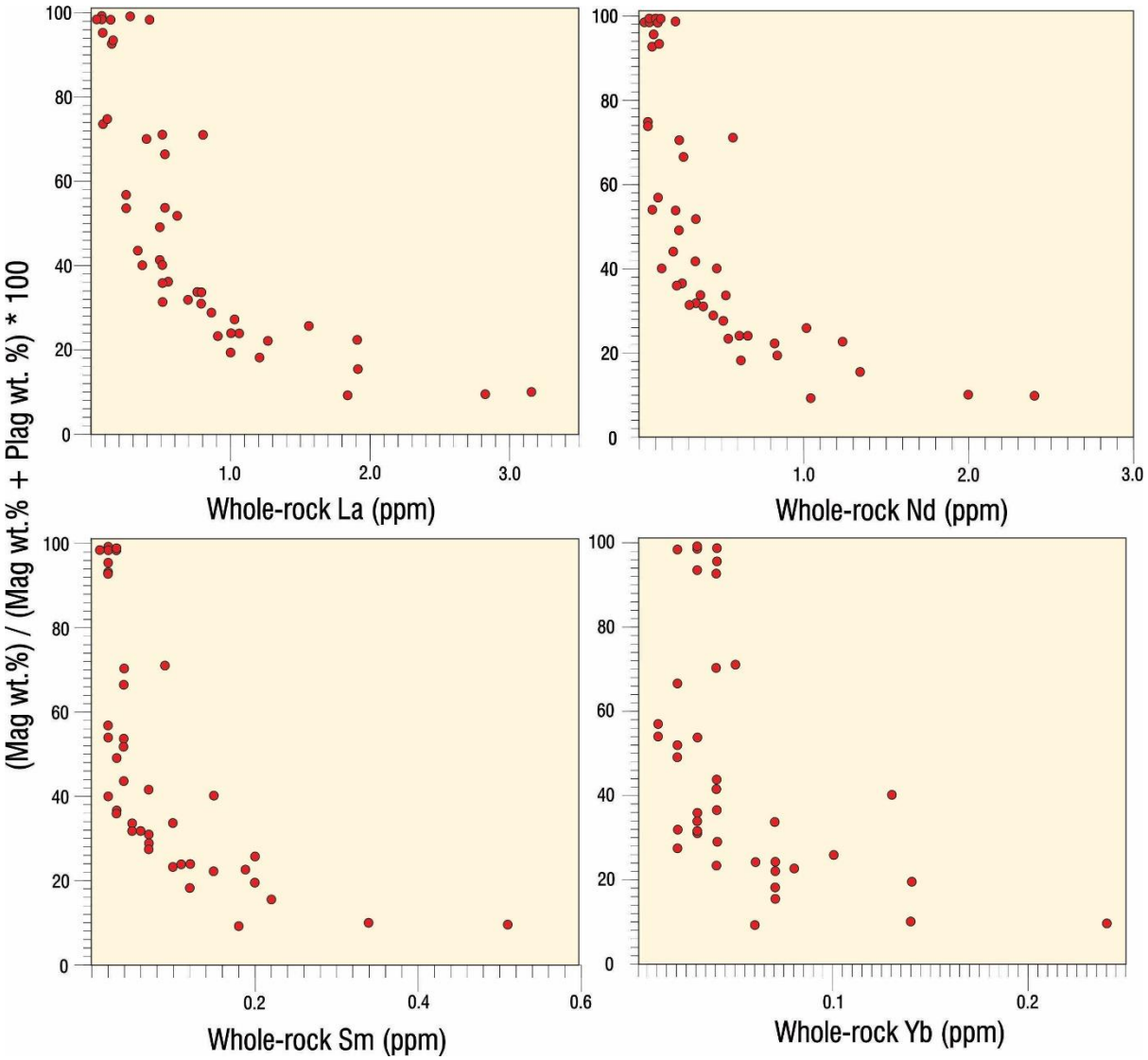

Figure 5.35 Variations in selected whole-rock incompatible element contents depending on the magnetite content of rocks containing only plagioclase and titano-magnetite primocrysts.

Previously we have argued that the solidification front of a massive magnetitite layer propagates as a completely solid surface (Kruger and Latypov, 2020a). This conclusion would explain why massive magnetitite deformed brittlely in the surrounding crystal mush. Since the upper gradational contact is still attached to the massive magnetitite, this may suggest that it was also relatively rigid prior to deformation. It therefore appears as though there is a transition from a completely (or near) solid solidification front that includes both the massive magnetitite and the upper gradational contact to a situation where the solidification front advances as a crystal mush. Why such a transition occurs is explained next.

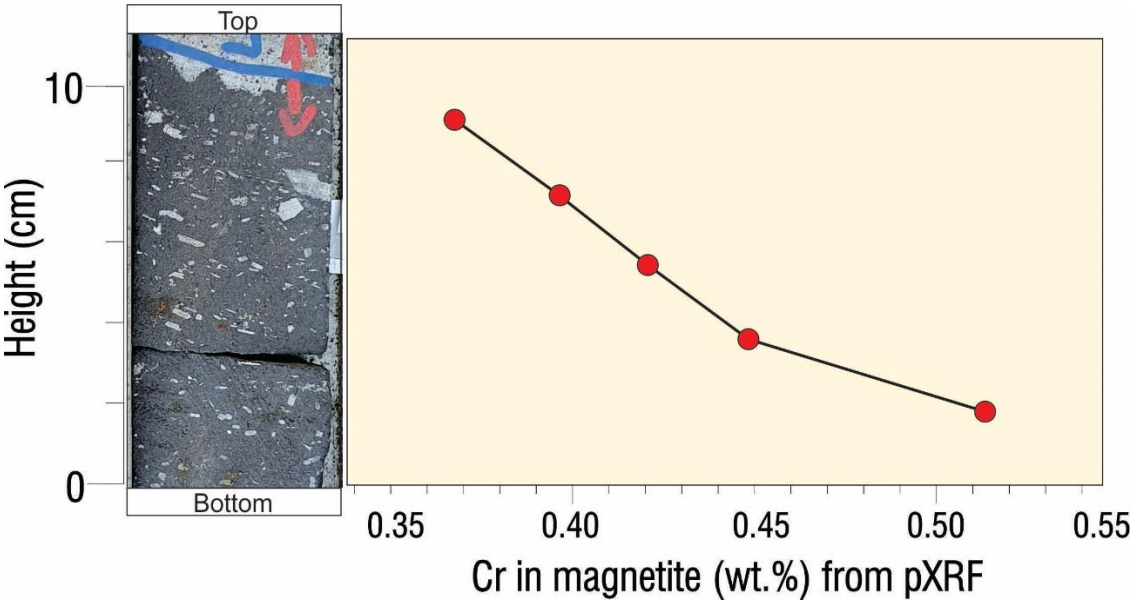

Figure 5.36 Detailed look at the variation in Cr in magnetite across a portion of the Bottom seam from Vametco containing non-cotectic proportions of primocrysts of plagioclase and magnetite. Such a regular depletion of Cr over very short distances has been previously interpreted as indicating the in situ crystallization of the rock (e.g. Cawthorn and McCarthy, 1980).

First, it is important to bear in mind that for *in situ* crystallization to occur, the basal melt layer needs to undergo a certain amount of undercooling before nuclei can form on the chamber floor (Martin *et al*., 1987; Campbell, 1996; Latypov *et al*., 2020). Once nucleation does occur, growth can proceed quickly, as the melt surrounding the magnetite nuclei is thermally located below the liquidus. As the magnetite crystallizes, melt within the boundary layer is forced towards the liquidus in temperature-compositional space (Figure 5.21). Tait and Juapart (1996) argued that, if the components necessary to construct the crystallizing phases are supplied at a sufficiently rapid rate, crystallization can occur isothermally, which allows for the production of a pure adcumulate. Here we expand on this idea by examining what exactly happens within the liquid boundary layer (Figure 5.37) to produce an adcumulate of pure magnetite.

If the boundary layer surrounding the crystal acquires sufficient buoyancy to be released from the crystallizing magnetite crystal before it reaches the liquidus, growth can continue without any cooling being necessary. This is because the resident melt is also cooled below the liquidus temperature, and the crystal is constantly kept in contact with melt that is ready to crystallize. The process ensures near-perfect adcumulus growth of the magnetitite, and the solidification front advances as an essentially completely solid surface (Figure 5.37a). When plagioclase finally joins the crystallizing assemblage, the above picture changes. Since plagioclase will extract components from the liquid phase that is less dense than the melt itself to build its

crystal structure, plagioclase will work against magnetite and effectively delay the convective removal of the boundary layer (Figure 5.37b). If the boundary layer reaches the liquidus before it can break away convectively, the melt surrounding the crystals can only further crystallize if some heat is removed from the solidification front. Across the gradational upper contact of magnetitite layers, plagioclase eventually reaches a certain modal abundance where new nuclei may start forming atop the solidification front before the underlying crystal mush has completely solidified (Figure 5.37c). This is because the resident melt is still supercooled relative to the liquidus and, as fresh melt comes into contact with the solidification front at the bottom of the chamber, new crystals may be deposited there before the underlying mush has solidified (Latypov *et al*. 2020). The process ensures that both the magnetitite and overlying gradational contact is at least sufficiently solid to remain in-tact during deformation while the overlying magnetite anorthosite is in a partially mushy state.

This model requires that the upper gradational contact is produced *in situ* with magnetite and plagioclase co-crystallizing. Together with the geochemical evidence presented above, the *in situ* production of non-cotectic cumulates may appear to fly in the face of decades of experimental work involving mineral phase equilibria. In the next section, we examine why the crystallization of abundant magnetite within a rock may cause a deviation from the generally expected features that we usually observe when a new phase joins the liquidus in a basaltic magma chamber.

5.9.4 Model for the formation of the upper gradational contact

As layered intrusions crystallize towards the interior of a magma chamber, the arrival of a new mineral phase on the liquidus can generally be identified in numerous stages. First, the mineral appears interstitially between previously formed cumulates, decorating their grain boundaries (Latypov *et al*., 2020). With continued crystallization the mineral appears as euhedral primocrysts that are initially produced in overabundance relative to the expected cotectic proportions (Morse, 1979; Namur *et al*., 2010; Latypov *et al*., 2020). Eventually the cumulus assemblage returns to the expected cotectic proportions. In the case of plagioclase joining magnetite as a crystallizing phase atop massive magnetitite, the behaviour is very different. Plagioclase immediately appears as a primocryst and not as an interstitial phase and an initial underproduction of plagioclase is observed instead of an overproduction. Thereafter the modal abundance of plagioclase steadily increases until cotectic proportions are reached in the overlying magnetite anorthosite. To understand why this occurs it is once again essential to

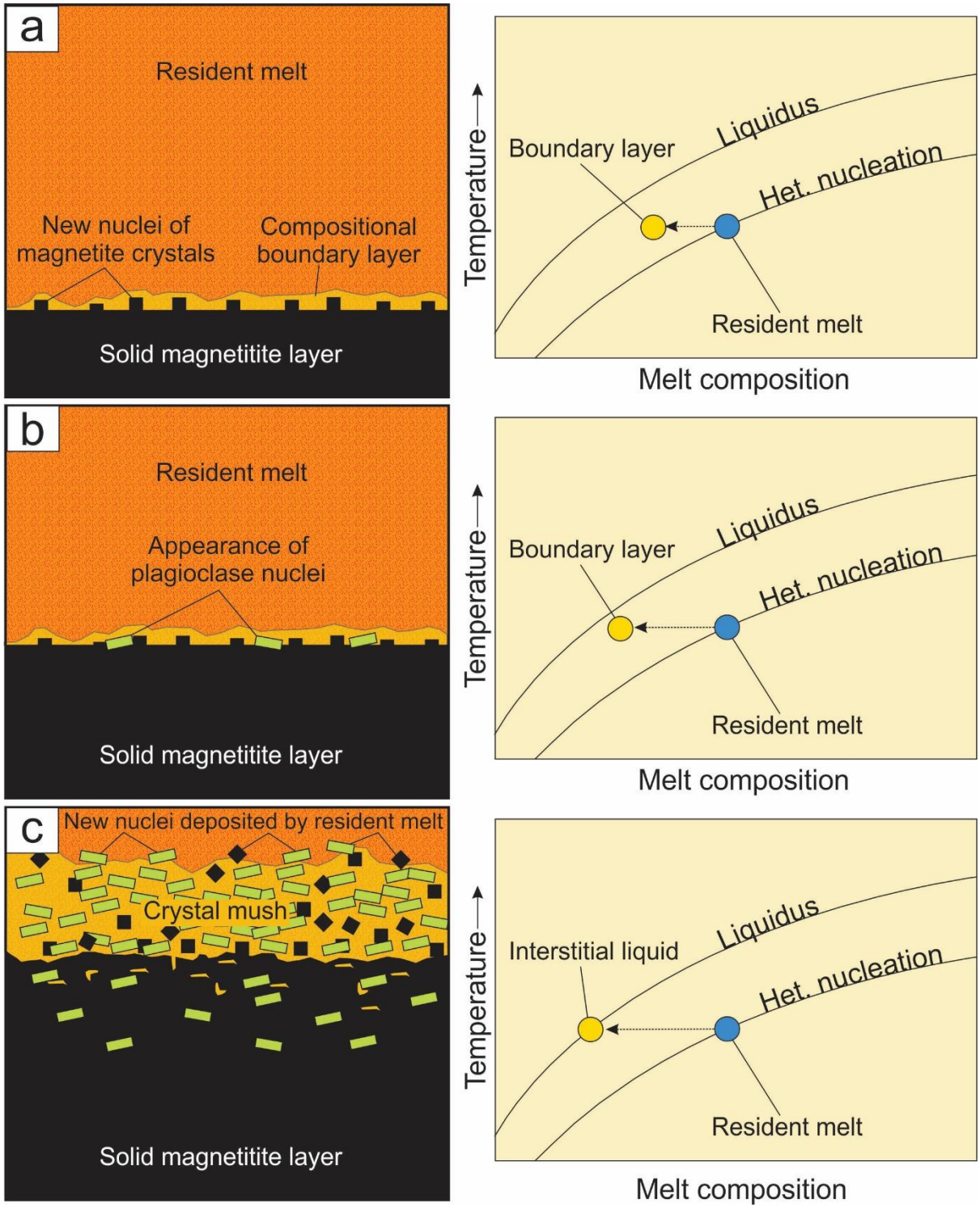

Figure 5.37 Transition from a solid solidification front in massive magnetitite to a partially liquid solidification front in the overlying magnetite anorthosite. (a) The melt within the basal layer undergoes sufficient cooling for heterogeneous nucleation to occur on pre-existing crystals. As the magnetite crystallizes, the melt within the boundary layer migrates towards the liquidus but breaks away convectively before it can be reached. Under these conditions adcumulates are formed under isothermal conditions. (b) When plagioclase joins the crystallizing assemblage, convective removal of the boundary layer is delayed, and each boundary layer migrates closer to the liquidus before it is removed. (c) Eventually sufficient plagioclase would crystallize within the boundary layer to prevent its removal before it reached the liquidus. At this stage adcumulus growth can no longer proceed isothermally. New nuclei may be added by the cooler magma above at a faster rate than the interstitial liquid can solidify and a crystal mush forms.

study the processes that occur within the liquid boundary layer (Figure 4.38) surrounding magnetite crystals.

Two factors are important to keep in mind when attempting to explain the above observation. Prior to the crystallization of the massive magnetite, a certain degree of supercooling must occur to allow the heterogeneous nucleation of magnetite on the underlying anorthosite (Figure 5.37; Figure 5.38a). The liquid surrounding the liquid boundary layer surrounding magnetite crystals are thus located on the nucleation curve of magnetite as explained in the previous section. Secondly, within the boundary layer itself, the composition of the liquid is shifted slightly towards plagioclase saturation as magnetite crystallizes from it (Figure 5.38b. When a boundary layer breaks away from the magnetite crystal, it mixes with the surrounding melt, causing the entire basal flow to steadily advance towards plagioclase saturation. The magnetite then comes into contact with fresh melt from the basal flow. This fresh layer of melt is still saturated in magnetite, and can allow the nucleation of more magnetite crystals on the pre-existing ones. However, because of mixing of the previous boundary layer with the melt in the basal flow, this new boundary layer lies ever so slightly closer to plagioclase saturation (Figure 5.38b). With sufficient magnetite crystallization, the new boundary layer is also released to the overlying melt, causing further differentiation. Thus, with each incremental step of crystallization, each subsequent boundary layer slowly approaches plagioclase saturation (Figure 5.38c).

For the first nucleation point of plagioclase to form, it is necessary that a certain amount of plagioclase building components join together simultaneously to produce a stable nuclei that will not immediately be redissolved into the melt (Vernon, 2018). As the above process continues, the probability of plagioclase nucleation increases as the amount of undercooling relative to the plagioclase liquidus increases. Eventually a nucleation point of plagioclase may appear somewhere within the boundary layer for the first time (Figure 5.38d). Because the melt is supercooled relative to the plagioclase liquidus, rapid growth of this crystal will occur. This pushes the local composition of the boundary layer surrounding the plagioclase crystal back towards the side of magnetite on the phase diagram. Eventually the grain of plagioclase is covered in new magnetite nuclei (Figure 5.38f) and magnetite growth continues (Figure 5.38g and h). As each boundary layer continues evolving along the path shown in Figure 5.38c, plagioclase nucleation becomes more and more likely. As time passes, more and more plagioclase nuclei will appear, and a gradational contact is produced overhead the massive magnetitite layer (Figure 5.38i). Random nucleation of plagioclase within the boundary layer

may produce plagioclase cumulates within massive magnetite as shown in Figure 5.7i and Figure 5.36.

The above mechanism explains how *in situ* crystallization can produce rocks with non-cotectic proportions if there is strong compositional convection as in the case of magnetite crystallization. One obstacle that still needs to be overcome is the lamination so commonly observed in plagioclase grains of the upper contact. It is difficult to explain why such a growth orientation would result from plagioclase crystallizing *in situ*, especially in the absence of evidence for compaction of igneous cumulates (Holness, 2017a; Vukmanovic *et al*., 2019). An interesting observation in the anorthosite layers underneath magnetitite may provide a potential solution to this problem. Plagioclase within the anorthosites are usually extremely well foliated. An exception to this rule is within oikocrysts of either magnetite or pyroxene where the orientation of plagioclase appears much more random. This may suggest that plagioclase does not become foliated with crystallization, but some secondary process may be responsible, like magmatic flow. This issue awaits further study.

5.10 Origin of underlying anorthosite layers

Finally, we come to one of the most challenging questions regarding the petrogenesis of Bushveld magnetitite: why are they so commonly underlain by anorthosite?

5.10.1 Comments on previous work

As mentioned in the introductory chapter, there are far fewer models dealing with the origin of massive magnetitite that attempts to explain its association with anorthosite. The model from Reynolds (1985b) that involves *in situ* fractionation of anorthosite has already been discussed earlier in this paper along with reasons why this model is considered unlikely. A model involving sinking of plagioclase and flotation of magnetite (Knipping *et al*., 2019) is also excluded based on the overwhelming evidence for the *in situ* crystallization of massive magnetitite. Cawthorn (2003) proposed that the crystallization of anorthosite was due to a pressure reduction in the magma chamber, possibly due to volcanic eruption (Cawthorn and Ashwal, 2009). This is based on the fact that a pressure reduction favours the crystallization of plagioclase over pyroxene (e.g. Naslund and McBirney, 1996), which may cause the disappearance of the latter phase from the liquidus. The crystallization of magnetitite after the deposition of the anorthosite would then require a pressure increase in the chamber by some tectonic event (Cawthorn and McCarthy, 1980; Cawthorn and Ashwal, 2009). However, there is currently no explanation as to why a pressure reduction would immediately be followed by

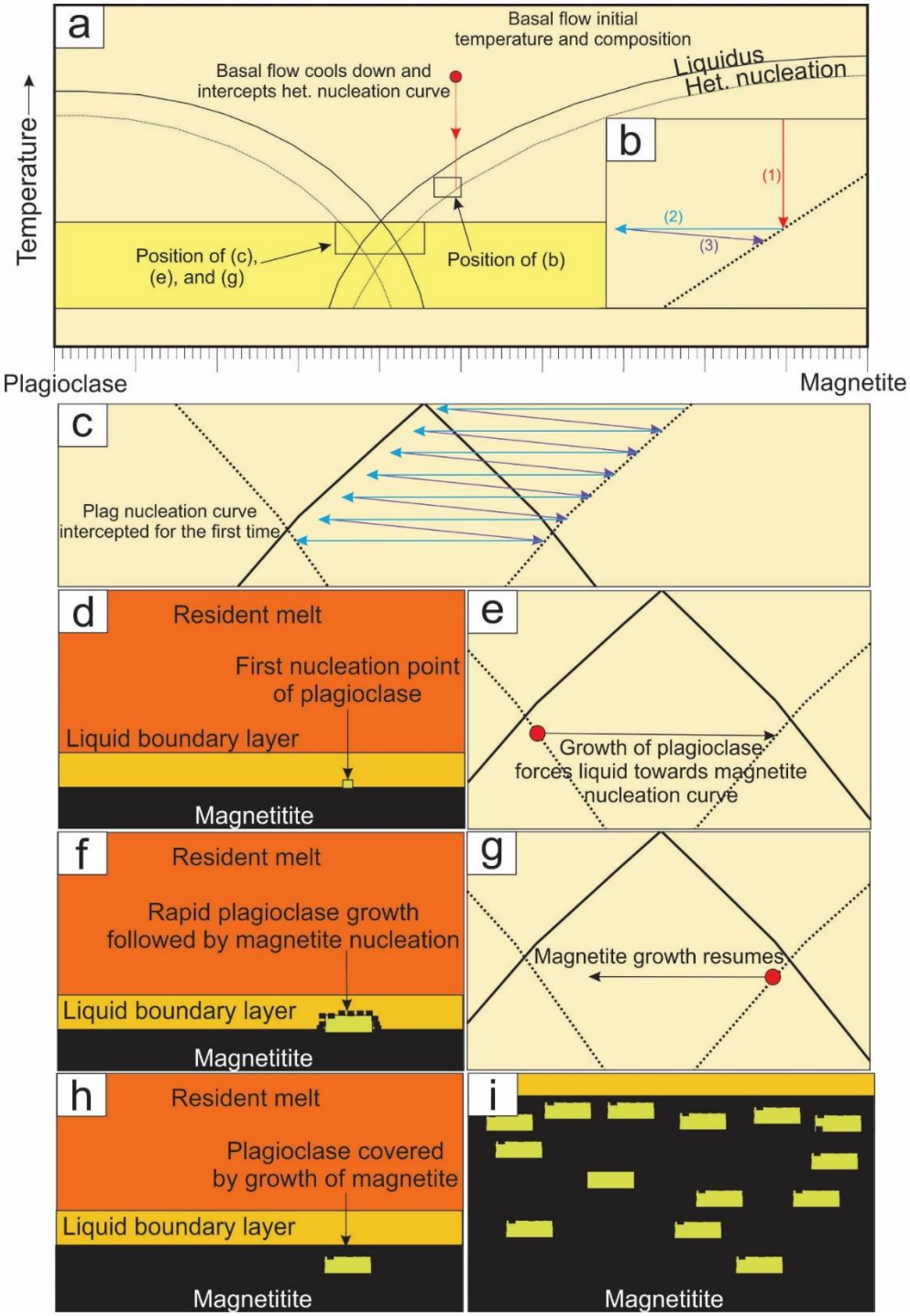

Figure 5.38 Evolution of melt within a liquid boundary layer atop a magnetitite solidification front. (a) Hypothetical binary phase diagram with magnetite and plagioclase. Red dot indicates the composition and temperature of a basal flow that cools down until it intercepts the heterogeneous nucleation curve for magnetite. (b) As magnetite crystallizes, a boundary layer forms that is depleted in magnetite component (2) during the diffusion of Fe_3O_4 towards the growing crystal. When the boundary reaches a critical size and buoyancy, it breakes away from the crystal, and the magnetite comes into contact with new, slightly more differentiated melt (3). This new boundary layer has a slightly lower temperature due to heat loss of the basal layer to its surroundings. (c) The above process continues and the melt keeps evolving towards the plagioclase side of the phase diagram. (d) Eventually, undercooling relative to the plagioclase liquidus is sufficient to allow the nucleation of plagioclase to occur within the boundary layer. (e) This results in rapid growth of the plagioclase crystal until magnetite nucleation becomes favourable again (f). (g) Magnetite growth resumes until the plagioclase grain is covered (h). (i) With each incremental boundary layer, plagioclase nucleation becomes increasingly more probable, resulitng in a progressive increase in the proportion of plagioclase to magnetite upwards.

a pressure increase to repeatedly produce anorthosite layers overlain by magnetitite layers in the Upper Zone of the Bushveld Complex. This model is therefore cosidered unlikely to have occurred.

As explained earlier, Scoon and Mitchell (2012) suggested that massive magnetitite of the Bushveld formed due to the introduction of magma carrying a crystal slurry of magnetite crystals. Regarding the origin of the anorthosite layer, they proposed that a layer initially formed with plagioclase flotation to produce a mat of plagioclase crystals, a model proposed by Vermaak (1976), just prior to the formation of the magnetitite. This results in the formation of a rock type that is enriched in plagioclase relative to the plagioclase-pyroxene cotectic. When magmatic recharge occurs, heat introduced by the magma results in the partial melting of this already plagioclase-enriched layer. Because pyroxene and plagioclase are then removed by melting in their cotectic proportions, the process further purifies the layer, and an anorthositic layer is left behind. This model, however, requires that a plagioclase-rich mat needs to form prior to the crystallization of almost every magnetitite layer. No explanation is given as to why this will be the case. In our data we also note that anorthosites underlying magnetitites are significantly enriched in incompatible elements such as La, Ce, and P_2O_5 (Figure 5.39). Incompatible elements are preferentially removed during partial melting (Rollinson, 1993), begging the question as to why the anorthosite layers are enriched. Rare-earth elements also preferentially partition into clinopyroxene, and its removal should lead to a depletion in these elements. As stated before, the enrichment in incompatible elements in anorthosites are probably due to less effective crystal-liquid fractionation during the formation of this rock type.

Yuan *et al*. (2017) preferred a model where plagioclase crystals are introduced as a crystal slurry from a staging chamber. As said before, this model requires crystal settling of magnetite to form a massive magnetitite layer, and thus seem incompatible with many other lines of evidence suggesting *in situ* crystallization. Secondly, this model does not allow for the thermochemical erosion of the footwall that seems to be important to produce the field characteristics observed between the massive magnetitite and the anorthosite.

More recently, Latypov *et al*. (2020) proposed that stratiform anorthosites may form in a near-identical way to Latypov *et al*.'s (2018) model dealing with the origin of chromitite layers, i.e. pressure reduction during magma ascent favours the crystallization of plagioclase within the magma chamber. This model would require that the emplacement of a magnetite-saturated melt

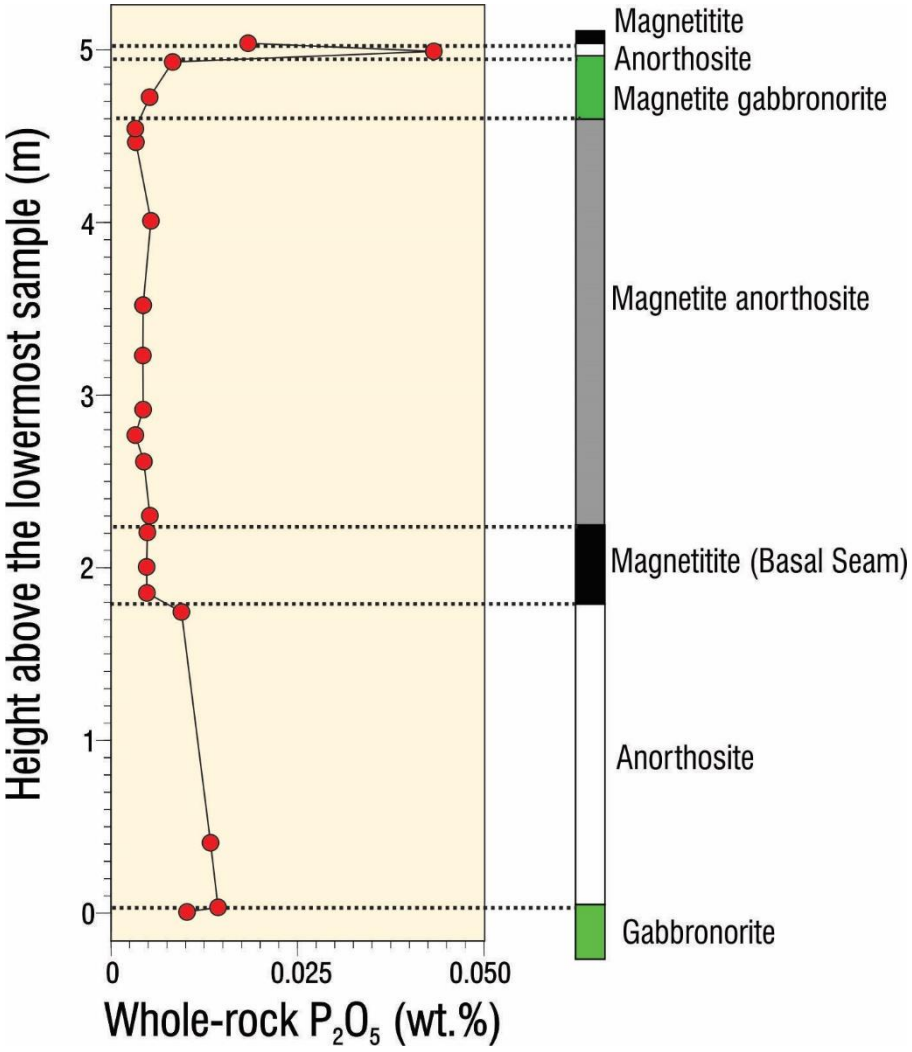

Figure 5.39 Variation of whole-rock of P_2O_5 in a section of the Rhovan drill core. If partial melting of gabbroic rocks occurred to produce anorthosite, we can expect them to be relatively depleted in incompatible elements such as P_2O_5. However, anorthosite layers underneath magnetitite layers are typically enriched in incompatible elements.

should frequently be preceded by the emplacement of a plagioclase-saturated melt. Currently there is no explanation as to why this should be the case.

5.10.2 Proposed model to produce underlying anorthosite layers

In this study we have proposed that magnetitite layers form by the introduction of a magnetite-only saturated melt in the chamber. If this really had occurred, this process must somehow be linked to the formation of anorthosite underneath magnetitite in most cases. Underneath the anorthosite layers of the Bottom seam and the MML occur gabbroic rocks that appear to be void of magnetite primocrysts. This implies that prior to the formation of anorthosite, pyroxene and plagioclase were the only liquidus phases in the melt. Therefore, this melt must be situated

on a pyroxene-plagioclase cotectic. In contrast, the melt that crystallizes massive magnetitite must first have been saturated in magnetite that is then joined by the crystallization of plagioclase to produce the overlying magnetite anorthosite. The incoming melt responsible for the crystallization of massive magnetitite must at first be situated within the field of magnetite close to the magnetite-plagioclase cotectic. A possible composition of such a melt is presented in our MELTS modelling from Kruger and Latypov (2020a) that crystallizes magnetite first followed by plagioclase. Based on the phase diagrams presented by Roeder and Osborn (1966), it is interesting to note that a hybrid of the incoming melt thay may crystallize a massive magnetitite layer and the resident melt (saturated in plagioclase and pyroxene) would likely end up in the field of plagioclase saturation (Figure 5.40).

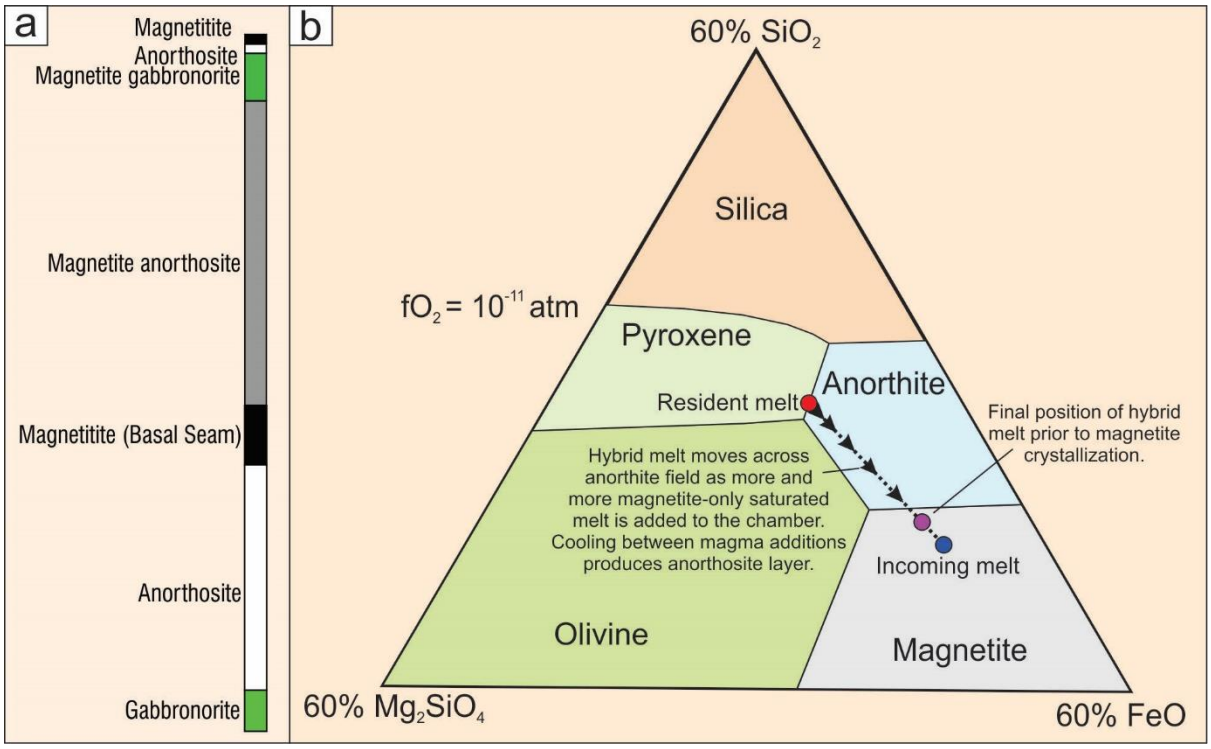

Figure 5.40 Model for the origin of anorthosite layers underneath magnetitite layers. (a) Rock types from a section of the Rhovan drill core that includes two massive magnetitite layers (b) A section through the system Mg_2SiO_4-FeO-Fe_2O_3-$CaAl_2Si_2O_8$-SiO_2 with a constant $CaAl_2Si_2O_8$ of 40 wt. %. Prior to anorthosite formation, the resident melt must be situated on the pyroxene-anorthite cotectic to produce the gabbronorite shown at the bottom of the drill core in (a). An incoming melt located in the field of magnetite is gradually added into the chamber in a number of pulses. Mixing, cooling, and crystallization in-between pulses gradaully builds up an anorthosite layer. When the hybrid melt enters the field of magnetite, a layer of magnetitite is deposited on top of the anorthosite layer.

When a magma chamber undergoes magmatic recharge, reversals are frequently observed to be gradual. One of the best examples of this (and magmatic recharge in general) comes from the Bushveld's own Pyroxenite Marker. The rocks below this pyroxenite layer show a gradual increase in plagioclase An contents, Mg# of pyroxene, and a constant shift in the Sr-isotopic ratios upwards (Cawthorn *et al*., 1991). To explain the gradual reversals, it is considered that the magma recharge event occured in increments, with intermediate mixing, cooling and crystallization (Cawthorn *et al*., 1991; VanTongeren and Mathez, 2013). A similar process may have occurred to produce the magnetite anorthosite. Multiple pulses of melt located in the field of magnetite close to the magnetite-plagioclase cotectic entered the chamber. Their higher Fe-contents imply they were probably denser than the resident melt. However, because the magma carries some momentum upon entry into the chamber, it first rises up to form a magmatic fountain (e.g. Campbell and Turner, 1989). This process is highly turbulent, causing some of the resident melt to become entrained in the fountain head and some mixing occurs (Campbell and Turner, 1989). As the fountain's upwards velocity reaches zero, it starts to move downwards to form a basal flow on the chamber floor (Figure 5.41b). After cooling, plagioclase crystallizes, and repetition of this process eventually builds up a layer of anorthosite. Evidence that the anorthosite layer results from multiple pulses of magma was already presented by Butcher and Merkle (1991) when they noticed occassional intervals of thermal erosion and crystallization in tha anorthosite layer underlying the bottom seam (Figure 5.19). An-reversals associated with anorthosite layers of the Bushveld's Upper Zone as recorded by Yuan *et al*. (2017) also serve as evidence that the formation of these layers were preceded by magmatic recharge. During the initial stages erosion must predominantly be thermal, as chemical erosion is less effective since the incoming melts would be located in the field of plagioclase upon entry. Some chemical erosion is still possible, however, since a superheated melt will be able to carry more plagioclase in solution. With time, incoming pulses causes the basal melt layer to grow larger and larger, and its overall composition slowly evolves towards the composition of the incoming melt. Eventually, the hybrid melt moves into the field of magnetite. Thermochemical erosion will be at a maximum at this stage as the greatest compositional contrast exists between the basal melt layer and the cumulates below. It is at this stage where the magmatic karst landscape likely developes. As the hybrid melt cools down in between magmatic recharge events, a massive magnetitite layer gradaully crystallizes on the partially eroded anorthosite layer below.

Evidence for magma mixing to produce the anorthosite comes from the presence of sulphides within this rock type (Von Greunewaldt, 1976). Originally it was considered that mixing occurred to produce the magnetitite layers in the Bushveld Complex. The mixing event also triggered the saturation of an immiscible sulphide liquid that then drained downwards into the underlying anorthosite (Harney and Von Gruenewaldt, 1995). However, Cawthorn and Street (1994) noticed that the abundance of sulphides where unaffected by the presence of a large xenolith straddling the boundary between Magnetite Layer 1 from Magnet Heights and the underlying anorthosite. The xenolith would have served as an obstacle to the downward percolation of sulphide-liquid from above. It is better to attribute the presence of these sulphides to the crystallization of the anorthosite from a hybrid melt and not the magnetitite.

As mentioned earlier, two magnetitite layers from this study do not contain anorthosite in their footwalls. In the case where a magnetitite layer is underlain by magnetite anorthosite (Figure 5.7h), this is probably because the melt was saturated in magnetite and plagioclase prior to the magmatic recharge event that produced the magnetitite layer. In such a case, mixing between the incoming and resident melt would only result in the crystallization of magnetite, not anorthosite. The magnetitite layer that contains a very thin pyroxenite layer in its footwall (Figure 5.7g) probably cannot be explained by the above model. While its origin is not known, it can be speculated that it formed from the intrusion of a clinopyroxene-saturated magma. Whatever the case may be, it is unusual and its presence is probably not important for understanding the origin of massive magnetitite.

5.11 Conclusion

The field and geochemical characteristics of magnetitite layers presented here have placed severe constraints on their formation. The major points are summarized below:

1. Large Cr reversals at magnetitite layer bases strongly suggests magmatic recharge occurred prior to the crystallization of massive magnetitite layers. Models that cannot explain this reversal, such as a pressure increase in the chamber, gravitative accumulation of dense-Fe-rich liquid, liquid immiscibility, and the *in situ* fractionation of plagioclase, are excluded.
2. Intricate depressions in anorthositic footwalls and anorthosite inclusions in magnetitite layers can be readily explained by the thermochemical erosion of footwall material by superheated magma following magmatic recharge.

3. Extreme lateral variability in the Cr contents along the bases of massive magnetitite layers is most consistent with the *in situ* crystallization of massive magnetitite due to the presence of growth nodes. Models that involve any movement or settling of magnetite crystals are discredited based on this observation.

The following series of events are proposed for the origin of massive magnetite layers in the Busvheld Complex (Figure 5.41):

1. Fractional crystallization of silicates in a deeper seated staging under low fO_2 conditions causes Fe-enrichment of the melt.
2. During magmatic ascent from the staging chamber, phase boundaries are shifted in such a manner that the melt finds itself within the field of magnetite close to the magnetite-plagioclase cotectic due to the drop in lithostatic pressure. The melt also becomes superheated during adiabatic rise. If some crustal material is assimilated by the magma during its ascent, it might results in an elevated fO_2 of the melt.
3. The incoming melt enters the chamber in a series of pulses and forms a basal flow on the chamber floor due to its relatively higher density.
4. Upon entry in the magma chamber, the melt's initial superheated nature prevents crystallization. Mixing with the resident melt in the head of a magma fountain and periodic cooling in-between magma additions stabilizes plagioclase as the sole phase on the liquidus. Intermittent cooling in between magma pulses gradually builds up an anorthosite layer.
5. Additional pulses of magma enter the chamber and mix with the basal melt layer. This causes the basal melt layer to grow in size and cooling between magma pulses become less pronounced. Eventually plagioclase crystallization stops, and thermochemical erosion of the anorthositic footwall occurs.
6. Due to the growth of the basal layer, the mixing effect with the resident melt becomes less significant, and the melt ends up within the field of magnetite.
7. Cooling now allows the crystallization of massive magnetitite *in situ* on the anorthositic footwall, forming a massive magnetitite layer.
8. Crystal-liquid fractionation occurs predominantly through the convective removal of a thin boundary layer of buoyant melt around magnetite crystals. As the magnetitite layer keeps crystallizing, nucleation of plagioclase within the boundary layer becomes more

and more probable. A gradational upper contact with non-cotectic proportoins into magnetite anorthosite results atop the massive magnetitite layer.

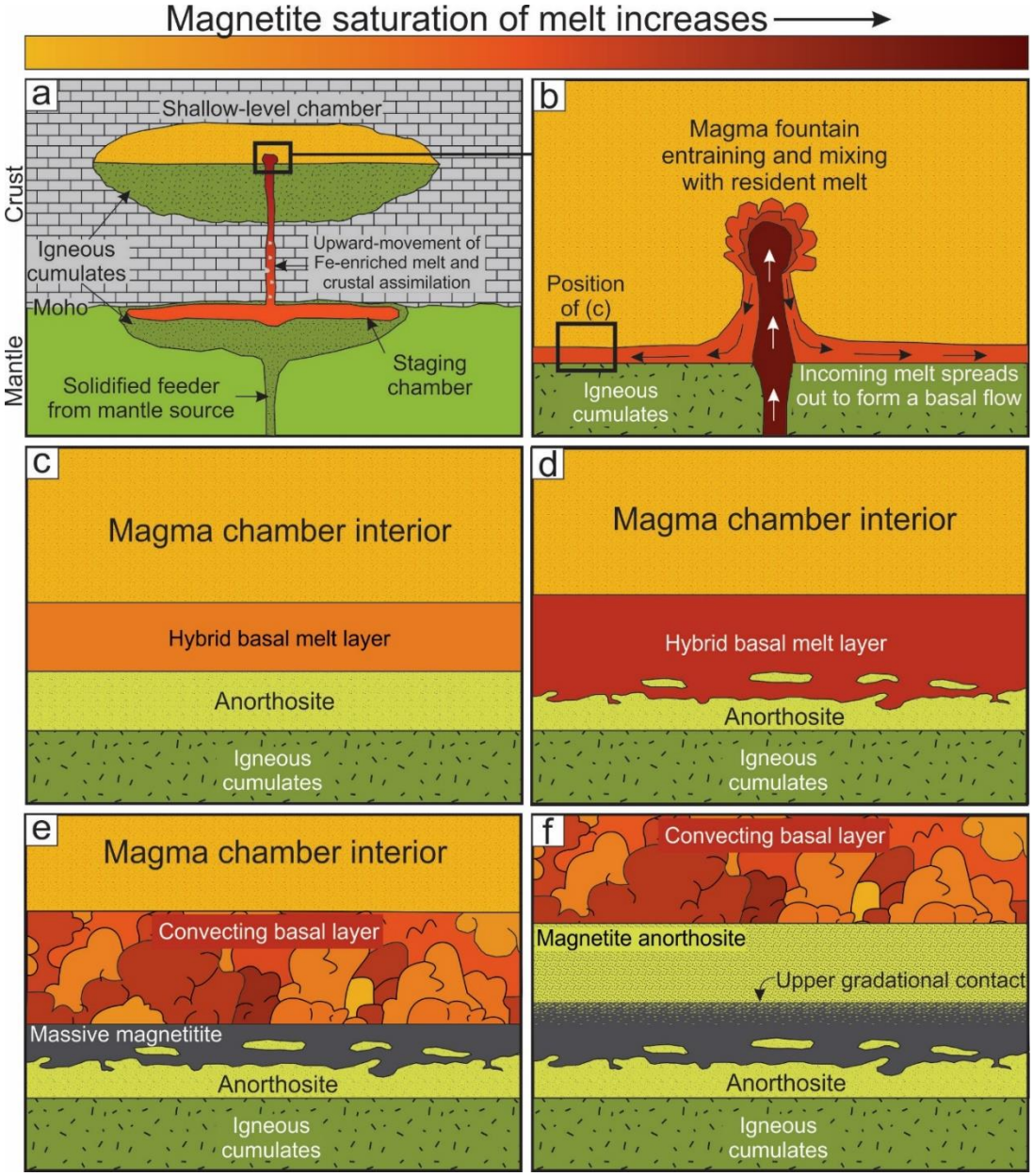

Figure 5.41 Model for the origin of massive magnetitite layers of the Bushveld Complex (not to scale). (a) Mafic melt ponds and fractionates at the base of the crust, driving the melt close to magnetite saturation. A pulse of magma is then released upwards and emplaced into a shallow-level magma chamber within the crust. The reduction in pressure associated with magmatic ascent coupled with crystal assimilation forces the liquid to within the field of magnetite close to the magnetite-plagioclase cotectic. Adiabtic rise of the melt ensures it is superheated upon entry into the chamber. (b) Momentum upon entry causes the incoming melt to initally form a fountain. Some of the resident melt is entrained due to turbulence at the head of the fountain that leads to magma mixing. Thereafter, the incoming melt spreads laterally to form a basal flow because of its higher density relative to the resident melt. (c) After some degree of cooling occurs, the hybrid melt crystallizes a layer of anorthosite on the chamber floor. (d) More pulses of melt enters the chamber and mixes with the basal melt layer, supplying heat and guiding its composition towards the field of magnetite. Eventually, thermochemical erosion produces an intricate morphology of the anorthosite layer. (e) Possibly due to a reduction in size of new magma pulses entering the chamber, the basalt melt cools sufficiently to allow the crystallization of magnetitite which causes vigorous convection in the basal layer due to the convective removal of thin boundary layers surrounding growing crystals. (f) With continued differentiation, plagioclase nuclei may appear within boundary layers. As crystallization proceeds, plagioclase nucleation grows more and more likely, producing a gradational contact into overlying magnetite anorthosite.

CHAPTER 6

CONCLUSIONS

In this study magnetitite layers from the Bushveld Complex were studied in an attempt to contribute to four important questions regarding our understanding of how magma chambers work: (1) To what extent is the Bushveld magma chamber liquid dominated during the crystallization of magnetitite? (2) By what means do crystals accumulate in magma chambers during magnetitite formation? (3) How may crystal/liquid fractionation occur to produce the wide variety of igneous rocks in layered intrusions? (4) How are stratiform monomineralic rocks formed in layered intrusions that consist of a mineral that only joins the crystallizing assemblage after some degree of magmatic differentiation has occurred? The findings are summarized below.

6.1 Thickness of the crystal mush during magnetitite crystallization

Detailed mapping of the two-dimensional distribution of Cr in massive magnetitite layers from the Bushveld Complex revealed fossilized solidification fronts on a scale never seen before. The extremely steep Cr gradients observed within these layers, coupled with a relatively constant V concentration, suggests that these solidification fronts propagate as an essentially solid surface. This is because of extremely effective compositional convection that eradicates nearly all interstitial liquid and efficiently prevents the solidification front to propagate in a mushy state. This discovery is more in line with the work of researchers than typically envision a thin crystal mush in layered intrusions (e.g. Morse, 2011; Holness, 2017a; Vukmanovic *et al*., 2019) than those that propose a thick crystal mush (e.g. McKenzie, 2011; Maier *et al*., 2013; Cashman, 2017). Since evidence has been presented for the *in situ* crystallization of similar monomineralic rocks like chromite (e.g. Latypov *et al*., 2017a; Kaufmann *et al*., 2019), the same process may very well apply to this rock type as well. However, very large magma volumes are necessary to crystallize chromite layers (Cawthorn, 2015), suggesting that large, liquid dominated magma chamber have existed in Earth's history. This is in contrast to recent suggestions that they are dominated by crystal mushes (e.g. Cashman *et al*., 2017).

6.2 Means of crystal accumulation in magnetitite layers

Two-dimensional geochemical mapping of magnetitite layers have provided spectacular confirmation of Cawthorn's (1994) original proposal that these layers crystallize *in situ* to

produce dome-shaped structures called growth nodes. Furthermore, these geochemical maps also revealed the *in situ* crystallization of magnetite on sub-vertical footwall contacts with their underlying anorthosite layers, as well as growth directly on the outer margins of anorthositic inclusions sometimes found within the massive magnetitite. *In situ* crystallization of massive magnetitite occurs on the chamber floor not only because heterogeneous nucleation is much more favourable than homogeneous nucleation within the liquid interior of the chamber (as explained by Campbell, 1978), but also because heat is lost through the underlying cumulates. This is indicated by the distribution of growth nodes where cooling is most efficient, such as in footwall depressions or in the vicinity of anorthositic inclusions. Although some investigators have stated that heat loss through cumulates on the chamber floor is impossible due to the production of latent heat by crystallization (e.g. Irvine, 1970; Hess, 1972; Morse, 1988) thermochemical erosion due to magmatic recharge ensures that potentially several metres of cumulates are excavated, bringing the melt into contact with deeper, cooler cumulates.

6.3 Mechanism of differentiation of during the crystallization of magnetitite

The existence of growth nodes and other lines of chemical evidence attesting to *in situ* crystallization of massive magnetitite precludes crystal settling as a means of differentiation. Extremely steep Cr concentration gradients over just a few cm and effective liquid exchange in very confined spaces (such as where solidification fronts converge in between the chamber floor and anorthositic inclusions) also precludes compaction and convection in thick crystal mushes as a viable mechanism. The fact that effective liquid exchange occurs even within veins of magnetitite also precludes a model that involves diffusion coupled by convective eddies descending from the chamber interior (Cawthorn and McCarthy, 1980). Diffusion alone would deplete the vein too rapidly in Cr than what is observed, while convective eddies would not be able to penetrate such a vein. The model by Martin *et al*., (1987), Campbell (1996), and Seedhouse and Donaldson (1996), where very thin (only a few mm) compositional boundary layers surrounding individual crystals may detach convectively and mix with the overlying magma, appears to be a viable mechanism to explain the above features that are observed within massive magnetitite. The action of the above process is also responsible for certain puzzling features regarding the propagation pattern of solidification fronts. These include the great tendency for lateral growth once growth nodes have formed, or the fact that humps of magnetitite is never observed atop anorthositic inclusions. Since the low-density liquid

boundary layers surrounding magnetite crystals would tend to flow to higher areas on the solidification front, lateral propagation is always preferred to vertical growth upwards.

6.4 Origin of massive magnetitite layers in the Bushveld Complex

Since the results provided here strongly support the *in situ* crystallization of magnetitite by heterogeneous nucleation, models that attempt to explain the origin of this rock type by any mechanism that involves movement of crystals are excluded. These include the intrusion of a magnetite crystal slurry during injection of magma into the chamber (Scoon and Mitchell, 2012), hydrodynamic sorting of crystal mushes (Maier *et al*., 2013), settling of magnetite crystals after magma mixing (Harney and Von Greunewaldt, 1995; Yuan *et al*., 2017), or deposition of a magnetite slurry from an immiscible Fe-rich melt (Vukmanovic *et al*., 2019). A second important constraint comes from an extremely large Cr reversals associated with the MML. Any models that cannot explain such a reversal are also considered improbable, such as accumulation of late Fe-rich liquids (Bateman, 1952) variations in fO_2 within the chamber (Irvine, 1975, Klemm *et al*., 1985), changes in pressure (Cawthorn and McCarthy, 1980), or liquid immiscibility (e.g. Scoon *et al*., 2017; Vukmanovic *et al*., 2019). A question remained as to whether or not this Cr reversal is generated by processes in a closed system, such as the collapse of layers in a stratified magma chamber (e.g. Harney and Von Greunewaldt, 1995; Tegner *et al*., 2006), or if it arose by magmatic recharge. The partial destruction of the anorthositic footwall of magnetitite layers, forming an undercut-embayed chamber floor, likely requires a superheated magma that probably cannot be sourced within the chamber itself (Latypov *et al*., 2020). The source of such a superheated melt is proposed to be a magma ascending from a staging chamber at depth. A drop in pressure associated with magmatic ascent as well as possible assimilation of crustal material ensures the melt is located within the field of magnetite upon entry in the Bushveld magma chamber. This melt is emplaced in a series of pulses and intermittent mixing with the resident liquid, cooling, and crystallization builds up a layer of anorthosite. Eventually the composition of the hybrid melt shifts closer to that of the incoming magma, and a layer of magnetitite crystallizes atop the anorthosite. As the magnetitite layer continues to crystallize, the melt is forced towards plagioclase saturation, making plagioclase nucleation within the compositional boundary layer surrounding the magnetite layer more and more likely as time passes. Plagioclase nucleation thus becomes more common towards the top of the layer, producing a gradational contact into the overlying magnetitite anorthosite.

6.5 General implications for magma chamber dynamics and future research

Magnetitite layers of the Bushveld Complex are remarkable in their ability to record the processes that occur within the magma chamber during their crystallization. A question remains of how applicable the findings of this study are to understanding magma chamber dynamics in general. The extremely effective crystal-liquid fractionation that occurs during magnetitite crystallization can only operate during the fractionation of a phase that is denser than the melt from which it is crystallizing. This excludes this model as a viable process for magmatic differentiation during the formation of rock types such as anorthosite. A mineral such as plagioclase will likely produce a melt within a compositional boundary layer that has a greater density than the surrounding liquid, preventing compositional convection. However, magnetite has a greater density than any other phase that crystallizes in layered mafic intrusions, casting doubt on whether or not this process can occur even during the crystallization of mafic phases like olivine. It is therefore significant that Seedhouse and Donaldson (1996) observed compositional convection during the crystallization of olivine from synthetic magma, suggesting that the process may occur during the crystallization of dunite, and potentially also during the crystallization of pyroxenite and chromitite in actual magma chambers. Given that these rock types are common in the lower sections of many layered intrusions (for example the Stillwater Complex or the Great Dyke of Zimbabwe), magmatic differentiation by the convective removal of a thin compositional boundary layer may be a common process.

An essential requirement for the above model to work is that the rocks crystallize *in situ* on the floor of a magma chamber. Although evidence for *in situ* crystallization of magnetite is appears to be very strong at this stage, the same evidence does not yet exist for most other rock types in layered intrusions. Different layers within magma intrusions may form in completely different ways. It is therefore essential that each suite of rocks be studied in great detail to seek out any chemical, geological or textural clues that may provide insights into the means of crystal accumulation. While the methods employed in this study may not be as effective to unravel the origin of most other rock types in layered intrusions, it would be of great interest to perform similar work on magnetitite layers in other localities around the world, such as the Stillwater Complex in the U.S. or the Panzhihua Intrusion in China.

REFERENCES

Ashwall, L.D., Webb, S.J. & Knoper, M.W. 2005. Magmatic stratigraphy in the Bushveld Northern Lobe: continuous geophysical and mineralogical data from the 2950 m Bellevue drillcore. South African Journal of Geology, vol. 108, pp. 199-232.

Bachmann, O. and Bergantz, G. W. (2004) On the origin of crystal-poor rhyolites: extracted from batholithic crystal mushes. Journal of Petrology, vol. 45, pp. 1565-1582.

Bachmann, O., Dungan, M.A. and Bussy, F. (2004) Insights into shallow magmatic processes in large silicic magma bodies: the trace element record in the Fish Canyon magma body, Colorado. Contributions to Mineralogy and Petrology, vol. 149, pp. 338-349.

Ballhaus, C.G. (1988) Potholes of the Merensky Reef at Brakspruit Shaft, Rustenburg platinum mines; primary disturbances in the magmatic stratigraphy. Economic Geology, vol. 83, no. 6, pp. 1140-1158.

Barnes, S.J. (1986) The effect of trapped liquid crystallization on cumulus mineral compositions in layered intrusions. Contributions to Mineralogy and Petrology, vol. 93, pp. 524-531.

Barnes, S.J. and Robertson, J.C. (2019) Time scales and length scales in magma flow pathways and the origin of magmatic Ni-Cu-PGE ore deposits. Geoscience Frontiers, vol. 10, pp. 77-87.

Bateman, A.M. (1951) The formation of late magmatic oxide ores. Economic Geology, vol. 46, pp. 404-426.

Bea, F. (2010) Crystallization dynamics of granite magma chambers in the absence of regional stress: multiphysics modeling with natural examples. Journal of Petrology, vol. 51, pp. 1541-1569.

Bédard, J.H. (1994) A procedure for calculating the equilibrium distribution of trace elements among the minerals of cumulate rocks, and the concentration of trace elements in coexisting liquids. Chemical Geology, vol. 118, pp. 143-153.

Berndt, J., Koepke, J. & Holtz, F. (2005) An experimental investigation of the influence of water and oxygen fugacity on the differentiation of MORB at 200 Mpa. Journal of Petrology, vol. 46, 135-167.

Bilenker L.D., VanTongeren, J.A., Lundstorm, C.C. and Simon, A.C. (2017) Iron isotope evolution during fractional crystallization of the uppermost Bushveld Complex layered mafic intrusion. Geochemistry, Geophysics, Geosystems, DOI: 10.1002/2016GC006660.

Boudreau, A.E. (1992) Volatile fluid overpressure in layered intrusions and the formation of potholes. Australian Journal of Earth Sciences, vol. 39, no. 3, pp. 277-287.

Boudreau, A.E. and McCallum I.S. (1992) Infiltration metasomatism in layered intrusions – an example from the Stillwater Complex, Montana. Journal of Volcanology and Geothermal Research, vol. 52, pp. 171-183.

Bowen, N.L. (1915) Crystallization-differentiation in silicate liquids. American Journal of Science, vol. 39, pp. 175-191.

Bowen, N.L. 1928. The evolution of igneous rocks. New York: Dover Publications, pp. 332.

Butcher, A.R. and Merkle, R.K.W. (1987) Postcumulus modification of magnetite grains in the Upper Zone of the Bushveld Complex, South Africa. Lithos, vol. 20, pp. 247-260.

Butcher, A.R. and Merkle, R.K.W. (1991) Unusal textures and structures associated with a magnetitite layer in the Bushveld Complex: a contribution to the adcumulus debate. Mineralogical Magazine, vol. 55, pp. 465-477.

Cameron, E.N. (1978) The Lower Zone of the eastern Bushveld Complex in the Olifants River trough. Journal of Petrology, vol. 19, pp. 437-462.

Campbell, I. H. (1977) A Study of Macro-Rhythmic Layering and Cumulate Processes in the Jimberlana Intrusion, Western Australia. Part I: The Upper Layered Series. Journal of Petrology, vol. 18, pp 183–215.

Campbell, I.H. (1978) Some problems with the cumulus theory. Lithos, vol. 11, pp. 311-323.

Campbell, I.H. (1986) A fluid dynamic model for the potholes of the Merensky Reef. Economic Geology, vol. 81, pp. 1118-1125.

Campbell, I.H. (1996) Fluid dynamic processes in basaltic magma chambers. In: Cawthorn, R.G., ed. Layered Intrusions. Elsevier Science, pp. 45-76.

Campbell, I.H. and Turner, J.S. (1989) Fountains in magma chambers. Journal of Petrology, vol. 30, no. 4, pp. 885-923.

Carr, H.W., Kruger, F.J., Groves, D.I. and Cawthorn, R.G. 1999. The petrogenesis of Merensky Reef potholes at the Western Platinum Mine, Bushveld Complex: Sr-isotopic evidence for synmagmatic deformation. Mineralium Deposita, vol. 34, pp. 335-347.

Cashmann, K.V., Sparks, R.S.J, and Blundy, J.D. (2017) Vertically extensive and unstable magmatic systems: a unified view of igneous processes. Science, DOI: 10.1126/science.aag3055.

Castle, N., Herd, D.K. (2017) Experimental petrology of the Tissint meteorite: redox estimates, crystallization curves, and evaluation of petrogenetic models. Meteoritics and Planetary Science, vol. 52, nr. 1, pp. 125-146.

Cawthorn, R.G. (1994) Vertical migration of residual magma in the Upper Zone of the Bushveld Complex. Mineralogy and Petrology, vol. 51, pp. 345-354.

Cawthorn, R.G (ed). (1996a) Layered intrusions. Developments in Petrology 15, Elsevier Science, B. V., 531 pp.

Cawthorn, R.G. (1996b) Models for the incompatible trace element abundances in cumulus minerals and their application to plagioclase and pyroxene compositions in the Bushveld Complex. Contributions to Mineralogy and Petrology, vol. 123, pp. 109-115.

Cawthorn, R.G. (2003) Genesis of magmatic oxide deposits – a review from the Bushveld Complex. Geological Survey of Norway Special Publication 9, pp. 11-21.

Cawthorn, R.G. (2013) Rare earth element abundances in apatite in the Bushveld Complex—A consequence of the trapped liquid shift effect. Geology, vol. 41, no. 5, pp. 603-606.

Cawthorn, R.G. (2015) The Bushveld Complex. In: Charlier, B., Namur, O., Latypov, R. and Tegner, C. eds. Layered intrusions. Springer Geology, pp. 517-648.

Cawthorn, R.G. and Ashwal, L.D. (2009) Origin of anorthosite and magnetitite layers in the Bushveld Complex, constrained by major element compositions of plagioclase. Journal of Petrology, vol. 50, nr. 9, pp. 1607-1637.

Cawthorn, R.G., Cooper, G.R.J. & Webb, S.J. 1998. Connectivity between the western and eastern limbs of the Bushveld Complex. South African Journal of Geology, vol. 101, pp. 291-298.

Cawthorn, R.G. (2019) A non-horizontal floor during accumulation of the Bushveld Complex – evidence and implications. Lithos, vol. 316-317, pp. 323-329.

Cawthorn, R.G. and McCarthy, T.S. (1980) Variations in Cr content of magnetite from the Upper Zone of the Bushveld Complex – evidence for heterogeneity and convection in magma chambers. Earth and Planetary Science Letters, vol. 46, pp. 336-343.

Cawthorn, R.G. and McCarthy, T.S. (1981) Bottom crystallization and diffusion control in layered complexes: evidence from Cr distributions in magnetite from the Bushveld Complex. Transactions of the Geological Society of South Africa, vol. 84, pp. 41-50.

Cawthorn, R.G., McCarthy, T.S. and Davies, G. (1983) Vertical chemical gradients in a single grain of magnetite from the Bushveld Complex, South Africa. Mineralocial Magazine, vol. 47, pp. 27-34.

Cawthorn R.G., McCarthy, T.S. and Davies, G. (1983) Vertical chemical gradients in a single grain of magnetite from the Bushveld Complex, South Africa. Mineralogical Magazine, vol. 47, pp. 27-34.

Cawthorn, R.G., Meyer, P.S. and Kruger, F.J. (1991) Major addition of magma at the Pyroxenite Marker in the western Bushveld Complex, South Africa. Journal of Petrology, vol. 32, no. 4, pp. 739-763.

Cawthorn, R.G. & Molyneux, T.G. (1986) Vanadiferous magnetite deposits of the Bushveld Complex. In: Anhaesser, C.R. and Maske, S. eds. Mineral deposits of South Africa, Johannesburg: Geological Society of South Africa, pp. 1251-1266.

Cawthorn, R.G., Latypov, R., Klemd, R. and Vuthuza, A. 2018. Origin of discordant ultramafic pegmatites in the Bushveld Complex from externally-derived magmas. South African Journal of Geology, vol. 121, pp. 287-310.

Cawthorn, R.G. and Street, J. (1994) Growth nodes at the base of magnetitite layers in the Upper Zone of the Bushveld Complex. South Africa Journal of Geology, vol. 97, no. 4, pp. 455-461.

Cawthorn, R.G and Walvaren, F. (1998) Emplacement and crystallization time for the Bushveld Complex. Journal of Petrology, vol. 39, no. 9, pp. 1669-1687.

Charlier, B., Namur, O., Latypov, R. & Tegner, C. 2015. Layered intrusions. Springer, 748 pp.

Chistyakova, S., Latypov, R., Hunt, E.J. & Barnes, S. (2019) Merensky-type platinum deposits and a reappraisal of magma chamber paradigms. Scientific Reports, DOI: 10.1038/s41598-019-45288-8.

Cole, J. (2018) Three dimensional geometry of the Bushveld Complex derived from potential field modelling. Thesis, University of the Witwatersrand.

Cousins, C.A. (1959) The structure of the mafic portion of the Bushveld Igneous Complex. Transactions of the Geological Society of South Africa, vol. 62, pp. 174-189.

Dare, A.S., Barnes, S.-J. and Beaudoin, G. (2012) Variation in trace element contents of magnetite crystallized from a fractionating sulfide liquid, Sudbury, Canada: implications for provenance discrimination. Geochemica Cosmochimica Acta, vol. 88, pp. 27-50.

Davies, G. and Cawthorn, R.G. (1984) Mineralogical data on a multiple intrusions intrusion in the Rustenburg Layered Suite of the Bushveld Complex. Mineralogical Magazine, vol. 48, pp. 469-480.

D'Ozario, M., Armienti, P. and Cerretini, S. (1998) Phenocryst/matrix trace element partition coefficients for hawaiite-trachyte lavas from the Ellittico volcanic sequence (Mt. Etna, Sicily, Italy). Mineralogy and Petrology, vol. 64, 65-68.

Du Plessis, A. and Kleywegt, R.J. (1987) A dipping sheet model for the mafic lobes of the Bushveld Complex. Transactions of the Geological Society of South Africa, vol. 90, pp. 1-6.

Eales, H.V. (2002) Caveats in defining the magmas parental to the mafic rocks of the Bushveld Complex,and the manner of their emplacement: review and summary. Mineralogical Magazine, vol. 66, no. 6, pp. 815-832.

Fearn, D.R. and Loper, D.E. (1981) Compositional convection and stratification of Earth's core. Nature, vol. 289, pp. 393-394.

Fischer, L.A., Wang, M., Charlier, B., Namur, O., Roberts, R.J., Veksler, I.V., Cawthorn, R.G., and Holtz, F. (2016). Immiscible iron- and silica-rich liquids in the Upper Zone of the Bushveld Complex. Earth and Planetary Science Letters, vol. 443, 108-117.

GERM (2020) Partition coefficient database https://earthref.org/KDD/

Harney, D.M.W. and Von Greunewaldt, G. (1995) Ore-forming processes in the upper part of the Bushveld Complex, South Africa. Journal of African Earth Sciences, vol. 20, pp. 77-89.

Harney, D.M.W., Merkle, R.K.W. and Von Greunewaldt, G. (1990) Platinum-group element behaviour in the lower part of the Upper Zone, eastern Bushveld Complex – implications for the formation of the Main Magnetite Layer. Economic Geology, vol. 85, pp. 1777-1789.

Helz, R.T. (1987) Differentiation behavior of Kīlauea Iki lava lake, Kilauea Volcano, Hawaii: an overview of past and current work. Magmatic Processes: Physicochemical Principles, vol. 1, pp. 241–258.

Hess, H.H. (1960) Stillwater igneous complex, Montana: a quantitative mineralogical study. Geological Society of America Memoir, vol. 80, pp. 230.

Hess, G. B. (1972) Heat and mass transport during crystallization of the Stillwater igneous complex. Geological Society of America Memoir, vol. 132, pp. 503-520.

Holness, M.B., Cawthorn, R.G. and Roberts, J. (2017a). The thickness of the crystal mush on the floor of the Bushveld magma chamber. Contributions to Mineralogy and Petrology, vol. 172:102.

Holness, M. B., Morris, C., Vukmanovic, Z. and Morgan, D. J. (2020) Insights into magma chamber processes from the relationship between fabric and grain shape in troctolitic cumulates. Frontiers in Earth Science, DOI: 10.3389/feart.2020.00352.

Holness, M.B., Vukmanovic, Z., and Mariani, E. (2017b) Assessing the role of compaction in the formation of adcumulates: a microstructural perspective. Journal of Petrology, vol. 58, pp. 643-673.

Hunt, E.J., Latypov, R. and Horváth, P. (2018) The Merensky Reef cyclic unit, Bushveld Complex, South Africa: reality or myth? Minerals, vol. 8, DOI: 10.3390/min8040144.

Hunter, R.H. & Sparks, R.S.J. 1987. The differentiation of the Skaergaard intrusion. Contributions to Mineralogy and Petrology, vol. 95, pp. 451-461.

Humphreys, M. C. S. (2009) Chemical evolution of intercumulus liquid, as recorded in plagioclase overgrowth rims from the Skaergaard intrusion. Journal of Petrology, vol. 50, pp. 127-145.

Hupper, H.E. and Sparks, R.S.J. (1980) The fluid dynamics of a basaltic magma chamber replenished by influx of hot, dense ultrabasic magma. Contributions to Mineralogy and Petrology, vol. 75, pp. 279-289.

Huppert, H.E. and Sparks, R.S.J. (1984) Double-diffusive convection due to crystallization in magmas. Annual Review of Earth and Planetary Science, vol. 12, pp. 11-37.

Huppert, H.E. and Turner, J.S. (1981) Double diffusive convection. Journal of Fluid Mechanics, vol. 106, pp. 299-329.

Huppert, H.E., Turner, J.S. and Sparks, R.S.J. (1982) Replenished magma chambers: effects of compositional zonation and input rates. Earth and Planetary Science Letters, vol. 57, pp. 345-357.

Irvine, T. N. (1970) Crystallization sequences in the Muskox intrusion and other layered intrusions, I. Olivine-pyroxene-plagioclase relations. Geological Society of South Africa Special Publication 1, pp. 441–476.

Irvine, T.N. (1975) Crystallization sequences in the Muskox intrusion and other layered intrusions-II. Origin of chromitite and similar deposits of other magmatic ores. Geochimica et Cosmochimica Acta, vol. 39, pp. 991-1008.

Irvine, T.N. (1977) Origin of chromitite layers in the Muskox intrusion and other stratiform intrusions: a new interpretation. Geology, vol. 5, pp. 273-277.

Irvine, T.N. (1980) Magmatic density currents and cumulus processes. American Journal of Science, vol. 280, pp. 1-58.

Irvine, T. N. (1987) Layering and related structures in the Duke Island and Skaergaard intrusions: similarities, differences, and origins. In: Parson, I. (ed) Origins of igneous layering. D. Reidel Publishing Company 196, pp. 185-245.

Irvine, T.N., Andersen, J.C. and Brooks, C.K. (1998) Included blocks (and blocks within blocks) in the Skaergaard intrusion: geological relations and the origins of rhythmic modally graded layers. Geological Society of America Bulletin, vol. 110, pp. 1398-1447.

Irving, A.J. (1978) A review of experimental studies of crystal/liquid trace element partitioning. Geochmica et Cosmochimica Acta, vol. 42, pp. 743-770.

Jackson, E.D. (1961) Primary textures and mineral associations in the Ultramafic Zone of the Stillwater Complex, Montana. Geological Survey Professional Paper 358.

Jackson E. D. (1970) The cyclic unit in layered intrusions, a comparison of repetitive stratigraphy in the ultramafic parts of the Stillwater, Muskox, Great Dyke and Bushveld Complex (with discussion). Geological Society of South Africa Special Publication 1, pp. 391-424.

Jackson, M.D., Blundy, J. and Sparks, R.S.J. (2018) Chemical differentiation, cold storage and remobilization of magma in the Earth's crust. Nature, vol. 564, pp. 405-409.

Jaupart, C. and Brandeis, G. (1986) The stagnant bottom layer of convecting magma chambers. Earth and Planetary Science Letters, vol. 80, pp. 183-199.

Jellinek, A.M., Kerr, R.C. and Griffiths, R.W. (1999) Mixing and compositional stratification produced by natural convection 1. Experiments and their application to Earth's core and mantle. Journal of Geophysical Research, vol. 104, pp. 7183-7201.

Kaufmann, F.E.D., Hoffmann, M.C., Bachmann, K., Veksler, I.V., Trumbull, R.B. and Hecht, L. Variations in composition, texture, and platinum group element mineralization in the Lower Group and Middle Group Chromitites of the northwestern Bushveld Complex, South Africa. Economic Geology, vol. 114, no. 3, pp. 569-590.

Klemm, D.D., Henckel, J. and Dehm, R. (1985) The geochemistry of titanomagnetite in magnetite layers and their host rocks of the Eastern Bushveld Complex. Economic Geology, vol. 80, pp. 1075-1088.

Kerr, R. C. (1994) Melting driven by vigorous compositional convection. Journal of Fluid Mechanics, vol. 280, pp. 255–285.

Knipping, J.L., Webster, J.D., Simon, A.C. and Holtz, F. (2019) Accumulation of magnetite by flotation on bubbles during decompression of silicate magma. Scientific Reports, vol. 9, DOI 10.1038/s41598-40376-1.

Koyaguchi, T. (1990) Graphical estimations of magma densities and compositional expansion coefficients. Contributions to Mineralogy and Petrology, vol. 105, pp. 173-176.

Kruger, F.J., Cawthorn, R.G. and Walsh, W.L. (1987) Strontium isotopic evidence against magma addition in the Upper Zone of the Bushveld Complex. Earth and Planetary Science Letters, vol. 84, pp. 51-58.

Kruger, F.J. (1994) The Sr-isotopic stratigraphy of the western Bushveld Complex. South African Journal of Geology, vol. 97, no. 4, pp. 393-398.

Kruger, F.J. (2005) Filling the Bushveld Complex magma chamber: lateral expansion, roof and floor interaction, magmatic unconformities, and the formation of giant chromitite, PGE and Ti-V-magnetitite deposits. *Mineralium Deposita*, DOI: 10.1007/s00126-005-0016-8.

Kruger F.J. and Smart, R. (1987) Diffusion of trace elements during bottom crystallization of double-diffusce convection systems: the magnetitite layers of the Bushveld Complex. Journal of Volcanology and Geothermal Research, vol. 34, pp. 133-142.

Kruger, W. and Latypov, R. (2020a) Fossilized solidification fronts in the Bushveld Complex argue for liquid-dominated magmatic systems. Nature Communications, DOI: 10.1038/s41467-020-16723-6.

Kruger, W. and Latypov, R. (2020b) Magmatic karst reveals dynamics of crystallization and differentiation in Earth's magma chambers. In progress.

Kushiro, I. 1969. The system forsterite-diopside-silica with and without water at high pressures. *American Journal of Science*, 267, 269-294.

Langmuir, C.H. (1989) Geochemical consequences of in situ crystallization. Nature, vol. 340, pp. 199-205.

Latypov, R.M. and Chistyakova, S. Yu. (2001) Physicochemical aspects of magnetite gabbro formation in the layered intrusion of the Western Pansky Tundra, Kola Peninsula, Russia. Petrology, vol. 9, pp. 25-45.

Latypov, R.M and Chistyakova, S. (2020) Origin of non-cotectic cumualtes: a novel approach. Geology, vol. 48, no. 6, pp. 604-608.

Latypov, R., Chistyakova, S., Costin, G., Namur, O., Barnes, S. and Kruger, W. (2020) Monomineralic anorthosites in layered intrusions are indicators of the magma chamber

replenishment by plagioclase-only-saturated melts. Scientific Reports, vol. 10, article number: 3839.

Latypov, R., Chistyakova, S. and Mukherjee, R. (2017a) A novel hypothesis for origin of massive chromitites in the Bushveld Igneous Complex. Journal of Petrology, vol. 58, no. 10, pp. 1899-1940.

Latypov, R. M., Chistyakova, S. Yu., Barnes, S. J. and Hunt, E. J. (2017b) Origin of platinum deposits in layered intrusions by in situ crystallization: evidence from undercutting Merensky Reef of the Bushveld Complex. Journal of Petrology, vol. 58, pp. 715-762.

Latypov, R.M., Chistyakova, S.Yu., Namur, O. and Barnes, S. (2020) Dynamics of evolving magma chambers: textural and chemical evolution of cumulates at the arrival of new liquidus phases. Earth-Science Reviews, vol. 210, article number: 103388.

Latypov, R., Chistyakova, S., Page, A. and Hornsey, R. (2016) Field evidence for the *in situ* crystallization of the Merensky Reef. Journal of Petrology, vol. 56, no. 12, pp. 2341-2372.

Latypov, R., Chistyakova, S., Van der Merwe, J. and Westraat, J. (2019a) A note on the erosive nature of potholes in the Bushveld Complex. South African Journal of Geology, DOI: 10.25131/sajg.122.0042.

Latypov, R. M., Chistyakova, S. Yu., Grieve, R. and Huhma, H. (2019b) Evidence for igneous differentiation in Sudbury Igneous Complex and impact-driven evolution of terrestrial planet proto-crusts. Nature Communications, vol. 10, article number: 508.

Latypov, R., Costin, G., Chistyakova, S., Hunt, E.J., Mukherjee, R. and Naldrett, T. (2018) Platinum-bearing chromite layers are caused by pressure reduction during magma ascent. Nature Communications, DOI: 10.1038/s41467-017-02773-w.

Latypov, R. M. and Egorova, V. (2012) Plagioclase compositions give evidence for in situ crystallization under horizontal flow conditions in mafic sills. Geology, vol. 40, pp. 883-161.

Latypov, R., Morse, T. Robins, B., Wilson, J. R., Cawthorn, G., Tegner, C., Holness, M., Lesher, C., Barnes, S., O'Driscoll, B., Veksler, I., Higgins, M. D., Wilson, A., Namur, O., Chistyakova, S., Naslund, H. R. and Thy, P. (2015) A fundamental dispute: A discussion

of “On some fundamentals of igneous petrology” by Bruce D. Marsh, Contributions to Mineralogy and Petrology (2013) 166:665–690. Contributions to Mineralogy and Petrology, vol. 169, article number: 20.

Lesher, C.M., Carson, H.J.E. and Houlé, M.G. (2019) Genesis of chromite deposits by dynamic upgrading of Fe ± Ti oxide xenocrysts. Geology, DOI: 10.1130/G45448.1.

Lesher, C.E. and Spera, F.J. (2015) Thermodynamic and transport properties of silicate melts and magma. In: Sigurdsson, H., Houghton, B., Rymer, H, Stix, J. and McNutt, S. (eds) The Encyclopedia Of Volcanoes, Amsterdaml: Academic Press, Elsevier, pp. 113–141.

Lomberg, K.G., Martin, E.S., Patterson, M.A. and Venter, J.E. (1999) The morphology of potholes in the UG2 chromitite layer and Merensky Reef (pothole reef facies) at Union Section, Rustenburg platinum mines. South African Journal of Geology, vol. 102, pp. 209-220.

Lundgaard, K.L., Tegner, C., Cawthorn, R.G., Kruger, F.J. and Wilson, J.R. (2006) Trapped intercumulus liquid in the Main Zone of the eastern Bushveld Complex, South Africa. Contributions to Mineralogy and Petrology, vol. 151, pp. 352-369.

Maier W.D., Barnes, S.J. and Groves, D.I. (2013) The Bushveld Complex, South Africa: formation of platinum–palladium, chrome- and vanadium-rich layers via hydrodynamic sorting of a mobilized cumulate slurry in a large, relatively slowly cooling, subsiding magma chamber. Mineral Deposita, vol. 48, no. 1, pp. 1-56.

Maier, W.D., Karykowski, B.T. and Yang, S-H. (2016) Formation of transgressive anorthosite seams in the Bushveld Complex via tectonically induced mobilisation of plagioclase-rich crystal mushes.

Maila, R.P. (2015) Geochemistry of magnetitite layers in the Upper Zone of the Bushveld Complex, South Africa. Thesis, University of the Witwatersrand.

Marsh, B.D. (1996) Solidification fronts and magmatic evolution. Mineralogical Magazine, vol. 60, pp. 5-40.

Marsh, B. D. (2006) Dynamics of magma chambers. Elements, vol. 2, pp. 287-292.

Marsh, B.D. (2013) On some fundamentals of igneous petrology. Contrib. Mineral. Petrol. 166, 665-690.

Martin, D., Griffiths, R.W. and Campbell, I.H. (1987) Compositional and thermal convection in magma chambers. Contributions to Mineralogy and Petrology, vol. 96, pp. 465-475.

McBirney, A.R. (1995) Mechanisms of differentiation of the Skaergaard Intrusion. Journal of the Geological Society of London, vol. 152, pp. 421-435.

McBirney, A.R. and Noyes, R.M. (1979) Crystallization and layering of the Skaergaard intrusion. Journal of Petrology, vol. 20, pp. 487-554.

McCarthy, T.S. and Cawthorn, R.G. (1983) The geochemistry of vanadiferous magnetite in the Bushveld Complex: implications for crystallization mechanisms in layered complexes. Mineralium Deposita, vol. 18, pp. 505-518.

McCarthy, T.S. and Cawthorn, R.G. (1985) Mineral layering in the Bushveld Complex: implications for Cr abundances in magnetite from closely spaced magnetitite and intervening silicate-rich layers. Economic Geology, vol. 50, pp. 1062-1074.

McKenzie, D.P. (2011) Compaction and crystallization in magma chambers: towards a model for the Skaergaard intrusion. Journal of Petrology, vol. 52, pp. 905–930.

Merkle, R.K.W. and Von Greunewaldt, G. (1986) Compositional variation of Co-rich pentlandite: relation to the evolution of the Upper Zone of the Western Bushveld Complex, South Africa. Canadian Mineralogist, vol. 24, pp. 529-546.

Molyneux, T.G. (1970) The geology in the area in the vicinity of Magnet Heights, Eastern Transvaal, with special reference to the magnetic iron ore. Geological Society of South Africa Special Publication 1, pp. 228-241.

Molyneux, T.G. (1972). X-ray data and chemical analysis of some titanomagnetite and ilmenite samples from the Bushveld Complex, South Africa. Mineralogical Magazine, vol. 38, pp. 863-871.

Molyneux, T.G. (1974) A geological investigation of the Bushveld Complex in Sekhukhuneland and part of the Steelpoort Valley. Transactions of the Geological Society of South Africa, vol. 77, 329-338.

Morse, S.A. (1979) Kiglapait geochemistry II: Petrography. Journal of Petrology, vol. 20, pp. 591-624.

Morse, S. A. (1986a) Thermal structure of crystallizing magma with two-phase convection. Geological Magazine, vol. 123, pp. 205-214.

Morse, S.A. (1986b) Convection in aid of adcumulus growth. Journal of Petrology, vol. 27, pp. 1183-1214.

Morse, S. A. (1988) Motion of crystals, solute, and heat in layered intrusions. Canadian Mineralogist, vol. 26, pp. 209-224.

Morse, S.A. (2002) No mushy zone in Earth's core. Geochimica Cosmochimica Acta, vol. 66, pp. 2155-2165.

Morse, S. A. (2015) Kiglapait Intrusion, Labrador. In: Charlier, B., Namur, O., Latypov, R. and Tegner, C., (eds.), Layered Intrusions. Springer, pp. 589-648.

Mukherjee, R., Latypov, R. and Balakrishna, A. (2017) An intrusive origin of some UG-1 chromitite layers in the Bushveld Igneous Complex, South Africa: insights from field relationships. Ore Geology Reviews, vol. 90, pp. 94-109.

Namur, O., Charlier, B. (2012) Efficiency of compaction and compositional convection during mafic crystal mush solidification: the Sept Iles layered intrusion, Canada. Contributions to Mineralogy and Petrology, vol. 163, pp. 1049-1068.

Namur, O., Charlier, B., Toplis, M.J., Higgins, M.D., Liégeois, J.P. and Vander Auwera, J. (2010) Crystallization sequence and magma chamber processes in the ferrobasaltic Sept Iles layered intrusion, Canada. Journal of Petrology, vol. 51, no. 6, pp. 1203-1236.

Namur, O. and Humphreys, M.C.S. (2018) Trace element constraints on the differentiation and crystal mush solidification in the Skaergaard Intrusion, Greenland. Journal of Petrology, vol. 59, pp. 387-418.

Namur, O., Higgins, M.D. and Vander Auwera, J. (2015) The Sept Iles intrusive suite, Quebec, Canada. In: Charlier, B., Namur, O., Latypov, R. and Tegner, C (eds). Layered Intrusions. Springer Geology, pp. 465-515.

Naslund, H.R. and McBirney, A.R. (1996) Mechanisms of formation of igneous layering. In: Cawthorn, R.G. (ed). Layered Intrusions. Amsterdam: Elsevier, pp. 1-44.

Nex, P.A.M. (2004) Formation of bifurcating chromitite layers of the UG1 in the Bushveld Igneous Complex, an analogy with sand volcanoes. Journal of the Geological Society, London, vol. 161, pp. 903-909.

O'Driscoll, B. and VanTongeren, J.A. (2017) Layered intrusions: from petrological paradigms to precious metal repositories. Elements, vol. 13, no. 6, pp. 383-389.

Parsons, I (ed). 1987. Origins of igneous layering. NATO ASI series C 196. D. Reidel Publishing Company, Dordrecht, Holland.

Pebane, M. and Latypov, R. (2017) The significance of magmatic erosion for bifurcation of UG1 chromitite layers in the Bushveld Complex. Ore Geology Reviews, vol. 90, pp. 65-93.

Philpotts, A.R. (1967) Origin of certain iron-titanium oxide and apatite rocks. Economic Geology, vol. 62, pp. 303–315.

Philpotts, A. R. and Dickson, L. D. (2000) The formation of plagioclase chains during convective transfer in basaltic magma. Nature, vol. 406, nr. 6791, pp. 59-61.

Reynolds, I.M. (1985a) Contrasted mineralogy and textural relationships in the uppermost titaniferous magnetite layers of the Bushveld Complex in the Bierkraal area north of Rustenburg. Economic Geology, vol. 80, 1027-1048.

Reynolds, I.M. (1985b) The nature and origin of titaniferous magnetite-rich layers in the Upper Zone of the Bushveld Complex: a review and synthesis. Ecnomic Geology, vol. 80, pp. 1089-1105.

Roeder, P.L. and Osborn, E.F. (1966) Experimental data for the system MgO-FeO-Fe_2O_3-$CaAl_2Si_2O_8$-SiO_2 and their petrological implications. American Journal of Science, vol. 264, pp. 428-480.

Roelofse, F. & Ashwal, L.D. (2012) The Lower Main Zone in the northern limb of the Bushveld Complex – a 1.3 km sequence of intruded and variably contaminated crystal mushes. Journal of Petrology, vol. 53, pp. 1449-1476.

Rollinson, H. (1993) Using geochemical data: evaluation, presentation, and interpretation. Edinburgh, Pearson.

Schmidt, E.R. (1952) The structure and composition of the Merensky Reef and associated rocks on the Rustenburg Platinum Mine. Transactions of the Geological Society of South Africa, vol. 55, pp. 233-279.

Schock, H.H. (1979) Distribution of rare-earth and other trace elements in magnetites. Chemical Geology, vol. 26, pp. 119-133.

Scoates, J. and Friedman, R. (2008) Precise age of the platiniferous Merensky Reef, Bushveld Complex, South Africa, by the U-Pb zircon chemical abrasion ID-TIMS technique. Economic Geology, vol. 103, no. 3, pp. 465-471.

Scoates, J.S., Wall, C.J., Friedman, R.M., Weis, D., Mathez, E. and VanTongeren, J.A. (2021) Dating the Bushveld Complex: timing of crystallization, duration of magmatism, and cooling of the world's largest layered intrusion and related rocks. Journal of Petrology, DOI: https://doi.org/10.1093/petrology/egaa107.

Scoon, R.N. and Mitchell, A.A. (2012) The Upper Zone of the Bushveld Complex at Roossenekal, South Africa: geochemical stratigraphy and evidence of multiple episodes of magma replenishment. South Africa Journal of Geology, vol. 115, no. 4, pp. 515-534.

Scoon, R.N., Costin, G. and Gräbe, P.J. (2017) Geology and origin of the vanadiferous Fe-Ti oxide-rich Kennedy's Vale discordant body, Eastern Limb of the Bushveld Complex, South Africa. South African Journal of Geology, vol. 120, nr. 2, pp. 251-270.

Seedhouse, J.K. and Donaldson, C.H. (1996) Compositional convection caused by olivine crystallization in a synthetic basalt melt. Mineralogical Magazine, vol. 60, pp. 115-130.

Shirley, D.N. (1986) Compaction of igneous cumulates. Journal of Geology, vol. 94, pp. 795-809.

Snyder, D. and Tait, S. (1995) Replenishment of magma chambers: comparison of fluid-mechanic experiments with field relations. Contributions to Mineralogy and Petrology, vol. 122, pp. 230-240.

Solomon, S. C. (1980) Differentiation of crusts and cores of the terrestrial planets: Lessons for the early Earth? Precambrian Research, vol. 10, pp. 177–194.

Sparks, R. S. J., Pinkerton, H., and Macdonald, R. (1977) The transport of xenoliths in magmas. Earth and Planetary Science Letters, vol. 35, pp. 234–238.

Tait, S.R., Huppert, H.E. and Sparks, R.S.J. (1984) The role of compositional convection in the formation of adcumulus rocks. Lithos, vol. 17, pp. 139-146.

Tait, S. and Jaupart, C. (1989) Compositional convection in viscous melts. Nature, vol. 338, pp. 571-574.

Tait, S.R. and Juapart, C. (1992) Compositional convection in a reactive crystalline mush and melt differentiation. Journal of Geophysical Research, vol. 97, pp. 6735-6756.

Tait, S.R. and Juapart, C. (1996) The production of chemically stratified and adcumulate plutonic igneous rocks. Mineralogical Magazine, vol. 60, pp. 99-114.

Tanner, D., Mavrogenes, J.A., Arculus, R.J. and Jenner, F.E. (2014) Trace element stratigraphy of the Bellevue core, Northern Bushveld: multiple magma injections obscured by diffusive processes. Journal of Petrology, vol. 55, pp. 859-882.

Tatsumi, Y. & Suzuki, T. 2009. Tholeiitic vs calc-alkali differentiation and evolution of arc crust: constraints from metling experiments on a basalt from the Izu-Bonin-Mariana Arc. *Journal of Petrology*, 50, 1575-1603.

Tegner, C., Cawthorn, R.G. and Kruger, F.J. (2006) Cyclicity in the Main and Upper Zones of the Bushveld Complex, South Africa: crystallization from a zoned magma sheet. Journal of Petrology, vol. 47, no. 11, pp. 2257-2279.

Tegner, C., Thy, P., Holness, M.B., Jakobsen, J.K. and Lesher, C.E. (2009) Differentiation and compaction in the Skaergaard intrusion. Journal of Petrology, vol. 50, pp. 813–840.

Thompson, R.N. and Patrick, D.J. (1968) Folding and slumping in a layered gabbro. Geological Journal, vol. 6, pp. 139-146.

Toplis, M.J and Corgne, A. (2002) An experimental study of element partitioning between magnetite, clinopyroxene, and iron-bearing silicate liquids with particular emphasis on vanadium. Contributions to Mineralogy and Petrology, vol. 144, pp. 22-37.

VanTongeren, J.A. and Mathez, E.A. (2013) Incoming magma composition and style of recharge below the Pyroxenite Marker, Eastern Bushveld Complex, South Africa. Journal of Petrology, vol. 54, pp. 1585-1605.

VanTongeren, J.A. Mathez, E.A. and Kelemen, P.B. (2010) A felsic end to Bushveld differentiation. Journal of Petrology, vol. 51, pp. 1891-1912.

VanTongeren, J.A. and Mathez, E.A. Large-scale liquid immiscibility at the top of the Bushveld Complex, South Africa. Geology, vol. 40, 491-494 (2012).

Vaughan, W.M., Head, J.W., Wilson, L. and Hess, P.C. (2013) Geology and petrology of enormous volumes of impact melt on the Moon: A case study of the Orientale impact melt sea. Icarus, vol. 223, pp. 749-765.

Veksler, I.V., Dorfman, A.M., Danyushevsky, L.V., Jakobsen, J.K. and Dingwell, D.B. (2006) Immiscible silicate liquid partition coefficients: implications for crystal-melt element partitioning and basalt petrogenesis. Contributions to Mineralogy and Petrology, vol. 152, pp. 685-702.

Vermaak, C.F. (1976) The Merensky Reef; thoughts on its environment and genesis. Economic Geology, vol. 71, no. 7, pp. 1270-1298.

Vernon, R.H. (2018) A practical guide to rock microstructure. 2nd ed. New York: Cambridge University Press.

Von Gruenewaldt, G. (1976) Sulfides in the Upper Zone of the Eastern Bushveld Complex. Economic Geology, vol. 71, pp. 1324-1336.

Viljoen, M. (2016) The Bushveld Complex. Episodes, vol. 39, no. 2, pp. 239-268.

Viljoen, M.J. and Scoon, R.N. The distribution and main geologic features of discordant bodies of iron-rich ultramafic pegmatites in the Bushveld Complex. Economic Geology, vol. 80, pp. 1109-1128.

Voordouw, R., Gutzmer, J. and Beukes, N.J. (2009) Intrusive origin for Upper Group (UG1, UG2) stratiform chromitite seams in the Dwars River area, Bushveld Complex, South Africa. Mineralogy and Petrology, vol. 97, pp. 75-94.

Vukmanovic, Z., Holness, B., Stock, M.J. and Roberts, R.J. (2019) The creation and evolution of crystal mush in the Upper Zone of the Rustenburg Layered Suite, Bushveld Complex, South Africa. Journal of Petrology, DOI: 10.1093/petrology/egz038.

Waele, J.D., Gutiérrez, F., Parise, M., and Plan, L. (2011) Geomorphology of natural hazards in karst areas: a review. Geomorphology, vol. 134, pp. 1-8.

Wager, L. R. (1963) The mechanism of adcumulate growth in the layered series of the Skaergaard Intrusion. Mineralogical Society of America Special Paper 1, pp. 1-9.

Wager, L.R. and Brown, G. M. (1939) Geological investigations in east Greenland. Part III. The petrology of the Skaergaard intrusion, Kangerdlugssuaq, East Greenland. Economic Geology, vol. 52, pp. 855-903.

Wager, L.R. and Brown, G.M. (1968) Layered igneous rocks. Oliver & Boyed, Edinburgh and London.

Webb, S., Ashwal, L.D. & Cawthorn, R.G. (2011) Continuity between eastern and western Bushveld Complex, South Africa, confirmed by xenoliths from kimberlite. Contributions to Mineralogy and Petrology, vol. 162, pp. 101-107.

Willemse, J. (1969) The geology of the Bushveld Igneous Complex, the largest repository of magmatic ore deposits in the world. Economic Geology Monograph, vol. 4, pp. 1-22.

Wilson, A.H. (2015) The earliest stages of emplacement of the Eastern Bushveld Complex: development of the Lower Zone, Marginal Zone and Basal Ultramafic Sequence. Journal of Petrology, vol. 56, pp. 347-388.

Wright, C.J., McCarthy, T.S. and Cawthorn, R.G. (1983) Numerical modelling of trace element fractionation during diffusion controlled crystallization. Computers and Geosciences, vol. 9, no. 3, pp. 367-389.

Yuan, Q., Namur, O., Fischer, L.A., Roberts, R.J., Lü, X., Charlier, B. (2017) Pulses of plagioclase-laden magmas and stratigraphic evolution in the Upper Zone of the Bushveld Complex, South Africa. Journal of Petrology, vol. 58, no. 8, pp. 1619-1644.

Zang, X.Q., Song, X.Y., Chen, L.M., Xie, W., Yu, S.Y., Zeng, W.Q., Deng, Y.F., Zhang, J.F., and Gui, S.G. (2012) Fractional crystallization and the formation of thick Fe-Ti oxide layers in the Baima layered intrusion, SW China. Ore Geology Reviews, vol. 49, pp. 96-108.

Zhang, Y., Ni, H. and Chen, Y. (2010) Diffusion data in silicate melts. Reviews in Mineralogy and Geochemistry, vol. 72, pp. 311-408.

Zeh, A., Ovtcharova, M., Wilson, A.H. and Schaltegger, U. (2015) The Bushveld Complex was emplaced and cooled in less than one million years – results of zirconology, and geotectonic implications. Earth and Planetary Science Letters, vol. 418, pp. 103-114.

APPENDICES

Appendix A: Data used for the construction of a calibration curve for the portable XRF

A.2 Data used for the construction of a calibration curve for the portable XRF for the Bottom seam.

Portable XRF Data							In-house XRF data
Sample	Ti (ppm)	Ti 2Θ error	V (ppm)	V 2Θ error	Cr (ppm)	Cr 2Θ error	Cr
3B	74584	732	7082	235	5804	122	8175
1D	49851	629	5578	209	1769	85	3398
1G	64403	669	6799	219	1152	74	1968
2G	96782	842	7498	260	2684	98	3872
2D	62650	638	6117	206	4548	104	6668
1H	85638	815	7549	258	1317	84	2593
1F	93057	839	7149	258	1747	89	2517
1C	87829	823	8856	267	4231	116	5447
2J	67386	731	7102	239	716	74	1781
2L	69345	771	7159	252	2541	101	2422
2E	60954	624	5768	200	2750	86	4920
2C	98734	937	8298	294	5853	139	6747
2N	93038	798	6754	244	265	63	708
4A	58200	600	5898	192	7948	124	12582

A.2 Data used for the construction of a calibration curve for the portable XRF for the Bottom seam.

Portable XRF Data							In-house XRF data
Sample	Ti (ppm)	Ti 2Θ error	V (ppm)	V 2Θ error	Cr (ppm)	Cr 2Θ error	Cr (ppm)
A	53371	617	5411	200	1903	79.75	6536
B	84557	780	9034	255	2692	96.89	5842
C	78663	730	8473	239	2350	89.76	5592
D	98284	902	10917	298	1119	90.63	2463
E	99525	896	10314	292	1341	91.11	2847
F	110170	907	9140	283	383	74.27	1269
G	93971	841	9921	275	523	76.83	1399
H	109696	940	10806	303	2053	101.13	4113
I	99916	889	10466	290	1517	92.79	3292
J	98172	858	10247	280	2289	97.82	4661

Appendix B: Portable XRF data for two-dimensional chemical contour maps of the Main Magnetite Layer

B.1 Portable XRF data for the outcrop analysed in Figure 2.3a.

Coordinates										
X (horizontal) cm	Y (vertical) cm	Ti (ppm)	Ti 2Θ Error (ppm)	V (ppm)	V 2Θ Error (ppm)	Cr (ppm)	Cr 2Θ Error (ppm)	Cr/V	Cr/V*9757	Cr/V* 9757 2Θ error
1	1	53383.82	625.68	5634.09	204.95	8157.76	136.23	1.44	14127	778
5	1	62482.77	677.55	6565.77	221.63	11081.27	157.28	1.68	16467	817
9	1	53894.91	654.15	5966.22	216.51	10277.2	157.34	1.72	16807	900
17	1	15758.95	285.89	1927.64	96.46	2644.69	65.23	1.37	13386	1053
29	1	49890.95	539.88	5447.76	177.93	9437.78	128.94	1.73	16903	809
33	1	31796.23	437.17	3887.41	147.54	5986.4	104.16	1.53	15025	864
37	1	62805.13	625.63	6404.78	203.27	8779.88	131.26	1.37	13375	645
41	1	21193.16	367.52	2777.82	125.84	3309.47	81.71	1.19	11624	852
53	1	43448.63	575.99	4863.91	191.31	5674.97	119.39	1.16	11384	715
61	1	40812.65	520.83	4477.08	172.2	5007.27	105.09	1.11	10912	675
65	1	31296.42	438.24	3629.05	146.64	4647.3	96.09	1.28	12495	795
69	1	57396.53	605.69	5945.64	197.62	7372.39	123.96	1.23	12098	626
73	1	26751.72	447.68	3241.91	151.79	3680.62	97.05	1.13	11077	851
77	1	60360.69	659.61	6283.06	215.52	8072.19	137.6	1.28	12535	667
81	1	26586.17	471.8	3231.92	160.2	3839.36	104.48	1.18	11591	936

B.1 (continued) Portable XRF data for the outcrop analysed in Figure 2.3a.

Coordinates										
X (horizontal) cm	Y (vertical) cm	Ti (ppm)	Ti 2Θ error (ppm)	V (ppm)	V 2Θ error (ppm)	Cr (ppm)	Cr 2Θ error (ppm)	Cr/V	Cr/V*9757	Cr/V* 9757 2Θ error
85	1	62163.72	630.94	6380.53	205.36	9117.28	136.32	1.42	13942	679
89	1	41878.65	498.37	4541.95	164.17	6447.07	109.87	1.41	13850	764
93	1	12597.12	289.31	1673.36	99.56	2862.07	75.18	1.71	16688	1522
97	1	15318.18	316.18	1881.14	106.15	3232.76	78.93	1.71	16768	1437
101	1	60988.09	633.22	6103.33	205.13	8271.8	131.59	1.35	13224	678
1	5	64450.36	688.11	6900.14	225.95	7751.1	136.76	1.12	10960	571
5	5	18799.47	387.63	2739.17	136.56	3058.16	89.51	1.11	10893	907
13	5	53201.18	577.75	5796.1	190.51	5949.48	112.58	1.02	10015	536
17	5	39668.7	496.62	4348.14	164.14	4243.65	95.23	0.97	9523	596
21	5	70070.61	693.56	6974.12	224.33	7459.15	131.13	1.06	10436	536
25	5	42521.43	534.76	4852.49	178.19	5793.03	112.47	1.19	11648	679
29	5	71190.28	738.17	7168.47	239.43	10216.53	157.3	1.42	13906	702
33	5	42623.15	524.46	4593.5	172.72	5525.85	108.16	1.20	11737	697
37	5	59188.14	619.13	5873.51	200.22	6412.99	117.92	1.09	10653	579
41	5	100868.9	859.66	9249.98	273.3	9147.22	151.01	0.98	9649	458
45	5	64276.97	682.89	6981.67	224.94	6990.8	131.01	1.00	9770	514
53	5	29656.94	438.35	3647.51	148.62	3363.99	87.06	0.92	8999	625
69	5	54529.16	599.84	5820.28	196.94	6225.7	117.44	1.06	10437	569
73	5	47533.43	614.02	5184.23	202.9	5342.4	120.52	1.03	10055	646
77	5	54394.82	573.27	5559.77	186.52	5414.19	105.51	0.97	9502	521
81	5	52672.41	588.73	6209.94	197.23	6436.99	118.34	1.03	10114	524

B.1 (continued) Portable XRF data for the outcrop analysed in Figure 2.3a.

Coordinates										
X (horizontal) cm	Y (vertical) cm	Ti (ppm)	Ti 2Θ Error (ppm)	V (ppm)	V 2Θ Error (ppm)	Cr (ppm)	Cr 2Θ Error (ppm)	Cr/V	Cr/V*9757	Cr/V* 9757 2Θ error
85	5	46570.7	575.17	5422.94	192.45	5693.85	116.39	1.049956	10244	594
97	5	36630.66	538.54	4863.47	185.56	5808.02	121.76	1.194213	11652	716
101	5	47927.25	547.47	5108.47	179.85	5680.44	109.5	1.111965	10849	613
1	9	56192.26	634.24	6066.07	208.8	5383.18	116.3	0.887425	8659	502
5	9	46233.39	519.49	4579.02	168.12	4245.39	93.54	0.927139	9046	552
9	9	64621.79	678.36	7082.55	223.84	6358.68	125.29	0.897795	8760	464
13	9	65580.29	688.86	7140.95	226.95	6309.53	125.67	0.88357	8621	460
17	9	56105.18	614.77	6411.57	204.65	5511.64	113.62	0.85964	8388	455
21	9	63032.21	711.33	7730.18	240.27	6740.01	135.63	0.871909	8507	450
25	9	35678.38	458.33	4867.82	158.38	4454.5	92.98	0.915091	8929	493
29	9	30450.62	463.03	4220.04	161.21	3335.49	92.02	0.790393	7712	528
33	9	48231.48	587.65	5807.8	197.98	4732.95	109.57	0.81493	7951	471
37	9	21466.92	340.22	2589.24	115.23	2273.33	67.5	0.877991	8567	665
41	9	46163.98	517.29	4684.69	168.23	3970.23	90.99	0.84749	8269	505
49	9	22450.45	366.46	3028.22	126.78	2284.4	70.74	0.754371	7360	560
53	9	28819.4	418.76	3640.57	142.79	3384.19	84.52	0.929577	9070	606
61	9	41932.84	535.33	5961.26	186.77	5286.85	109.48	0.886868	8653	465
65	9	43513.71	524.16	5172.39	176.12	4478.86	99.45	0.865917	8449	492
69	9	36570.26	475.77	4841.68	163.29	4220.92	93.32	0.871788	8506	492
77	9	63188.07	656.27	6573.53	214.24	5461.74	114.79	0.830869	8107	449

B.1 (continued) Portable XRF data for the outcrop analysed in Figure 2.3a.

Coordinates										
X (horizontal) cm	Y (vertical) cm	Ti (ppm)	Ti 2Θ Error (ppm)	V (ppm)	V 2Θ Error (ppm)	Cr (ppm)	Cr 2Θ Error (ppm)	Cr/V	Cr/V*9757	Cr/V* 9757 2Θ error
89	9	42453.45	541.63	5506.61	185.16	4628.54	104.2	0.84	8201	476
93	9	46777.1	543.78	5587.05	182.68	5423.64	106.88	0.97	9472	513
97	9	44019.52	549.16	4873.22	181.97	4555.64	104.64	0.93	9121	571
101	9	58479.56	625.67	5890.49	203.04	5556.52	113.67	0.94	9204	524
1	13	51311.5	544.45	5535.69	179.08	4475.95	95.9	0.80	7889	438
9	13	47735.31	598.22	7017.74	210.21	5713.36	119.8	0.81	7943	417
13	13	58902.92	661.44	7034.02	222.16	5694.97	121.24	0.80	7900	431
33	13	41521.03	480.29	4574.06	158.78	3521.07	84.4	0.76	7511	457
37	13	38597.68	505.59	4962.82	172.58	3516.31	91.43	0.70	6913	435
41	13	63408.75	682.4	7314.76	227.41	5505.32	119.26	0.75	7343	400
45	13	45097.66	582.42	5192.71	194.43	3894.09	103.2	0.75	7317	486
49	13	53092.45	580.31	6546.88	196.04	5147.07	105.74	0.78	7671	399
65	13	39577.49	531.38	4687.61	178.71	3579.19	97.21	0.76	7450	506
77	13	20622.35	360.3	2924.63	126.32	2063.57	70.73	0.71	6884	557
81	13	48731.56	614.63	5619.06	205.17	4297.71	109.26	0.76	7463	480
85	13	38520.6	502.18	4849.15	170.89	3642.8	92.93	0.75	7330	462
93	13	20129.13	350.98	2923.13	123.54	2501.96	73.6	0.86	8351	625
1	17	71290.53	769.59	8579.51	258.93	5877.22	133.32	0.69	6684	364
5	17	71203.59	710.99	7698.62	233.79	5376.23	118.13	0.70	6814	368
9	17	63237.51	644.31	6918.42	212.33	4920.06	107.77	0.71	6939	376
13	17	66462.67	691.01	7834.16	231.26	5654.47	119.92	0.72	7042	368
17	17	60726.49	667.26	7837.59	227.74	5631.82	120.45	0.72	7011	364

B.1 (continued) Portable XRF data for the outcrop analysed in Figure 2.3a.

Coordinates										
X (horizontal) cm	Y (vertical) cm	Ti (ppm)	Ti 2Θ Error (ppm)	V (ppm)	V 2Θ Error (ppm)	Cr (ppm)	Cr 2Θ Error (ppm)	Cr/V	Cr/V*9757	Cr/V* 9757 2Θ error
21	17	59165.02	606.57	6579.9	200.58	4822.17	103.29	0.73	7151	383
25	17	60682.75	684.25	7737.52	232.98	5520.47	122.72	0.71	6961	376
29	17	58775.38	712.68	8417.5	248.93	5791.31	132.46	0.69	6713	363
37	17	69321.03	727.53	7832.54	241.5	5571.84	124.24	0.71	6941	381
41	17	74500.63	779.7	8613.74	259.99	6320.57	135.52	0.73	7159	381
45	17	68591.8	694.36	7340.81	227.82	5178.76	114.66	0.71	6883	378
49	17	62213.33	714.22	8245.08	244.91	5922.72	129.2	0.72	7009	372
53	17	65019.17	687.26	6446.72	222.31	4568.77	111.07	0.71	6915	421
57	17	40907.97	515.86	4263.24	168.57	3034.71	83.49	0.71	6945	485
61	17	52760.54	656.34	6341.32	220.33	4606.77	113.31	0.73	7088	436
65	17	58230.91	694.01	6892.52	232.16	5062.83	119.1	0.73	7167	424
69	17	50952.68	632.18	5908.58	210.7	4390.73	108.05	0.74	7251	453
73	17	52663.7	666.8	6023.72	221.7	4431.84	113.11	0.74	7179	465
77	17	73439.35	812.87	8645.53	271.43	6314.43	137.96	0.73	7126	392
81	17	57392.36	689.17	6795.72	230.65	4803.36	116.99	0.71	6896	416
85	17	56609.06	700.69	7240.51	237.8	5178.37	121.67	0.72	6978	406
89	17	39018.19	545.36	5358.89	188.06	3980.23	100.24	0.74	7247	453
1	21	79405.37	819.94	7897.33	265.15	5325.26	126.56	0.67	6579	390
5	21	63886.29	702.58	6418	227.73	4558.01	110.97	0.71	6929	430
9	21	62710.86	664.22	6004.89	213.39	4271.99	103.14	0.71	6941	430
13	21	66441.72	759.77	7989.5	254.96	5384.35	127.37	0.67	6576	377

B.1 (continued) Portable XRF data for the outcrop analysed in Figure 2.3a.

Coordinates										
X (horizontal) cm	Y (vertical) cm	Ti (ppm)	Ti 2Θ Error (ppm)	V (ppm)	V 2Θ Error (ppm)	Cr (ppm)	Cr 2Θ Error (ppm)	Cr/V	Cr/V*9757	Cr/V* 9757 2Θ error
17	21	58868	617	5851	199	4070	96.5	0.69	6787	406
21	21	55448	619	5673	201	3904	97.49	0.69	6715	421
25	21	52168	664	7058	228	4715	115.01	0.67	6518	382
29	21	57811	685	7085	230	4605	113.74	0.65	6341	375
37	21	37655	523	5398	181	3580	92.92	0.66	6472	399
45	21	47344	564	5000	184	3038	86.84	0.61	5929	404
49	21	51106	646	5978	215	3893	106.16	0.65	6354	418
53	21	32442	513	4268	175	2656	88.76	0.62	6072	472
57	21	51092	653	6599	222	4478	113.37	0.68	6621	405
69	21	60662	725	7897	247	5023	121.34	0.64	6206	355
73	21	53918	691	7095	236	4550	117.91	0.64	6258	383
77	21	70570	774	7816	255	5185	124.24	0.66	6472	379
81	21	61582	728	8114	248	5085	121.94	0.62	6115	344
85	21	54457	682	7331	233	4706	116.21	0.64	6263	366
89	21	63560	761	8386	260	5534	130.12	0.66	6439	362
97	21	26282	419	3142	141	2217	73.15	0.71	6884	562
1	25	64369	692	6843	226	4367	108.54	0.64	6227	374
5	25	65184	701	6325	226	4148	106.54	0.66	6398	407
9	25	64784	741	7515	246	4480	116.36	0.59	5816	354
13	25	73208	754	7113	242	4570	113.17	0.64	6268	382
17	25	53027	633	5964	209	3685	100.04	0.61	6029	389

B.1 (continued) Portable XRF data for the outcrop analysed in Figure 2.3a.

Coordinates										
X (horizontal) cm	Y (vertical) cm	Ti (ppm)	Ti 2Θ Error (ppm)	V (ppm)	V 2Θ Error (ppm)	Cr (ppm)	Cr 2Θ Error (ppm)	Cr/V	Cr/V*9757	Cr/V* 9757 2Θ error
25	25	47725	587	5665	196.52	3352.86	93.43	0.591793	5774	374
29	25	43037	609	5806	209.56	3080.97	99.88	0.53062	5177	368
37	25	63158	721	7580	241.9	4379.57	113.68	0.577753	5637	337
41	25	62153	748	6475	244.57	4091.51	116.32	0.631818	6165	424
45	25	60525	657	5930	212.28	3754.24	99.24	0.633092	6177	399
49	25	44066	628	5082	209.44	3207.73	102.45	0.631131	6158	470
53	25	51773	650	6466	220.06	3914.73	106.6	0.605393	5907	375
57	25	60659	735.	6502	241.38	4018.4	114.12	0.618014	6030	410
61	25	44091	612	4738	201.69	3182.64	99.77	0.671678	6554	506
73	25	37876	515	4291	171.38	2347.29	79.86	0.547006	5337	411
77	25	54932	631	6421	211.16	3435.56	98.45	0.535006	5220	332
81	25	53906	623	6761	211.58	3658.11	100.48	0.541024	5279	320
85	25	85418	847	8578	274.46	4966.57	126.6	0.578983	5649	335
89	25	79070	808	7998	262.47	4604.68	121.5	0.575702	5617	344
97	25	45726	594	6037	203.91	3603.9	101.33	0.596925	5824	373
101	25	72723	728	7058	234.55	4487.97	111.71	0.635846	6204	373
1	33	50325	665	5970	223.48	2843.16	103.48	0.476234	4647	356

B.1 (continued) Portable XRF data for the outcrop analysed in Figure 2.3a.

Coordinates										
X (horizontal) cm	Y (vertical) cm	Ti (ppm)	Ti 2Θ Error (ppm)	V (ppm)	V 2Θ Error (ppm)	Cr (ppm)	Cr 2Θ Error (ppm)	Cr/V	Cr/V*9757	Cr/V* 9757 2Θ error
9	33	60652	707	6855	235	3171	105	0.46	4514	317
17	33	41760	582	5536	200	2618	94	0.47	4614	346
25	33	52132	641	6080	214	3095	100	0.51	4968	349
81	33	61753	668	4886	207	2378	89	0.48	4748	397
13	41	52476	652	5938	216	2552	95	0.43	4195	322
21	41	55553	675	6466	225	2771	99	0.43	4182	307
29	41	49440	646	6320	220	2464	96	0.39	3805	292
37	41	49601	645	6117	218	2347	94	0.38	3744	294
53	41	42151	622	5378	212	2407	97	0.44	4367	363
61	41	39929	558	4608	186	1779	81	0.39	3767	339
69	41	51346	629	5142	204	2084	85	0.41	3955	332
85	41	41662	542	4507	179	1852	78	0.41	4010	342
25	25	47725	587	5665	196	3352	93	0.59	5774	374

B.2 Portable XRF data for the outcrop analysed in Figure 2.3b.

Coordinates										
X (horizontal) cm	Y (vertical) cm	Ti (ppm)	Ti 2Θ Error (ppm)	V (ppm)	V 2Θ Error (ppm)	Cr (ppm)	Cr 2Θ Error (ppm)	Cr/V	Cr/V*9757	Cr/V* 9757 2Θ error
1	1	93342	884	8648	282.14	10276.08	169.88	1.19	12557	638.06
2.5	1	75881	759	7057	242.67	8856.24	149.47	1.25	13263	704.11
4	1	79044	777	7595	249.78	9360.64	154.25	1.23	13025	664.88
5.5	1	28443	376	2930	123.05	3571.55	78.57	1.22	12879	860.24
7	1	60262	668	6007	216.63	8965.07	146.75	1.49	15771	857.74
8.5	1	50269	596	5069	193.84	8150.84	136.58	1.61	16993	971.66
10	1	74430	721	6955	230.66	12053.45	164.32	1.73	18316	886.54
11.5	1	77067	717	7276	229.71	12210.21	161.88	1.68	17734	820.86
13	1	85966	827	8362	266.60	12577.44	180.43	1.50	15896	759.02
14.5	1	87085	842	8488	271.46	12632.75	183.15	1.49	15728	755.15
16	1	70144	702	6848	226.49	10171.47	152.23	1.49	15696	779.78
17.5	1	55804	618	5295	198.60	7721.44	132.13	1.46	15410	874.39
19	1	50535	560	5015	181.54	6732.66	117.53	1.34	14186	789.66
20.5	1	60727	618	5717	198.02	6953.60	122.52	1.22	12853	695.72
22	1	36593	519	3396	165.93	3476.97	95.84	1.02	10818	869.20
23.5	1	51006	544	4786	174.25	4848.68	100.33	1.01	10705	634.35
25	1	32490	395	3066	126.81	3053.78	72.87	1.00	10524	715.96
26.5	1	69744	671	6607	214.91	7271.87	126.62	1.10	11632	600.44
28	1	63665	659	6166	212.32	6625.07	124.00	1.07	11355	625.08

B.2 (continued) Portable XRF data for the outcrop analysed in Figure 2.3b.

Coordinates										
X (horizontal) cm	Y (vertical) cm	Ti (ppm)	Ti 2Θ Error (ppm)	V (ppm)	V 2Θ Error (ppm)	Cr (ppm)	Cr 2Θ Error (ppm)	Cr/V	Cr/V*9757	Cr/V* 9757 2Θ error
29.5	1	18022.43	318.06	1705.19	102.28	1832.91	61.72	1.07	11360	1131.87
31	1	71593.72	719.07	7005.67	231.87	7462.25	135.75	1.07	11257	597.17
32.5	1	38896.80	485.03	3894.31	157.56	3744.08	90.35	0.96	10161	684.00
34	1	38699.21	504.53	4041.87	165.35	3849.91	95.40	0.95	10067	689.50
35.5	1	44449.35	522.89	4529.15	170.19	4604.95	99.47	1.02	10745	660.74
37	1	76010.36	715.74	7238.40	229.44	8753.85	140.56	1.21	12781	630.37
38.5	1	90081.17	843.35	8489.71	269.83	11341.67	172.05	1.34	14119	684.71
1	2.5	95124.39	864.54	7521.33	267.62	8623.42	152.99	1.15	12117	669.99
2.5	2.5	87904.69	816.69	7732.28	257.82	9394.86	155.75	1.22	12841	663.18
4	2.5	86594.55	804.39	7967.36	256.14	10298.57	160.87	1.29	13661	674.27
5.5	2.5	70771.18	662.23	6393.92	210.12	8477.20	132.43	1.33	14012	702.48
7	2.5	32858.67	461.57	3367.13	150.98	4644.01	99.87	1.38	14576	1012.50
8.5	2.5	75432.70	751.61	7228.45	241.40	11151.32	164.52	1.54	16304	812.19
10	2.5	89747.40	845.33	8209.47	268.87	13310.74	184.32	1.62	17136	825.57
11.5	2.5	53035.13	583.62	5096.83	187.80	7524.87	126.16	1.48	15603	868.56
13	2.5	52625.99	584.92	4421.98	183.63	6403.20	118.24	1.45	15304	957.92
14.5	2.5	82573.60	795.75	7941.63	255.68	11575.32	169.50	1.46	15404	745.54
16	2.5	74518.55	748.10	6971.80	239.18	9294.73	152.71	1.33	14090	740.30
17.5	2.5	85639.54	797.21	7874.24	253.78	10313.83	159.69	1.31	13843	682.50
19	2.5	62039.25	633.09	5499.25	200.41	6857.97	122.91	1.25	13180	743.65
20.5	2.5	77354.05	740.85	6486.72	231.82	7089.51	133.73	1.09	11551	654.08

B.2 (continued) Portable XRF data for the outcrop analysed in Figure 2.3b.

Coordinates										
X (horizontal) cm	Y (vertical) cm	Ti (ppm)	Ti 2Θ Error (ppm)	V (ppm)	V 2Θ Error (ppm)	Cr (ppm)	Cr 2Θ Error (ppm)	Cr/V	Cr/V*9757	Cr/V* 9757 2Θ error
26.5	2.5	64680.13	646.35	6203.82	207.62	6732.35	122.31	1.09	11469.42	612.72
28	2.5	66116.15	669.77	6382.68	215.45	6930.20	127.06	1.09	11475.63	618.64
29.5	2.5	52615.99	584.73	5056.32	188.19	5260.19	109.54	1.04	10995.14	662.86
31	2.5	87808.73	801.65	8503.85	257.76	8506.80	147.33	1.00	10572.67	519.32
32.5	2.5	69388.76	684.68	6842.08	221.09	6950.47	127.82	1.02	10736.43	562.55
34	2.5	85311.18	776.51	7473.87	244.83	7734.37	138.47	1.03	10937.38	572.87
35.5	2.5	50928.27	580.76	5276.54	189.69	5527.88	111.97	1.05	11072.44	645.54
37	2.5	80807.57	725.87	7081.17	228.85	8729.26	139.11	1.23	13028.86	649.69
38.5	2.5	68885.63	713.10	6583.06	229.00	7877.80	139.64	1.20	12647.68	688.09
1	4	88925.50	811.88	8217.36	258.63	8590.82	148.94	1.05	11049.34	556.85
2.5	4	69713.98	735.33	5874.23	230.65	6005.33	129.81	1.02	10804.88	684.69
4	4	72416.68	785.56	7073.21	253.51	7353.36	147.65	1.04	10987.61	637.27
5.5	4	50102.52	648.51	5023.94	211.05	5679.95	129.51	1.13	11949.07	808.38
7	4	57025.66	678.12	5441.37	218.21	6403.09	133.64	1.18	12436.99	790.00
8.5	4	79120.54	815.51	7707.67	262.91	9294.88	162.91	1.21	12745.43	681.38
10	4	84529.20	798.66	7853.27	254.80	10006.06	159.40	1.27	13466.24	673.28
11.5	4	24996.77	434.26	2956.44	146.69	3145.54	91.76	1.06	11245.02	932.23
13	4	67601.98	689.72	6533.35	221.94	8389.20	139.66	1.28	13571.21	711.10
14.5	4	75975.18	757.28	7282.16	243.22	9106.86	151.75	1.25	13217.29	684.56
16	4	70397.13	732.96	6795.99	235.91	7733.96	142.07	1.14	12027.71	661.42
17.5	4	80372.16	799.34	7790.98	257.26	8811.55	154.33	1.13	11953.47	624.69

B.2 (continued) Portable XRF data for the outcrop analysed in Figure 2.3b.

Coordinates										
X (horizontal) cm	Y (vertical) cm	Ti (ppm)	Ti 2Θ Error (ppm)	V (ppm)	V 2Θ Error (ppm)	Cr (ppm)	Cr 2Θ Error (ppm)	Cr/V	Cr/V*9757	Cr/V* 9757 2Θ error
19	4	75196.55	709.85	7023.20	226.68	7510.01	131.81	1.07	11301.59	581.91
20.5	4	77434.02	771.47	7463.34	248.10	7835.78	144.10	1.05	11096.42	592.64
22	4	80328.82	784.63	7831.04	252.79	8183.09	147.58	1.04	11044.14	574.22
23.5	4	85229.56	839.22	8137.47	269.30	8256.50	154.34	1.01	10723.60	574.35
25	4	92055.73	874.01	8710.55	279.82	8546.36	156.89	0.98	10369.78	540.86
26.5	4	73777.51	712.07	7061.68	228.54	6928.73	128.78	0.98	10370.02	546.02
28	4	62053.68	671.30	6163.42	217.32	6110.93	124.59	0.99	10478.99	604.44
29.5	4	42882.12	534.83	4650.76	176.50	4321.61	101.07	0.93	9821.00	626.16
31	4	61862.41	645.36	5675.25	205.68	5669.82	116.24	1.00	10558.89	621.67
32.5	4	83477.38	810.80	8030.22	260.51	7602.16	145.12	0.95	10005.61	532.88
34	4	60552.81	618.87	6045.66	200.40	5456.77	111.33	0.90	9539.50	528.35
35.5	4	59180.75	621.48	6054.90	202.32	5616.55	113.76	0.93	9803.85	544.35
37	4	78353.13	763.04	7622.86	245.69	7397.72	138.72	0.97	10256.85	540.33
38.5	4	79957.11	784.49	7705.24	252.15	7789.42	143.97	1.01	10684.47	565.63
1	5.5	64259.93	652.47	6155.91	209.62	6130.74	120.02	1.00	10525.79	584.38
2.5	5.5	89928.64	883.89	7775.95	278.34	7769.22	154.57	1.00	10559.85	609.91
4	5.5	71299.86	692.49	6389.09	219.47	6343.05	122.45	0.99	10492.84	583.02
7	5.5	61932.34	725.71	5822.35	232.82	5924.61	135.46	1.02	10754.63	704.10
8.5	5.5	73506.34	715.24	6649.31	227.11	6884.33	129.16	1.04	10942.56	599.52
10	5.5	58848.69	665.45	4805.71	207.87	4942.89	117.19	1.03	10870.69	760.85
11.5	5.5	33494.32	471.13	3501.72	154.83	3273.88	90.12	0.93	9881.33	741.70
13	5.5	64267.66	673.42	5498.26	211.83	5226.41	115.98	0.95	10046.44	634.44

B.2 (continued) Portable XRF data for the outcrop analysed in Figure 2.3b.

Coordinates										
X (horizontal) cm	Y (vertical) cm	Ti (ppm)	Ti 2Θ Error (ppm)	V (ppm)	V 2Θ Error (ppm)	Cr (ppm)	Cr 2Θ Error (ppm)	Cr/V	Cr/V*9757	Cr/V* 9757 2Θ error
14.5	5.5	39678.86	565.75	4114.07	185.78	3658.86	106.59	0.89	9399.57	731.31
16	5.5	74545.88	724.88	7295.46	233.72	6911.91	130.90	0.95	10013.35	527.32
17.5	5.5	42194.60	586.92	4104.01	190.12	3871.99	108.88	0.94	9971.48	778.39
19	5.5	60586.77	662.05	6152.51	215.39	5724.43	122.14	0.93	9833.63	574.18
20.5	5.5	70032.24	702.84	6660.96	225.41	6394.86	125.91	0.96	10146.78	562.18
22	5.5	91444.05	873.07	8650.86	279.55	8023.08	154.48	0.93	9802.02	522.36
23.5	5.5	72649.44	757.84	7079.16	244.31	6608.10	135.66	0.93	9865.72	562.42
25	5.5	89575.51	834.92	8319.05	266.31	7569.44	145.03	0.91	9616.65	508.38
28	5.5	71046.09	745.26	7182.34	242.00	6356.32	133.58	0.88	9353.49	529.56
29.5	5.5	54587.47	559.89	5355.30	180.66	4938.98	99.74	0.92	9747.37	544.02
31	5.5	42665.52	532.24	4860.49	177.40	4367.03	101.00	0.90	9495.98	587.66
32.5	5.5	76069.51	707.19	7042.61	225.40	6269.31	120.84	0.89	9408.49	498.42
34	5.5	54250.23	544.33	5347.18	175.76	5042.57	98.29	0.94	9966.92	539.62
35.5	5.5	62582.06	604.62	5943.80	193.73	5481.78	106.51	0.92	9747.46	524.18
37	5.5	65269.52	632.63	6082.59	201.97	5813.15	112.35	0.96	10100.83	548.84
38.5	5.5	76992.41	748.95	7853.46	243.39	7059.33	134.08	0.90	9500.28	490.06

B.3 Portable XRF data for the outcrop analysed in Figure 2.4a.

Coordinates										
X (horizontal) cm	Y (vertical) cm	Ti (ppm)	Ti 2Θ Error (ppm)	V (ppm)	V 2Θ Error (ppm)	Cr (ppm)	Cr 2Θ Error (ppm)	Cr/V	Cr/V*9757	Cr/V* 9757 2Θ error
1	1	77981	746	7276	238	8347	141	1.15	11194	621
5	1	44019	525	4212	169	4949	102	1.17	11463	944
9	1	84453	828	8001	265	10132	165	1.27	12355	666
13	1	62246	637	5903	204	7170	125	1.21	11850	717
17	1	69620	698	6743	225	8351	139	1.24	12084	672
21	1	81865	791	7664	253	11194	166	1.46	14250	699
25	1	74674	724	6946	231	12177	164	1.75	17104	769
29	0.4	50182	560	4652	179	9048	133	1.94	18976	1074
33	0.3	22631	374	2037	119	3356	84	1.65	16075	2352
37	0.3	57022	592	5093	188	8641	131	1.70	16553	927
41	0.3	83537	802	7257	253	14939	191	2.06	20087	893
45	0.3	37359	510	3216	161	5813	115	1.81	17634	1743
53	1	63016	621	6102	200	11855	150	1.94	18956	786
57	1	55043	587	5608	191	10314	142	1.84	17946	839
61	1	70314	696	7061	226	10559	153	1.50	14589	674
65	1	79370	764	7753	246	10622	159	1.37	13368	637
69	1	81655	787	8022	254	11039	166	1.38	13426	638
73	1	74230	728	7807	238	10449	156	1.34	13060	595
77	1	46262	534	4613	173	6833	118	1.48	14453	935

B.3 (continued) Portable XRF data for the outcrop analysed in Figure 2.4a.

Coordinates										
X (horizontal) cm	Y (vertical) cm	Ti (ppm)	Ti 2Θ Error (ppm)	V (ppm)	V 2Θ Error (ppm)	Cr (ppm)	Cr 2Θ Error (ppm)	Cr/V	Cr/V*9757	Cr/V* 9757 2Θ error
81	1	81981	786	8035	253	9691	156	1.21	11768	596
85	1	30884	479	3238	157	4415	103	1.36	13303	1511
89	1	78020	749	7499	240	10103	155	1.35	13144	645
93	1	90262	864	8526	277	12130	180	1.42	13882	669
97	1	78959	755	7518	242	10464	158	1.39	13580	658
1	5	82059	766	7613	244	7579	138	1.00	9714	566
5	5	30587	444	3434	148	3324	87	0.97	9444	1066
9	5	72278	750	7779	247	7068	139	0.91	8865	552
13	5	62076	610	5950	196	5800	110	0.97	9511	591
17	5	41451	503	4014	162	3911	91	0.97	9506	896
21	5	61146	704	6002	227	6366	132	1.06	10348	815
61	5	51467	511	5164	166	6416	104	1.24	12121	632
65	5	60278	642	6158	209	6571	124	1.07	10412	666
69	5	62014	625	6269	203	6233	116	0.99	9701	585
73	5	59791	630	5968	204	5801	116	0.97	9483	649
77	5	75711	703	7382	226	6133	120	0.83	8106	486
81	5	82533	792	7976	255	7672	143	0.96	9385	558
85	5	55723	553	5330	177	4994	98	0.94	9141	597
89	5	74387	726	6982	232	7419	134	1.06	10367	622
93	5	75970	747	7440	241	7737	139	1.04	10146	592
97	5	66061	644	6309	207	6337	118	1.00	9800	598

B.3 (continued) Portable XRF data for the outcrop analysed in Figure 2.4a.

Coordinates										
X (horizontal) cm	Y (vertical) cm	Ti (ppm)	Ti 2Θ Error (ppm)	V (ppm)	V 2Θ Error (ppm)	Cr (ppm)	Cr 2Θ Error (ppm)	Cr/V	Cr/V*9757	Cr/V* 9757 2Θ error
1	9	62882	615	6108	198	5530	109	0.91	8833	565
5	9	62865	617	6214	199	5505	109	0.89	8644	548
9	9	83221	782	8129	252	6809	134	0.84	8172	500
13	9	54121	554	5526	180	4398	95	0.80	7765	550
17	9	55161	558	5655	182	4941	100	0.87	8525	552
21	9	66133	646	6540	208	5658	113	0.87	8441	536
25	9	85785	806	8412	260	9073	153	1.08	10524	549
28	10	25251	399	2701	131	3656	87	1.35	13207	1533
32	10	65700	685	6276	220	9663	149	1.54	15021	811
61	9	39811	495	4239	162	5926	109	1.40	13641	959
65	9	96082	903	9147	289	9703	168	1.06	10350	567
69	9	57412	592	5710	191	4998	105	0.88	8540	600
73	9	68665	707	7019	230	5537	121	0.79	7697	552
77	9	53182	533	5206	172	4059	89	0.78	7607	550
81	9	71376	693	6910	223	5360	115	0.78	7568	522
85	9	77532	774	7456	249	6130	131	0.82	8022	570
89	9	69603	683	6711	219	5531	115	0.82	8041	548
93	9	90595	861	8921	278	7214	147	0.81	7890	500
97	9	80525	762	7953	246	6422	130	0.81	7878	492
1	13	76076	725	7766	236	5830	122	0.75	7325	464
5	13	54680	565	5430	183	4297	96	0.79	7721	579

B.3 (continued) Portable XRF data for the outcrop analysed in Figure 2.4a.

Coordinates										
X (horizontal) cm	Y (vertical) cm	Ti (ppm)	Ti 2Θ Error (ppm)	V (ppm)	V 2Θ Error (ppm)	Cr (ppm)	Cr 2Θ Error (ppm)	Cr/V	Cr/V*9757	Cr/V* 9757 2Θ error
9	13	86482	828	8367	266	6466	138	0.77	7540	511
13	13	45666	566	4468	183	3589	96	0.80	7838	860
17	13	75417	697	6753	221	5528	114	0.82	7987	540
21	13	77254	743	7581	240	6307	127	0.83	8117	517
25	13	72950	695	6928	223	6675	125	0.96	9402	564
29	13	57879	605	5972	197	6654	119	1.11	10871	643
33	13	49101	521	5011	170	6305	107	1.26	12276	704
37	13	78826	755	7958	245	10517	158	1.32	12895	595
41	13	60194	605	6205	197	8691	131	1.40	13666	656
57	14	47578	574	4764	186	7780	131	1.63	15933	1045
61	13	75703	739	7499	239	11647	163	1.55	15154	676
65	13	66127	654	6407	211	6953	124	1.09	10589	620
69	13	63507	641	6424	208	5541	112	0.86	8416	551
73	13	43716	535	3911	169	3315	89	0.85	8270	965
77	13	66823	695	6309	223	5245	118	0.83	8112	641
81	13	52295	625	4999	201	3884	103	0.78	7580	809
85	13	82584	794	8176	257	6090	131	0.74	7267	491
89	13	83471	812	7834	260	6298	134	0.80	7844	554
93	13	66677	652	6224	208	4910	108	0.79	7697	565
97	13	60594	595	5809	191	4549	99	0.78	7641	545
1	17	73426	715	7113	230	5233	116	0.74	7177	514

B.3 (continued) Portable XRF data for the outcrop analysed in Figure 2.4a.

Coordinates										
X (horizontal) cm	Y (vertical) cm	Ti (ppm)	Ti 2Θ Error (ppm)	V (ppm)	V 2Θ Error (ppm)	Cr (ppm)	Cr 2Θ Error (ppm)	Cr/V	Cr/V*9757	Cr/V* 9757 2Θ error
5	17	83304	807	8031	259	5515	128	0.69	6700	502
9	17	82598	763	6813	238	5361	119	0.79	7678	594
13	17	78412	757	7363	242	5267	120	0.72	6980	525
17	17	62745	628	6245	203	4884	106	0.78	7631	537
21	17	67187	664	6920	216	5307	113	0.77	7482	498
25	17	67559	661	6832	214	5245	111	0.77	7491	498
29	17	61742	610	5900	196	5123	105	0.87	8471	575
33	17	76413	745	7381	239	6413	128	0.87	8477	550
37	17	76223	779	7427	251	7161	141	0.96	9409	625
41	17	63563	653	6132	210	6776	124	1.11	10782	677
45	17	69087	670	6638	215	7818	130	1.18	11490	620
49	17	56149	577	5977	189	8014	124	1.34	13081	640
53	17	60721	609	6059	197	9239	134	1.52	14879	702
57	17	52250	541	5440	177	7987	120	1.47	14325	698
61	17	65332	712	6515	231	7896	143	1.21	11826	757
65	17	71096	728	6920	234	6021	126	0.87	8490	604
69	17	51088	590	5079	191	3863	98	0.76	7421	707
73	17	61274	594	5978	191	4624	98	0.77	7546	514
77	17	74243	726	7156	233	5348	118	0.75	7292	525
81	17	55485	563	5203	180	3996	92	0.77	7495	597
85	17	81535	741	6827	232	5050	114	0.74	7217	551

B.3 (continued) Portable XRF data for the outcrop analysed in Figure 2.4a.

Coordinates										
X (horizontal) cm	Y (vertical) cm	Ti (ppm)	Ti 2Θ Error (ppm)	V (ppm)	V 2Θ Error (ppm)	Cr (ppm)	Cr 2Θ Error (ppm)	Cr/V	Cr/V*9757	Cr/V* 9757 2Θ error
89	17	69210	666	6398	212	4839	107	0.76	7379	544
93	17	77149	753	7159	240	5526	122	0.77	7532	559
97	17	38606	494	3747	159	2866	82	0.76	7461	900
1	21	62992	624	6424	203	4567	102	0.71	6937	491
5	21	56793	570	5574	184	3915	92	0.70	6854	530
9	21	65017	642	6091	205	4552	103	0.75	7292	556
13	21	59392	596	5581	190	3964	95	0.71	6930	566
17	21	58029	592	5635	191	4217	97	0.75	7301	567
21	21	52911	546	5307	177	3723	88	0.70	6846	542
25	21	57599	591	5850	192	4171	97	0.71	6956	530
29	21	60852	591	5732	189	4389	96	0.77	7471	540
33	21	72751	720	7202	233	5350	117	0.74	7248	514
37	21	43001	511	4245	165	3486	87	0.82	8011	780
41	21	72178	692	7049	223	5192	113	0.74	7186	493
45	21	55239	567	5735	185	4526	97	0.79	7700	533
49	21	64594	630	6343	203	5052	106	0.80	7771	521
53	21	56537	559	5634	181	4846	98	0.86	8393	544
57	21	81345	785	7826	252	7144	138	0.91	8907	554
61	21	55162	562	5584	182	5532	104	0.99	9666	596
65	21	59988	584	5853	188	5367	104	0.92	8947	554

B.3 (continued) Portable XRF data for the outcrop analysed in Figure 2.4a.

Coordinates										
X (horizontal) cm	Y (vertical) cm	Ti (ppm)	Ti 2Θ Error (ppm)	V (ppm)	V 2Θ Error (ppm)	Cr (ppm)	Cr 2Θ Error (ppm)	Cr/V	Cr/V*9757	Cr/V* 9757 2Θ error
69	21	40417	494	3991	160	3204	84	0.80	7832	818
73	21	85721	813	8096	260	6057	131	0.75	7300	508
77	21	67990	647	6542	208	4803	105	0.73	7163	496
81	21	51798	527	5075	170	3678	85	0.72	7071	549
85	21	68336	661	6398	211	4560	105	0.71	6954	529
89	21	44339	522	4088	166	2927	83	0.72	6986	801
93	21	74120	714	7024	229	4782	111	0.68	6643	503
97	21	71681	695	6659	222	4603	108	0.69	6744	526
1	25	47878	606	4659	195	3992	104	0.86	8360	917
5	25	50943	532	5161	173	3882	89	0.75	7340	565
9	25	66985	666	6664	215	4582	107	0.69	6708	506
13	25	54366	569	5680	186	3830	92	0.67	6580	520
17	25	55067	557	5562	181	3712	89	0.67	6513	508
21	25	66389	663	6638	215	4195	103	0.63	6167	491
25	25	62530	627	6184	202	3983	98	0.64	6284	505
29	25	53805	553	5400	179	3666	89	0.68	6624	533
33	25	65995	660	6965	216	4228	104	0.61	5922	450
37	25	67959	652	6540	209	4289	102	0.66	6398	485
41	25	52753	532	5192	172	4005	89	0.77	7528	552
45	25	54963	552	5553	179	4160	92	0.75	7309	522
49	25	50194	510	5281	167	3694	84	0.70	6826	492

B.3 (continued) Portable XRF data for the outcrop analysed in Figure 2.4a.

Coordinates										
X (horizontal) cm	Y (vertical) cm	Ti (ppm)	Ti 2Θ Error (ppm)	V (ppm)	V 2Θ Error (ppm)	Cr (ppm)	Cr 2Θ Error (ppm)	Cr/V	Cr/V*9757	Cr/V* 9757 2Θ error
53	25	69834	716	7104	233	4438	113	0.62	6095	507
57	25	65866	644	6796	210	4349	102	0.64	6243	454
61	25	60603	610	5920	197	4029	97	0.68	6641	531
65	25	65419	638	6602	207	4234	100	0.64	6258	464
69	25	64496	631	6511	205	4679	103	0.72	7012	487
73	25	73914	719	7043	231	5151	116	0.73	7135	525
77	25	69966	658	6676	211	4508	103	0.68	6587	476
81	25	65185	628	5907	200	3993	97	0.68	6595	541
85	25	58587	563	5721	181	3672	88	0.64	6263	473
89	25	46651	570	4769	185	3209	92	0.67	6566	731
93	25	41626	512	4043	165	2788	81	0.69	6730	800
97	25	71138	695	6877	224	4570	109	0.66	6484	501
17	29	68183	618	5856	194	3573	89	0.61	5953	494
21	29	56267	611	4408	189	2844	87	0.65	6294	821
25	29	52847	519	4633	164	2745	75	0.59	5780	561
29	29	64328	630	6434	204	4033	98	0.63	6116	472
33	29	52046	535	5345	174	2881	80	0.54	5260	477
37	29	63946	618	6045	198	3640	93	0.60	5875	489
41	29	50266	522	5092	169	3128	81	0.61	5994	516
45	29	52919	548	5535	179	3181	85	0.57	5609	484
49	29	50517	515	5346	169	2882	79	0.54	5260	453

B.3 (continued) Portable XRF data for the outcrop analysed in Figure 2.4a.

Coordinates										
X (horizontal) cm	Y (vertical) cm	Ti (ppm)	Ti 2Θ Error (ppm)	V (ppm)	V 2Θ Error (ppm)	Cr (ppm)	Cr 2Θ Error (ppm)	Cr/V	Cr/V*9757	Cr/V* 9757 2Θ error
53	29	85084	811	8366	262	4266	116	0.51	4975	423
57	29	54917	558	5704	182	3294	86	0.58	5635	471
61	29	48085	586	5057	192	2970	92	0.59	5731	671
65	29	66429	642	6701	208	3938	98	0.59	5733	442
69	29	64180	631	6224	203	3854	97	0.62	6041	498
73	29	40996	490	4030	158	2534	76	0.63	6134	721
77	29	67264	646	6597	208	4117	100	0.62	6089	466
81	29	65340	632	6431	204	3797	96	0.59	5760	461
85	29	43093	533	4239	172	2675	83	0.63	6157	772
89	29	40256	478	3656	152	2543	74	0.70	6786	824
93	29	47839	590	5012	193	3116	94	0.62	6065	700
97	29	64785	634	6358	205	3719	96	0.58	5707	474
17	33	67525	624	5886	196	3570	91	0.61	5917	503
21	33	79745	693	5958	212	3548	94	0.60	5811	547
25	33	55352	642	5264	206	2699	92	0.51	5004	664
29	33	54020	538	5589	176	2881	80	0.52	5029	436
33	33	71177	715	7445	234	4006	107	0.54	5251	440
37	33	57960	573	5904	186	3041	84	0.52	5026	437

B.3 (continued) Portable XRF data for the outcrop analysed in Figure 2.4a.

Coordinates										
X (horizontal) cm	Y (vertical) cm	Ti (ppm)	Ti 2Θ Error (ppm)	V (ppm)	V 2Θ Error (ppm)	Cr (ppm)	Cr 2Θ Error (ppm)	Cr/V	Cr/V*9757	Cr/V* 9757 2Θ error
41	33	75072	701	7311	225	3501	98	0.48	4673	405
45	33	64117	625	6277	201	3275	90	0.52	5091	449
49	33	63820	622	6309	201	3281	90	0.52	5073	445
53	33	80238	771	8022	249	3901	110	0.49	4745	415
57	33	70289	701	7222	228	3488	101	0.48	4712	429
61	33	68818	658	6774	212	3615	96	0.53	5207	434
65	33	67726	624	6051	198	3214	87	0.53	5182	460
69	33	81538	783	7992	252	3875	111	0.48	4731	427
73	33	94983	878	8773	280	4679	125	0.53	5204	442
77	33	69166	670	6429	214	3474	96	0.54	5273	485
85	33	61372	594	5843	190	3302	87	0.57	5514	475
89	33	74084	695	7073	223	3802	100	0.54	5244	437
93	33	62412	618	6454	201	3537	92	0.55	5348	435
97	33	69050	664	6775	214	3581	97	0.53	5158	439

B.4 Portable XRF data for the outcrop analysed in Figure 2.5a.

Coordinates										
X (horizontal) cm	Y (vertical) cm	Ti (ppm)	Ti 2Θ Error (ppm)	V (ppm)	V 2Θ Error (ppm)	Cr (ppm)	Cr 2Θ Error (ppm)	Cr/V	Cr/V*9757	Cr/V* 9757 2Θ error
1	34.4	80960	754	7955	243	8652	144	1.09	10612	539
1	30.7	93698	839	8757	268	9811	158	1.12	10931	539
1	27	89096	795	7603	250	9060	148	1.19	11626	623
1	23.3	97836	809	6721	244	8030	137	1.19	11657	721
1	19.6	73174	755	8968	255	8983	152	1.00	9773	472
1	15.9	106240	856	7483	259	8480	143	1.13	11058	648
1	12.2	86745	797	8306	256	9403	153	1.13	11046	552
1	8.5	40899	499	3669	158	4815	99	1.31	12805	1136
1	4.8	75409	717	6803	228	8325	138	1.22	11941	663
3.8	38.1	56109	598	6531	200	6134	114	0.94	9164	522
3.8	34.4	39599	527	4032	171	3700	96	0.92	8953	983
3.8	30.7	99683	885	8572	278	7452	145	0.87	8483	535
3.8	27	74261	717	7849	235	7205	131	0.92	8956	487
3.8	23.3	84904	829	9047	272	7950	150	0.88	8574	485
3.8	19.6	71516	728	7945	241	7148	135	0.90	8778	503
3.8	15.9	55932	576	6497	192	5987	110	0.92	8992	489
3.8	12.2	95064	852	8445	269	8515	150	1.01	9838	554
3.8	8.5	62171	625	6604	205	6777	120	1.03	10012	550
3.8	4.8	101244	867	7823	267	9046	152	1.16	11282	647

B.4 (continued) Portable XRF data for the outcrop analysed in Figure 2.5a.

Coordinates										
X (horizontal) cm	Y (vertical) cm	Ti (ppm)	Ti 2Θ Error (ppm)	V (ppm)	V 2Θ Error (ppm)	Cr (ppm)	Cr 2Θ Error (ppm)	Cr/V	Cr/V*9757	Cr/V* 9757 2Θ error
3.8	1.1	47328	585	5255	194	6630	125	1.26	12310	853
6.6	38.1	42395	492	5245	167	4238	92	0.81	7885	543
6.6	30.7	85773	813	8291	261	6488	134	0.78	7634	498
6.6	27	71046	640	5956	200	4990	103	0.84	8175	565
6.6	19.6	82445	737	7057	231	6130	121	0.87	8475	547
6.6	15.9	77772	815	9546	275	7676	151	0.80	7846	444
6.6	12.2	70861	679	7262	221	6548	122	0.90	8797	498
6.6	8.5	22990	306	2514	101	2814	62	1.12	10921	960
6.6	4.8	67816	736	7613	244	7744	144	1.02	9925	591
6.6	1.1	45521	501	4502	162	6361	107	1.41	13786	830
9.4	38.1	81053	730	5498	220	5330	113	0.97	9460	801
9.4	34.4	66650	671	6717	217	5482	113	0.82	7963	531
9.4	30.7	69617	786	8840	267	6578	140	0.74	7260	465
9.4	27	68071	760	8455	257	6155	134	0.73	7103	469
9.4	23.3	90287	831	7343	259	6164	130	0.84	8190	608
9.4	19.6	87556	866	8550	279	6929	144	0.81	7908	535
9.4	15.9	68997	745	8160	249	6388	132	0.78	7638	480
9.4	12.2	70394	828	9426	284	7920	157	0.84	8198	490
9.4	8.5	73042	773	7920	254	7507	143	0.95	9249	565
9.4	4.8	50479	613	4088	191	4747	109	1.16	11332	1210

B.4 (continued) Portable XRF data for the outcrop analysed in Figure 2.5a.

Coordinates										
X (horizontal) cm	Y (vertical) cm	Ti (ppm)	Ti 2Θ Error (ppm)	V (ppm)	V 2Θ Error (ppm)	Cr (ppm)	Cr 2Θ Error (ppm)	Cr/V	Cr/V*20290	Cr/V* 9757 2Θ error
143	5	48461	558	5095	182	1719	73	0.34	6846	554
146	5	48442	540	4954	175	1645	69	0.33	6739	539
140.5	6	56851	616	5511	198	1748	75	0.32	6435	528
146.5	6.5	58756	668	6668	222	1741	82	0.26	5298	442
137	7	28516	354	2643	113	984	46	0.37	7557	703
143.6	7.8	59612	667	5995	216	1699	80	0.28	5749	496
136	8	49906	589	5258	192	1676	75	0.32	6466	546
148	8.5	75622	690	8181	227	2118	83	0.26	5254	362
141.25	8.8	58259	660	6260	217	1668	81	0.27	5406	465
134.5	9	51290	607	5036	195	1750	76	0.35	7052	603
131.5	9.5	28920	371	2956	120	1120	50	0.38	7687	684
139	9.5	71739	704	8237	234	2496	90	0.30	6148	408
144.5	9.8	73485	666	8878	224	2209	82	0.25	5048	324
129	10	44327	524	5021	174	1660	69	0.33	6707	531
77.5	10.5	90568	840	10735	281	6655	137	0.62	12578	604
124.5	10.5	64460	610	6958	200	2838	83	0.41	8277	494
137	10.5	47182	565	5441	188	1587	73	0.29	5919	494
148.5	10.8	81867	723	9531	241	3167	95	0.33	6741	382
73.5	11	74594	679	7878	222	5272	109	0.67	13578	683

Appendix C: Portable XRF data for two-dimensional chemical contour maps of the Bottom Seam

C.1 Portable XRF data for the outcrop analysed in Figure 3.1a

Coordinates										
X (horizontal) cm	Y (vertical) cm	Ti (ppm)	Ti 2Θ Error (ppm)	V (ppm)	V 2Θ Error (ppm)	Cr (ppm)	Cr 2Θ Error (ppm)	Cr/V	Cr/V*20290	Cr/V* 9757 2Θ error
80	11	57082	569	7014	192	3942	92	0.56	11405	593
135	11	62263	599	6441	195	2327	77	0.36	7332	479
142	11	60298	569	6367	186	1702	69	0.27	5423	389
40	11.5	13890	238	1732	81	1001	41	0.58	11729	1074
36.6	11.7	27819	348	2552	111	1636	53	0.64	13008	1030
80.5	12	80776	748	9696	251	4440	111	0.46	9291	484
83.5	12	84087	740	8382	239	3882	103	0.46	9398	531
90	12	73662	674	8149	222	3664	97	0.45	9124	504
94	12	91770	826	9696	270	4445	116	0.46	9302	516
122	12	90593	822	9585	269	4489	116	0.47	9501	528
133	12	69458	650	7545	214	3016	88	0.40	8109	479
140	12	64177	598	7417	199	2543	80	0.34	6956	417
145.5	12	76667	677	7835	220	2544	85	0.32	6588	415
69.5	12.5	84645	711	7970	227	5586	111	0.70	14221	709
77.5	12.5	75674	729	9221	246	4092	107	0.44	9004	489
88	12.5	23576	317	2591	104	1176	46	0.45	9208	766
97.5	12.5	64532	617	7642	206	3821	94	0.50	10146	537
73.5	13	85309	832	9863	277	5695	131	0.58	11716	617
118.5	13	84267	762	8367	246	4503	110	0.54	10921	607
130	13	84361	803	9414	265	3923	111	0.42	8455	490

C.1 (continued) Portable XRF data for the outcrop analysed in Figure 3.1a

Coordinates										
X (horizontal) cm	Y (vertical) cm	Ti (ppm)	Ti 2Θ Error (ppm)	V (ppm)	V 2Θ Error (ppm)	Cr (ppm)	Cr 2Θ Error (ppm)	Cr/V	Cr/V*20290	Cr/V* 9757 2Θ error
138	13	74230	705	8870	237	3372	99	0.38	7714	444
125.5	13.5	66553	621	6868	202	3592	90	0.52	10612	596
127	13.5	73409	708	7836	232	3993	103	0.51	10338	590
144	13.5	43048	545	5311	184	1360	69	0.26	5196	461
33	14	20925	318	2348	105	1211	48	0.52	10464	929
39.5	14	91232	826	9720	271	3182	105	0.33	6642	416
97.5	14	59833	595	7345	201	3407	90	0.46	9412	519
101	14	89247	756	8254	241	5169	113	0.63	12706	666
122.5	14	65516	637	7209	210	3421	91	0.47	9630	553
136	14	74335	708	8063	233	3025	93	0.38	7612	466
150	14	77743	712	8571	235	2021	84	0.24	4785	340
116.5	14.5	91935	849	10092	280	5815	131	0.58	11692	605
118.5	14.5	67626	634	7593	210	3989	96	0.53	10658	566
133.8	14.5	70806	661	7525	216	3050	89	0.41	8224	489
141	14.5	74403	655	7788	214	2237	80	0.29	5827	379
36.3	14.7	46438	530	4674	171	1684	68	0.36	7313	587
42.5	15	68598	655	8134	219	3496	95	0.43	8720	485
104	15	65438	605	7120	199	4866	100	0.68	13868	691
113.5	15	74499	690	7828	225	5619	114	0.72	14565	737
148	15	91597	812	9783	266	2162	94	0.22	4483	325

C.1 (continued) Portable XRF data for the outcrop analysed in Figure 3.1a

Coordinates										
X (horizontal) cm	Y (vertical) cm	Ti (ppm)	Ti 2Θ Error (ppm)	V (ppm)	V 2Θ Error (ppm)	Cr (ppm)	Cr 2Θ Error (ppm)	Cr/V	Cr/V*20290	Cr/V* 9757 2Θ error
106.8	15.5	92665	835	9967	274	7568	142	0.76	15407	733
110	16	54294	540	5943	178	3903	88	0.66	13325	720
131	16	84766	786	9359	259	3711	107	0.40	8046	467
139	16	49906	589	5258	192	1676	75	0.32	6466	546
39.5	17	88610	753	8663	242	1968	84	0.23	4610	335
46	17	48246	558	5509	185	3000	87	0.54	11048	717
63.5	17	59230	659	5902	213	4543	109	0.77	15618	974
129	17	78266	740	8663	244	3598	101	0.42	8428	488
137	17	61515	607	6749	200	1665	72	0.25	5006	374
36	17.2	65694	628	7837	211	2077	79	0.26	5377	357
42.5	17.5	64013	640	8102	217	1755	78	0.22	4396	322
49.5	17.5	76730	725	9163	243	4851	113	0.53	10741	550
52.5	17.5	54456	636	6722	215	3475	100	0.52	10491	658
55.5	17.5	64171	629	8202	214	4311	100	0.53	10664	540
126	17.5	64645	629	7408	209	2951	86	0.40	8083	478
152	17.5	73339	648	7128	208	1162	68	0.16	3306	298
59	18	44742	529	5271	177	3429	89	0.65	13198	813
66	18	59218	579	7489	196	1994	73	0.27	5402	349
68	18	24625	312	3110	106	1036	42	0.33	6755	524
134	18	54181	617	5831	202	1584	75	0.27	5513	467

C.1 (continued) Portable XRF data for the outcrop analysed in Figure 3.1a

Coordinates										
X (horizontal) cm	Y (vertical) cm	Ti (ppm)	Ti 2Θ Error (ppm)	V (ppm)	V 2Θ Error (ppm)	Cr (ppm)	Cr 2Θ Error (ppm)	Cr/V	Cr/V*20290	Cr/V* 9757 2Θ error
142.2	18	65125	619	7038	203	1348	69	0.19	3886	321
149	18	68077	678	8270	228	1296	77	0.16	3179	284
132	19	69353	659	7581	217	1735	77	0.23	4645	348
140	19	82448	757	8652	247	1731	84	0.20	4059	323
146	19	57992	605	8087	210	1165	71	0.14	2924	261
124	19.2	82494	766	9403	254	3957	107	0.42	8538	474
129.5	19.5	75355	713	7640	231	1832	81	0.24	4866	375
30	20	12513	177	1335	58	799	28	0.60	12149	995
39	20	93382	868	10944	290	2241	101	0.20	4155	306
63	20	78190	709	8488	233	1873	81	0.22	4478	325
68	20	57879	577	7644	197	2836	82	0.37	7528	422
110	20	83693	785	10190	264	3264	103	0.32	6498	384
113	20	63804	613	7650	206	2475	81	0.32	6565	401
137.5	20	73262	675	7586	220	1466	74	0.19	3921	321
33	20.3	61747	631	7486	212	2169	81	0.29	5879	396
36	20.5	77635	736	9455	248	2093	89	0.22	4492	316
121	20.5	42190	506	5281	171	2133	72	0.40	8196	562
42.2	21	90928	829	10324	275	2010	95	0.19	3950	299
66	21	66507	656	8907	225	2242	83	0.25	5107	327
128	21	78763	753	8984	250	2189	91	0.24	4945	352

C.1 (continued) Portable XRF data for the outcrop analysed in Figure 3.1a

Coordinates										
X (horizontal) cm	Y (vertical) cm	Ti (ppm)	Ti 2Θ Error (ppm)	V (ppm)	V 2Θ Error (ppm)	Cr (ppm)	Cr 2Θ Error (ppm)	Cr/V	Cr/V*20290	Cr/V* 9757 2Θ error
135	21	76718	735	8215	241	1470	80	0.18	3630	313
153.5	21	73297	695	8120	229	995	72	0.12	2487	257
46	21.5	69932	625	7380	204	1409	69	0.19	3873	306
49.5	21.5	100044	881	10784	289	2147	97	0.20	4039	300
52	21.5	60335	702	7339	236	1803	86	0.25	4985	411
55	21.5	69600	637	7626	210	1620	72	0.21	4309	320
59	21.5	47623	570	5872	192	1180	67	0.20	4078	379
117.5	21.5	80931	769	9486	257	3390	103	0.36	7251	429
141	21.5	62369	576	6733	189	1159	63	0.17	3492	296
125	21.8	85952	778	9693	258	2090	90	0.22	4375	313
70	22	48772	584	6522	200	1793	77	0.27	5579	423
106.5	22	75275	738	9253	249	2971	97	0.32	6514	399
114	22	80517	776	9426	259	3294	103	0.35	7090	429
122	22	61036	590	6812	195	1779	71	0.26	5300	375
133	22	69013	670	7847	222	1440	75	0.18	3723	309
138.5	22	75073	713	7936	233	1364	77	0.17	3487	309
150	22	67464	647	7553	214	965	68	0.13	2591	264
76.5	22.4	87196	834	11612	286	4212	118	0.36	7360	396
79.5	22.5	60000	606	7686	206	2355	80	0.31	6217	389
82.5	22.5	67744	679	9100	233	2910	92	0.32	6488	381

C.1 (continued) Portable XRF data for the outcrop analysed in Figure 3.1a

Coordinates										
X (horizontal) cm	Y (vertical) cm	Ti (ppm)	Ti 2Θ Error (ppm)	V (ppm)	V 2Θ Error (ppm)	Cr (ppm)	Cr 2Θ Error (ppm)	Cr/V	Cr/V*20290	Cr/V* 9757 2Θ error
86	22.5	61357	596	7889	203	2722	82	0.35	7000	401
90	22.5	65175	625	8692	214	2729	85	0.31	6370	363
93	22.5	57407	646	7116	218	2074	83	0.29	5915	432
103	22.5	77535	740	9457	249	3549	102	0.38	7614	431
110	22.5	65293	614	7544	204	2632	81	0.35	7079	421
131	22.5	66693	614	6430	197	1355	67	0.21	4276	353
147	22.5	66788	636	7268	209	1005	68	0.14	2804	277
63.5	23	66144	649	8468	221	1666	77	0.20	3992	296
73.5	23	73211	712	9873	245	3293	99	0.33	6768	380
96	23	78919	741	9485	248	2929	96	0.31	6265	379
144.7	23	56032	603	7318	206	885	67	0.12	2453	262
99.5	23.5	52017	619	6538	210	2016	82	0.31	6257	469
129	23.5	77905	732	7889	237	1565	80	0.20	4025	337
136.5	23.5	62370	585	6565	191	1222	65	0.19	3776	319
29.9	24	57050	594	6968	200	2046	77	0.29	5958	405
33	24	56826	652	6055	214	1521	77	0.25	5098	453
39	24	78077	725	8798	240	1806	83	0.21	4166	314
42	24	59924	592	7502	201	1483	70	0.20	4009	306
142	24	64711	611	7275	202	880	63	0.12	2455	252
51.5	24.5	55085	629	6230	208	1077	69	0.17	3507	356

C.1 (continued) Portable XRF data for the outcrop analysed in Figure 3.1a

Coordinates										
X (horizontal) cm	Y (vertical) cm	Ti (ppm)	Ti 2Θ Error (ppm)	V (ppm)	V 2Θ Error (ppm)	Cr (ppm)	Cr 2Θ Error (ppm)	Cr/V	Cr/V*20290	Cr/V* 9757 2Θ error
118	24.5	37223	485	4728	165	1184	63	0.25	5081	462
35.8	25	48275	572	5971	193	1248	69	0.21	4243	385
46	25	62530	609	8681	211	1688	75	0.19	3946	277
49	25	51092	583	5940	194	1175	67	0.20	4013	371
54.2	25	64097	683	6688	223	1127	72	0.17	3419	344
60	25	53909	636	6841	216	1383	76	0.20	4101	366
66	25	83466	759	9453	251	2748	94	0.29	5897	369
102.5	25	48923	570	6062	192	1992	76	0.33	6668	482
128	25	78468	738	8074	240	1611	81	0.20	4049	334
134	25	74864	683	7763	223	1238	73	0.16	3235	291
23.5	25.5	43240	513	4909	170	1637	68	0.33	6768	534
79.5	25.5	83497	830	11556	287	3706	114	0.32	6506	371
82.5	25.5	55947	656	7312	224	2452	90	0.34	6805	471
86	25.5	66100	648	8882	222	3098	91	0.35	7079	394
90	25.5	71159	709	8979	240	3128	96	0.35	7068	418
106.5	25.5	78681	733	8965	243	2653	92	0.30	6004	382
114	25.5	64209	585	6395	189	1607	67	0.25	5098	376
139.5	25.5	47665	561	5433	186	688	59	0.13	2567	320
76.5	25.7	46229	588	6442	203	2253	83	0.35	7096	502
122	25.8	62010	707	6772	233	1545	82	0.23	4628	419

C.1 (continued) Portable XRF data for the outcrop analysed in Figure 3.1a

Coordinates										
X (horizontal) cm	Y (vertical) cm	Ti (ppm)	Ti 2Θ Error (ppm)	V (ppm)	V 2Θ Error (ppm)	Cr (ppm)	Cr 2Θ Error (ppm)	Cr/V	Cr/V*20290	Cr/V* 9757 2Θ error
73.5	26	68033	682	9181	234	2956	93	0.32	6533	382
110	26	66268	665	7938	223	2089	83	0.26	5340	373
132	26	57669	650	5949	212	943	69	0.16	3217	364
20	26.5	54925	545	6647	183	2388	75	0.36	7291	443
26.5	26.5	54532	645	6272	214	1660	80	0.26	5369	457
30	26.5	64976	632	6848	206	1542	71	0.23	4569	360
64	26.5	76729	742	9327	249	3251	100	0.35	7073	418
93.5	26.5	61326	700	7143	233	2071	88	0.29	5884	458
96.5	26.5	81079	788	9744	264	2818	100	0.29	5867	378
130	26.5	78970	735	8569	242	1358	79	0.16	3216	286
137.5	26.5	61087	595	6871	197	902	63	0.13	2664	269
13.7	27	50433	562	4983	181	2474	79	0.50	10074	714
17	27	75051	704	8410	233	3900	102	0.46	9410	520
49	27	73584	695	9055	234	1660	80	0.18	3720	283
51	27	38795	461	4741	155	1157	57	0.24	4950	420
67	27	72452	686	8571	229	3153	92	0.37	7465	429
70	27	50940	607	6337	205	2301	84	0.36	7368	523
100	27	64572	663	8460	226	2135	84	0.25	5120	347
135	27	55637	628	5841	205	853	66	0.15	2963	345
32.5	27.5	60491	687	6688	227	1415	78	0.21	4293	396

C.1 (continued) Portable XRF data for the outcrop analysed in Figure 3.1a

Coordinates										
X (horizontal) cm	Y (vertical) cm	Ti (ppm)	Ti 2Θ Error (ppm)	V (ppm)	V 2Θ Error (ppm)	Cr (ppm)	Cr 2Θ Error (ppm)	Cr/V	Cr/V*20290	Cr/V* 9757 2Θ error
39	27.5	102220	816	9118	258	1887	86	0.21	4198	318
41.7	27.5	59630	565	7098	189	1268	64	0.18	3625	288
45.5	28	94727	815	10137	267	1787	88	0.18	3576	278
54	28	75807	693	8343	228	2257	84	0.27	5488	364
60	28	69572	678	8414	228	2749	90	0.33	6629	406
77.5	28	92261	860	11625	292	3643	114	0.31	6359	368
127.5	28	54542	607	5730	198	935	65	0.16	3312	359
74	28.5	94649	841	11089	281	3735	111	0.34	6834	386
26.5	29	90839	789	8916	254	2074	89	0.23	4720	346
36	29	76588	718	8860	239	1612	81	0.18	3690	294
118	29	57886	616	6625	205	1305	71	0.20	3997	352
123	29	86536	820	9738	272	1592	90	0.16	3318	289
133	29	72308	687	7758	225	1000	71	0.13	2616	269
10	29.5	52693	610	5964	202	2503	86	0.42	8514	602
106.5	29.5	48338	580	6325	198	1181	71	0.19	3787	357
110	29.5	44840	546	5646	185	1234	68	0.22	4433	404
114	29.5	58966	603	5789	195	1200	67	0.21	4205	390
21	29.8	69089	681	8580	230	2075	85	0.24	4907	342
17	30	33628	397	3672	131	1120	51	0.30	6187	518
23.5	30	70646	664	8311	222	1812	79	0.22	4425	319

C.1 (continued) Portable XRF data for the outcrop analysed in Figure 3.1a

Coordinates										
X (horizontal) cm	Y (vertical) cm	Ti (ppm)	Ti 2Θ Error (ppm)	V (ppm)	V 2Θ Error (ppm)	Cr (ppm)	Cr 2Θ Error (ppm)	Cr/V	Cr/V*20290	Cr/V* 9757 2Θ error
30	30	62064	650	7742	220	1503	76	0.19	3938	321
89.5	30	63564	620	7197	206	2199	80	0.31	6200	413
94	30	53348	625	6098	208	1597	77	0.26	5312	454
128	30	80380	765	8698	251	1088	79	0.13	2539	265
13.5	30.5	71391	625	6384	198	2637	79	0.41	8381	528
48.5	30.5	59948	600	6901	200	2333	79	0.34	6858	443
97.5	30.5	43358	528	5205	178	1212	67	0.23	4725	439
101	30.5	42766	508	4731	168	1094	62	0.23	4691	449
49.8	30.7	65109	655	7718	219	2507	87	0.32	6591	428
39	30.8	58723	590	7110	198	1241	67	0.17	3542	300
7	31	49334	591	5678	196	2652	87	0.47	9477	660
33	31	64132	620	7725	208	1238	69	0.16	3252	275
41.5	31	62750	601	7611	202	1558	71	0.20	4153	309
46	31	58612	613	5631	197	1298	68	0.23	4679	424
118	31	68166	636	7266	208	1129	68	0.16	3151	289
54.5	31.5	79868	770	9053	255	2773	98	0.31	6215	406
60	31.5	76385	725	8346	238	2372	89	0.28	5767	391
64	31.5	83517	761	8590	248	2559	92	0.30	6045	404
26.7	31.8	76792	721	9143	242	1688	83	0.18	3747	292
20.8	32	48235	569	5749	191	1225	68	0.21	4323	396

C.1 (continued) Portable XRF data for the outcrop analysed in Figure 3.1a

Coordinates										
X (horizontal) cm	Y (vertical) cm	Ti (ppm)	Ti 2Θ Error (ppm)	V (ppm)	V 2Θ Error (ppm)	Cr (ppm)	Cr 2Θ Error (ppm)	Cr/V	Cr/V*20290	Cr/V* 9757 2Θ error
23.5	32	63386	643	7782	217	1493	76	0.19	3892	316
71	32	70193	672	7730	222	2286	84	0.30	6000	405
106.5	32	49060	571	6359	195	1086	69	0.17	3467	337
17	32.5	55224	642	6106	212	1447	76	0.24	4810	435
80.5	32.5	65407	627	7029	206	2117	78	0.30	6112	416
114	32.5	48547	557	6344	191	835	64	0.13	2670	295
13.5	33	67921	692	8371	234	2182	88	0.26	5288	371
69	33	71176	673	7579	220	2331	84	0.31	6239	419
74.5	33	65333	614	6829	200	2170	77	0.32	6448	430
77.5	33	76461	709	8136	232	2492	89	0.31	6215	411
83	33	68565	641	7427	211	2281	81	0.31	6230	409
87	33	79725	737	8457	241	2443	90	0.29	5862	395
90	33	48747	567	4928	184	1351	68	0.27	5562	506
94	33	85097	771	9371	254	2010	89	0.21	4351	318
123	33	82615	774	9447	257	1151	81	0.12	2472	247
10	33.5	74899	656	7333	211	2031	77	0.28	5620	387
29.5	33.5	78987	750	9217	250	1729	85	0.19	3807	298
6	34	63962	622	7463	208	2440	82	0.33	6634	420
39	34	63220	638	7592	214	2005	80	0.26	5358	376
41.8	34	65092	636	7501	212	2572	85	0.34	6957	439

C.1 (continued) Portable XRF data for the outcrop analysed in Figure 3.1a

Coordinates										
X (horizontal) cm	Y (vertical) cm	Ti (ppm)	Ti 2Θ Error (ppm)	V (ppm)	V 2Θ Error (ppm)	Cr (ppm)	Cr 2Θ Error (ppm)	Cr/V	Cr/V*20290	Cr/V* 20290 2Θ error
65	34	77723	743	8678	246	2250	90	0.26	5260	370
72.5	34	47569	583	5282	193	1495	72	0.28	5741	504
118	34	77810	732	8818	243	1145	77	0.13	2634	257
21	34.5	70614	659	7950	218	1517	75	0.19	3871	306
24	34.5	103702	843	9182	266	1863	88	0.20	4117	322
26.5	34.5	70541	687	8778	232	1486	79	0.17	3434	280
45.5	34.5	62625	613	7273	204	2319	80	0.32	6471	418
17.2	35	77908	726	8183	237	1730	82	0.21	4288	337
33	35	77614	712	8417	234	1915	82	0.23	4615	335
36.5	35	58326	587	7239	198	2091	77	0.29	5861	386
54	35	75827	733	8637	243	2150	89	0.25	5051	361
59	35	84995	791	9032	259	2330	94	0.26	5235	372
69.5	35	64043	612	7142	202	1775	73	0.25	5042	361
81	35	87686	825	9122	269	2449	98	0.27	5447	390
90.5	35	79355	724	7846	234	1523	78	0.19	3938	329
101	35	53434	593	6611	200	1222	70	0.18	3749	340
103.5	35	47540	540	6119	184	982	63	0.16	3257	317
106.5	35	59522	641	7523	217	1049	72	0.14	2830	284
114	35.3	62026	650	7739	220	850	70	0.11	2229	254
78.2	35.5	27406	355	2863	116	804	44	0.28	5699	569

C.1 (continued) Portable XRF data for the outcrop analysed in Figure 3.1a

Coordinates										
X (horizontal) cm	Y (vertical) cm	Ti (ppm)	Ti 2Θ Error (ppm)	V (ppm)	V 2Θ Error (ppm)	Cr (ppm)	Cr 2Θ Error (ppm)	Cr/V	Cr/V*20290	Cr/V* 20290 2Θ error
30	36	98939	856	10085	278	2612	98	0.26	5255	352
76	36	71216	671	7541	219	1936	80	0.26	5210	377
83.5	36	61131	594	6477	194	1813	73	0.28	5679	410
87	36	75261	699	7850	228	1730	79	0.22	4471	345
94	36	92749	784	9246	253	1631	82	0.18	3578	287
13.7	36.5	65799	668	7908	224	1634	79	0.21	4191	332
26.5	37	53310	558	6868	190	1295	67	0.19	3826	313
65	37	45780	541	4837	177	1048	62	0.22	4395	437
98	37	53705	590	6785	200	1098	68	0.16	3284	310
73.5	37.5	60730	584	6568	192	1537	68	0.23	4748	361
90.5	37.5	47859	545	5239	179	839	59	0.16	3248	353
6	38	61072	649	5796	208	1288	72	0.22	4508	427
60	38	57697	645	6087	211	1500	76	0.25	5000	442
83.5	38	60808	590	6478	193	1263	66	0.20	3957	336
106	38	59164	581	6614	192	1084	65	0.16	3326	303
118.5	38	27920	417	3697	143	433	51	0.12	2377	386
114	38.5	36676	538	3852	176	370	57	0.10	1949	410
17	39	77385	727	8792	241	1793	84	0.20	4137	316
70	39	78235	682	6717	214	1527	72	0.23	4612	378
110	39	44157	566	5392	191	672	62	0.12	2530	334

C.1 (continued) Portable XRF data for the outcrop analysed in Figure 3.1a

Coordinates										
X (horizontal) cm	Y (vertical) cm	Ti (ppm)	Ti 2Θ Error (ppm)	V (ppm)	V 2Θ Error (ppm)	Cr (ppm)	Cr 2Θ Error (ppm)	Cr/V	Cr/V*20290	Cr/V* 20290 2Θ error
14	39.5	51427	606	6024	202	1439	74	0.24	4848	425
19.5	39.5	74209	729	9698	249	1793	87	0.18	3751	285
26.5	39.5	80509	723	9445	242	2520	90	0.27	5413	340
87	39.5	58594	665	6273	218	1240	75	0.20	4010	396
12.5	40	60011	574	7227	193	1288	65	0.18	3615	288
23	40	78436	715	9480	240	1998	85	0.21	4277	297
30	40	89292	777	9038	252	3021	98	0.33	6782	420
81	40	59120	594	6407	195	1312	67	0.20	4156	351
94	40	61495	608	6659	200	1139	67	0.17	3470	317
98	40	58666	598	6872	200	1072	66	0.16	3164	297
101	40	68361	669	7730	222	1053	71	0.14	2764	274
103.5	40	42032	521	4943	174	695	57	0.14	2853	346
33	40.5	55991	627	7019	212	2281	85	0.32	6594	459
36	40.5	58079	586	7091	198	1941	76	0.27	5555	382
38.5	40.5	35358	440	4344	148	1224	57	0.28	5718	477
52	40.5	69879	658	7677	217	1776	78	0.23	4694	349
54.5	40.5	71904	676	8208	225	1701	79	0.21	4205	319
41.5	40.8	50172	546	6016	183	1644	70	0.27	5543	418
48	41	67174	634	7168	208	1941	77	0.27	5494	388
50.2	41	67333	622	6910	202	1763	73	0.26	5176	378

C.1 (continued) Portable XRF data for the outcrop analysed in Figure 3.1a

Coordinates										
X (horizontal) cm	Y (vertical) cm	Ti (ppm)	Ti 2Θ Error (ppm)	V (ppm)	V 2Θ Error (ppm)	Cr (ppm)	Cr 2Θ Error (ppm)	Cr/V	Cr/V*20290	Cr/V* 20290 2Θ error
77.5	41	74001	680	7676	221	1648	77	0.21	4356	338
74	41.5	83034	776	8909	255	1743	87	0.20	3969	321
76.5	41.5	73411	684	7950	225	1537	77	0.19	3921	316
118.5	41.5	61371	603	6961	200	688	61	0.10	2005	243
6	42	64412	642	8083	218	1450	75	0.18	3641	294
14	42	35416	511	5571	182	1020	66	0.18	3716	373
22.5	42	75396	729	9935	250	2878	98	0.29	5878	356
65.5	42	62386	644	6421	209	1224	71	0.19	3866	362
106.5	42	50069	556	5271	182	659	57	0.13	2537	316
109.5	42	62412	576	6702	189	1039	62	0.15	3144	283
114	42	74277	696	7520	226	1113	72	0.15	3003	292
12	42.5	68672	675	8509	228	1626	80	0.19	3878	302
17	42.5	72928	676	8305	224	1803	79	0.22	4405	320
87	42.5	66778	642	6955	209	1140	69	0.16	3325	310
20	43	71113	659	8493	221	2196	82	0.26	5245	342
26.5	43	42972	529	5352	179	1772	72	0.33	6716	517
30	43	54707	550	6858	187	1891	72	0.28	5595	375
55	43	69290	658	7537	217	1581	76	0.21	4257	336
60	43	54833	551	6298	183	1249	64	0.20	4024	334
71	43	63902	583	6269	188	1209	63	0.19	3913	332

C.1 (continued) Portable XRF data for the outcrop analysed in Figure 3.1a

Coordinates										
X (horizontal) cm	Y (vertical) cm	Ti (ppm)	Ti 2Θ Error (ppm)	V (ppm)	V 2Θ Error (ppm)	Cr (ppm)	Cr 2Θ Error (ppm)	Cr/V	Cr/V*20290	Cr/V* 20290 2Θ error
81.5	43	50602	599	5667	198	1001	67	0.18	3583	378
84	43	83020	948	8761	310	1478	103	0.17	3422	372
90	43	66057	627	7103	206	1053	67	0.15	3009	286
101.5	43	74908	693	7656	225	1021	71	0.13	2704	275
103.5	43	46856	552	5140	182	596	57	0.12	2355	319
33.5	43.5	54706	674	7317	231	1872	87	0.26	5190	419
36.5	43.5	52790	603	7338	209	1784	80	0.24	4933	372
40	43.5	60970	609	7169	204	1828	75	0.25	5173	370
47	44	11656	303	2298	114	402	48	0.17	3549	631
51.8	44	62157	668	6129	215	1291	73	0.21	4275	408
52.8	44	51004	606	6023	203	1236	72	0.21	4164	395
79	44	73099	794	7300	257	1227	84	0.17	3410	366
94	44	80460	727	8721	239	1151	76	0.13	2678	257
98	44	75206	684	7855	223	1102	71	0.14	2847	273
44.5	44.5	67078	666	8121	224	1747	80	0.22	4364	329
6	45	84251	749	8534	243	1572	80	0.18	3737	306
48	45	49780	576	5391	189	1213	68	0.22	4565	430
65.5	45	64556	628	7194	208	1294	71	0.18	3649	313
77	45	84352	780	8957	255	1494	84	0.17	3385	296
74	45.5	47747	550	5049	180	848	60	0.17	3406	377

C.1 (continued) Portable XRF data for the outcrop analysed in Figure 3.1a

Coordinates										
X (horizontal) cm	Y (vertical) cm	Ti (ppm)	Ti 2Θ Error (ppm)	V (ppm)	V 2Θ Error (ppm)	Cr (ppm)	Cr 2Θ Error (ppm)	Cr/V	Cr/V*20290	Cr/V* 20290 2Θ error
17	46	63617	596	7671	200	2360	79	0.31	6243	381
23	46	48199	567	6101	192	1793	74	0.29	5962	449
60	46	83207	787	9147	259	1801	89	0.20	3995	320
70.5	46	82927	754	8581	246	1550	82	0.18	3666	307
26.5	46.5	81306	726	8081	234	2427	87	0.30	6093	408
20	47	54541	561	7530	194	2206	77	0.29	5943	369
29.5	47	77359	735	9002	245	2412	91	0.27	5437	364
33	47	43237	520	5680	178	1411	69	0.25	5041	418
55.5	47	45633	533	4879	175	903	59	0.19	3755	396
39	47.5	53786	608	7113	208	1391	74	0.20	3968	337
53	47.5	62279	669	6065	215	1222	73	0.20	4088	403
6	48	60011	574	7227	193	1288	65	0.18	3615	288
44.5	48	44361	501	5625	170	1073	61	0.19	3871	347
51	48	61457	592	6813	195	1292	67	0.19	3846	319
66.5	48	61854	613	6790	202	1162	68	0.17	3471	314
48.2	48.8	60186	576	6733	190	1417	67	0.21	4269	331
15	49	65421	650	8149	220	2437	86	0.30	6069	389
17	50	96525	843	10316	276	3204	106	0.31	6303	387
29.7	50	70482	678	8478	228	2147	84	0.25	5138	350
60	50	59272	569	6323	186	1139	63	0.18	3656	318

C.1 (continued) Portable XRF data for the outcrop analysed in Figure 3.1a

Coordinates										
X (horizontal) cm	Y (vertical) cm	Ti (ppm)	Ti 2Θ Error (ppm)	V (ppm)	V 2Θ Error (ppm)	Cr (ppm)	Cr 2Θ Error (ppm)	Cr/V	Cr/V*20290	Cr/V* 20290 2Θ error
23	50.5	72984	683	8065	225	2395	86	0.30	6025	396
56	50.5	65313	603	6652	196	1223	66	0.18	3730	319
26.5	51	60389	639	7879	219	1909	83	0.24	4916	359
54	51	67726	647	7470	213	1430	73	0.19	3884	319
33	51.5	45119	521	5474	175	1309	66	0.24	4853	414
36	51.5	82227	753	9440	251	1990	88	0.21	4278	311
38.5	51.5	70297	693	8717	234	1752	83	0.20	4078	310
45	51.5	60628	594	7640	202	1275	69	0.17	3386	279
41.2	51.8	72909	710	9180	241	1742	84	0.19	3849	295
52.5	52.5	72252	655	7226	212	1478	73	0.20	4151	335
49	53	76622	716	8175	234	1695	81	0.21	4208	332
17	53.5	87592	796	9843	264	2881	100	0.29	5940	376
20	54	48942	521	6560	179	1603	67	0.24	4957	353
23.3	54.5	63964	643	8361	220	1930	81	0.23	4684	330
26.5	54.6	41286	547	5319	187	1223	70	0.23	4666	446
29.8	55	47785	535	6146	182	1458	68	0.24	4813	379
33	55	58536	555	6697	184	1429	65	0.21	4328	324

Appendix D: Portable XRF data for magnetitite analysis in drill core

D.1 Portable XRF data for the Bottom seam in Figure 3.2d and Figure 4.11c

X (horizontal) cm	Ti (ppm)	Ti 2Θ Error (ppm)	V (ppm)	V 2Θ Error (ppm)	Cr (ppm)	Cr 2Θ Error (ppm)	Cr/V	Cr/V*20290	Cr/V* 20290 2Θ error
0	123726	916	11595	292	5072	119	0.44	8875	443
2	100435	882	11038	291	4374	120	0.40	8039	444
4	96194	881	11184	294	3549	115	0.32	6439	387
6	90954	842	10960	283	2779	105	0.25	5144	335
8	96882	890	11848	300	2466	106	0.21	4223	295
10	94406	879	11826	298	2232	102	0.19	3829	279
12	86568	822	11100	280	2004	96	0.18	3663	275
14	99026	929	12407	315	2690	112	0.22	4400	302
16	95459	892	12018	303	2831	110	0.24	4779	314
18	96712	902	12150	306	3477	117	0.29	5806	350
20	88727	831	10975	281	3617	112	0.33	6687	388
24	96991	888	10508	292	3413	113	0.32	6590	413
26	115410	921	9671	288	3349	107	0.35	7026	448
28	112566	951	10453	303	3503	115	0.34	6800	433
30	111511	949	10483	303	3424	114	0.33	6627	425
32	94676	867	10446	286	2916	107	0.28	5663	373
48	86985	774	9083	252	1756	85	0.19	3923	308
68	82208	770	9049	254	1064	79	0.12	2386	251
88	94671	859	10128	281	743	81	0.07	1489	209
108	91735	845	9788	277	392	76	0.04	812	186

D.2 Portable XRF data for the Bottom seam in Figure 3.2e and Figure 4.11d

X (horizontal) cm	Ti (ppm)	Ti 2Θ Error (ppm)	V (ppm)	V 2Θ Error (ppm)	Cr (ppm)	Cr 2Θ Error (ppm)	Cr/V	Cr/V*20290	Cr/V* 20290 2Θ error
1	107539	897	15731	314	5703	130	0.36	7356	321
3	111092	973	15527	338	4332	130	0.28	5660	299
5	102009	943	13021	321	3003	116	0.23	4680	304
7	98072	937	13098	321	2664	113	0.20	4127	283
9	98447	941	13677	325	2358	111	0.17	3499	254
11	98571	932	13168	320	2415	110	0.18	3721	267
13	98743	915	13093	314	2343	107	0.18	3630	260
15	103890	956	13416	326	2762	115	0.21	4177	282
17	100030	938	13521	323	3014	117	0.22	4522	290
19	95189	897	12846	309	4539	127	0.35	7169	382
21	93140	862	10700	287	3638	115	0.34	6898	413
23	95605	891	11224	298	3540	116	0.32	6400	390
25	96697	893	11084	297	3348	114	0.30	6129	384
27	55904	645	6295	214	1843	82	0.29	5939	484
29	96532	899	10704	297	2875	110	0.27	5451	369
31	88363	836	10362	279	2759	105	0.27	5403	360
33	105485	951	11983	316	3105	116	0.26	5257	344
35	102883	928	11577	307	2745	110	0.24	4810	330

D.2 (continued) Portable XRF data for the Bottom seam in Figure 3.2e and Figure 4.11d

X (horizontal) cm	Ti (ppm)	Ti 2Θ Error (ppm)	V (ppm)	V 2Θ Error (ppm)	Cr (ppm)	Cr 2Θ Error (ppm)	Cr/V	Cr/V*20290	Cr/V* 20290 2Θ error
37	90144	811	9567	265	2233	94	0.23	4736	341
39	108300	942	11133	306	2557	107	0.23	4659	333
41	102172	931	11509	309	2434	108	0.21	4290	313
43	95380	873	10846	290	2058	99	0.19	3850	296
45	102941	934	11384	308	2150	105	0.19	3832	299
47	98344	866	10008	281	1960	95	0.20	3973	313
49	103048	918	11199	302	2024	101	0.18	3667	290
51	94605	890	11257	298	1844	99	0.16	3325	274
53	96541	871	10545	287	1847	96	0.18	3554	288
55	97995	881	10637	290	1808	96	0.17	3449	285
57	97830	890	10810	294	1991	99	0.18	3738	296
59	90358	800	9349	260	1413	84	0.15	3067	275
61	105907	944	11346	309	1566	98	0.14	2801	258
63	98836	904	11048	299	1528	96	0.14	2806	258
65	101872	923	11257	304	1449	96	0.13	2611	250
67	101849	924	11227	305	1484	97	0.13	2682	254
69	86886	807	9774	267	1217	84	0.12	2527	250
71	77553	730	8877	243	1219	78	0.14	2787	262

D.2 (continued) Portable XRF data for the Bottom seam in Figure 3.2e and Figure 4.11d

X (horizontal) cm	Ti (ppm)	Ti 2Θ Error (ppm)	V (ppm)	V 2Θ Error (ppm)	Cr (ppm)	Cr 2Θ Error (ppm)	Cr/V	Cr/V*20290	Cr/V* 20290 2Θ error
73	66355	633	7151	208	923	66	0.13	2620	271
75	72696	654	7527	213	827	65	0.11	2229	246
77	99311	891	11064	295	1096	89	0.10	2009	223
79	98609	882	10602	289	938	86	0.09	1795	219
81	102573	932	11512	308	934	91	0.08	1646	209
83	102733	898	10693	293	950	86	0.09	1803	219
85	106009	953	11435	313	758	89	0.07	1345	201
87	102718	925	11187	304	831	88	0.07	1508	207
89	97144	894	11057	297	933	88	0.08	1713	213
91	121790	917	8757	278	701	75	0.08	1625	234
93	101940	918	10933	301	708	86	0.06	1313	201
95	111299	892	8817	276	636	75	0.07	1463	226
97	105017	951	11448	313	496	86	0.04	879	181
99	91291	814	9849	267	544	75	0.06	1121	191

D.3 Portable XRF data for the Bottom seam in Figure 4.11a.

Height above layer base (cm)	Ti (ppm)	Ti 2Θ Error (ppm)	V (ppm)	V 2Θ Error (ppm)	Cr (ppm)	Cr 2Θ Error (ppm)	Cr/V	Cr/V*20290	Cr/V* 20290 2Θ error
0	76874	800	12054.12	284	9579	159	0.79	16124	664
2	78743	799	12467.75	284	8473	150	0.68	13789	572
4	64797	690	10012.49	245	5570	120	0.56	11288	532
6	70412	760	11273.87	271	5800	129	0.51	10438	495
8	61883	649	9279.27	228	4010	102	0.43	8768	450
10	78887	811	12670.39	289	5260	128	0.42	8423	407
12	76106	780	12025.77	277	4847	121	0.40	8178	403
16	83814	795	9244.62	262	3104	103	0.34	6812	431
18	93823	823	9185.96	265	3239	103	0.35	7154	446
20	83016	790	9235.18	261	2901	100	0.31	6373	412
22	84896	795	9186.21	261	2866	100	0.31	6330	411
24	69116	687	7525.43	226	2007	83	0.27	5411	399
26	75724	738	8231.21	243	2112	89	0.26	5206	383
28	79251	735	8037.56	238	2011	85	0.25	5077	377
30	78151	716	7694.82	231	1943	82	0.25	5123	381

D.3 (continued) Portable XRF data for the Bottom seam in Figure 4.11a.

Height above layer base (cm)	Ti (ppm)	Ti 2Θ Error (ppm)	V (ppm)	V 2Θ Error (ppm)	Cr (ppm)	Cr 2Θ Error (ppm)	Cr/V	Cr/V*20290	Cr/V* 20290 2Θ error
32	76708	737	8705.26	244	1922	87	0.22	4480	338
34	74258	712	8164.87	235	1691	81	0.21	4203	332
36	82726	775	9015.62	255	1757	86	0.19	3955	315
38	75584	725	8565.3	240	1557	81	0.18	3689	304
45	38483	483	3878.89	157	1053	59	0.27	5507	552
68	99731	849	8695.92	267	1620	86	0.19	3780	327
70	119450	921	8479.45	280	1443	84	0.17	3454	326
72	84801	802	9271.92	264	1403	85	0.15	3070	282
74	88345	808	8694.18	260	1227	82	0.14	2862	284
76	82908	763	8943.38	250	1109	78	0.12	2516	253
78	86463	793	9275.93	260	1136	81	0.12	2485	253
80	80540	751	8846.73	248	1137	78	0.13	2607	259
82	87315	820	9378.67	269	1031	82	0.11	2230	249
84	82760	755	8659.57	246	852	74	0.10	1995	236

D.3 (continued) Portable XRF data for the Bottom seam in Figure 4.11a.

Height above layer base (cm)	Ti (ppm)	Ti 2Θ error (ppm)	V (ppm)	V 2Θ error (ppm)	Cr (ppm)	Cr 2Θ error (ppm)	Cr/V	Cr/V*20290	Cr/V* 20290 2Θ error
86	83806	798	9128.85	262	961	80	0.11	2135	246
88	86064	809	9612.45	267	756	79	0.08	1596	216
90	96899	861	9472.52	277	857	80	0.09	1837	233
92	85941	798	8333.36	256	612	73	0.07	1491	231
94	71131	652	7058.07	211	475	59	0.07	1364	218
96	86655	812	9067.09	265	563	75	0.06	1259	211
98	85201	806	9072.59	264	627	76	0.07	1403	217
100	94706	848	9102.52	272	568	76	0.06	1266	213
102	82603	790	8758.84	258	452	72	0.05	1048	204
104	92745	834	8988.87	268	515	74	0.06	1162	208
106	70550	681	7876.13	225	483	65	0.06	1245	208
108	82816	754	7975.59	242	361	66	0.05	919	202
110	75780	714	8343.2	235	308	64	0.04	749	183
112	80396	763	9177.5	254	409	71	0.04	904	186
114	65412	642	7301.77	212	286	59	0.04	794	192
116	56223	558	6080.32	183	271	51	0.04	904	205
118	57807	636	5178.99	201	194	54	0.04	759	253
120	46302	555	4828	181	249	52	0.05	1047	267
122	38867	485	4390.76	161	183	46	0.04	847	253

D.4 Portable XRF data for the Bottom seam in Figure 4.11b.

Height above layer base (cm)	Ti (ppm)	Ti 2Θ Error (ppm)	V (ppm)	V 2Θ Error (ppm)	Cr (ppm)	Cr 2Θ Error (ppm)	Cr/V	Cr/V*20290	Cr/V* 20290 2Θ error
1	97319	920	12608	314	10086	172	0.80	16231	698
3	96176	902	12271	307	8644	160	0.70	14294	638
5	87838	806	11841	277	9928	154	0.84	17012	678
9	78394	774	10367	265	4684	119	0.45	9167	479
11	73673	712	10286	247	4721	113	0.46	9313	457
17	104586	909	10660	295	4946	128	0.46	9413	518
19	100804	900	10765	295	4034	120	0.37	7602	446
21	108276	943	11084	306	3479	117	0.31	6369	401
23	57249	640	6795	215	2234	88	0.33	6671	488
25	101110	888	10044	287	2840	106	0.28	5738	388
27	81375	779	8637	255	2610	99	0.30	6132	425
29	111354	940	10649	301	2804	108	0.26	5342	367
31	109932	913	10682	294	2579	104	0.24	4898	341
33	74810	698	7420	225	1803	81	0.24	4930	383
35	101758	877	9660	280	2154	97	0.22	4524	345
37	105321	885	9891	283	2058	96	0.21	4221	326
39	102025	915	11078	301	1956	101	0.18	3583	291

D.4 (continued) Portable XRF data for the Bottom seam in Figure 4.11b.

Height above layer base (cm)	Ti (ppm)	Ti 2Θ Error (ppm)	V (ppm)	V 2Θ Error (ppm)	Cr (ppm)	Cr 2Θ Error (ppm)	Cr/V	Cr/V*20290	Cr/V* 20290 2Θ error
41	107146	936	10984	304	1714	99	0.16	3166	278
43	104170	926	11243	304	1661	98	0.15	2997	266
45	97405	885	10884	293	1366	92	0.13	2547	247
47	104704	935	11169	306	1536	97	0.14	2791	261
49	96375	876	10805	290	1275	91	0.12	2395	241
51	77468	722	7518	232	882	72	0.12	2380	275
53	102741	936	11802	312	1170	95	0.10	2011	222
55	90382	824	10077	273	881	82	0.09	1773	219
57	97196	891	10600	293	1033	89	0.10	1977	231
59	109955	936	10979	302	825	87	0.08	1525	208
61	94822	834	9847	272	987	82	0.10	2034	231
63	95428	864	10606	286	670	82	0.06	1281	197
65	88366	836	9805	276	744	82	0.08	1540	219
67	73268	704	8156	233	445	67	0.05	1107	205
69	90311	824	9850	271	472	76	0.05	973	189

D.4 Portable XRF data for the Main Magnetite Layer in Figure 4.11e.

Height above layer base (cm)	Ti (ppm)	Ti 2Θ Error (ppm)	V (ppm)	V 2Θ Error (ppm)	Cr (ppm)	Cr 2Θ Error (ppm)	Cr/V	Cr/V*9757	Cr/V* 9757 2Θ error
0	87686	833	8946	271	15927	196	1.78	17370	762
2	81370	789	8472	257	14811	184	1.75	17057	753
4	91917	887	9297	288	12394	182	1.33	13008	612
6	93440	886	9271	286	9666	163	1.04	10174	501
8	88117	848	8859	275	7165	143	0.81	7892	415
10	83081	795	8458	258	6196	129	0.73	7147	379
12	84741	805	8438	260	5539	124	0.66	6405	352
14	87133	820	8400	263	5257	123	0.63	6107	345
16	93205	864	9086	278	5201	126	0.57	5585	316
18	90762	832	8811	268	4332	115	0.49	4797	282
28	92549	886	9017	285	3142	111	0.35	3400	235
38	95010	882	8504	280	2385	101	0.28	2736	212
48	95496	877	8737	279	1450	89	0.17	1620	157
58	101671	916	8980	289	1029	86	0.11	1118	134
78	99017	890	9034	283	565	78	0.06	610	107

D.4 (continued) Portable XRF data for the Main Magnetite Layer in Figure 4.11e.

Height above layer base (cm)	Ti (ppm)	Ti 2Θ Error (ppm)	V (ppm)	V 2Θ Error (ppm)	Cr (ppm)	Cr 2Θ Error (ppm)	Cr/V	Cr/V*9757	Cr/V* 9757 2Θ error
98	93589	842	7831	264	440	71	0.06	549	111
118	61821	588	5515	186	100	71	0.02	177	136
128	94350	883	8155	278	118	71	0.01	141	93
138	85993	806	7637	255	100	97	0.01	128	133
148	80915	799	7423	254	100	100	0.01	131	141
150	87434	865	8905	281	706	82	0.08	774	118
152	96186	916	9424	295	1479	94	0.16	1531	150
154	86265	822	8326	264	1727	89	0.21	2024	174
156	83354	804	8282	260	1792	89	0.22	2111	177
158	99449	919	9903	297	2203	102	0.22	2171	170
160	96456	887	9302	285	1663	92	0.18	1744	155
162	93031	900	9603	293	1445	93	0.15	1468	144
168	94608	866	9232	279	1373	87	0.15	1451	140

D.5 Portable XRF data for the Main Magnetite Layer in Figure 4.11f.

Height above layer base (cm)	Ti (ppm)	Ti 2Θ Error (ppm)	V (ppm)	V 2Θ Error (ppm)	Cr (ppm)	Cr 2Θ Error (ppm)	Cr/V	Cr/V*9757	Cr/V* 9757 2Θ error
1	93661	867	8589	276	7523	147	0.88	8547	456
20	94131	867	9049	278	5162	127	0.57	5566	318
22	93692	853	8685	272	4568	120	0.53	5131	305
24	97733	878	8953	279	4324	120	0.48	4713	286
26	81216	766	7778	246	3388	103	0.44	4250	272
28	85402	818	8394	264	3368	109	0.40	3915	258
40	86950	818	7836	259	2528	98	0.32	3147	234
60	93602	866	8775	277	1863	95	0.21	2072	176
80	99411	903	9173	287	888	85	0.10	944	124
100	100124	904	9020	287	534	80	0.06	578	108
120	100662	916	9078	290	160	75	0.02	172	89
140	105070	920	8932	288	100	108	0.01	109	125
150	92082	834	8256	264	117	68	0.01	138	87
160	100316	900	9449	288	1431	92	0.15	1477	144
170	104389	930	9127	293	1642	95	0.18	1755	164

Appendix E: Whole-rock data for Rhovan drill core samples

E.1 Major and minor elements data for Rhovan drill core samples

Sample	PB19	PB18	PB40	PB17	PB01	PB02	PB03	PB04	PB05	PB06.1
Height above lowermost sample (m)	0	0.03	0.4	1.75	1.85	2	2.2	2.3	2.62	2.77
Weight. %										
SiO_2	51.87	53.03	52.52	49.19	1.28	2.22	2.09	37.11	10.92	9.56
TiO_2	0.41	0.09	0.17	0.88	12.81	13.55	13.72	4.41	11.56	11.96
Al_2O_3	20.94	27.94	27.43	25.56	4.12	4.16	3.89	20.08	7.99	7.39
Fe_2O_3	8.55	1.33	2.07	7.05	78.81	77.38	78.06	25.82	64.41	66.58
MnO	0.13	0.02	0.03	0.05	0.26	0.27	0.28	0.1	0.23	0.24
MgO	4.92	0.23	0.37	0.88	1.81	2.06	1.98	0.89	1.6	1.72
CaO	9.5	11.35	11.16	10.07	0.09	0.21	0.18	7.82	2.11	1.85
Na_2O	3.33	4.55	4.53	4.05	0.03	0.07	0.05	3.06	0.84	0.69
K_2O	0.22	0.36	0.42	0.43	X**	X	X	0.22	0.07	0.05
P_2O5	0.01	0.014	0.013	0.009	0.005	0.005	0.005	0.005	0.004	0.003
SO_3	0.03	0.02	0.04	0.03	0.065	0.025	0.030	0.02	0.02	0.01
LOI*	X	0.44	0.58	0.93	X	X	X	X	X	X
Total	99.91	99.37	99.33	99.13	99.28	99.95	100.29	99.54	99.75	100.05

* Loss on ignition. ** Below detection limit

E.1 (continued) Major and minor elements data for Rhovan drill core samples

Sample	PB06.2	PB07	PB08	PB09	PB10	PB11	PB12	PB13.1	PB13.2	PB13.3
Height above lowermost sample (m)	2.92	3.23	3.52	4.02	4.47	4.55	4.74	4.96	4.995	5.03
Weight. %										
SiO_2	16.12	17.09	26.65	46.51	39.05	22.5	42.63	45.36	51.11	19.7
TiO_2	10.14	9.99	7.3	1.78	3.84	8.48	2.97	2.39	0.64	9.9
Al_2O_3	10.46	10.99	15.33	16.76	11.86	11.6	17.78	22.7	25.48	10.62
Fe_2O_3	57.13	55.82	40.98	16.55	28.62	48.61	20.86	14.86	5.06	51.97
MnO	0.2	0.2	0.15	0.16	0.23	0.2	0.15	0.07	0.04	0.23
MgO	1.5	1.42	1.13	5.01	6.06	2.26	3.42	1.04	0.79	2.42
CaO	3.24	3.42	5.47	10.31	8.99	5.03	9.41	9.56	10.72	2.9
Na_2O	1.3	1.41	2.15	2.7	1.81	1.56	2.84	3.74	4.32	1.03
K_2O	0.1	0.1	0.16	0.17	0.1	0.11	0.2	0.31	0.48	0.12
P_2O5	0.004	0.004	0.004	0.005	0.003	0.003	0.005	0.008	0.043	0.018
SO_3	X	X	X	X	X	X	X	0.02	0.03	0.295
LOI*	X	X	X	X	X	X	X	0.02	0.54	X
Total	100.19	100.44	99.32	99.96	100.56	100.35	100.27	100.08	99.25	99.20

E.1 (continued) Major and minor elements data for Rhovan drill core samples

Sample	S65.2	S64	S63	S62	S61	S60	S59	S56	S55	S54
Height above lowermost sample (m)	6.23	6.63	7.63	9.63	10.63	11.63	12.63	13.63	14.63	18.1
Weight. %										
SiO_2	45.2	46.81	44.34	40.55	40.63	40.98	42.03	41.89	36.72	35.98
TiO_2	1.75	1.67	2.32	3.09	3.53	3.4	3.15	3.13	4.64	4.72
Al_2O_3	12.62	15.7	18.95	13.98	17.03	17.89	17.21	17.45	18.19	13.01
Fe_2O_3	17.44	16.31	16.85	23.45	23.46	22.12	21.57	21.30	27.53	30.63
MnO	0.22	0.18	0.13	0.16	0.15	0.14	0.15	0.14	0.13	0.19
MgO	6.64	5.39	3.16	4.88	3.37	2.95	3.54	3.32	1.81	4.47
CaO	13.29	11.1	9.96	7.63	9.06	9.05	9.38	9.32	7.94	8.54
Na_2O	1.63	2.45	2.88	2.26	2.65	2.83	2.75	2.82	2.86	2.03
K_2O	0.47	0.17	0.65	0.82	0.18	0.21	0.19	0.22	0.19	0.12
P_2O5	0.012	0.007	0.007	0.003	0.007	0.008	0.005	0.006	0.005	0.004
SO_3	0.02	X	X	X	0.01	X	X	0.02	0.15	0.29
LOI*	0.33	X	0.55	2.22	X	X	X	X	X	X
Total	99.62	99.79	99.80	99.04	100.08	99.58	99.98	99.62	100.17	99.98

E.1 (continued) Major and minor elements data for Rhovan drill core samples

Sample	S53	S52	S51	S50	S49	S48	S47	S46	S45	S44
Height above lowermost sample (m)	19.63	20.63	22.63	23.63	24.63	25.63	29.58	35.63	45.63	55.63
Weight. %										
SiO_2	34.99	26.32	36.45	28.73	37.73	29.85	38.75	39.02	43.23	45.12
TiO_2	5.18	7.69	4.81	7.04	4.48	X	4.27	4.22	2.93	2.27
Al_2O_3	15.65	14.45	14.41	13.74	16.06	13.9	16.51	16.98	14.75	12.31
Fe_2O_3	30.59	42.21	29.82	39.60	27.40	38.02	26.07	25.55	21.48	20.58
MnO	0.15	0.17	0.18	0.18	0.16	0.18	0.16	0.15	0.19	0.23
MgO	2.86	1.54	3.81	2.51	3.16	2.67	3.13	3.09	5.22	7.19
CaO	7.88	5.61	8.41	6.4	8.57	6.73	8.57	8.28	9.86	10.4
Na_2O	2.46	2.12	2.25	2.05	2.55	2.08	2.65	2.74	2.4	2
K_2O	0.15	0.14	0.14	0.12	0.16	0.13	0.17	0.17	0.15	0.12
P_2O5	0.005	0.004	0.004	0.004	0.005	0.004	0.005	0.005	0.004	0.004
SO_3	0.3	0.47	0.26	0.31	0.26	0.27	0.28	0.25	0.18	0.07
LOI	X	X	X	X	X	X	X	X	X	X
Total	100.22	100.72	100.54	100.68	100.54	93.83	100.57	100.46	100.39	100.29

E.1 (continued) Major and minor elements data for Rhovan drill core samples

Sample	S43	S42	S41.2	S41.1	S40	S39	S38	S37	S36	S35
Height above lowermost sample (m)	65.63	75.63	82.58	82.78	84.28	84.63	85.63	86.63	87.63	88.63
Weight. %										
SiO_2	44.79	46.06	46.63	12.63	9.92	44.71	27.62	33.98	32.5	41.24
TiO_2	2.4	2.02	1.53	13.82	15.86	2.37	7.02	4.98	5.22	3.02
Al_2O_3	13.84	12.79	14.09	2.62	3.23	23.72	16.13	18.4	17.92	16.11
Fe_2O_3	20.08	19.98	17.43	63.15	65.63	14.28	39.38	31.16	33.11	21.93
MnO	0.2	0.23	0.21	0.34	0.34	0.07	0.14	0.12	0.12	0.14
MgO	6.21	7.2	6.83	4.04	3.57	0.96	1.35	1.37	1.4	4.12
CaO	10.25	10.47	11.37	4.27	3.31	9.55	5.95	7.19	6.9	10.21
Na_2O	2.25	2.03	2.19	0.1	0.16	3.66	2.31	2.85	2.71	2.58
K_2O	0.14	0.1	0.2	0.02	0.02	0.25	0.15	0.15	0.15	0.17
P_2O5	0.004	0.004	0.008	0.011	0.007	0.008	0.004	0.006	0.005	0.006
SO_3	0.12	0.11	0.17	1.411	1.883	0.02	0.02	0.05	0.32	0.34
LOI	X	X	X	X	X	X	X	X	X	X
Total	100.28	100.99	100.66	102.41	103.93	99.60	100.07	100.26	100.36	99.87

E.1 (continued) Major and minor elements data for Rhovan drill core samples

Sample	S34	S33	S32.3	S32.2	S32.1	S31	S30.4	S30.3	S30.2	S30.1
Height above lowermost sample (m)	89.63	90.63	91.47	91.59	91.88	92.17	93.18	93.29	93.555	93.65
Weight. %										
SiO_2	36.28	43.6	42.8	1.45	30.31	32.63	36.83	3.65	8.63	44.29
TiO_2	4.17	1.55	1.76	14.86	5.92	5.42	4.61	18.57	16.18	2.71
Al_2O_3	14.01	11.75	10.93	3.15	17.36	17.81	18.76	2.77	2.99	16.01
Fe_2O_3	30.14	20.33	22.87	78.68	36.07	33.06	26.05	73.02	67.16	17.96
MnO	0.18	0.21	0.22	0.31	0.13	0.12	0.15	0.38	0.36	0.18
MgO	4.29	6.7	6.97	2.24	1	1.35	2.59	3.36	3.98	4.4
CaO	9.01	10.76	11.02	0.39	6.5	6.93	8.98	0.3	2.73	12.09
Na_2O	2.03	1.82	1.66	0.04	2.5	2.72	2.31	0.04	0.09	2.4
K_2O	0.11	0.16	0.13	X	0.15	0.16	0.17	X	X	0.16
P_2O5	0.004	0.009	0.009	0.007	0.006	0.005	0.014	0.007	0.007	0.015
SO_3	0.26	4.06	4.5	1.069	1.41	0.44	0.33	0.774	0.869	0.36
LOI	X	0.65	0.26	X	X	X	X	X	X	X
Total	100.48	101.60	103.13	102.20	101.36	100.65	100.79	102.87	102.99	100.58

E.1 (continued) Major and minor elements data for Rhovan drill core samples

Sample	WLS Bot	WLS Top	S29	S28,3	S28,2	S28,1	S27,3	S27.1	S26	S25
Height above lowermost sample (m)	93.75	93.83	94.42	95.76	95.92	96.13	97.34	97.6	98.63	99.63
Weight. %										
SiO_2	40.82	27.59	15.65	22.59	7.23	7.73	14.32	19.52	26.92	33.14
TiO_2	3.63	7.47	10.12	8.58	12.7	12.7	11.07	9.86	7.75	5.95
Al_2O_3	8.75	15.91	10.34	13.57	6.44	6.51	9.74	12.09	15.34	18.09
Fe_2O_3	25.26	39.45	57.95	47.90	69.72	69.47	59.57	52.20	40.49	31.29
MnO	0.25	0.16	0.2	0.17	0.25	0.25	0.22	0.2	0.15	0.12
MgO	7.12	1.14	1.6	1.41	1.83	1.91	1.64	1.36	1.2	1.2
CaO	12.97	5.94	3.35	4.8	1.6	1.67	3.05	3.93	5.62	6.79
Na_2O	1.24	2.29	1.27	1.94	0.53	0.55	1.19	1.68	2.35	2.85
K_2O	0.07	0.11	0.06	0.06	0.02	0.02	0.05	0.1	0.12	0.2
P_2O5	0.009	0.004	0.004	0.004	0.003	0.003	0.004	0.004	0.004	0.006
SO_3	0.68	0.26	0.39	0.36	0.38	0.39	0.54	0.47	0.38	0.25
LOI	X	X	X	X	X	X	X	X	X	X
Total	100.80	100.32	100.93	101.38	100.70	101.20	101.39	101.41	100.32	99.89

E.1 (continued) Major and minor elements data for Rhovan drill core samples

Sample	S24	S23	S22.2	CX	S22.1	S20	N2	S19	S18.6	S18.5
Height above lowermost sample (m)	101.63	102.63	103.33	103.49	103.54	105.63	110.63	115.63	118.53	118.68
Weight. %										
SiO_2	29.47	27.84	24.77	20.44	21.78	31.85	39.01	39.96	36.89	14.55
TiO_2	7.39	8.2	9.06	10.3	9.86	6.66	4.33	3.85	4.38	11.59
Al_2O_3	16.45	15.73	14.4	12.95	13.48	17.71	19.37	18.08	15.82	3.41
Fe_2O_3	36.82	39.91	43.27	48.82	47.31	33.37	24.35	22.59	26.43	59.49
MnO	0.14	0.16	0.17	0.19	0.19	0.13	0.11	0.13	0.15	0.29
MgO	1.19	1.06	1.31	1.45	1.53	1.47	2.72	5.19	6.52	11.25
CaO	6.01	5.69	5.04	4.33	4.54	6.09	7.34	6.88	5.71	0.54
Na_2O	2.58	2.47	2.18	1.75	1.84	2.86	3.21	2.92	2.49	0.2
K_2O	0.17	0.15	0.12	0.08	0.11	0.18	0.23	0.22	0.31	0.02
P_2O5	0.005	0.005	0.004	0.003	0.004	0.009	0.008	0.012	0.011	0.011
SO_3	0.31	0.3	0.42	0.37	0.34	0.35	0.36	0.08	1.94	0.110
LOI	X	X	X	X	X	X	X	X	0.18	X
Total	100.54	101.52	100.74	100.68	100.98	100.68	101.04	99.91	100.83	101.46

E.1 (continued) Major and minor elements data for Rhovan drill core samples

Sample	S18.4	S18.3	S18.2	S18.1	S21.3	S21.2	S21.1	S17	N6	N5
Height above lowermost sample (m)	118.86	118.945	119.1	119.21	120.36	120.46	120.63	125.63	130.73	130.93
Weight. %										
SiO_2	16.57	14.69	3.26	38.18	34.23	51.63	40	38.83	37.51	52.25
TiO_2	10.69	11.71	18.53	4.46	6.77	0.57	3.75	3.88	3.98	0.09
Al_2O_3	3.65	3.82	4.39	17.2	18.45	26.11	17.39	18.1	16.29	27.5
Fe_2O_3	56.09	58.53	71.04	24.39	28.73	3.66	20.51	24.07	27.49	1.60
MnO	0.29	0.29	0.27	0.13	0.12	0.03	0.13	0.13	0.16	0.02
MgO	12.46	11.19	3.47	5.33	1.49	0.73	5.92	5.37	6.26	0.46
CaO	0.67	0.62	0.29	6.36	6.7	10.74	6.25	7.12	6.66	11.37
Na_2O	0.26	0.26	0.1	2.65	2.87	4.57	2.37	2.78	2.22	4.44
K_2O	0.02	0.02	0.01	0.32	0.19	0.49	0.14	0.2	0.17	0.58
P_2O5	0.014	0.014	0.007	0.008	0.007	0.019	0.013	0.01	0.01	0.014
SO_3	0.175	0.447	0.444	0.58	0.54	0.11	0.22	0.2	0.03	0.23
LOI	X	X	X	0.31	0.03	1.17	2.76	X	X	1.01
Total	100.89	101.60	101.82	99.92	100.13	99.83	99.45	100.69	100.78	99.56

E.1 (continued) Major and minor elements data for Rhovan drill core samples

Sample	N7	N8.2	N8.1	S16	S15	N4.2	N4.1	N3	S14	S13.1
Height above lowermost sample (m)	132.03	132.53	132.78	135.63	146.63	152.13	152.38	154.63	154.73	155.38
Weight. %										
SiO_2	52.39	51.85	48.63	42.8	39.76	40.49	46.19	47.53	48.69	49.96
TiO_2	0.15	0.11	1.16	2.04	1.86	2.05	0.31	1.23	0.83	0.68
Al_2O_3	28.12	27.27	26.6	19.36	16.92	20.72	18.61	18.65	19.28	25.92
Fe_2O_3	1.45	1.57	7.12	20.31	24.77	21.22	15.11	15.03	12.19	5.64
MnO	0.02	0.02	0.04	0.13	0.15	0.11	0.16	0.16	0.16	0.05
MgO	0.26	0.36	0.39	4.17	6.59	3.37	8.11	5.21	4.34	0.88
CaO	11.41	10.94	11.15	8.88	7.63	9.43	8.92	9.35	9.99	11.31
Na_2O	4.44	4.6	3.9	2.59	2.04	2.49	2.37	2.64	2.83	3.97
K_2O	0.56	0.75	0.3	0.21	0.19	0.21	0.22	0.25	0.45	0.47
P_2O5	0.012	0.02	0.016	0.011	0.013	0.014	0.017	0.016	0.031	0.012
SO_3	0.01	0.02	0.06	0.08	0.1	0.03	0.05	0.08	0.05	0.17
LOI	0.77	1.69	0.28	X	X	X	X	X	0.81	0.64
Total	99.59	99.20	99.65	100.58	100.02	100.13	100.07	100.15	99.65	99.70

E.1 (continued) Major and minor elements data for Rhovan drill core samples

Sample	S12	S11	N1	S10.3	S10.2	S10.1	S09.2	S09.1	S08	S07
Height above lowermost sample (m)	161.63	167.13	167.83	170.69	170.87	171.12	171.17	171.28	171.43	171.63
Weight. %										
SiO_2	50.92	51.38	51.55	51.72	50.08	50.63	4.85	2.51	1.47	0.97
TiO_2	0.5	0.42	0.29	0.25	0.61	0.06	12.26	11.54	13.11	13.62
Al_2O_3	20.89	18.67	20.4	18.98	15.66	26.55	5.77	3.91	4.13	3.72
Fe_2O_3	9.75	10.84	8.68	9.91	13.70	5.23	69.11	76.54	76.79	77.61
MnO	0.14	0.17	0.14	0.16	0.23	0.04	0.26	0.2	0.19	0.19
MgO	4.17	5.58	4.54	5.32	6.82	0.47	2.45	0.97	0.61	0.86
CaO	10	10.26	10.67	9.68	8.89	6.66	0.02	0.02	0.03	0.03
Na_2O	3.21	2.79	3.1	2.88	2.43	4.21	0.02	0.04	0.07	0.07
K_2O	0.26	0.22	0.26	0.33	0.39	1.6	X	X	X	X
P_2O5	0.024	0.028	0.026	0.033	0.016	0.011	0.005	0.005	0.005	0.005
SO_3	0.13	0.08	0.08	0.03	0.03	0.03	0.062	0.162	0.147	0.195
LOI	0.1	0.03	0.16	0.28	1.02	3.8	1.64	2.14	0.97	0.59
Total	100.09	100.47	99.90	99.57	99.88	99.29	96.45	98.03	97.52	97.86

E.1 (continued) Major and minor elements data for Rhovan drill core samples

Sample	S06	S05	S04	S03	S02	S01
Height above lowermost sample (m)	172.33	173.13	173.68	173.79	174.13	175.63
Weight. %						
SiO_2	1.07	0.51	1.47	12.59	44.19	39.53
TiO_2	13.8	13.72	13.17	10.34	2.41	3.56
Al_2O_3	3.89	3.74	3.46	9.33	23.94	21.92
Fe_2O_3	78.37	78.39	78.87	62.04	15.00	21.67
MnO	0.24	0.16	0.19	0.21	0.06	0.08
MgO	0.76	0.33	0.5	1.66	0.42	0.51
CaO	0.02	0.02	0.03	1.81	9.26	8.18
Na_2O	0.03	0.04	0.07	0.61	3.4	3.09
K_2O	X	X	X	0.08	0.3	0.28
P_2O5	0.005	0.005	0.005	0.005	0.012	0.01
SO_3	0.055	0.170	0.102	0.13	0.03	0.13
LOI	0.24	1.33	0.53	0.12	0.75	0.55
Total	98.47	98.42	98.39	98.93	99.77	99.51

E.2 Trace element elements data for Rhovan drill core samples

Sample	PB19	PB18	PB40	PB17	PB01	PB02	PB03	PB04	PB05	PB06.1
Height above lowermost sample (m)	0	0.03	0.4	1.75	1.85	2	2.2	2.3	2.62	2.77
Parts per million										
Cr	90	9	7	227	6937	3634	1183	144	147	128
V	330	35	69	618	13293	10901	10638	3342	8764	8710
Ni	89	5.7	10.3	40.8	560.6	480.1	445.6	150.2	375.5	387.3
Sc	16.8	0.8	1.5	5.3	27.8	28.8	28.3	9.9	25.9	26.6
Rb	1.63	1.14	1.25	7.39	0.16	0.16	0.24	0.69	0.65	0.36
Sr	383.42	411.73	353.64	437.63	3.81	10.54	10.08	317.96	100.14	85.29
La	2.56	1.59	1.41	2.53	0.09	0.15	0.16	1.21	0.53	0.4
Ce	4.47	2.95	2.59	4.16	0.16	0.25	0.26	1.79	0.79	0.61
Pr	0.51	0.32	0.27	0.44	0.02	0.02	0.03	0.19	0.09	0.07
Nd	1.88	1.13	0.98	1.61	0.09	0.08	0.12	0.62	0.27	0.24
Sm	0.44	0.17	0.2	0.29	0.02	0.02	0.02	0.12	0.04	0.04
Eu	0.49	0.37	0.28	0.59	0.01	0.02	0.02	0.48	0.15	0.13
Gd	0.44	0.15	0.17	0.3	0.02	0.02	0.01	0.08	0.03	0.04
Tb	0.08	0.03	0.03	0.05	X	X	X	0.02	X	0.01
Dy	0.5	0.14	0.18	0.25	0.02	0.02	0.03	0.08	0.03	0.03
Ho	0.11	0.03	0.04	0.05	X	X	X	0.02	0.01	0.01
Er	0.34	0.08	0.11	0.15	0.03	0.02	0.02	0.05	0.02	0.02
Tm	0.05	0.01	0.02	0.02	X	X	X	0.01	X	X
Yb	0.37	0.07	0.11	0.13	0.04	0.04	0.03	0.07	0.02	0.04
Lu	0.07	0.01	0.02	0.02	X	X	X	0.02	0.01	0.01
Zr	6.8	4.1	4.7	4.7	19.3	25.3	24.4	8.8	20.7	20.8
Y	2.88	0.55	0.75	1.23	0.17	0.14	0.12	0.38	0.12	0.11
Pb	1.9	2	2.6	3.5	0.8	X	X	1.8	X	0.7
Zn	66	13	23	43	388	383	366	129	346	332
Th	0.17	0.19	0.18	0.1	0.02	0.02	0.04	0.04	0.04	0.03
U	0.05	0.04	0.04	0.03	0.02	0.02	0.01	0.01	0.01	0.02

E.2 (continued) Trace element elements data for Rhovan drill core samples

Sample	PB06.2	PB07	PB08	PB09	PB10	PB11	PB12	PB13.1	PB13.2	PB13.3
Height above lowermost sample (m)	2.92	3.23	3.52	4.02	4.47	4.55	4.74	4.96	4.995	5.03
Parts per million										
Cr	112	78	47	15	22	41	16	32	16	391
V	7412	7231	5346	1366	2808	5870	2161	1597	425	7442
Ni	317	314.4	226.3	102.7	172.7	263.5	125	84	30	330.7
Sc	21.7	21.4	15.8	36.9	50	26.4	28.9	10.8	6	21.7
Rb	0.63	0.73	0.9	0.82	0.37	0.64	0.84	2	2.6	1.87
Sr	140.4	155.33	243.71	283.65	190	169.25	290.03	386.58	419.24	130.3
La	0.53	0.62	0.76	1.06	0.68	0.51	1.21	2.82	3.74	1.57
Ce	0.78	0.91	1.05	2.07	1.45	0.8	2.18	5.02	7.17	2.86
Pr	0.08	0.09	0.11	0.29	0.25	0.1	0.3	0.59	0.89	0.34
Nd	0.22	0.34	0.37	1.35	1.25	0.47	1.34	2.4	3.58	1.22
Sm	0.04	0.04	0.05	0.45	0.49	0.15	0.41	0.51	0.74	0.22
Eu	0.2	0.22	0.34	0.49	0.4	0.26	0.47	0.67	0.72	0.24
Gd	0.03	0.03	0.03	0.61	0.77	0.17	0.49	0.53	0.66	0.21
Tb	0.01	X	X	0.11	0.14	0.03	0.1	0.09	0.11	0.03
Dy	0.03	0.02	0.04	0.74	0.92	0.21	0.57	0.55	0.64	0.16
Ho	X	X	X	0.15	0.21	0.04	0.13	0.11	0.13	0.03
Er	0.02	0.02	0.02	0.44	0.59	0.14	0.34	0.27	0.33	0.11
Tm	X	X	X	0.07	0.09	0.02	0.06	0.04	0.05	0.02
Yb	0.03	0.02	0.03	0.46	0.58	0.13	0.35	0.24	0.26	0.1
Lu	X	X	X	0.07	0.1	0.02	0.06	0.04	0.04	0.02
Zr	17	16.8	12.1	4.7	7.7	11.6	7.4	8	4.8	14.8
Y	0.13	0.09	0.15	3.79	4.8	1.08	2.95	2.47	2.98	0.9
Pb	X	0.5	1	0.7	0.6	0.6	1.4	1.6	2.4	2.1
Zn	277	271	198	86	143	238	108	78	32	240
Th	0.03	0.03	0.02	0.04	0.02	0.03	0.05	0.09	0.43	0.31
U	0.01	0.01	X	0.01	X	X	0.02	0.03	0.05	0.02

E.2 (continued) Trace element elements data for Rhovan drill core samples

Sample	S65.2	S64	S63	S62	S61	S60	S59	S56	S55	S54
Height above lowermost sample (m)	6.23	6.63	7.63	9.63	10.63	11.63	12.63	13.63	14.63	18.1
Parts per million										
Cr	22	25	39	36	30	24	16	13	15	9
V	1008	1257	1685	2150	2272	2395	2179	2202	3170	3239
Ni	97.7	97.3	101.8	119.8	126.7	120.2	117.8	129.4	165.9	194.6
Sc	60.9	45.4	29.2	42.9	29.2	26.1	30.8	29.6	18.5	43.8
Rb	13.48	1.7	23.47	25.76	1.66	1.98	1.15	2.37	1.02	0.38
Sr	195.85	261.1	331.4	117.9	268.78	296.1	275.9	281.55	282.31	211.89
La	2	1.53	1.65	1.1	1.29	1.48	1.13	1.38	1	0.78
Ce	5.23	3.56	3.1	2.77	2.44	2.76	2.14	2.5	1.65	1.58
Pr	0.86	0.53	0.41	0.39	0.31	0.38	0.29	0.32	0.19	0.25
Nd	4.36	2.7	1.79	1.5	1.48	1.6	1.36	1.41	0.84	1.18
Sm	1.46	0.87	0.48	0.46	0.36	0.43	0.37	0.39	0.2	0.44
Eu	0.68	0.61	0.58	0.54	0.43	0.54	0.47	0.47	0.44	0.4
Gd	1.76	1.03	0.65	0.79	0.45	0.54	0.48	0.47	0.24	0.61
Tb	0.29	0.16	0.1	0.16	0.08	0.09	0.08	0.09	0.03	0.1
Dy	1.92	1.15	0.71	1.1	0.53	0.55	0.55	0.57	0.26	0.7
Ho	0.39	0.23	0.14	0.24	0.12	0.11	0.12	0.12	0.05	0.15
Er	1.05	0.68	0.44	0.7	0.33	0.35	0.34	0.38	0.15	0.44
Tm	0.17	0.11	0.06	0.11	0.05	0.06	0.05	0.06	0.03	0.06
Yb	1.06	0.71	0.4	0.68	0.28	0.34	0.33	0.32	0.14	0.43
Lu	0.16	0.1	0.07	0.1	0.05	0.04	0.05	0.06	0.02	0.07
Zr	11.6	7.3	7.2	4.6	6.3	7.4	5.8	6.5	6.9	8
Y	9.58	5.77	3.49	5.86	2.74	2.86	2.91	2.97	1.26	3.71
Pb	6.5	2.1	8.5	2	1.4	1	0.6	1.3	1.6	1.5
Zn	92	90	93	66	115	111	106	106	126	150
Th	0.13	0.04	0.04	0.03	0.04	0.05	0.05	0.05	0.03	0.02
U	0.03	0.01	0.01	0.05	0.01	0.01	0.01	0.01	X	X

E.2 (continued) Trace element elements data for Rhovan drill core samples

Sample	S53	S52	S51	S50	S49	S48	S47	S46	S45	S44
Height above lowermost sample (m)	19.63	20.63	22.63	23.63	24.63	25.63	29.58	35.63	45.63	55.63
Parts per million										
Cr	9	11	7	9	7	9	6	8	5	4
V	3387	5139	3234	4640	2939	4318	2641	2602	1773	1364
Ni	191.5	256.2	181.7	223.2	165.3	217.4	149	133.9	111.7	98.6
Sc	29.6	20.1	37.2	27.8	31.3	29.1	20.5	26.4	45.2	57.5
Rb	0.42	0.3	0.42	0.32	0.56	0.48	0.79	0.71	1.27	0.61
Sr	259.59	228.69	236.33	222.29	267.35	227.99	228.26	288.7	252.19	207.99
La	0.89	0.79	0.82	0.73	1.06	0.79	0.84	1.08	1.07	0.85
Ce	1.45	1.26	1.61	1.23	1.81	1.37	1.49	1.82	1.96	1.81
Pr	0.18	0.14	0.22	0.15	0.23	0.17	0.18	0.23	0.28	0.27
Nd	0.78	0.52	1.01	0.63	1.06	0.73	0.79	0.98	1.29	1.42
Sm	0.22	0.1	0.31	0.16	0.34	0.2	0.21	0.26	0.42	0.5
Eu	0.4	0.34	0.42	0.33	0.45	0.35	0.32	0.42	0.4	0.39
Gd	0.29	0.12	0.46	0.23	0.39	0.26	0.27	0.34	0.62	0.72
Tb	0.05	0.02	0.08	0.04	0.07	0.05	0.05	0.06	0.11	0.13
Dy	0.32	0.13	0.57	0.25	0.44	0.3	0.35	0.36	0.74	0.95
Ho	0.08	0.02	0.12	0.05	0.1	0.06	0.07	0.08	0.15	0.2
Er	0.2	0.07	0.35	0.16	0.29	0.19	0.21	0.23	0.43	0.58
Tm	0.03	0.01	0.05	0.03	0.05	0.03	0.03	0.04	0.07	0.09
Yb	0.18	0.07	0.31	0.14	0.29	0.19	0.24	0.22	0.43	0.59
Lu	0.03	0.01	0.05	0.03	0.05	0.03	0.03	0.04	0.07	0.09
Zr	8.6	10.1	7	9	8.5	8.2	5.8	5.4	5	4.5
Y	1.66	0.55	2.86	1.31	2.43	1.57	1.67	1.93	3.92	4.91
Pb	1.6	1.9	1.6	1.6	1.7	2	2.1	1.2	2	0.6
Zn	146	211	150	196	144	190	133	130	107	103
Th	0.03	0.02	0.03	0.03	0.04	0.03	0.02	0.04	0.04	0.03
U	X	X X	X	X	0.01	X	X	X	0.01	X

E.2 (continued) Trace element elements data for Rhovan drill core samples

Sample	S43	S42	S41.2	S41.1	S40	S39	S38	S37	S36	S35
Height above lowermost sample (m)	65.63	75.63	82.58	82.78	84.28	84.63	85.63	86.63	87.63	88.63
Parts per million										
Cr	5	4	6	542	951	390	441	37	32	8
V	1525	1277	1007	3826	3823	1564	4765	4053	4807	2425
Ni	96.8	89.5	96.2	280.2	310.8	63.2	246.9	218.1	312.1	208.9
Sc	52.2	56.1	55.4	54.5	48.2	6.4	16	16.3	17.6	37.3
Rb	0.83	0.55	2.68	0.88	0.54	1.51	0.87	0.92	0.89	1.45
Sr	240.67	217.13	230.8	4.74	14.85	404.21	241.49	295.47	296.03	236.53
La	0.9	0.78	1.08	0.99	0.61	1.84	0.79	1.27	1.06	1.15
Ce	1.89	1.6	2.34	3.08	1.95	3.04	1.27	2.08	1.75	2.34
Pr	0.27	0.24	0.34	0.51	0.32	0.31	0.12	0.23	0.18	0.3
Nd	1.39	1.24	1.55	2.77	1.81	1.04	0.39	0.82	0.66	1.36
Sm	0.45	0.46	0.5	0.9	0.59	0.18	0.07	0.15	0.11	0.38
Eu	0.41	0.36	0.37	0.19	0.16	0.54	0.22	0.25	0.22	0.25
Gd	0.63	0.61	0.72	1.09	0.75	0.16	0.07	0.16	0.15	0.44
Tb	0.12	0.12	0.13	0.19	0.12	0.02	0.01	0.03	0.02	0.07
Dy	0.79	0.79	0.87	1.18	0.77	0.13	0.05	0.15	0.12	0.51
Ho	0.17	0.17	0.18	0.23	0.15	0.03	X	0.03	0.02	0.1
Er	0.52	0.5	0.54	0.68	0.44	0.07	0.03	0.09	0.08	0.29
Tm	0.08	0.08	0.08	0.1	0.06	0.01	X	0.02	0.01	0.04
Yb	0.5	0.5	0.57	0.61	0.37	0.06	0.03	0.07	0.07	0.28
Lu	0.08	0.08	0.08	0.1	0.06	X	X	0.01	0.01	0.04
Zr	5	3.5	4.8	48.8	35.2	5.6	5.8	6.6	6.4	6.2
Y	4.24	4.06	4.45	6	3.8	0.62	0.26	0.76	0.59	2.63
Pb	0.9	0.6	1.8	10	X	1.3	0.7	0.7	1.6	1.4
Zn	98	109	81	386	366	75	178	132	146	92
Th	0.04	0.04	0.03	0.16	0.08	0.07	0.06	0.06	0.06	0.07
U	X	0.01	X	0.08	0.04	0.02	X	0.02	0.01	0.01

E.2 (continued) Trace element elements data for Rhovan drill core samples

Sample	S34	S33	S32.3	S32.2	S32.1	S31	S30.4	S30.3	S30.2	S30.1
Height above lowermost sample (m)	89.63	90.63	91.47	91.59	91.88	92.17	93.18	93.29	93.555	93.65
Parts per million										
Cr	9	5	6	1453	307	242	90	1006	1115	50
V	3347	1256	1348	8707	4326	4001	2991	5804	4845	745
Ni	247.1	499.3	688.5	623.3	463.9	260.4	169.2	316.2	282.3	88.9
Sc	41.1	56.9	59.6	33.8	13.6	15.2	21.1	30.4	45.3	48.1
Rb	0.84	3.2	1.98	0.15	0.67	0.82	1.61	0.17	0.17	1.67
Sr	231.32	172.73	169.33	0.86	282.21	279.05	313.42	1.8	5.35	286
La	0.52	1.19	1.73	0.09	1.03	1	1.99	0.12	0.51	2.28
Ce	1.09	2.47	4.28	0.26	1.57	1.68	3.67	0.29	1.71	5.3
Pr	0.16	0.34	0.62	0.04	0.17	0.18	0.43	0.04	0.31	0.77
Nd	0.82	1.73	3.11	0.22	0.51	0.61	1.72	0.25	1.61	3.83
Sm	0.32	0.55	0.88	0.09	0.07	0.12	0.38	0.07	0.56	1.16
Eu	0.29	0.4	0.46	0.02	0.39	0.25	0.71	0.02	0.12	0.88
Gd	0.41	0.84	1.07	0.08	0.06	0.13	0.38	0.09	0.66	1.45
Tb	0.08	0.14	0.17	0.02	0.01	0.02	0.07	0.02	0.11	0.24
Dy	0.51	0.92	1.18	0.1	0.04	0.1	0.38	0.1	0.72	1.53
Ho	0.11	0.2	0.25	0.02	X	0.02	0.08	0.02	0.14	0.3
Er	0.32	0.58	0.73	0.07	0.03	0.05	0.22	0.06	0.39	0.84
Tm	0.05	0.09	0.1	0.01	X	0.01	0.04	0.01	0.05	0.12
Yb	0.3	0.57	0.68	0.07	0.02	0.06	0.24	0.07	0.36	0.79
Lu	0.05	0.08	0.1	X	X	0.01	0.03	0.01	0.06	0.13
Zr	3.6	7	9.6	19.4	8.7	6.8	10.9	34.9	31.2	11.6
Y	2.65	4.91	6.1	0.47	0.19	0.56	2.08	0.54	3.4	7.5
Pb	1.1	21.5	12	0.7	8.2	1.5	1.6	X	X	1
Zn	126	92	99	396	163	146	139	430	398	93
Th	0.01	0.32	0.18	0.01	0.03	0.05	0.17	0.06	0.07	0.16
U	X	0.07	0.04	0.01	X	0.01	0.04	0.03	0.02	0.02

E.2 (continued) Trace element elements data for Rhovan drill core samples

Sample	WLS Bot	WLS Top	S29	S28,3	S28,2	S28,1	S27,3	S27.1	S26	S25
Height above lowermost sample (m)	93.75	93.83	94.42	95.76	95.92	96.13	97.34	97.6	98.63	99.63
Parts per million										
Cr	64	27	23	6	12	9	53	48	6	4
V	959	4245	6939	5666	8250	8305	6719	6254	4516	3177
Ni	166.5	209.2	353.1	270.5	343.2	335.2	288.2	250.1	179	126.9
Sc	78.9	14.2	22.3	19	25.7	18.2	22.9	19	16.1	11.3
Rb	0.66	0.53	0.09	0.11	0.06	X	0.07	0.24	0.22	0.93
Sr	136.96	246.96	140.54	205.04	60.62	57.68	134.91	180.31	250.3	252.36
La	1.83	0.52	0.25	0.37	0.12	0.09	0.25	0.5	0.52	0.91
Ce	5.36	0.89	0.33	0.54	0.17	0.14	0.36	0.7	0.71	1.42
Pr	0.96	0.1	0.03	0.05	0.01	0.02	0.03	0.06	0.07	0.15
Nd	5.11	0.31	0.08	0.14	0.05	0.05	0.11	0.24	0.23	0.54
Sm	1.62	0.06	0.02	0.02	X	X	0.02	0.03	0.03	0.1
Eu	0.73	0.26	0.14	0.15	0.05	0.05	0.15	0.26	0.28	0.25
Gd	2.16	0.05	0.02	0.02	X	0.01	0.02	0.02	0.04	0.08
Tb	0.37	0.01	X	X	X	X	X	X	X	0.01
Dy	2.33	0.04	0.02	0.02	X	0.01	X	0.02	0.03	0.06
Ho	0.45	0.01	X	X	X	X	X	X	X	0.01
Er	1.25	0.03	X	X	X	0.01	X	0.01	0.02	0.05
Tm	0.19	X	X	X	X	X	X	X	X	X
Yb	1.13	0.03	0.01	X	X	X	0.01	0.02	0.03	0.04
Lu	0.18	X	X	X	X	X	X	X	X	X
Zr	14.8	9.6	9.2	10	14.6	14.8	11.9	13	9.2	6.9
Y	11.31	0.17	X	0.06	X	X	0.06	0.08	0.15	0.35
Pb	0.9	1.7	2.4	1.9	1.1	1.2	2.2	2.5	1.9	3
Zn	130	204	300	227	357	342	284	258	200	146
Th	0.09	0.02	0.01	0.01	X	X	X	0.02	0.02	0.07
U	0.02	X	X	X	X	X	X	X	0.01	0.02

E.2 (continued) Trace element elements data for Rhovan drill core samples

Sample	S24	S23	S22.2	CX	S22.1	S20	N2	S19	S18.6	S18.5
Height above lowermost sample (m)	101.63	102.63	103.33	103.49	103.54	105.63	110.63	115.63	118.53	118.68
Parts per million										
Cr	3	7	9	124	130	11	19	13	15	45
V	3884	3895	4076	4954	4683	2889	1653	1022	937	2878
Ni	137.9	123.1	130.3	141.5	136.3	90	54.2	37.7	109.6	113
Sc	15	15.4	17.1	19.5	18.9	11.2	9.4	8.6	9	19.9
Rb	0.86	0.34	0.33	0.32	0.68	1.71	1.67	2.51	7.07	0.26
Sr	266.3	257.45	230.53	185.12	191.42	265.2	303.69	315.6	257.85	20.05
La	0.86	0.7	0.55	0.34	0.5	1.56	1.81	1.86	2.19	0.38
Ce	1.34	1.03	0.78	0.54	0.87	2.68	3.02	3.12	3.93	0.74
Pr	0.14	0.1	0.07	0.06	0.09	0.3	0.31	0.33	0.4	0.08
Nd	0.45	0.34	0.26	0.21	0.34	1.01	1.16	1.11	1.53	0.31
Sm	0.07	0.05	0.03	0.04	0.07	0.2	0.23	0.21	0.29	0.06
Eu	0.33	0.39	0.24	0.13	0.12	0.36	0.49	0.47	0.39	0.04
Gd	0.08	0.04	0.03	0.06	0.07	0.18	0.17	0.21	0.25	0.08
Tb	0.01	X	X	X	0.01	0.03	0.03	0.03	0.04	0.02
Dy	0.07	0.03	0.04	0.07	0.05	0.16	0.13	0.15	0.26	0.11
Ho	0.01	X	X	X	0.01	0.03	0.03	0.03	0.06	0.03
Er	0.04	0.02	0.02	0.03	0.04	0.11	0.09	0.1	0.18	0.11
Tm	X	X	X	X	0.01	0.02	0.02	0.02	0.03	0.02
Yb	0.04	0.02	0.04	0.04	0.04	0.1	0.12	0.13	0.21	0.15
Lu	X	X	X	X	X	0.02	0.02	0.02	0.04	0.02
Zr	9	6.5	5.3	7.5	7.7	11.5	10.2	9.4	13.1	17.5
Y	0.33	0.14	0.18	0.24	0.32	0.94	0.77	0.82	1.53	0.76
Pb	2	2.4	1.3	1.1	2	1.5	2	1.4	4.9	0.7
Zn	185	199	217	251	234	126	74	83	107	293
Th	0.08	0.03	0.03	0.04	0.06	0.15	0.1	0.1	0.34	0.1
U	0.02	X	0.01	0.01	0.02	0.04	0.03	0.03	0.07	0.05

E.2 (continued) Trace element elements data for Rhovan drill core samples

Sample	S18.4	S18.3	S18.2	S18.1	S21.3	S21.2	S21.1	S17	N6	N5
Height above lowermost sample (m)	118.86	118.945	119.1	119.21	120.36	120.46	120.63	125.63	130.73	130.93
Parts per million										
Cr	50	60	230	13	10	3	7	6	152	2
V	2503	2731	4265	915	1578	133	871	1085	881	25
Ni	113.8	123.4	125.6	66.5	62.9	9.4	57.2	81.1	63.1	17.3
Sc	18.7	19	26.2	9	8.3	2	8.1	7.6	10.5	2.3
Rb	0.39	0.49	0.38	6	1.23	3.39	1.54	1.67	1.3	1.38
Sr	26.03	23.18	23.11	303.38	302.54	473.35	247.03	352.51	301.83	397
La	0.49	0.43	0.24	1.61	1.9	3.64	2.16	1.95	1.7	2.34
Ce	0.85	0.75	0.38	2.67	3.31	6.95	3.77	3.2	2.85	4.76
Pr	0.1	0.08	0.04	0.29	0.36	0.77	0.38	0.33	0.3	0.55
Nd	0.33	0.29	0.18	1.01	1.23	2.99	1.36	1.2	1.1	2.11
Sm	0.06	0.05	0.07	0.19	0.19	0.56	0.26	0.19	0.22	0.44
Eu	0.06	0.06	0.03	0.41	0.4	0.61	0.46	0.42	0.35	0.49
Gd	0.07	0.05	0.05	0.19	0.18	0.53	0.28	0.16	0.18	0.44
Tb	0.02	0.01	0.02	0.03	0.03	0.09	0.04	0.02	0.04	0.08
Dy	0.1	0.08	0.09	0.15	0.15	0.49	0.3	0.12	0.22	0.45
Ho	0.03	0.02	0.02	0.04	0.02	0.1	0.06	0.03	0.05	0.1
Er	0.1	0.1	0.06	0.12	0.07	0.27	0.2	0.09	0.17	0.28
Tm	0.02	0.02	0.01	0.02	0.01	0.04	0.03	0.02	0.04	0.04
Yb	0.14	0.14	0.1	0.13	0.08	0.23	0.21	0.1	0.2	0.24
Lu	0.03	0.03	0.02	0.03	0.02	0.03	0.04	0.02	0.04	0.04
Zr	15.6	16.6	26.9	7.9	21.9	10.3	10.5	9	11.8	8.9
Y	0.68	0.59	0.4	0.85	0.66	2.5	1.55	0.7	1.18	2.14
Pb	0.8	1.5	1.5	4.1	4.1	2.9	3.2	1.5	3.3	3.5
Zn	272	281	367	117	140	19	100	122	148	17
Th	0.08	0.06	0.1	0.12	0.08	0.74	0.15	0.09	0.1	0.43
U	0.04	0.04	0.05	0.02	0.04	0.18	0.04	0.02	0.03	0.1

E.2 (continued) Trace element elements data for Rhovan drill core samples

Sample	N7	N8.2	N8.1	S16	S15	N4.2	N4.1	N3	S14	S13.1
Height above lowermost sample (m)	132.03	132.53	132.78	135.63	146.63	152.13	152.38	154.63	154.73	155.38
Parts per million										
Cr	4	3	38	59	6	45	4	233	246	63
V	34	19	434	756	1561	1055	151	603	368	309
Ni	2.5	3.5	22.3	23.6	23.4	18.4	36.4	147.7	110.4	62.6
Sc	1	1.1	2.7	14	11.6	11.3	9.1	18	19.5	7.1
Rb	2.36	3.68	1.47	1.65	1.75	1.71	2.47	3.91	8.06	6.81
Sr	408.3	351.77	459.16	334.25	247.87	331.48	270.7	270.27	296.66	440.24
La	2.44	1.79	3.55	2.39	1.94	2.74	2.84	3.91	6.34	4.53
Ce	4.78	3.64	6.33	4.39	3.54	4.92	5.32	7.49	12.63	8.02
Pr	0.53	0.41	0.71	0.51	0.4	0.55	0.62	0.92	1.48	0.86
Nd	1.76	1.58	2.51	2.04	1.58	2.25	2.58	3.61	5.96	3.09
Sm	0.34	0.33	0.43	0.45	0.36	0.44	0.54	0.85	1.4	0.57
Eu	0.45	0.29	0.67	0.53	0.34	0.47	0.42	0.56	0.74	0.81
Gd	0.28	0.35	0.4	0.49	0.32	0.47	0.61	0.99	1.49	0.58
Tb	0.04	0.06	0.06	0.09	0.07	0.07	0.11	0.17	0.26	0.09
Dy	0.29	0.35	0.32	0.6	0.41	0.5	0.69	1.12	1.6	0.56
Ho	0.05	0.08	0.07	0.13	0.09	0.1	0.14	0.24	0.33	0.12
Er	0.15	0.23	0.18	0.38	0.26	0.29	0.43	0.75	0.99	0.33
Tm	0.03	0.04	0.03	0.06	0.05	0.05	0.07	0.12	0.17	0.05
Yb	0.12	0.24	0.15	0.41	0.31	0.28	0.45	0.78	1.09	0.29
Lu	0.02	0.04	0.02	0.07	0.05	0.05	0.08	0.13	0.17	0.05
Zr	7.4	10.5	10.8	10.9	10.7	12.2	8.6	18.6	27.5	10.4
Y	1.21	1.75	1.48	3.21	2.27	2.38	3.46	6.03	9.11	3
Pb	2.2	2.7	2.8	1.9	1.8	5.4	3.1	4.4	5.8	4.6
Zn	13	19	47	103	115	96	81	109	98	35
Th	0.46	0.42	0.49	0.2	0.21	0.17	0.35	0.53	1.49	0.36
U	0.1	0.11	0.13	0.05	0.05	0.04	0.1	0.15	0.33	0.11

E.2 (continued) Trace element elements data for Rhovan drill core samples

Sample	S12	S11	N1	S10.3	S10.2	S10.1	S09.2	S09.1	S08
Height above lowermost sample (m)	161.63	167.13	167.83	170.69	170.87	171.12	171.17	171.28	171.43
Parts per million									
Cr	92	115	74	82	187	7	12606	5669	4328
V	229	211	159	160	349	142	9091	8506	9902
Ni	66.3	86.5	64.8	94.9	109.8	305	547	505.1	490.1
Sc	18.3	27.6	22.4	24.7	34	0.7	23.6	21.4	27.6
Rb	2.72	2.32	3.39	6.94	8.28	18.7	0.19	0.09	X
Sr	341.89	305.34	326.54	310.12	257.92	438.67	2.78	2.6	1.12
La	3.6	3.64	3.77	4.1	2.86	3.74	0.42	0.28	0.08
Ce	6.75	6.96	7.26	7.75	5.7	6.62	0.56	0.38	0.16
Pr	0.74	0.82	0.88	0.88	0.7	0.68	0.05	0.03	0.02
Nd	2.95	3.46	3.64	3.45	3.05	2.28	0.22	0.12	0.06
Sm	0.65	0.83	0.87	0.82	0.81	0.35	0.03	0.02	0.01
Eu	0.7	0.66	0.67	0.65	0.53	0.62	0.05	0.03	X
Gd	0.77	1	0.98	0.97	0.96	0.34	0.04	0.02	0.02
Tb	0.13	0.18	0.16	0.16	0.16	0.05	X	X	X
Dy	0.82	1.23	1.08	1.06	1.11	0.24	0.04	0.03	0.02
Ho	0.18	0.26	0.23	0.22	0.25	0.05	X	X	X
Er	0.56	0.76	0.69	0.74	0.78	0.12	0.03	0.01	0.01
Tm	0.09	0.13	0.11	0.11	0.12	0.02	X	X	X
Yb	0.57	0.82	0.71	0.76	0.8	0.13	0.04	0.03	0.02
Lu	0.09	0.13	0.12	0.12	0.11	0.03	X	X	X
Zr	10.4	11.5	12.5	14.4	15.1	9.4	20.2	19.8	23.8
Y	4.69	6.75	5.7	6.16	6.44	1.31	0.25	0.12	0.07
Pb	3.9	2.7	2.9	3.3	4.7	10.1	9.3	1.9	1.2
Zn	73	82	67	98	63	92	755	334	290
Th	0.46	0.51	0.58	1.05	0.6	1.6	0.05	0.02	0.07
U	0.12	0.12	0.17	0.2	0.16	0.37	0.06	0.04	0.05

E.2 (continued) Trace element elements data for Rhovan drill core samples

Sample	S07	S06	S05	S04	S03	S02	S01
Height above lowermost sample (m)	171.63	172.33	173.13	173.68	173.79	174.13	175.63
Parts per million							
Cr	2037	830	388	2271	730	116	100
V	10136	9907	9656	9480	6383	1424	2118
Ni	558.8	567.4	440.5	459	396.2	107.3	145.7
Sc	29.1	29.2	26	28	22.7	6	7
Rb	X	X	X	0.13	1.45	3.58	1.6
Sr	1.28	1.61	1	2.06	81.52	398.09	320.35
La	0.05	0.08	0.09	0.14	0.8	3.15	1.91
Ce	0.12	0.14	0.2	0.28	1.37	5.24	3.43
Pr	0.01	0.02	0.03	0.03	0.14	0.56	0.35
Nd	0.03	0.06	0.1	0.11	0.57	2	1.34
Sm	0.02	0.02	0.03	0.03	0.09	0.34	0.22
Eu	X	X	X	X	0.17	0.64	0.47
Gd	0.02	0.02	0.03	0.02	0.09	0.3	0.2
Tb	X	X	X	X	0.02	0.05	0.03
Dy	0.02	0.02	0.03	0.03	0.08	0.25	0.14
Ho	X	X	X	X	0.02	0.04	0.03
Er	0.02	0.02	0.03	0.02	0.05	0.14	0.07
Tm	X	X	X	X	0.01	0.02	0.02
Yb	0.02	0.03	0.03	0.03	0.05	0.14	0.07
Lu	X	X	X	X	X	0.02	X
Zr	23.9	22.5	21.6	22.2	19.9	11.6	11.2
Y	0.1	0.12	0.12	0.18	0.42	1.27	0.73
Pb	0.9	0.9	1.3	1.7	2.3	3.1	3.6
Zn	347	311	400	302	286	106	190
Th	0.03	0.03	0.03	0.06	0.11	0.38	0.29
U	0.04	0.17	0.02	0.08	0.06	0.07	0.08

Appendix F: Portable XRF data for the lateral profile long the base of the Main Magnetite Layer

F.1 Portable XRF data for the lateral profile long the base of the Main Magnetite Layer (Figure 4.12)

Lateral distance (m)	Ti (ppm)	Ti 2Θ Error (ppm)	V (ppm)	V 2Θ Error (ppm)	Cr (ppm)	Cr 2Θ Error (ppm)	Cr/V	Cr/V*9757	Cr/V* 9757 2Θ error
0	21759	323	2295	106	4650	82	2.02	19768	1432
0.04	61781	704	6724	232	17711	205	2.63	25701	1330
0.08	26608	429	3058	144	7283	122	2.38	23236	1684
0.12	43256	513	3927	163	9740	134	2.48	24203	1512
0.16	34529	473	3236	152	7670	123	2.36	23123	1651
0.2	43313	503	4612	165	8161	122	1.76	17267	985
0.24	64214	677	6815	222	13428	172	1.97	19225	976
0.28	68434	720	7067	235	14733	184	2.08	20340	1043
0.32	56207	622	5994	204	7928	134	1.32	12904	738
0.36	62289	608	6006	196	11026	141	1.83	17912	909
0.4	46730	509	5156	168	12278	143	2.38	23236	1151
0.44	41618	514	4656	171	10303	140	2.21	21590	1221
0.48	60281	630	6238	206	13735	167	2.20	21483	1086
0.52	59164	624	6296	205	14829	171	2.35	22980	1132
0.56	46781	554	5196	183	14386	166	2.76	27013	1420
0.6	57778	608	5967	198	19013	189	3.18	31087	1504
0.64	77461	794	8013	259	24655	243	3.07	30021	1419
0.68	66917	695	6642	225	25139	231	3.78	36929	1781
0.72	48964	533	5159	174	13012	151	2.52	24606	1252

F.1 (continued) Portable XRF data for the lateral profile long the base of the Main Magnetite Layer (Figure 4.12)

Lateral distance (m)	Ti (ppm)	Ti 2Θ Error (ppm)	V (ppm)	V 2Θ Error (ppm)	Cr (ppm)	Cr 2Θ Error (ppm)	Cr/V	Cr/V*9757	Cr/V* 9757 2Θ error
0.76	51592	570	5266	186	9796	139	1.860319	18151	1006
0.8	9840	220	1048	71	3288	67	3.138352	30621	3135
0.84	48234	515	4718	166	17239	167	3.653664	35649	1797
0.88	28495	408	3037	134	10450	133	3.441377	33578	2162
0.92	19786	331	2151	108	6024	98	2.800854	27328	2076
1.04	30801	426	3362	141	4248	92	1.263766	12331	888
1.08	72057	699	7494	228	9192	144	1.226595	11968	616
1.12	51235	531	5418	174	7725	117	1.425843	13912	736
1.16	53228	557	5478	182	11881	146	2.168979	21163	1077
1.2	54655	579	5726	189	14824	165	2.588796	25259	1251
1.24	70838	714	6976	230	17685	197	2.534933	24733	1223
1.28	51930	545	5150	176	18360	176	3.565138	34785	1708
1.32	30022	407	2962	132	12193	140	4.116702	40167	2546
1.36	41100	547	4128	178	16956	189	4.107234	40074	2456
1.4	70548	720	6871	232	18446	202	2.684775	26195	1312
1.44	22382	329	2396	108	9969	117	4.160717	40596	2622
1.48	53554	562	4922	179	21921	194	4.453825	43456	2212
1.52	74035	750	6778	239	29620	258	4.369841	42637	2104
1.56	62540	657	6060	212	25035	225	4.131031	40306	1986
1.6	62406	684	6098	221	24263	231	3.978567	38819	1996

F.1 (continued) Portable XRF data for the lateral profile long the base of the Main Magnetite Layer (Figure 4.12)

Lateral distance (m)	Ti (ppm)	Ti 2Θ Error (ppm)	V (ppm)	V 2Θ Error (ppm)	Cr (ppm)	Cr 2Θ Error (ppm)	Cr/V	Cr/V*9757	Cr/V* 9757 2Θ error
1.64	24386	337	2473	109	8164	105	3.300788	32206	2083
1.68	38157	484	4220	160	12225	149	2.896567	28262	1596
1.72	36519	525	3964	173	6099	121	1.538436	15011	1079
1.76	53333	587	5556	192	7774	127	1.399178	13652	780
1.8	34571	456	4247	155	10812	138	2.545721	24839	1373
1.84	24915	396	3302	137	5467	103	1.655824	16156	1099
1.88	40469	552	4515	183	9508	146	2.106123	20549	1296
1.92	58136	596	6319	196	10763	143	1.703211	16618	824
1.96	26103	329	2679	107	4217	75	1.573953	15357	999
2	73009	710	6917	228	8425	140	1.21795	11884	658
2.04	55587	566	4926	179	7011	116	1.423185	13886	825
2.08	54664	545	5081	174	7594	115	1.494556	14582	808
2.2	62386	668	5705	213	6934	129	1.215587	11860	746
2.24	81996	753	7217	238	9198	145	1.2746	12436	679
2.28	33050	413	2974	131	3870	82	1.301142	12695	940
2.32	69948	667	6188	211	8130	131	1.313721	12818	721
2.36	49009	534	5124	174	6656	112	1.298995	12674	723
2.4	64016	602	5780	191	8273	123	1.431213	13964	749
2.44	54861	619	4935	196	7068	127	1.432165	13974	911
2.48	53234	541	5246	175	8323	121	1.586554	15480	830

F.1 (continued) Portable XRF data for the lateral profile long the base of the Main Magnetite Layer (Figure 4.12)

Lateral distance (m)	Ti (ppm)	Ti 2Θ Error (ppm)	V (ppm)	V 2Θ Error (ppm)	Cr (ppm)	Cr 2Θ Error (ppm)	Cr/V	Cr/V*9757	Cr/V* 9757 2Θ error
2.52	64289	650	6669	212	10439	147	1.56	15272	784
2.56	72277	756	7494	247	11944	174	1.59	15551	827
2.6	61280	613	6150	199	9606	138	1.56	15238	795
2.64	70128	679	6865	219	10460	148	1.52	14868	766
2.68	49458	528	5011	172	7347	116	1.46	14307	804
2.72	83469	808	8452	262	13108	180	1.55	15131	757
2.76	60857	622	6297	203	8845	136	1.40	13704	730
2.8	79225	770	8129	251	13176	177	1.62	15815	782
2.84	76118	737	7761	240	13421	174	1.72	16872	826
2.88	81434	789	8266	256	13138	178	1.58	15508	772
2.92	51540	610	5280	198	8423	140	1.59	15567	949
2.96	60806	619	6235	201	11297	149	1.81	17679	900
3	15078	281	1655	93	2442	65	1.47	14395	1370
3.08	59391	598	5723	192	11137	144	1.94	18986	990
3.12	47707	517	4898	169	7833	118	1.59	15604	866
3.16	57052	586	5907	191	10900	143	1.84	18003	916
3.2	70921	695	7104	225	9946	148	1.39	13660	710
3.24	74101	748	7737	244	10858	162	1.40	13693	713
3.28	13704	272	1397	87	1897	57	1.35	13254	1417
3.32	4391	128	547	42	1189	35	2.17	21210	2624

F.1 (continued) Portable XRF data for the lateral profile long the base of the Main Magnetite Layer (Figure 4.12)

Lateral distance (m)	Ti (ppm)	Ti 2Θ Error (ppm)	V (ppm)	V 2Θ Error (ppm)	Cr (ppm)	Cr 2Θ Error (ppm)	Cr/V	Cr/V*9757	Cr/V* 9757 2Θ error
3.36	52979	576	5614	189	6927	120	1.23	12040	689
3.44	52058	559	5250	181	7052	117	1.34	13106	752
3.48	67369	677	6621	219	8792	140	1.32	12956	710
3.52	56857	565	5881	184	6580	111	1.11	10917	588
3.56	36964	457	3840	149	4069	88	1.05	10339	704
3.6	36992	530	3909	174	4326	106	1.10	10798	844
3.64	50273	539	5153	175	6326	110	1.22	11977	690
3.68	61806	639	6399	208	15060	173	2.35	22964	1133
3.72	58769	614	6216	201	15115	171	2.43	23727	1160
3.76	63575	650	6912	214	16528	180	2.39	23330	1093
3.8	46905	589	4758	191	10072	151	2.11	20655	1285
3.92	45977	501	3951	158	4254	89	1.07	10506	722
3.96	55160	582	5614	189	5923	111	1.05	10293	605
4	32198	501	3496	165	3506	98	1.00	9786	837
4.04	66473	630	6051	200	5995	112	0.99	9667	561
4.08	25689	594	2569	192	2621	110	1.02	9953	1364
4.12	51275	589	4314	185	4618	103	1.07	10444	770
4.16	48103	522	4617	168	4666	95	1.01	9862	627
4.2	56520	632	5614	205	5882	119	1.04	10223	651
4.36	36599	523	3753	170	3658	97	0.97	9512	775

F.1 (continued) Portable XRF data for the lateral profile long the base of the Main Magnetite Layer (Figure 4.12)

Lateral distance (m)	Ti (ppm)	Ti 2Θ Error (ppm)	V (ppm)	V 2Θ Error (ppm)	Cr (ppm)	Cr 2Θ Error (ppm)	Cr/V	Cr/V*9757	Cr/V* 9757 2Θ error
4.4	60581	610	5388	193	5762	109	1.06	10434	643
4.44	87379	846	7693	267	8452	152	1.09	10720	634
4.48	57734	639	5633	206	5796	118	1.02	10040	643
4.52	71328	758	6855	244	7116	139	1.03	10127	626
4.56	58085	647	5466	207	5553	117	1.01	9913	660
4.6	56542	615	5586	199	5986	115	1.07	10457	644
4.8	52453	648	5573	213	9794	154	1.75	17147	1042
4.84	64805	682	6530	221	9032	143	1.38	13495	752
4.88	80909	802	8244	261	11582	170	1.40	13708	710
4.92	68032	693	6854	225	9919	148	1.44	14121	754
5.24	87927	814	8293	260	10691	160	1.28	12579	653
5.28	68174	672	6281	214	9204	139	1.46	14297	789
5.32	81056	784	7867	252	10758	160	1.36	13342	701
5.36	73709	727	7017	233	9731	148	1.38	13530	735
5.4	74952	749	7317	241	10636	158	1.45	14184	761
5.44	61257	630	6045	203	7916	128	1.30	12778	713
5.48	76975	752	7622	243	10546	157	1.38	13499	706
5.52	76045	761	7847	248	12556	171	1.60	15612	790
5.56	80702	828	8659	272	14409	192	1.66	16236	812